Behavior of low-mass X-ray binaries and their formation in globular clusters

by

Arash Bahramian

A thesis submitted in partial fulfillment of the requirements for the degree of

Doctor of Philosophy

Department of Physics
University of Alberta

Abstract

Low mass X-ray binaries (LMXBs) are systems of compact stellar remnants accreting from a low mass companion star. These systems show various levels of mass transfer on various timescales. Many aspects of accretion in these systems are still not fully understood, specifically the emission processes involved in various states of mass transfer.

The population of LMXBs has been found to be orders of magnitude higher (per unit mass) in globular clusters (GCs) compared to the Galactic field. This overabundance has been explained as due to the formation of LMXBs by stellar encounters in GCs.

In this thesis, we study GC LMXB populations, and the details of accretion in these systems. First, we focus on the population of LMXBs and the role of stellar encounters in their formation in GCs. We calculate model-independent stellar encounter rates for 124 Galactic GCs, and show that core-collapsed clusters tend to have *lower* numbers of LMXBs compared to other clusters with similar values of the stellar encounter rate. Then, we focus on studying accretion in LMXBs in various classes of systems (quiescent, transient, ultra-compact and symbiotic). We provide evidence for the presence of low-level accretion in the rise and decay of outbursts in transient LMXBs, and the ab-

sence of low-level accretion in many quiescent neutron star LMXBs. Finally we study two peculiar LMXBs, and show that one is an ultra-compact X-ray binary, and another one is a symbiotic X-ray binary.

Preface

This thesis is original work by Arash Bahramian, conducted under supervision by Craig O. Heinke. Chapter 2 has been published as A. Bahramian, C. Heinke, G. Sivakoff, and J. Gladstone 2013, "Stellar Encounter Rate in Galactic Globular Clusters", ApJ, 766, 136. In this work, we calculate accurate values for stellar encounter rate for 124 Galactic globular clusters and for the first time, we estimate uncertainties on stellar encounter rates based on observational uncertainties using Monte-Carlo simulations. I performed all the data analyses, developed the simulation script, and wrote the paper. C. Heinke planned the project, supervised my work, and contributed to the introduction and discussion. G. Sivakoff and J. Gladstone provided suggestions and edits to the manuscript.

In Chapter 3, we describe our discovery of the third transient X-ray binary in globular cluster Terzan 5 and give details of our monitoring during this outburst. Our early detection of the outburst and continuous monitoring enabled us to find the first direct evidence regarding presence of a thermal component in rise (and fall) of an outburst in LMXBs. This chapter has been published as A. Bahramian, C. Heinke, G. Sivakoff, D. Altamirano, R. Wijnands, J. Homan, M. Linares, D. Pooley, N. Degenaar and J. Gladstone 2014, "Discovery of the Third Transient X-ray Binary in the Galactic Globular Cluster Terzan 5", ApJ, 780, 127. I performed all the data analysis in this chapter, and wrote the paper. C. Heinke planned much of the work, supervised my analyses, and contributed to the introduction and discussion. C. Heinke, D. Altamirano, R. Wijnands, D. Pooley, and N. Degenaar wrote proposals for X-ray observations that were used in this work. R. Wijnands first identified the outburst, and D. Altamirano

and M. Linares first identified the X-ray burst. All authors contributed to the manuscript.

In Chapter 4, we search for evidence of low-level accretion in quiescent ($L_X \sim 10^{32}$ erg s^{-1}) neutron star LMXBs (NS-LMXBs). We study X-ray spectral changes in a sample of 12 NS-LMXB candidates in globular clusters and we find no conclusive evidence for presence of accretion in any of these source. These results adds to the evidence against presence of accretion in quiescent NS-LMXBs. This was published as A. Bahramian, C. Heinke, N. Degenaar, L. Chomiuk, R. Wijnands, J. Strader, W. Ho and D. Pooley 2015, "Limits on thermal variations in a dozen quiescent neutron stars over a decade", MNRAS, 452, 3475. I performed all the data analysis in this chapter and wrote the paper. C. Heinke proposed the initial project plan, obtained some of the observations, supervised the work, and contributed to the introduction and discussion sections. N. Degenaar, L. Chomiuk, R. Wijnands, and D. Pooley wrote proposals for X-ray observations used in this work. W. Ho provided calculations of helium neutron star atmospheres. All authors contributed to the manuscript.

In Chapter 5, we study the X-ray (and radio) properties of one the first Galactic globular cluster candidate black holes, 47 Tuc X9. Our spectral analysis indicates presence of overabundant photo-ionized oxygen in the system, suggesting the companion is a C/O white dwarf and thus the system is an ultra-compact X-ray binary (with an orbital period of $\lesssim$80 min). This, if confirmed, makes 47 Tuc X9 the first detected ultracompact black hole X-ray binary. Additionally, we find evidence for reflected X-ray emission in this system, which given the source's luminosity ($\sim$ a few $\times 10^{33}$ erg s^{-1}), makes X9 one of the faintest LMXB to show X-ray reflection. This paper is submitted to MNRAS, as A. Bahramian, C. Heinke, V. Tudor, J. Miller-Jones, S. Bogdanov, T. Maccarone, C. Knigge, G. Sivakoff, L. Chomiuk, J. Strader, J. Garcia-Martinez, and T. Kallman 2016, "The ultracompact nature of the the black hole candi-

date 47 Tuc X9". I performed all of the X-ray analysis in this paper, had the ideas for several of the analyses, and wrote the paper. The radio analysis in this chapter was performed by V. Tudor and J. C. A. Miller-Jones. T. Kallman and J. Garcia-Martinez produced spectral models that I used in my X-ray analysis. C. Heinke prepared the original project plan, secured some of the X-ray data, supervised the work, and contributed to the introduction and discussion. J. Miller-Jones and S. Bogdanov obtained radio and X-ray observations used here. All authors contributed to the manuscript.

Finally in Chapter 6, we study X-ray and near infrared spectrum of a transient X-ray binary (XMMU J174445.5-295044). Through X-ray spectral analysis, we indicate that the accretor may be a neutron star (or less likely, a black hole) and our infrared analysis indicates that the donor is a cold M giant. Given the nature of the two stars in the system and sporadic nature of the outburst, we conclude this system is a symbiotic X-ray binary. This chapter was published as A. Bahramian, C. Heinke, J. Gladstone, R. Wijnands, R. Kaur and D. Altamirano 2014, "Revealing a new symbiotic X-ray binary with Gemini Near-infrared Integral Field Spectrograph", MNRAS, 441, 640. I performed most of the analysis in this chapter, and wrote the paper. J. C. Gladstone assisted with analysis of the near infrared data. C. Heinke planned the project, obtained the observations, and supervised the analysis. All authors contributed to the manuscript.

A significant part of results presented in this thesis are based on observations obtained from the following observatories: Chandra X-ray Observatory (in Chapters 3, 4, and 5), the Swift Gamma Ray Burst Explorer (in Chapters 3, 5, and 6), MAXI all sky X-ray monitor (in Chapter 3), NuSTAR astrophysical observatory (in Chapter 5), Gemini observatory (in Chapter 6), and the Jansky Very Large Array (in Chapter 5).

"No matter where I am, the sky is mine."

Sohrab Sepehri

To my mother, father and sister.

In memory of my brother, Arman Bahramian, who was the first to show me the wonders of night sky.

Acknowledgements

I thank my supervisor, Craig O. Heinke, for his mentoring, guidance, continuous support and great patience during my studies. I thank my family for their love and support.

I would like to thank members of my thesis committee, G. R. Sivakoff and N. Ivanova, for their helpful insights. I thank my mentors and collaborators, Jeanette C. Gladstone, Rudy Wijnands, Nathalie Degenaar, Erik W. Rosolowski, Diego Altamirano, Thomas J. Maccarone, James C. A. Miller-Jones, Nathan Leigh, Slavko Bogdanov, Sharon Morsink and Alessandro Patruno for their help and guidance. I would also like to thank my friends Robin M. Arnason, Stuart Gladstone, Kourosh Sartipi, Eric W. Koch, Alex J. Tetarenko, Bailey E. Tetarenko, Kaylie S. Green, Jose L. Nandez, Khaled Elshamouty and Sarah C. Nowicki for their support and friendship during my studies.

I acknowledge helpful discussions with Haldan Cohn, Phylis Lugger, Brian Murphy, Kevin S. D. Beach, Ivan Mizera, Hans A. Krimm, Tatehiro Mihara, Keith A. Arnaud, John Tomsick and Fiona A. Harrison.

Contents

List of Tables

List of Figures

xxiv

Chapter 1

Introduction

1.1 Low-mass X-ray binaries

Low mass X-ray binaries (LMXBs) are systems in which a compact object (white dwarf, neutron star or black hole) accretes matter from a low-mass companion star (typically a main sequence star). This may occur through Roche-lobe overflow (where material at the point on the companion star closest to the compact object feels equal gravitational pull from both stars, and thus a stream of matter leaks towards the compact object, Fig. 1.1) or, for red giants, wind-fed accretion (where the companion star produces a strong wind, a portion of which is captured by the compact object). (High-mass X-ray binaries, which are not the focus of this thesis, have a high-mass star, $\gtrsim$ twice the mass of our Sun, as the donor star.)

LMXBs can be classified into persistent systems with X-ray luminosities $\gtrsim 10^{36}$ erg/s, in which accretion continues at high rates, and transient systems, which show short (days to months) intervals of enhanced accretion as "outbursts", followed by long (years to decades) periods of quiescence, with X-ray luminosities $\sim 10^{30} - 10^{33}$ erg/s, and little or no accretion happening.
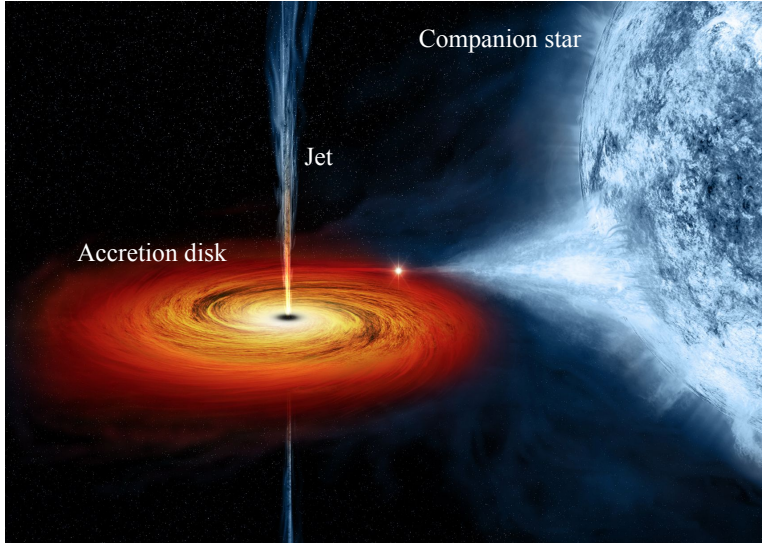
Figure 1.1: Illustration of accretion in an X-ray binary. Credit: NASA/CXC/M.Weiss

Outburst The transitions between outbursts ($L_X > 10^{36}$ erg/s) and quiescence ($L_X < 10^{33}$ erg/s) in LMXBs are not fully understood. The main obstacle in observational study of these stages is the limited sensitivity of monitoring X-ray telescopes. During the rise, the X-ray spectra of LMXBs become gradually harder, possibly due to increasing Comptonization of infalling matter. Although this has been postulated previously (Deufel et al., 2001), we present the first observational evidence for this effect in Chapter 3. The rise and spectral hardening continue until the LMXB reaches the "hard" or "low-hard" state, with $L_X \sim$ a few $\times 10^{36}$ erg/s. In this "low-hard" state, the X-ray spectrum is dominated by a non-thermal component with substantial emission between 1 and $\sim$ 50-100 keV, thought to be produced by a Comptonized corona around the compact object (e.g., see Mayer and Pringle, 2007). Generally (but not always), the low-hard state is followed by a brighter ($L_X \gtrsim 10^{37}$ erg/s) "soft state" (the "high-soft" state). In the high-soft state, the accretion disk reaches in closer to the compact object, such that a larger fraction of the total luminosity is radiated from the optically thick disk. Thus, the X-ray spectrum

2

becomes dominated by thermal blackbody-like emission from the disk, which is predominantly below ∼4 keV (e.g., see Gierliński et al., 1999). Figure 1.2 demonstrates the evolution of a typical outburst from an X-ray binary, and Figure 1.3 shows an X-ray light curve for such an outburst.

Nature of the Donor   One of the key factors affecting the length, brightness and evolution of the outburst in LMXBs is the nature of the donor star, as this then sets the orbital period, orbital separation, and thus the size and total accumulated mass of the accretion disk. The donor may be a main sequence star filling its Roche lobe (with orbital period of a few hours, up to a day), or can be a cool red giant in a wider orbit filling its Roche lobe (period of a few days, up to a month) or producing a strong wind (even longer periods). In cases with a cool giant donor, if accretion is via the giant's wind, these are known as symbiotic X-ray binaries. Symbiotic X-ray binaries tend to show very short outbursts (timescale of minutes to hours) as the accretion timescale is set by the size of clumps of wind that interact with the compact object (Kenyon, 1986; Belczyński et al., 2000). Yet another scenario is a white dwarf donor star, which requires a very tight orbit (orbital period $\lesssim$ 80 mins; Nelson et al., 1986). Such systems are called ultra-compact X-ray binaries, which can show either persistent and transient behavior (e.g., see Nelemans et al., 2010; Heinke et al., 2013). In Chapter 5, we identify a transient LMXB in quiescence as an ultracompact X-ray binary, by measuring the chemical composition of the accretion disk.

Quiescent behavior   In quiescence, X-ray emission from LMXBs typically includes non-thermal emission with a spectral shape described by a power-law (number of photons per energy bin goes as energy to a specified power, e.g. N(E)=$E^{-\alpha}$, where α is called the photon index). In black hole LMXBs (BH-LMXBs), this non-thermal emission may be associated with the jet or synchrotron radiation near the black hole (Plotkin et al., 2013). In neutron
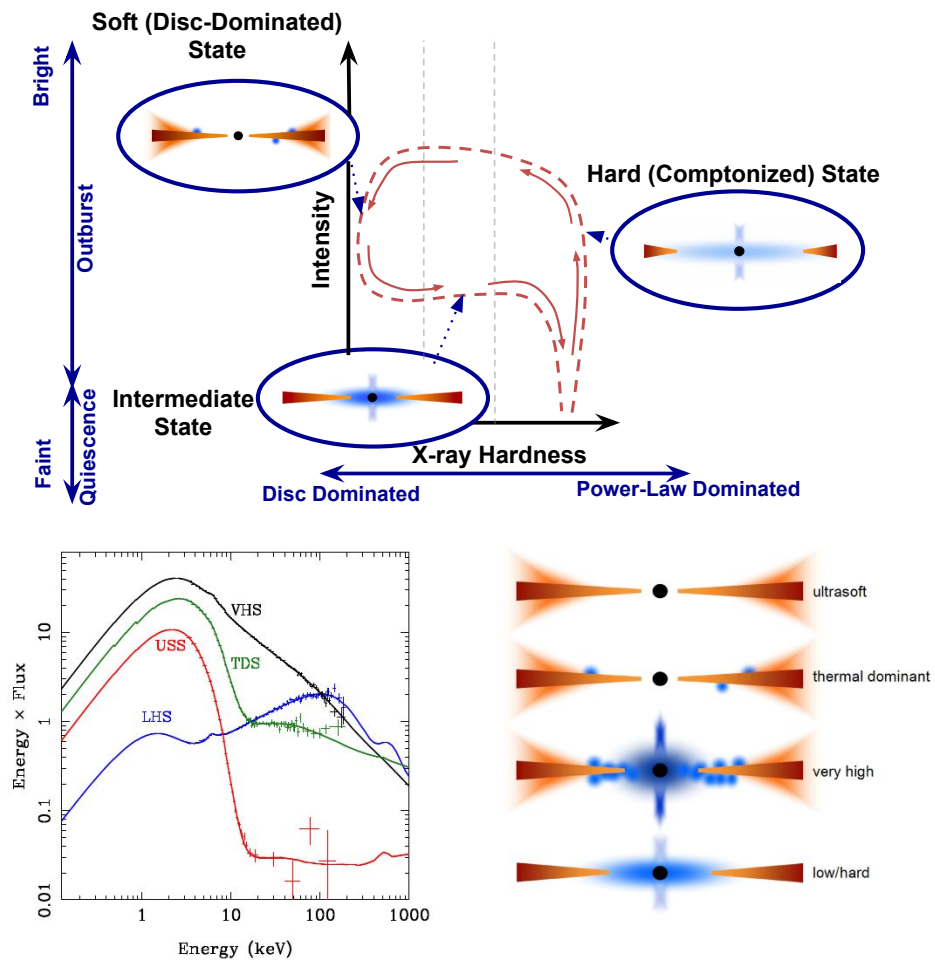
Figure 1.2: Top: Hardness-intensity diagram for outbursts of X-ray binaries. Image courtesy of B.E. Tetarenko, with inset figures from Done et al. (2007). Bottom: X-ray spectra of a typical X-ray binary in various accretion states. The spectra in this case are from the 2005 outburst of GRO J1655−40. Figure from Done et al. (2007).
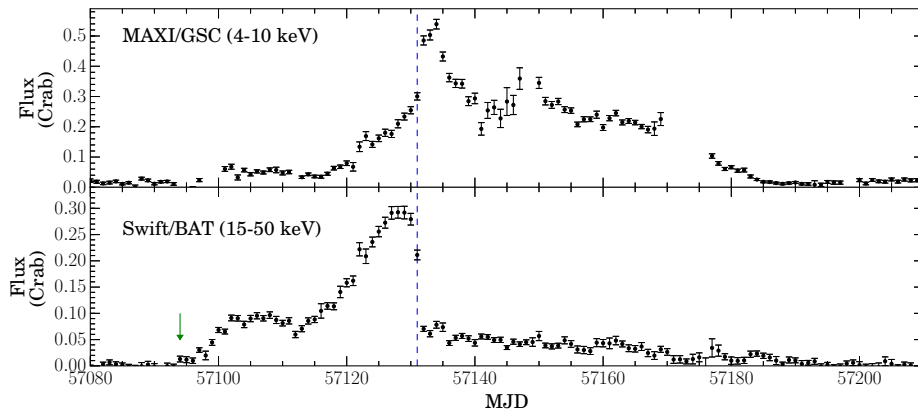
Figure 1.3: Light curve of the 2015 outburst of the transient LMXB EXO 1745−248 (in the globular cluster Terzan 5) as observed by the MAXI/GSC X-ray monitor in soft X-rays (4-10 keV) and Swift/BAT in hard X-rays (15-50 keV). The green arrow shows the time of initial detection of outburst from the source. The blue dashed line indicates the point of the state transition from low-hard to high-soft. Plot from Tetarenko et al. (2016a).

star LMXBs (NS-LMXBs), such power law emission was thought to be due to continuing low-level accretion onto the NS, an accretion shock between infalling matter and either the NS's magnetosphere or a pulsar wind, or synchrotron radiation from a pulsar wind nebula (e.g., Campana et al., 1998; Bogdanov et al., 2005; Chakrabarty et al., 2014; D'Angelo et al., 2015; Archibald et al., 2015; Wijnands et al., 2015). Quiescent NS-LMXBs often show soft, blackbody-like X-ray emission from the NS surface, which has been proposed to originate either from heat deposited in prior outbursts escaping the surface (Brown et al., 1998), or from continued accretion (Zampieri et al., 1995; Zane et al., 2000). In Chapter 4, we study a sample of 12 candidate NS-LMXBs in quiescence and suggest that low-level accretion in quiescence is an unlikely origin for the thermal emission.

Nature of the compact object One of the challenges in the study of LMXBs is identification of the nature of the compact object. While there are
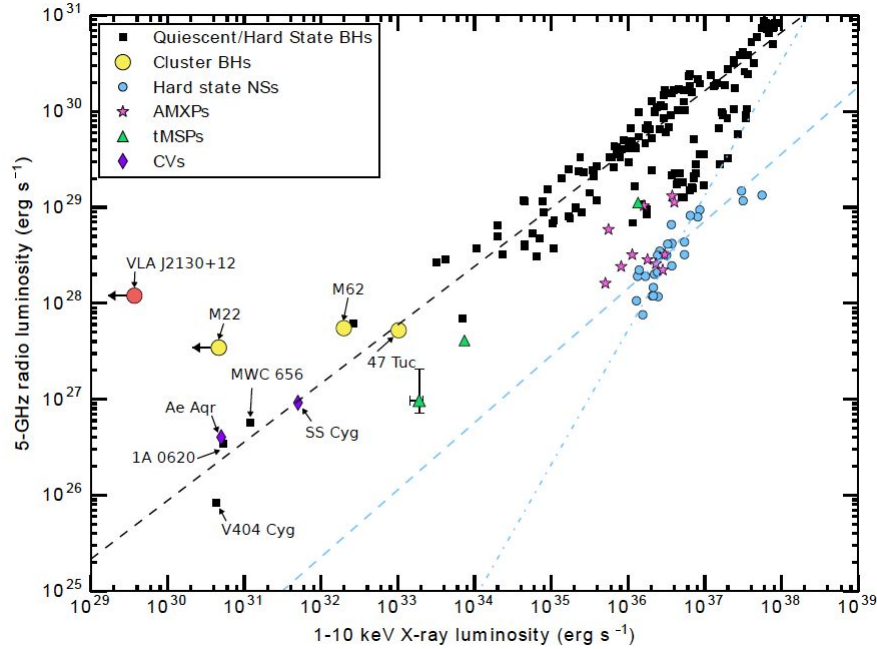
Figure 1.4: Demonstration of radio - X-ray luminosity correlation for stellar mass black holes, neutron stars, accreting millisecond pulsars, transitional millisecond pulsars and CVs. Plot from Tetarenko et al. (2016b).

observable signatures that require a NS accretor, like pulsations in the light curve (from hot spots on the NS surface), thermo-nuclear bursts (from burning of accreted material on the NS surface), and presence of a thermal component in the quiescent spectrum (from the surface of the NS), absence of these signatures does not necessarily imply a black hole nature for the accretor. One of the major diagnostics to separate BH-LMXBs from NS-LMXBs is based on the ratio of radio/X-ray luminosities of the system (Maccarone, 2005). BH-XRBs show compact, partially-absorbed jet emission in quiescence (and in the hard state during outbursts), making them brighter in the radio compared to NS-LMXBs with similar X-ray luminosities (Gallo et al., 2003; Fender et al., 2003, , see also Fig. 1.4). In Chapter 5, we use this diagnostic to investigate an ultra-compact X-ray binary in the core of globular cluster 47 Tuc.

1.2 Globular clusters

Globular clusters (GCs) are spherical collections of 10^5 to 10^6 stars orbiting galaxies. These clusters are among the oldest structures in our Galaxy, dating from the first epochs of star formation in the Galaxy, and generally have lower abundances of most chemical elements than other stars born later.

Population of LMXBs in GCs Early observations have shown that the formation rate of LMXBs (per unit mass) in GCs is orders of magnitude higher than in the galactic disk (Katz, 1975, see also Fig. 1.5). This has been attributed to the high stellar density in globular clusters. The stellar density in the core of a globular cluster can reach a million times our local stellar density. While in the rest of the Galaxy, most LMXBs are formed through binary evolution of primordial binaries, it has been shown that in GCs, the dominant channel to form LMXBs is through encounters between stars. These scenarios include tidal capture of another single star by a NS or BH producing a close binary, exchange of a compact object into an already-existing binary, or the collision of a compact object with a red giant, which tears off the outer envelope of the red giant, leaving the compact object in a close orbit with the white dwarf core of the red giant (Clark, 1975; Fabian et al., 1975; Sutantyo, 1975).

Stellar encounter rate in GCs To investigate the effects of GC properties on populations of LMXBs, we can calculate a relative stellar encounter rate (Γ) for different GCs. The stellar encounter rate depends on the density and velocity dispersion profiles of the GC (Verbunt and Hut, 1987). A challenge in the calculation of stellar encounter rates has been the conversion of observable quantities to physical quantities (e.g., surface brightness profile to luminosity density profile, and ultimately mass density profile). Additionally, propagation of observational uncertainties to the final results is a key step that was not taken before. Comparison of simplified estimates of stellar encounter rates
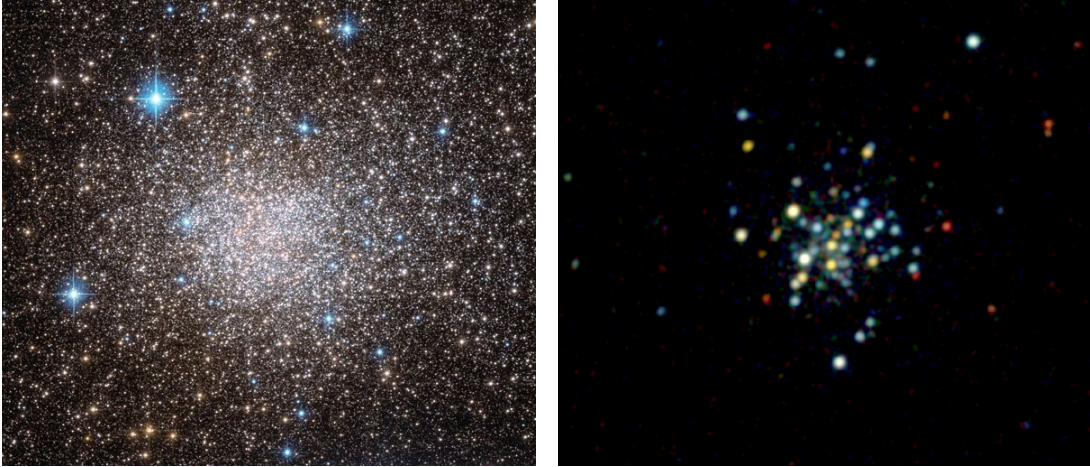
Figure 1.5: Globular cluster Terzan 5 as seen in Optical (left) and X-rays (right). Images not to the same scale. Terzan 5 has the highest stellar encounter rate among all Galactic globular clusters and it contains a high number of X-ray sources. Credit ESA/Hubble & NASA (optical) and Chandra/NASA, Bahramian et al. (X-rays).

with the numbers of X-ray sources in different GCs indicate a strong correlation between Γ and the LMXB population in GCs (Pooley et al., 2003; Heinke et al., 2003d). However, model-dependent assumptions for GCs and difficulties in incorporation of observational uncertainties made further progress challenging. In Chapter 2, we present a complete catalog of model-independent stellar encounter rates and propagated uncertainties for 124 Galactic GCs. This catalog paves the path for future studies on the effects of GC properties on formation of LMXBs.

1.3 Observations of X-ray binaries

Multi-wavelength studies of X-ray binaries can help us constrain various properties of these systems. Below I summarize the wavelength bands focused on in this thesis:

X-rays High energy emission from LMXBs is mostly produced by the energetic viscous accretion flow near the accreting compact object (white dwarf, neutron star, or black hole), due to the high temperatures in these regions. In this thesis we used data obtained by the *Chandra*, *NuSTAR*, *Swift* and *MAXI* X-ray observatories.

The principal detector technology for most of these observatories is a CCD (charge-coupled device), wherein impacting X-rays eject a number of electrons, which are read out and counted to estimate the energy of the event. Thus, X-ray telescopes can measure the time, location, and energy of each photon, though with limited precision. As focusing X-rays requires only small deflection angles, and thus large focal lengths, focusing X-ray telescopes are limited in their field of view, while X-ray monitors typically cover a substantial fraction of the sky at once with the penalty of greatly reduced (factors of $\sim 10^4$) sensitivity. Combining X-ray monitors with focusing telescopes allows efficient scheduling, in that new outbursts can be detected with X-ray monitors and then followed up with focusing telescopes.

The *Chandra* X-ray observatory is a focusing, CCD-based telescope sensitive in the soft X-ray range (0.1-10 keV, Weisskopf et al., 2002). It uses an array of cylindrical paraboloid and hyperboloid mirrors to focus X-rays. *Chandra* has two detectors: the Advanced CCD Imaging Spectrometer (ACIS) and the High Resolution Camera (HRC, a microchannel plate detector). While ACIS has superior sensitivity, spectral and angular resolution, it has limited time resolution (typically 3.2 seconds) compared to HRC (microseconds). HRC has almost no spectral resolution, however, while ACIS has moderate ($\lambda/(\Delta\lambda) \sim 10$) spectral resolution. ACIS is susceptible to pileup[1], which can degrade data from bright sources, while HRC can observe brighter sources without pile up. *Chandra* has the best angular resolution ($\sim 0.5''$) ever achieved in an X-ray observatory. This makes Chandra the principal observatory for study of X-ray binaries in

---

[1]Pile up occurs when two photons are recorded as a single event.

crowded regions like globular clusters.

NuSTAR is the first focusing hard X-ray ($\geq$ 10 keV) telescope (Harrison et al., 2013). Prior to *NuSTAR*, due to the increased focal length required for hard X-rays, the typical instrumentation for hard X-ray observatories involved use of coded aperture mask imaging (e.g., the SPI instrument in *INTEGRAL* observatory), which resulted in relatively low sensitivity and resolution. Superior sensitivity plus timing, focusing imaging, and spectroscopic capabilities in a wide band ($3 - 79$ kev) of *NuSTAR*, make it the best hard X-ray telescope to study the hard component (e.g., Comptonization and reflection) in the spectra of X-ray binaries.

The primary mission of the *Swift* Gamma-Ray Burst Explorer is detection and rapid (timescale of minutes) follow-up of gamma-ray bursts (Gehrels et al., 2004). However, its effective monitoring and fast pointing capabilities have been crucial in catching outbursts from X-ray binaries early in their outbursts. *Swift* has three telescopes: the Burst Alert Telescope (BAT), a hard X-ray telescope sensitive in the 15–150 keV band with a coded aperture mask. The BAT's wide field of view (1.4 steradians) makes it a great hard X-ray all-sky monitor. *Swift*'s X-ray Telescope (XRT) is a soft X-ray telescope operating in the 0.3–10 keV band with a CCD detector similar to ACIS. Its Ultraviolet/Optical Telescope (UVOT) is sensitive in the optical and ultraviolet bands (170-650 nm).

MAXI is an all-sky X-ray monitor on board the international space station as a part of the Japanese Experiment Module (Isobe et al., 2007). The principal useful detector is the gas slit camera (GSC), which works in the 2-20 keV band and has a wide field of view (0.05 steradians). *MAXI* has the capability to observe the entire celestial sphere every 96 minutes, making it a crucial tool for early detection of X-ray binaries in outbursts.

Optical and near-infrared Optical and near-infrared (NIR) emission from LMXBs are produced in cooler parts of the system, like the outer parts of the accretion disk and the surface of the companion star. The emission from the companion dominates the emission in these bands during quiescence. Thus, optical and NIR spectroscopy (and to a lesser extent, photometry) can help determine the nature of the donor, and search for signatures of accretion (e.g., hydrogen emission lines like Hα; see Fender et al., 2009; Beccari et al., 2014). These studies can ultimately help us constrain the orbital period of the system, and study the mechanisms involved in mass-transfer.

A major problem in the study of LMXBs in the direction of the Galactic plane is the large interstellar absorption, which makes ultraviolet and optical observations of LMXBs in the bulge and Galactic center region difficult. However, interstellar absorption affects the NIR significantly less than optical and UV bands, making the NIR the preferred band to study the donor in highly absorbed LMXBs.

The Gemini observatory, of which Canada is a partner country, consists of two 8.1 meter diameter optical telescopes, one in the northern hemisphere (Gemini North, located in Hawaii) and one in the southern hemisphere (Gemini South, in Chile). The two observatories can collectively observe the entire sky. Each of the two telescopes have multiple imagers and spectrographs sensitive in the optical and the infrared. Each Gemini telescope also has an adaptive optics system (ALTAIR at North, GeMS at South) that can be used (with some infrared instruments) to rectify atmospheric distortions and enhance the image/spectrum quality. In Chapter 6, we present our NIR spectroscopy of a transient LMXB using the Near-infrared Integral Field Spectrograph (NIFS, McGregor et al., 2002) mounted on Gemini North.

Chapter 2

Stellar Encounter Rate in Galactic Globular Clusters

Arash Bahramian[1], Craig O. Heinke[1], Gregory R. Sivakoff[1], Jeanette C. Gladstone[1]

[1] Dept. of Physics, CCIS 4-183, University of Alberta, Edmonton, AB, Canada

Abstract

The high stellar densities in the cores of globular clusters cause significant stellar interactions. These stellar interactions can produce close binary mass-transferring systems involving compact objects and their progeny, such as X-ray binaries and radio millisecond pulsars. Comparing the numbers of these systems and interaction rates in different clusters drives our understanding of how cluster parameters affect the production of close binaries. In this paper we estimate stellar encounter rates (Γ) for 124 Galactic globular clusters based on observational data as opposed to the methods previously employed, which assumed "King-model" profiles for all clusters. By deprojecting cluster surface brightness profiles to estimate luminosity density profiles, we treat "King-model" and "core-collapsed" clusters in the same way. In addition, we use Monte-Carlo simulations to investigate the effects of uncertainties in various observational parameters (distance, reddening, surface brightness) on Γ, producing the first catalog of GC stellar encounter rates with estimated errors. Comparing our results with published observations of likely products of stellar interactions (numbers of X-ray binaries, numbers of radio millisecond pulsars, and γ-ray luminosity) we find both clear correlations and some differences with published results.

2.1 Introduction

Soon after the discovery of bright X-ray binaries (XRBs) ($L_X \geq 10^{34}$ erg/s) in our Galaxy, it became apparent that they were overabundant (by a factor of $\sim$100 per stellar mass) in globular clusters (GCs). This overabundance was attributed to the formation of XRBs by stellar interactions (Clark, 1975). Models of how neutron star XRBs could be produced dynamically include tidal capture of a companion star by a neutron star (Fabian et al., 1975), collisions of neutron stars with giant stars (Sutantyo, 1975), and exchange of neutron stars into existing primordial binaries (Hills, 1976). These interactions depend

13

on bringing two stars, or a star and a binary, close together, and thus depend on the square of the stellar density. Gravitational focusing will bring stars closer together and is reduced by the stellar velocity dispersion, leading to a dependence of the stellar encounter rate (typically denoted Γ) on cluster properties as $\Gamma \propto \int \rho^2/\sigma \, dV$, where ρ is the stellar density, σ is the velocity dispersion and integral is over the volume.

Globular cluster stellar distributions have often been found to be accurately described by lowered, truncated Maxwellian potentials, known as King models (King, 1962, 1966). These models possess a core region of nearly constant and a rapid falling off of density outside the core. The majority of past work approximated the total Γ of a cluster by only considering the summed Γ within the core, assuming a constant density in the core; thus $\Gamma_1 \propto \rho^2 r_c^3/\sigma$, where r_c is the physical radius of the cluster core. Additional approximations based on King model profiles have been used, particularly when σ is not well-known for a cluster. In a King model profile, $\sigma \propto \rho^{0.5} r_c$, so $\Gamma_2 \propto \rho^{1.5} r_c^2$ (Verbunt and Hut, 1987). To date, even the most advanced calculations of Γ that have integrated ρ^2/σ have assumed the GCs follow a King model profile (e.g., Pooley et al., 2003).

These estimates have allowed comparison of the stellar interaction rates between different clusters in our galaxy, which showed that bright XRBs in Galactic globular clusters are indeed most concentrated in the highest-Γ clusters (Verbunt and Hut, 1987; Verbunt, 2003). Although it is more difficult to measure the surface brightness (SB) profiles of globular clusters in other galaxies, analysis of extragalactic globular cluster XRBs shows that they, too, tend to be concentrated in clusters that show evidence of higher Γ values (Jordán et al., 2004; Sivakoff et al., 2007; Jordán et al., 2007; Peacock et al., 2009). Evidence for a weaker-than-linear relation between Γ and the probability of hosting a bright XRB in other galaxies (e.g., the nonlinear dependence of Jordán et al. 2004 can be explained by random errors in the measurements of cluster struc-

tural parameters, Maccarone and Peacock 2011).

In our own Galaxy, however, we have accurate radial SB measurements of globular clusters, allowing precise estimates of Γ. The number of bright Galactic globular cluster XRBs is still too small for precise tests of stellar encounter theories. However, recent X-ray, radio, and γ-ray observational advances provide large numbers of faint X-ray sources (Pooley and Hut, 2006), radio millisecond pulsars (MSPs, Ransom, 2008), and integrated γ-ray emission that is presumed to arise from MSPs (Abdo et al., 2010). These results allow detailed comparisons between Γ and the progeny of stellar encounters, X-ray binaries (both neutron star and white dwarf systems) and millisecond pulsars (the descendants of X-ray binaries).

However, current literature calculations of globular cluster stellar encounter rates only approximate the true density profile of the stellar cluster. The actual density profiles of many clusters do not exactly fit King models–there are 29 clusters in the Harris catalog (Harris, 1996, 2010 edition; hereafter HC) with designations of "core-collapsed", or possibly core-collapsed. Core-collapsed is an observational designation indicating that instead of showing a clear, flat central core, the radial SB profile of a cluster continues to increases towards its center. These observations are linked to theoretical models of a gravitational instability that leads to a rapidly shrinking core (Meylan and Heggie, 1997), although the definition of core-collapse used by theorists does not necessarily coincide with the definition used by observers (compare Hurley and Shara 2012 and Chatterjee et al. 2013). In addition to core-collapsed clusters, many clusters that have generally been considered to be well-fit by King models (e.g., NGC 6388) show radial SB gradients down to their centers, which are not predicted by King models (Noyola and Gebhardt, 2006). Calculations of stellar encounter rates using different methods (e.g. Γ_1, Heinke et al. 2003d; Γ_2, Maxwell et al. 2012; integration of ρ^2/σ of a King-model fit, Pooley et al. 2003) can get significantly different results, implying that the choice of method introduces

a systematic uncertainty. This is a particular concern when considering how observationally core-collapsed clusters compare to other clusters, as none of the methods cited above use accurate descriptions of core-collapsed cluster properties (e.g., King-model fits to core-collapsed clusters simply assume a concentration parameter, c, of 2.5, which overestimates the SB gradient outside the core).

Moreover, previous calculations of stellar encounter rates have not, to our knowledge, quantified the uncertainties in their calculations. This makes it difficult to understand, when comparing Γ versus observations of close binaries, whether uncertainties in the input quantities, such as reddening, distance, or core radius (for Γ_1 or Γ_2), cause scatter in the correlations.

Our goal in this paper is to rectify these two problems by calculating the 3-d radial luminosity density profile and integrating it to obtain an estimate of Γ. We then quantify the uncertainties in our calculations by Monte Carlo sampling from distributions of the observational inputs. Finally, we compare our results with some recent works to determine how our estimates affect the correlation of stellar encounter progeny with stellar encounter rates. Note that the goal of this paper is simply to perform an accurate computation of the simplest stellar encounter rate estimate, and its errors. We do not attempt here to include issues such as mass segregation, neutron star escape at birth, subsequent binary destruction, dynamical evolution of GCs, finite lifetimes, etc., which have been discussed in several works (e.g. Verbunt and Meylan, 1988; Verbunt, 2003; Smits et al., 2006; Ivanova et al., 2008), as they do not yet have simple, agreed-upon recipes that could be used to address these details. We will model these effects in an upcoming paper, where we will draw further conclusions about the dynamics of XRB production.

2.2 Data reduction and analysis

To calculate Γ based on $\int \rho^2(r)/\sigma \; r^2 dr$ over several half-light radii, we need the luminosity density profile (as a function of radius), and velocity dispersions (ideally, also as a function of radius, but see below), along with estimates of the distance modulus and extinction.

2.2.1 Surface Brightness Profiles

Our sample includes 124 Galactic GCs for which found published SB profiles. For 85 GCs we used the SB profiles compiled by Trager et al. (1995, hereafter T95). These datasets were obtained from various ground-based observations, mostly from the Berkeley Globular Cluster survey by Djorgovski and King (1986). T95 indicate the quality of the datapoints with a weight and their best data are labeled with weight=1.

Noyola and Gebhardt (2006, hereafter, NG06) provide SB profiles for 38 GC, some of which are also listed in HC. In these overlapping cases, we use the SB profiles provided by NG06 as they were constructed from *Hubble Space Telescope* (*HST*) observations, which are much higher resolution than ground-based data and were processed with attention to reducing the influence of the brightest (giant) stars.

The quality of the observed SB data varies strongly from one GC to another (Fig. 2.1). For all GCs except Terzan 5 (see details below), we used the Chebyshev polynomial fits provided in T95 or the spline fits provided by NG06, instead of the raw photometric data. Given both the noise in the SB profile data and the strong dependence of our method on the derivatives of the SB profiles, we used the smoothed profiles throughout this paper. As we show in §2.3, for GCs where the data is of high quality this choice has little effect on our calculations. For GCs with poor quality data, the Chebyshev

polynomial fits lead to a smoother luminosity density profile that should be more representative of the actual luminosity density profile.

For three GCs (Palomar 10, Terzan 7, and Tonantzintla 2) the T95 SB profiles are uncalibrated. Following McLaughlin and van der Marel (2005), we calibrated these profiles by assuming that their central SB values are equal to the central SB values from the HC. For Terzan 7, in addition to calibrating the data, we ignored the polynomial fit data for $\log r_{\mathrm{arcsec}} > 1.9$ to avoid the non-physical increase of the fit SB profile with radius. Such a problem can be attributed to the lack of large-radius data points, and the high order of the Chebyshev polynomial fit. T95 also present two sets of data for NGC 2419. We choose the dataset which shows agreement with the central SB reported by HC.

We estimated uncertainties on the SB profiles using the reported uncertainties in the photometric data. For the NG06 SB profiles, we used the maximum reported uncertainty in photometric data (requiring $\log r_{\mathrm{arcsec}} > 0$). For the T95 SB profiles, we used estimates of the photometric uncertainties calculated by McLaughlin and van der Marel (2005).

As all the profiles were reported as a function of angular radius, we first calculated 1-D profiles as a function of physical radius using the reported GC distances. To obtain 3-dimensional luminosity density profiles from the 1-dimensional observational SB profiles, we used the non-parametric deprojection of Gebhardt et al. (1996) assuming spherical symmetry:

$$\rho(r) = -\frac{1}{\pi} \int_r^\infty \frac{d\mu(R)}{dR} \frac{dR}{\sqrt{R^2 - r^2}} \tag{2.1}$$

where $\mu(R)$ is the 1-D SB profile as a function of projected radius (R) and $\rho(r)$ is the luminosity density as a function of deprojected (spatial) radius (r). When calculating the luminosity density function, we first linearly interpolated the (T95 and NG06) fits to the SB profile to allow for a finer numerical integra-
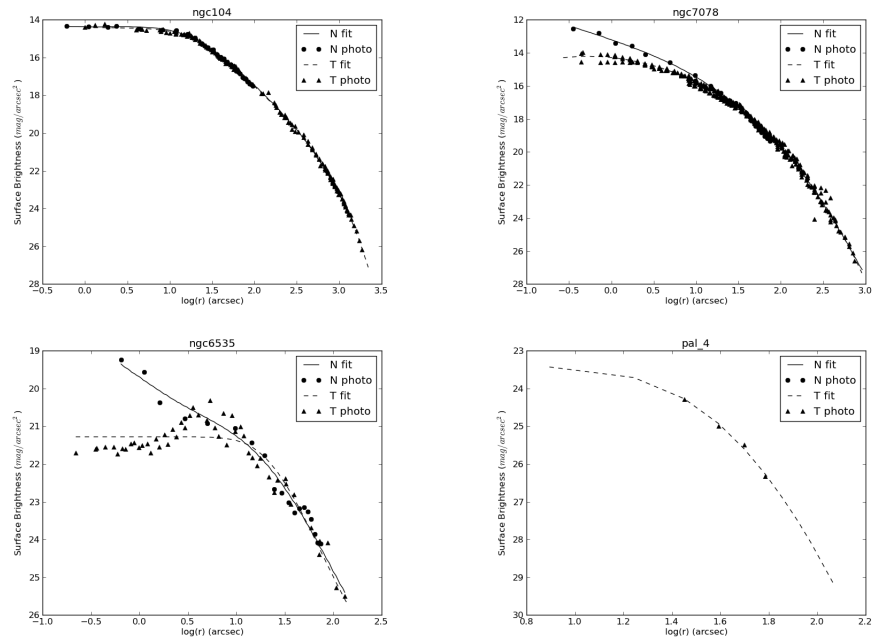
Figure 2.1: Illustrations of SB profiles with different qualities. N fit is the fit provided by NG06. N photo are the photometric data points from NG06. T fit is the fit provided by T95. T photo are the photometric data points with weight=1.0 from T95.
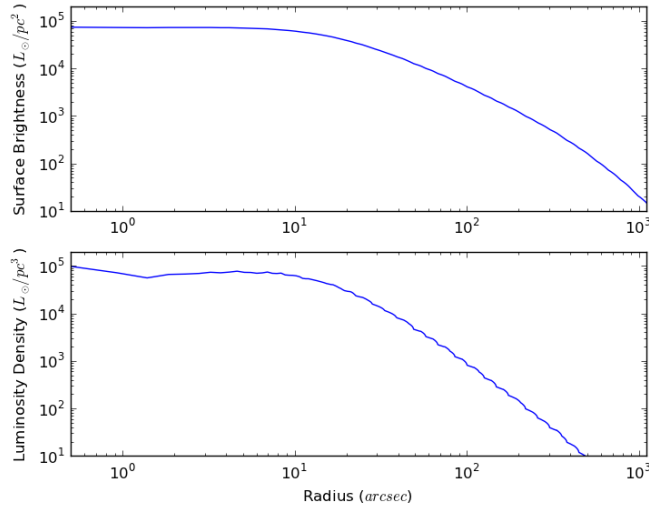
Figure 2.2: Interpolated surface brightness profile (top, interpolated from values given by NG06) and deprojected luminosity density profile (bottom) for NGC 104.

tion. To integrate over the entire GC, we first set the central SB equal to the innermost data point (a very small extrapolation). We then set the integration upper limit to be the outermost available data point which is in all cases > 2.5 half-light radii, checking to ensure that this truncation did not affect our final results. In some cases where the SBD decreases inside the core (e.g., due to noise or contribution of light from giant stars outside the core), this integration yields a complex result. In all such cases, the imaginary component is less than 10^{-6} the size of the real component. By ignoring this small imaginary component, we can reliably calculate the radial density distribution. Fig. 2.2 shows the result of interpolation and deprojection for NGC 104, one of the most well-studied clusters.
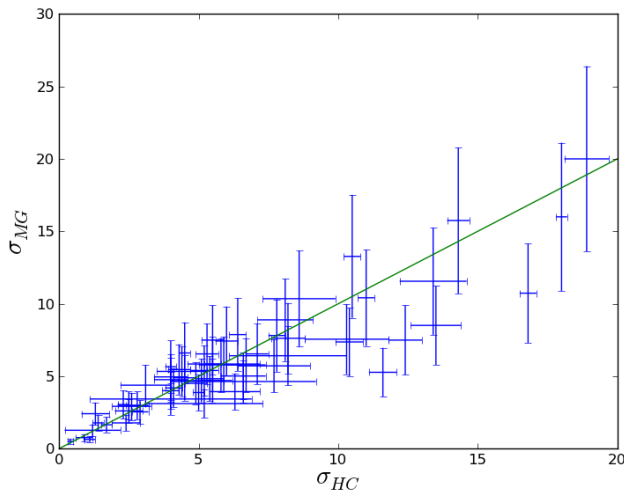
Figure 2.3: Comparison of the modified central velocity dispersions from G02 ($\sigma_{\text{Modified Gnedin}} = \sigma_{\text{Gnedin}}/1.57$) to those from HC for 62 GCs in common (values in km/s). The line represents $\sigma_{HC} = \sigma_{MG}$.

2.2.2 Velocity Dispersion

We have full velocity dispersion (σ) profiles for only 14 clusters (see Table 2.3 for these sources). For the remaining clusters, we only consider the central σ value. Since σ falls off much more slowly than SB with radius in the cluster, using the central σ value for all radii produces very small changes in the inferred Γ (see §2.4). Our primary source for central values of σ and their errors was HC, which compiles central velocity dispersion measurements for 62 GCs (σ_{HC}). For other GCs, we referred to theoretical estimates by Gnedin et al. (2002, hereafter G02). For GCs where HC reports velocity dispersion, the G02 values are 1.57 times larger on average. So for the cases where HC does not report velocity dispersion, we used modified values from G02, ($\sigma_{\text{MG}} \equiv \sigma_{\text{G02}}/1.57$). Fig. 2.3 shows our comparison between the σ values from G02 (modified) and HC for the 62 clusters in common.

For GCs where HC reports velocity dispersion, we used estimations he provides for uncertainty in the velocity dispersion. For the rest of our sample, we

used the average fractional discrepancy between σ_{MG} and σ_{HC} for the 62 GCs they both report, as our uncertainty δ:

$$\delta = \sqrt{\frac{1}{N}\sum^{N}\left(\frac{\sigma_{\mathrm{HC}} - \sigma_{\mathrm{MG}}}{\sigma_{\mathrm{HC}}}\right)^{2}} \approx 0.32 \qquad (2.2)$$

For the 14 GCs where we had detailed velocity dispersion profiles, we could compare the effects of assuming a constant velocity dispersion instead of using the true velocity dispersion profile. For these clusters, we deprojected the 1D velocity dispersion profile to a 3D profile making the assumption of spherical symmetry. We used the non-parametric integration for deprojection:

$$\rho(r)\sigma(r) = -\frac{1}{\pi}\int_{r}^{\infty}\frac{d(\mu(R)\sigma_{p}(R))}{dR}\frac{dR}{\sqrt{R^{2}-r^{2}}} \qquad (2.3)$$

where $\sigma_{p}(R)$ is the projected 1D profile and $\sigma(r)$ is the deprojected 3D profile. Since the velocity dispersion data had not been previously smoothed, we applied a third-order interpolation prior to deprojecting the velocity dispersion. We truncated the integration at the outermost data point. This method produces a drop to zero at the outer radii, due to our choice of integration limits (choosing the outermost data point instead of infinity). To check the overall validity of the first method, we used a second method of deprojection assuming a discrete sum of shells, where we set σ_{p} and σ to be equal in the outermost layer of the GC (we omit the factor of $\sqrt{3}$ in converting from 1-D to 3-D velocities, as it will be identical in all clusters, assuming isotropic orbits). By these assumptions, we calculate a discrete sum for the projection:

$$\sigma_{p}(R_{n}) = \frac{\sum_{i}^{n}\rho(r_{i})\sigma(r_{i})}{\sum_{i}^{n}\rho(r_{i})} \qquad (2.4)$$

where i starts from the outermost radius and goes towards the center. Starting from the outermost layer, we found values for the deprojected σ at different points and interpolated them as a function of r. To compute Γ for these 14 GCs,
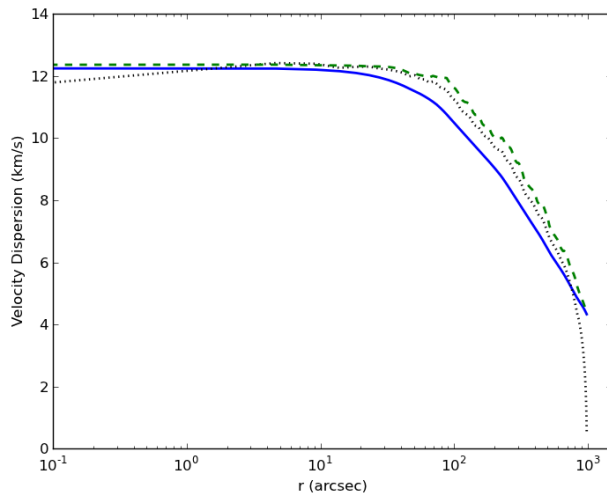
Figure 2.4: Velocity dispersion profile for NGC 104. The solid line is the projected profile, the dashed line is the deprojected profile obtained from the sum, Eq. 2.4, and the dotted line is the deprojected profile obtained from the integration, Eq. 2.3. Note that the core radius for NGC 104 is $\approx 21''$.

we used the deprojected profile obtained from the latter method. In Fig. 2.4 we present a comparison of the projected σ_p profile and the deprojected σ obtained from both methods for NGC 104. In §2.4 we discuss the effects on Γ of using a full deprojected σ profile versus assuming a constant σ throughout the cluster.

2.2.3 Distance Modulus and Extinction

To estimate luminosity density as a function of physical radius for GCs, we need to calculate the physical radius using distance and angular radius. To calculate distance and estimate uncertainties on it, we used values for the apparent distance modulus $D(m - M)$ and foreground reddening $E(B - V)$ from HC. Based on the different claimed measurements in the literature for a few GCs, we assumed an uncertainty of 0.1 magnitude in distance modulus for all GCs (except Terzan 5, see below). Following HC, we generally assumed a 10 % uncertainty for the reddening, $E(B - V)$, imposing a minimum uncertainty of 0.01 magnitude for any cluster. We used $A_V = R_V E(B - V)$ with $R_V = 3.1$

to obtainthe extinction. Since R_V is not the same for all parts of the sky (Hendricks et al., 2012; Nataf et al., 2013), we assumed a further uncertainty of 10 % in R_V. For 3 GCs (AM 1, NGC 5466, and NGC 7492) HC reports $E(B-V) = 0.0$, in these cases we used alternative sources to improve these estimates. For AM 1 we chose 0.02 (Dotter et al., 2008), for NGC 5466, 0.02 (Schlegel et al., 1998), and for NGC 7492, 0.04 (Schlegel et al., 1998).

2.2.4   Special case of Terzan 5

Terzan 5 is a highly extincted GC near the Galactic core that contains $>$ 50 XRBs (Heinke et al., 2006b) and > 33 millisecond radio pulsars (Ransom et al., 2005). This large population of sources makes it an ideal GC for more detailed analysis. Although SB profiles are available in T95, we note that higher quality data was available in Lanzoni et al. (2010, hereafter L10), derived using *HST* observations (ACS - F606W). However, L10 did not provide clear fit parameters. As a result, we use their photometric data to derive SB (Fig. 2.5). We assume an uncertainty of 0.2 magnitudes for the SB profile, as reported by L10. Recently Massari et al. (2012) presented a high resolution reddening map of Terzan 5. From their map, we find $E(B-V) = 2.61$ for the core of Terzan 5 and used their estimate of $R_V = 2.83$ to obtain our A_V estimate. For its distance modulus we used the value of $(m-M)_v$=21.27 from HC, which with our A_V gives the same $(m-M)_0$=13.87 as Valenti et al. (2007) derive. However, due to the uncertainty in measuring $(m-M)_0$ in this highly reddened case, we assumed a conservative uncertainty of 0.2 for this quantity.

2.3   Stellar encounter rate, Γ

To calculate Γ, we numerically integrated $a\rho(r)^2/\sigma(r)$ using the luminosity density and velocity dispersion profiles derived above, where a is an arbitrary constant that was set by requiring the Γ value for NGC 104 be equal to 1000.
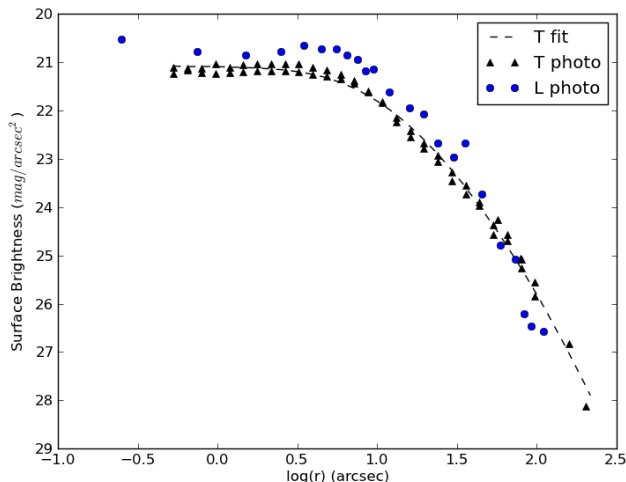
Figure 2.5: Available SB data for Terzan 5. T fit: fit provided by T95. T photo: photometric data points with weight=1.0 from T95. L photo: Photometric data from L10. In comparison L10 shows a higher SB value for the core.

To ensure that the first-order interpolation of the fits to the SB profile were appropriate, we recalculated Γ using both second-order and third-order interpolation. This led to no significant differences in the final results ($\lesssim 0.1$ % change).

To estimate the uncertainty in Γ, we performed Monte-Carlo simulations of the Γ calculation with different inputs. Our principal code is written in *Mathematica*[1] and the average number of iterations for each GC was ≈ 400. We assumed gaussian distributions for the input parameters (distance modulus, reddening, R_V, SB profile amplitude, velocity dispersion) with the reported values as the mean value, and the reported uncertainties as the standard deviations of the distributions. We used these distributions with caution, modifying them when they were unphysical. For low values of extinction, the gaussian distributions include negative values. For the velocity dispersion, values very near to zero also produce unphysical results (since velocity dispersion is in the

---

[1]http://www.wolfram.com

denominator in $\Gamma \sim \int \rho/\sigma$). So we did not run simulation for those values.

In the case of extinction, we required positive values, and in the case of velocity dispersion, we required that the simulated velocity dispersion was within two standard deviations (eq.2.2) of the measured velocity dispersion. For 2 GCs, NGC 7492 and NGC 5946, the reported uncertainties from HC on σ are more than 50 %, so for these two, we truncated the σ distribution at one standard deviation instead.

When the photometric data was of high quality, we found that integrating this data directly gave similar results as integrating the fitted Chebyshev polynomials. The differences in the final results were typically < 1 % (e.g. NGC 104). In Table 2.1 we provide a comparison between Γ calculated based on the photometric data, and based on the Chebyshev fit for some of the GCs where data were available from NG06. In the few cases with a large difference between the two values (e.g., NGC 5897, NGC 6205 & NGC 6254), the observational data did not extend out to the outer portions of the GC. In these cases, by truncating the Chebyshev fit profile to the outermost point of the photometric data, we greatly reduce the difference in results; for NGC 5897 it drops to 26.7 % and for NGC 6254 to 13.2 %.

2.4   Results

The final Γ values we report (Table 2.2) are calculated based on the default values for quantities described in §2.2. For most clusters, the Γ calculated from the default values lies within 5% of the median of the histogram of Γ values produced in our simulations (Generally the discrepancy between default value and median of the distribution is caused by truncation of the input parameters distribution described in §2.3). Uncertainties in Γ for each source are calculated based on the histograms of Γ values produced from our Monte-Carlo simulations (Fig. 2.6). We identify the 1-σ upper bound by increasing Γ from

GC	$\Gamma_{photometric}$	Γ_{fit}	difference (%)
NGC 104	992.6	1000	0.7
NGC 1851	1637	1528	7.1
NGC 1904	115.6	115.7	0.9
NGC 2298	4.091	4.314	5.2
NGC 2808	882.8	922.9	4.3
NGC 5272	172.4	194.4	11.3
NGC 5286	449.0	458.0	1.9
NGC 5694	207.1	191.1	8.3
NGC 5824	1046.4	984.3	6.3
NGC 5897	0.2845	0.850	66.5*
NGC 5904	152.42	164.1	7.1
NGC 6093	568.24	531.6	6.9
NGC 6205	48.475	68.91	29.6*
NGC 6254	13.656	31.37	56.5*
NGC 6266	1827.1	1666.5	9.6
NGC 6284	670.77	665.54	0.8

Table 2.1: Comparison between Γ calculated based on photometric data and based on the Chebyshev fits to the SB profiles (from NG06). Incompleteness in the photometric data appears to explain the cases with a large difference between the two Γ values (marked by a *). In these cases, truncating the fit to the region where photometric data is available reduces the difference in results.
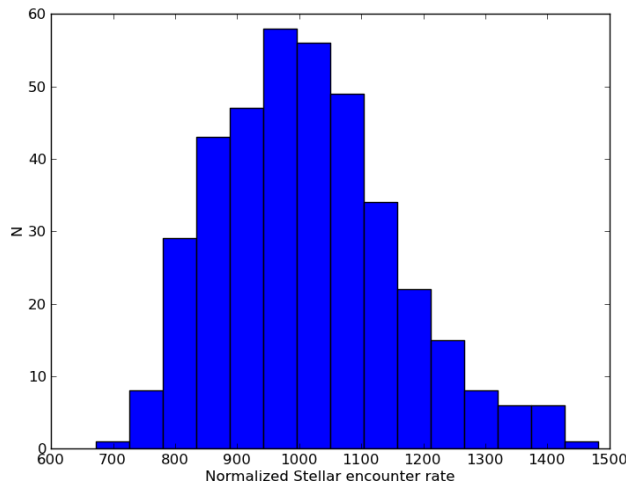
Figure 2.6: Results of Monte-Carlo simulations for NGC 104, showing the number of trials giving each value for Γ. Due to our choice of normalization, the histogram is forced to be centered on 1000.

the median of the distribution upwards until we include an additional 34% of the simulations, and similarly identify the 1-σ lower bound. (Note that the Γ probability distribution is not necessarily a Gaussian.)

We also investigated the effects of assuming a constant velocity dispersion profile by comparing the Γ computed based on a constant σ profile versus the actual measured (and deprojected) σ profile for 14 GCs. For the purposes of this comparison alone, we used the central velocity dispersion values reported by these profiles as the value for the constant velocity dispersion calculations (instead of the values from HC or G02). For deprojecting the observed velocity dispersion profiles we used the method of sums described in Section 2.2.2. As shown in Table 2.3, the difference between the results is always less than 15%, and usually less than 5%. For the final values, for consistency, we used a constant σ for all GC for the calculations presented in Table 2.2 and 2.5.

To have a complete set of calculations, we also included Γ calculations and uncertainty estimations based on the simplified equations ($\rho_c^2 r_c^3 \sigma_c^{-1}$ and $\rho_c^{1.5} r_c^2$) for 143 GCs (19 GCs in addition to the main sample) using HC (Table 2.5). To

28
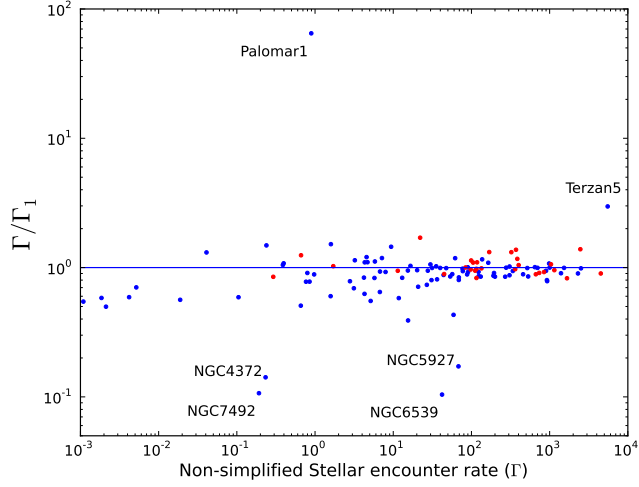
Figure 2.7: Comparing $\Gamma_1 = \rho_c^2 r_c^3 \sigma_c^{-1}$ and $\Gamma = \sigma_c^{-1} \int \rho^2(r) d^3 r$. Core-Collapsed GCs are denoted in red.

do this, we used central surface brightness (in magnitude per arcsec^2), μ, extinction, distance modulus, estimated core radius, r_c and concentration parameter, c, to calculate central luminosity density, ρ_c. Following the prescription from Djorgovski (1993):

$$\rho = \frac{10^{0.4(26.362-\mu)}}{p \ r_c} \tag{2.5}$$

where $p = 10^{-0.603 \times 10^{-c} + 0.302}$ and r_c is in parsec.

For velocity dispersion we used the central values that we aggregated from the literature in §2.2.2. Similar to the method described in §2.3 we did Monte-Carlo simulations to estimate their effects on Γ. We assumed uncertainties on extinction, distance modulus and surface brightness as before. We also assumed an uncertainty of 5% for the core radius. Since the concentration parameter c has little effect, we did not include any error on c. Comparing these simplified values of Γ to our main results, the differences are relatively small for many GCs (Fig. 2.7). Although the value of Γ for Terzan 10 calculated by the simplified method (Γ_2) is extremely high, we found it to be untrustworthy. While HC reports the core radius of Terzan 10 is $\sim 0.9'$, inspection of a 2-MASS J-band

image from the Infrared Science Archive[2] suggests it is $< 0.2'$.

2.5 Applications

2.5.1 X-ray sources

A significant difference between our results and previous works comes in the case of core-collapsed clusters. For instance, Maxwell et al. (2012) derives similar values for Γ_2, with differences principally arising in the core-collapsed clusters (Fig. 2.8).

Comparing our values for Γ to results from Pooley et al. (2003) (which calculate Γ by integration over the half-mass radius assuming king models) and Fregeau (2008), our calculations show that, at about the same values of Γ, core-collapsed GCs have lower numbers of X-ray sources compared to typical GCs (Fig. 2.9). This is in contrast with the results of Fregeau (2008). Fregeau (2008) suggested that, contrary to previous thinking, most globular clusters are currently still in their "early" contraction phase, and that only those clusters observationally defined as "core-collapsed" have reached the binary-burning phase. These clusters would then need to be currently "burning" binaries to support themselves at their current core radius. The initial impetus for this suggestion was the apparent excess of X-ray sources in three "core-collapsed" clusters, NGC 6397, M30, and Terzan 1, compared to other GCs with similar values of Γ. This would be explained if X-ray binaries were created a few Gyrs ago, at a time when non-core-collapsed clusters were substantially larger and less dense, but core-collapsed clusters presumably were at their current size. Thus, the Γ relevant for producing the current X-ray sources in non-core-collapsed clusters would be smaller than the currently observed Γ, as those clusters will have contracted and become denser. Our calculations remove

---

[2]http://irsa.ipac.caltech.edu/

the evidence for NGC 6397 and M30 having higher-than average X-ray source numbers for their Γ values. Instead our results suggest that core-collapsed clusters underproduce X-ray binaries.

One cluster that may not fit with this picture is Terzan 1. This is a GC that appears to be core collapsed, but its structural parameters are poorly determined at present. However, its position near the Galactic centre suggests an alternative scenario, that it may have been tidally stripped (Cackett et al., 2006a).

Fig. 2.9 indicates that, although the assertion about globular cluster evolution by Fregeau (2008) may or may not be true, the numbers of X-ray sources above 4×10^{30} erg s^{-1} do not provide evidence for this assertion. Other evidence, perhaps from comparing detailed Monte Carlo models of gravitational interactions between stars with observed quantities (e.g., Chatterjee et al., 2013), may illuminate this question. On the other hand, the X-ray sources in core-collapsed clusters will experience substantial binary destruction (Verbunt, 2003), which may explain their rather different luminosity functions (Pooley et al., 2002; Heinke et al., 2003d; Stacey et al., 2012).

2.5.2 Numbers of radio MSPs

Large numbers of radio MSPs have been detected in several GCs, with the largest numbers in very high-Γ clusters (Camilo and Rasio, 2005). Several works have attempted to compare the numbers of MSPs in different clusters, accounting for the detection limits of the surveys of each cluster, to determine how cluster properties relate to MSP numbers (Johnston et al., 1992; Hessels et al., 2007; Ransom, 2008; Hui et al., 2010; Lynch and Ransom, 2011; Bagchi et al., 2011). These analyses must estimate the radio luminosity functions of cluster MSPs and the sensitivity of different surveys (involving complex estimates of pulsar detectability). Perhaps the most sophisticated of these is that of Bagchi et al. (2011), which incorporates information from diffuse
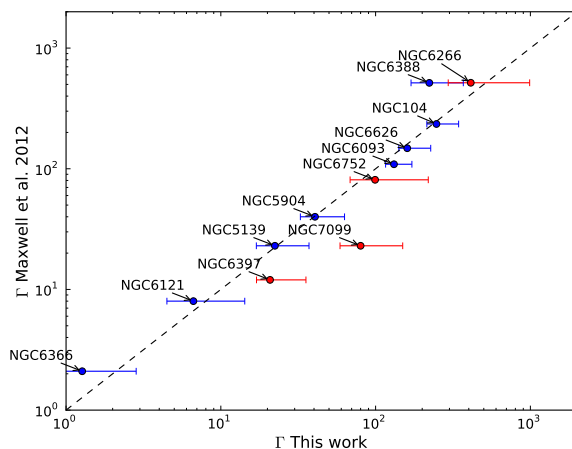
Figure 2.8: Comparison of Γ estimates by Maxwell et al. 2012 versus values calculated in this work (using a different normalization). Core-collapsed clusters have errors shown in red, and show many of the largest differences. Note also that NGC 6388 has a lower Γ in our calculations. We choose our Γ normalization to give average values similar to those of Maxwell et al. 2012.
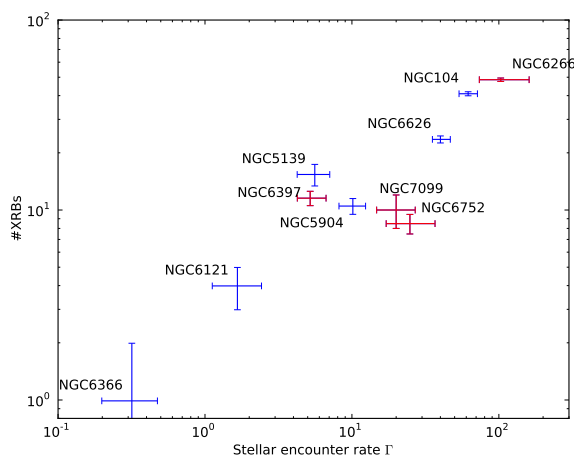
Figure 2.9: Numbers of XRBs (from Pooley et al. 2003, Lugger et al. 2007), excluding the GCs with only lower limits determined), compared to our Γ estimates, with appropriate error bars. Core-collapsed clusters are in red, and show a tendency towards fewer XRBs for their Γ than other clusters. We choose a Γ normalization assuming $\Gamma=20$ for NGC 7099.

radio flux measurements (Fruchter and Goss, 2000; McConnell et al., 2004) and summed γ-ray emission (e.g. Abdo et al. 2010; Hui et al. 2011; see also below).

Bagchi et al. (2011) calculate the most likely numbers of MSPs in 10 globular clusters, based on their simulations of the detectability of MSPs in these clusters, and from the observations discussed above. They make the striking claim that there is no compelling evidence for any direct relationship between any GC parameter and the number of MSPs per cluster; in particular, they claim that there is no correlation between Γ and the number of MSPs. Bagchi et al. (2011) use Pearson, Spearman, and Kendall statistical correlation tests, and report the relevant coefficients and null-hypothesis probabilities. We note that the null-hypothesis probabilities for the Spearman and Kendall tests for correlation between their calculated Γ and the numbers of MSPs are 0.02 and 0.01, rather less than the typical 0.05 criterion for significance. However, the Pearson test's null-hypothesis probability is only 0.07, which does not provide clear evidence of correlation.

Here we assume that their calculations of the numbers of MSPs are correct, and recalculate these correlations using our new Γ values. We use model 1 (FK06) from Bagchi et al. (2011) for comparisons, as do they. In Fig. 2.10 and Table 2.4, we show and calculate the correlations between our values for Γ and their MSP population results. Our statistical correlation tests indicate a very strong correlation between Γ and the number of MSPs in a GC, with null-hypothesis probabilities of no correlation below 0.013.

2.5.3 γ-ray fluxes

The Fermi γ-ray Space Telescope's Large Area Telescope's unprecedented sensitivity and spatial resolution to GeV γ-rays have allowed detection of numerous radio MSPs as γ-ray sources (Abdo et al., 2009c,a), showing characteristic hard GeV spectra with cutoffs around 1-3 GeV (Abdo et al., 2009a). Fermi has re-
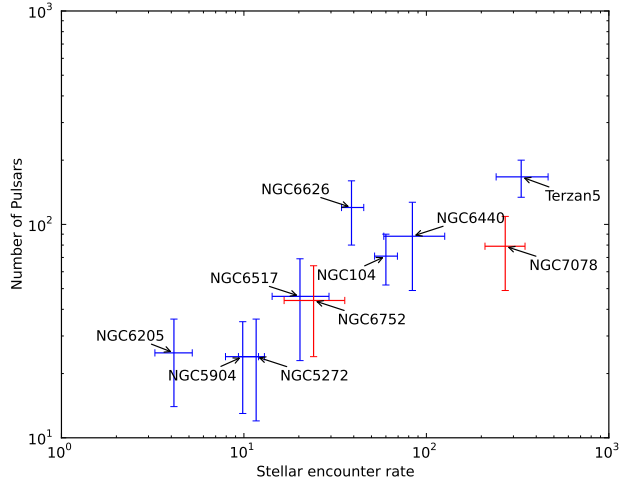
Figure 2.10: Number of recycled pulsars within a GC (from Bagchi et al. 2011) compared to our calculated Γ values. Core-collapsed clusters are shown in red. A correlation is clearly seen, and tabulated in Table 2.4. The normalization of Γ is chosen to be similar to the choice of normalization in Bagchi et al. 2011 ($\Gamma_{\text{NGC 6266}} = 100$).

cently detected gamma-ray emission from several globular clusters, including 47 Tuc and Terzan 5 (Abdo et al., 2009b; Kong et al., 2010; Abdo et al., 2010), showing similar γ-ray spectra as radio MSPs, indicating that the observed γ-ray flux is likely due to a population of γ-ray-emitting MSPs. In many clusters, no periodicities have been identified in the γ-ray emission, indicating that numerous MSPs contribute to the total emission, and thus that measurements of the total γ-ray flux can be used to estimate the number of MSPs in the cluster. However, NGC 6624 shows a counter-example, where a single MSP dominates the γ-ray flux (Freire et al., 2011), indicating that this method of estimating MSP numbers has limitations. Recent claims of detections of γ-ray fluxes from globular clusters have been made for γ-ray sources lying well outside the half-mass radius of clusters, at low significance, and without evidence of spectral similarity to radio MSPs (Tam et al., 2011). We do not trust that these γ-ray sources represent the MSP population of these GCs and therefore choose to
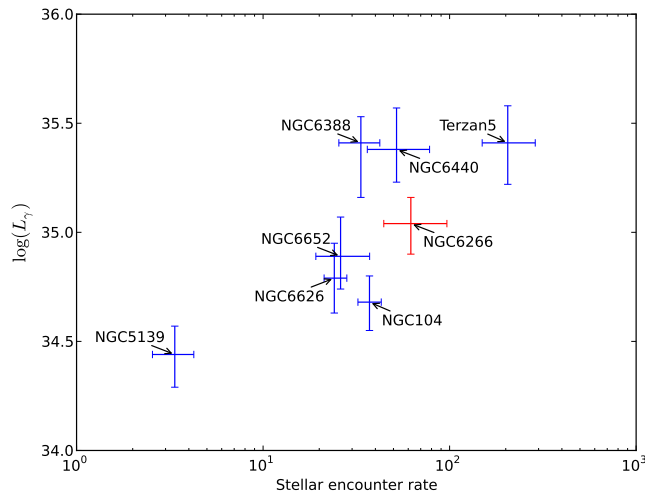
Figure 2.11: Gamma-ray flux measurements from Abdo et al. 2010 (γ) versus our calculated Γ values (Γ). Core-collapsed clusters are shown in red. A correlation is suggested, and tabulated in Table 2.4. The normalization of Γ is scaled so that $\Gamma_{\text{NGC 6121}} = 1$.

evaluate the effects of our calculations of Γ on the correlations between integrated γ-ray flux and Γ discussed by Abdo et al. (2010).

Abdo et al. (2010) measured γ-ray luminosities and calculated Γ for 8 GCs to investigate for a correlation. Using their reported values for γ-ray luminosities and our estimates for Γ, we find evidence (i.e., the probability that such a correlation occurs randomly is less than 10 %) for a correlation between the two parameters (Fig. 2.11, Table 2.4), in agreement with the conclusions of Abdo et al. (2010).

2.6 Conclusions

In this paper we calculated the stellar interaction rate Γ for Galactic globular clusters, directly deprojecting observed surface brightness profiles and then calculating $\Gamma \propto \int \rho^2/\sigma \, dV$. Previous calculations have used simplified relations such as $\Gamma_1 \propto \rho_c^2 r_c^3/\sigma$, $\Gamma_2 \propto \rho_c^{1.5} r_c^2$, or have assumed King-model structures to

perform integrations of Γ for clusters. Although our results are generally similar to previous analyses, we find significant differences in several cases, particularly for core-collapsed clusters, which we treat for the first time in the same way as non-core-collapsed clusters. A major advance in this work is the calculation of uncertainties in our final Γ estimates, by using Monte-Carlo simulations to incorporate the effects of observational uncertainties.

Comparing our Γ calculations with observations of close binaries produced by stellar interactions, we found strong evidence for correlations. This is in agreement with most previous work, but we do find significant differences with key recent results. Comparing our Γ to the numbers of XRBs in a GC (Pooley et al., 2003; Fregeau, 2008), there is a suggestion that core-collapsed clusters may have *fewer* XRBs than other GCs of similar Γ, in contrast to Fregeau (2008). Comparing Γ to the number of MSPs in GCs, we find extremely strong correlations, in contrast to Bagchi et al. (2011). Finally, we found evidence for correlation of Γ with the total γ-ray fluxes from GCs, in agreement with Abdo et al. (2010).

Name	E(B-V)	(m-M)	D(kpc)	σ_c(km/s)	σ Ref.	SBP Ref.	CC	$\delta\mu$	Γ	Lower bound	Upper bound
Terzan 5	2.61±0.1	21.27±0.2	5.98	8.06±2.58	g	l	0.2		6800	3780	7840
NGC 7078	0.1±0.02	15.39±0.1	10.38	13.5±0.9	h	n	0.14	c	4510	3520	5870
NGC 6715	0.15±0.02	17.58±0.1	26.49	10.5±0.3	h	n	0.03		2520	2250	2750
Terzan 6	2.35±0.35	21.44±0.1	6.78	5.27±1.69	g	t	0.1	c	2470	7530	7540
NGC 6441	0.47±0.07	16.78±0.1	11.6	18±0.2	h	n	0.1		2300	1660	3270
NGC 6266	0.47±0.07	15.63±0.1	6.83	14.3±0.4	h	n	0.16	c:	1670	1100	2380
NGC 1851	0.02±0.01	15.47±0.1	12.07	10.4±0.5	h	n	0.06		1530	1340	1730
NGC 6440	1.07±0.16	17.95±0.1	8.45	13.71±4.39	g	t	0.11		1400	923	2030
NGC 6624	0.28±0.04	15.36±0.1	7.91	5.4±0.5	h	n	0.06	c	1150	972	1260
NGC 6681	0.07±0.01	14.99±0.1	9.01	5.2±0.5	h	n	0.12	c	1040	848	1310
NGC 104	0.04±0.01	13.37±0.1	4.46	11±0.3	h	n	0.08		1000	866	1150

Table 2.2: The 11 GCs with the highest Γ values, providing basic input data for them, their Γ values (normalized to give NGC 104's Γ=1000), and 1-σ bounds. $\delta\mu$ is the assumed error on surface brightness profile. σ Ref. represents the reference of velocity dispersion (g: G02, h: HC) and SBP Ref shows the reference for surface brightness profile (l: L10, n: NG06, t: T95). "c" in the CC column denotes a core-collapsed cluster (from HC). Note that for Terzan5, extinction calculation is based on Massari et al 2012. To calculate A_v based on this value, we used $R_v = 2.83$; although for the rest we assumed $R_v = 3.1$. The complete table is available in the appendix.

name	Difference (%)	Ref.
NGC 104	1.13	(1)
NGC 288	2.86	(1)
NGC 362	2.63	(1)
NGC 2419	2.94	(1)
NGC 3201	5.00	(1)
NGC 5024	0.23	(2)
NGC 5139	1.32	(1)
NGC 6121	0.08	(1)
NGC 6218	14.7	(1)
NGC 6254	0.15	(1)
NGC 6341	2.56	(1)
NGC 6656	4.05	(1)
NGC 6809	7.89	(1)
NGC 7078	2.84	(3)

Table 2.3: Difference between Γ calculated based on a constant velocity dispersion and the measured velocity dispersion profile. References for velocity dispersion profiles - (1): Zocchi et al. 2012 (using their King model fits to the profiles), (2):Sollima et al. 2012, (3):Murphy et al. 2011

Parameter	XRBs[1]	Recycled PSs[2]	γ-ray flux[3]
Pearson r	0.942	0.745	0.589
$p(> |r|)$	4.5×10^{-5}	0.013	0.124
Spearman r	0.770	0.863	0.670
$p(> |r|)$	0.009	0.001	0.068
Kendall τ	0.600	0.674	0.588
$p(> |\tau|)$	0.016	0.006	0.059

Table 2.4: Results of statistical tests for correlations of several different measurements of close binaries with our calculations of Γ. For all of these tests, the p values show the probability that a correlation arises randomly. Given such low probabilities, there is clear evidence of correlations in all cases. 1: Pooley et al. (2003), 2: Bagchi et al. (2011), 3: Abdo et al. (2010)

Name	$4\pi\sigma_c^{-1}\int\rho^2(r)r^2dr$	$-\delta$	$+\delta$	$\rho_c^2 r_c^3\sigma_c^{-1}$	$-\delta$	$+\delta$	$\rho_c^{1.5}r_c^2$	$-\delta$	$+\delta$
Terzan 5	6.80E+3	3.02E+3	1.04E+3	1.86E+3	9.34E+2	1.99E+3	1.40E+3	2.85E+2	3.23E+2
NGC 7078	4.51E+3	9.86E+2	1.36E+3	5.01E+3	2.77E+2	3.00E+2	6.46E+3	1.76E+2	1.66E+2
NGC 6715	2.52E+3	2.74E+2	2.26E+2	2.55E+3	1.33E+2	1.05E+2	2.03E+3	4.35E+1	5.11E+1
Terzan 6	2.47E+3	1.72E+3	5.07E+3	1.78E+3	8.51E+2	2.34E+3	1.30E+3	2.41E+2	2.79E+2
NGC 6441	2.30E+3	6.35E+2	9.74E+2	2.56E+3	1.84E+2	1.80E+2	3.15E+3	1.03E+2	1.08E+2
NGC 6266	1.67E+3	5.69E+2	7.09E+2	2.02E+3	1.86E+2	1.71E+2	2.47E+3	8.15E+1	7.78E+1
NGC 1851	1.53E+3	1.86E+2	1.98E+2	1.54E+3	7.66E+1	6.98E+1	1.91E+3	5.41E+1	5.48E+1
NGC 6440	1.40E+3	4.77E+2	6.28E+2	1.54E+3	5.43E+2	1.02E+3	1.75E+3	1.47E+2	1.55E+2
NGC 6624	1.15E+3	1.78E+2	1.13E+2	1.20E+3	1.13E+2	1.51E+2	1.08E+3	2.61E+1	2.45E+1
NGC 6681	1.04E+3	1.92E+2	2.67E+2	9.81E+2	6.04E+1	6.59E+1	9.64E+2	2.75E+1	2.63E+1
NGC 104	1.00E+3	1.34E+2	1.54E+2	1.00E+3	4.81E+1	4.64E+1	1.00E+3	2.85E+1	3.08E+1
NGC 5824	9.84E+2	1.55E+2	1.71E+2	9.16E+2	4.15E+1	4.89E+1	1.22E+3	3.18E+1	2.98E+1
Pal 2	9.29E+2	5.55E+2	8.36E+2	1.18E+3	4.43E+2	8.02E+2	4.57E+2	4.89E+1	4.27E+1
NGC 2808	9.23E+2	8.27E+1	6.72E+1	1.15E+3	9.79E+1	1.11E+2	1.21E+3	2.49E+1	2.67E+1
NGC 6388	8.99E+2	2.13E+2	2.38E+2	9.53E+2	7.52E+1	7.41E+1	1.77E+3	4.89E+1	4.41E+1
NGC 6293	8.47E+2	2.39E+2	3.77E+2	9.18E+2	1.51E+2	2.24E+2	1.22E+3	3.26E+1	3.00E+1
NGC 362	7.35E+2	1.17E+2	1.37E+2	8.09E+2	3.61E+1	3.31E+1	5.69E+2	1.49E+1	1.56E+1
NGC 6652	7.00E+2	1.89E+2	2.92E+2	7.03E+2	1.29E+2	3.60E+2	8.05E+2	2.25E+1	2.13E+1
NGC 6284	6.66E+2	1.05E+2	1.22E+2	7.50E+2	9.82E+1	1.22E+2	7.97E+2	1.95E+1	1.76E+1
NGC 6626	6.48E+2	9.11E+1	8.38E+1	6.43E+2	1.03E+2	1.28E+2	6.88E+2	1.92E+1	1.79E+1

Table 2.5: Γ calculations and 1-σ error estimations based on different equations, all normalized assuming $\Gamma_{NGC104} = 1000$. A portion is shown here, the complete table is available in the appendix.

39

Chapter 3

Discovery of the Third Transient X-ray Binary in the Galactic Globular Cluster Terzan 5

Arash Bahramian[1], Craig O. Heinke[1], Gregory R. Sivakoff[1], Diego Altamirano[2,3], Rudy Wijnands[2], Jeroen Homan[4], Manuel Linares[5,6], David Pooley[7,8], Nathalie Degenaar[9,10], Jeanette C. Gladstone[1]

[1] Dept. of Physics, University of Alberta, CCIS 4-183, Edmonton, AB T6G 2E1, Canada. [2] Astronomical Institute 'Anton Pannekoek', University of Amsterdam, Science Park 904, 1098 XH Amsterdam, the Netherlands. [3] Physics & Astronomy, University of Southampton, Southampton, Hampshire SO17 1BJ, UK. [4] Kavli Institute for Astrophysics & Space Research, MIT, 70 Vassar St., Cambridge, MA 02139, USA. [5] Instituto de Astrofísica de Canarias, c/ Vía Láctea s/n, E-38205 La Laguna, Tenerife, Spain. [6] Universidad de La Laguna, Dept. Astrofísica, E-38206 La Laguna, Tenerife, Spain. [7] Dept. of Physics, Sam Houston State University, Huntsville, TX 77341, USA. [8] Eureka Scientific, Inc., Oakland, CA, USA. [9] Dept. of Astronomy, University of Michigan, 500 Church Street, Ann Arbor, MI 48109, USA. [10] Hubble fellow.

Abstract

We report and study the outburst of a new transient X-ray binary (XRB) in Terzan 5, the third detected in this globular cluster, Swift J174805.3-244637 or Terzan 5 X-3. We find clear spectral hardening in *Swift/XRT* data during the outburst rise to the hard state, thanks to our early coverage (starting at $L_X \sim 4 \times 10^{34}$ ergs/s) of the outburst. This hardening appears to be due to the decline in relative strength of a soft thermal component from the surface of the neutron star (NS) during the rise. We identify a Type I X-ray burst in *Swift/XRT* data with a long (16 s) decay time, indicative of hydrogen burning on the surface of the NS. We use *Swift/BAT*, *MAXI/GSC*, *Chandra/ACIS*, and *Swift/XRT* data to study the spectral changes during the outburst, identifying a clear hard-to-soft state transition. We use a *Chandra/ACIS* observation during outburst to identify the transient's position. Seven archival *Chandra/ACIS* observations show evidence for variations in Terzan 5 X-3's non-thermal component, but not the thermal component, during quiescence. The inferred long-term time-averaged mass accretion rate, from the quiescent thermal luminosity, suggests that if this outburst is typical and only slow cooling processes are active in the neutron star core, such outbursts should recur every ~ 10 years.

3.1   Introduction

Transient low-mass X-ray binaries (LMXBs) experience long periods (often years to tens of years) of quiescence. In quiescence matter flowing from the companion builds up in the accretion disk, punctuated by outbursts when the accretion disk crosses a pressure and temperature threshold, increases in viscosity, and dumps large quantities of matter onto the accreting compact object (e.g., see Lasota, 2001, for a review). Their outbursts go through phases of varying X-ray spectra. These phases are generally interpreted as indicating the changing relative contributions of Comptonized optically thin emission vs. blackbody-like emission from an accretion disk, as the accretion rate and ge-

ometry change (e.g., Remillard and McClintock, 2006; Done et al., 2007, for reviews). These X-ray spectral states have been studied both for black hole LMXBs, and for NS LMXBs (e.g., Hasinger and van der Klis, 1989; Gierliński and Done, 2002; Gilfanov et al., 2003; Gladstone et al., 2007; Lin et al., 2007), which show an additional component from the NS surface.

The spectra of NS LMXBs in quiescence ($L_X \lesssim 10^{33}$ ergs/s) include thermal radiation from the (usually hydrogen) NS atmosphere (blackbody-like; Zavlin et al., 1996; Rajagopal and Romani, 1996), and often a harder nonthermal component, usually fit with a power-law (Campana et al., 1998). Several NS LMXBs have shown rapid, strong variability in quiescence indicative of accretion events, which can sometimes be clearly attributed to variation in both the thermal and power-law components (e.g., Rutledge et al., 2002b; Campana et al., 2004; Cackett et al., 2010; Fridriksson et al., 2011). The thermal component can be produced either by re-radiation of stored heat from the cooling NS (Brown et al., 1998), or by low-level accretion (Zampieri et al., 1995; Deufel et al., 2001), which produce similar spectra (Zampieri et al., 1995).

Studies of the spectra of black hole LMXBs during their decline from the low/hard state into quiescence (as L_X falls below 10^{35} ergs/s) have found clear softening (Corbel et al., 2006, 2008; Armas Padilla et al., 2013a; Plotkin et al., 2013). The softening of black hole LMXB spectra has been interpreted as a change in the origin of the X-ray emission, produced at low luminosities by either a radiatively inefficient hot flow (Esin et al., 1997; Gardner and Done, 2013) or synchrotron emission from a jet (Yuan and Cui, 2005; Pszota et al., 2008). A similar softening in the spectrum from the accretion flow occurs in NS systems at similar luminosities, where emission from the NS surface can play a role (Armas Padilla et al., 2011; Degenaar et al., 2013b; Linares et al., 2014).

Thermonuclear X-ray bursts burn accumulated hydrogen and/or helium on the NS surface, producing blackbody-like emission with a rapid rise, cooling

over timescales of seconds to minutes (Lewin et al., 1993; Galloway et al., 2008). X-ray bursts occurring in hydrogen-poor environments (either due to no hydrogen being present in the accreted material, or hydrogen being stably burned during accretion) show different properties from those in hydrogen-rich environments. The ratio of energy released by fusion in a burst to energy released during accretion is lower for helium bursts compared to hydrogen bursts due to the lower energy available from fusion.

Helium bursts generally have faster rise and decline times, since hydrogen burning involves the CNO cycle and thus is limited by the speed of β-decays (Fujimoto et al., 1981). Pure He bursts can be ignited in neutron stars that accrete hydrogen at low mass accretion rates (e.g., Peng et al. 2007), but neutron stars known to be accreting hydrogen-poor material (ultracompact systems with white dwarf donors) never show evidence of hydrogen-rich bursts (Galloway et al., 2008). Some bursts from ultracompact systems are relatively long, but these "giant" (or "intermediate-duration") bursts exhibit dramatic photospheric radius expansion, thought to be produced by a thick layer of accumulated He, which can accumulate only at low ($L_X < 0.01 L_{Edd}$) accretion rates (in't Zand et al., 2005).

Globular clusters are highly efficient at producing X-ray binaries through dynamical interactions, such as the exchange of (heavy) NSs into pre-existing binary stars, replacing the lower-mass star in the binary. Of perhaps 200 galactic LMXBs known to have reached $L_X \sim 10^{36}$ ergs/s , 18 (including Terzan 5 X-3) are located in globular clusters, a factor of ~ 100 overabundance per unit stellar mass compared to the galactic disk. LMXBs are concentrated in the densest, most massive globular clusters, which have the highest predicted rates of stellar interactions (e.g., Verbunt and Hut, 1987; Heinke et al., 2003d). Studying the number and types of LMXBs in different globular clusters can help us understand the dynamical processes that produce LMXBs in clusters. For example, identifying multiple LMXBs in one cluster has implications for

interpreting observations of X-ray emission from extragalactic globular clusters (such as their luminosity functions), where multiple LMXBs cannot be resolved (e.g., Sivakoff et al., 2007). Before Terzan 5 X-3, no more than two bright LMXBs had been identified in any one globular cluster (White and Angelini, 2001; Heinke et al., 2010; Pooley et al., 2010).

Terzan 5 is a dense and massive globular cluster close to the center of our Galaxy (d=5.9±0.5 kpc, Valenti et al., 2007), showing evidence of two separate stellar populations of different iron abundances, ages and helium content (Ferraro et al., 2009; D'Antona et al., 2010). Calculations of its stellar encounter rate suggest it may produce more X-ray binaries than any other Galactic globular cluster (Verbunt and Hut, 1987; Lanzoni et al., 2010; Bahramian et al., 2013). This status is supported by the largest population of known millisecond radio pulsars in any globular cluster, which are thought to be the descendants of LMXBs (Ransom et al., 2005; Hessels et al., 2006). Terzan 5 also hosts more than 50 known X-ray sources (Heinke et al., 2006b), including a dozen likely quiescent LMXBs (again the most numerous in any cluster).

Outburst of transient LMXBs have frequently been observed from Terzan 5 (Makishima et al., 1981; Warwick et al., 1988; Verbunt et al., 1995). *Chandra* observed one such outburst in 2000 (Heinke et al., 2003a), pinning down the location of an LMXB called EXO 1745-248[1], which was shown to have an unusually hard spectrum in quiescence during later *Chandra* observations (Wijnands et al., 2005; Degenaar and Wijnands, 2012). Another Terzan 5 outburst was identified in 2002 in *RXTE* All-Sky Monitor data (Wijnands et al., 2002b), but no imaging observations were taken. In 2010 an outburst was seen from an 11 Hz pulsar, IGR J17480-2446 (Terzan 5 X-2, Bordas et al. 2010; Strohmayer and Markwardt 2010), leading to a variety of detailed studies of the orbit and spin period, bursts, spectrum, burst oscillations, and evolution (e.g., Papitto

---

[1]Note that the true identity of the transient seen by EXOSAT in the 1980s (leading to the EXO name) is not known.

et al., 2011; Chakraborty et al., 2011; Miller et al., 2011; Motta et al., 2011; Cavecchi et al., 2011; Linares et al., 2011, 2012; Patruno et al., 2012; Papitto et al., 2012; Altamirano et al., 2012a). A *Chandra* observation identifying the outbursting source (Pooley et al., 2010) allowed follow-up observations to track the crustal cooling of the NS (Degenaar and Wijnands, 2011; Degenaar et al., 2011a, 2013a), while the even more precise moon occultation position (Riggio et al., 2012) permitted identification of the near-IR counterpart (Testa et al., 2012). Another Terzan 5 outburst, in 2011, was identified as EXO 1745-248 through a *Chandra* observation (Pooley et al., 2011a), and showed a superburst (a very long and energetic X-ray burst, thought to be powered by the burning of a thick layer of carbon) at the beginning of the outburst (Serino et al., 2012; Altamirano et al., 2012b)

In this paper we identify and study the outburst of the third transient X-ray binary in the globular cluster Terzan 5, Swift J174805.3-244637 (henceforth Terzan 5 X-3). We detected this transient using *Swift/XRT* (Wijnands et al., 2012), and identified spectral hardening in the rise of the outburst (Heinke et al., 2012), a Type I X-ray burst (Altamirano et al., 2012c), and the quiescent X-ray counterpart in *Chandra* images (Homan and Pooley, 2012). In §3.2 we present the X-ray data used and describe our data extraction. In §3.3 we derive the position of Terzan 5 X-3 by comparing observations before and during the outburst, analyze the spectral variation of the persistent emission throughout the outburst, study the properties of the thermonuclear burst, and analyze its quiescent X-ray spectrum. Finally, we discuss our results in §3.4.

3.2   Data Extraction

3.2.1   *Swift/XRT*

We monitored Terzan 5 up to a few times per week for part of 2012 with the *Swift/XRT*, covering the 0.3-10 keV energy range (Burrows et al., 2005),

as part of our monitoring campaigns of globular cluster X-ray transients (see Altamirano et al., 2012b, Altamirano et al. *in prep.*). This monitoring enabled us to observe the rising outburst of a new transient (and the 3rd known transient LMXB in this cluster) first detected on July 6th, 2012 (Wijnands et al., 2012).

We used *Swift/XRT*'s photon counting (PC) mode, which produces two-dimensional images, and windowed timing (WT) mode for which CCD data is collapsed into a one-dimensional image for fast readout. PC mode data should be checked for pile-up when the count rate exceeds 0.5 count s^{-1}. Pile-up is the recording of multiple photons as a single event, leading in the worst case to rejection of all events from the center of the point-spread function, or PSF. Our *Swift/XRT* observations include 22 observations during the outburst, with 8 observations in WT and the rest in PC mode (Table 3.1).

We used HEASOFT 6.12 and FTOOLS[2] (Blackburn, 1995) to reduce and analyze the data. We reprocessed the data with the FTOOLS *xrtpipeline* and manually extracted data for spectral analysis. We investigated every observation for pile-up, following the *Swift/XRT* pile-up thread[3], and extracted data from an annulus around the source in PC mode observations that suffered from pile-up.We subtracted background from a circular region in the vicinity of the source in all PC observations. The extraction region for WT data was chosen to be a box around the event array (background subtraction was unnecessary for these countrates), as discussed in the *Swift/XRT* data reduction guide[4]. We extracted spectra in the 0.5-10 keV bandpass using FTOOLS *xselect*, and created ancillary response function (ARF) files for each observations using FTOOLS *xrtmkarf*. We performed spectral analysis using XSPEC 12.7.1 (Arnaud, 1996).

For heavily absorbed sources, WT data show low energy spectral residuals, which look like a "bump" in the spectrum, and cause spectral uncertainties in

---

[2]http://heasarc.gsfc.nasa.gov/ftools/
[3]http://www.swift.ac.uk/analysis/xrt/pileup.php
[4]http://heasarc.nasa.gov/docs/swift/analysis

the $\lesssim 1.0$ keV region[5]. We compared *Swift/XRT* WT mode data to *Chandra* data (§3.2.2) taken within a few days, fitting them with the same model to find the energy range in which discrepancies appear. Based on this comparison, we ignored data below 1.4 keV in all WT observations during the outburst.

[5]http://www.swift.ac.uk/analysis/xrt/digest_cal.php

Obs. ID	Date	MJD	Exposure	avg. count rate (count s^{-1})	Notes
Swift/XRT observations					
32148002	2012-02-09	55966.9	985 s	1.75×10^{-2}	PC mode; quiescent
91445001	2012-06-11	56089.8	913 s	2.67×10^{-2}	PC mode; quiescent
91445002	2012-06-16	56094.5	1028 s	1.48×10^{-2}	PC mode; quiescent
91445003	2012-06-21	56099.0	1033 s	1.66×10^{-2}	PC mode; quiescent
91445004	2012-06-26	56104.8	1050 s	9.68×10^{-3}	PC mode; quiescent
91445005	2012-06-30	56108.6	935 s	1.40×10^{-2}	PC mode; quiescent
91445006	2012-07-06	56114.8	1197 s	7.65×10^{-2}	PC mode; First detection of rise;(1)
32148003	2012-07-07	56115.8	987 s	0.154	PC mode;(2)
32148004	2012-07-08	56117.0	987 s	0.245	PC mode;(2)
32148005	2012-07-10	56118.1	781 s	1.26	PC mode; Piled up;(2)
32148006	2012-07-12	56120.7	978 s	3.19	PC mode; Piled up; Hard/soft transition
526511000	2012-07-13	56121.7	251 s	11.4	WT mode
91445008	2012-07-16	56124.3	253 s	14.2	WT mode
526892000	2012-07-16	56124.9	596 s	14.9	WT mode
32148007	2012-07-17	56125.9	960 s	$20.4(16.3)^{a}$	WT mode; Type I X-ray burst;(3)

91445009	2012-07-21	56129.1	1173 s	71.8	WT mode
91445010	2012-07-26	56134.1	612 s	23.5	PC mode; Piled up
91445011	2012-08-01	56140.1	985 s	52.1	WT mode
91445012	2012-08-05	56144.8	1057 s	24.1	WT mode; Return to hard state?
91445013	2012-08-10	56149.4	1031 s	4.15	WT mode
32148008	2012-08-11	56150.1	1488 s	3.16	PC mode; Piled up
32148011	2012-08-13	56152.2	1480 s	2.47	PC mode; Piled up
530808000	2012-08-13	56152.4	774 s	2.97	PC mode; Piled up
32148010	2012-08-14	56153.2	1494 s	2.51	PC mode; Piled up
91445014	2012-08-15	56154.3	1060 s	2.17	PC mode; Piled up
32148012	2012-08-19	56158.3	2153 s	1.78	PC mode; Piled up
91445015	2012-08-20	56159.1	1006 s	2.14	PC mode; Piled up
91445016	2012-08-24	56163.2	1131 s	1.05	PC mode
32148013	2012-08-30	56169.3	2075 s	2.95×10^{-2}	PC mode; quiescent
32148014	2012-09-13	56177.6	1953 s	2.02×10^{-2}	PC mode; quiescent
32148015	2012-09-20	56184.6	1976 s	1.98×10^{-2}	PC mode; quiescent

Chandra/ACIS observations

3798	2003-07-13	52833.6	39.34 ks	9.91×10^{-3}	quiescent; (4,5)

10059	2009 -07-15	55027.7	36.26 ks	7.42×10^{-3}	quiescent; (6,7)
13225	2011-02-17	55609.3	29.67 ks	5.56×10^{-3}	quiescent; (6,7)
13252	2011-04-29	55680.7	39.54 ks	6.78×10^{-3}	quiescent; (7,8)
13705	2011-09-05	55809.7	13.87 ks	5.69×10^{-3}	quiescent; (9)
14339	2011-09-08	55812.1	34.06 ks	6.08×10^{-3}	quiescent; (9)
13706	2012-05-13	56060.7	46.46 ks	7.58×10^{-3}	quiescent; (9)
13708	2012-07-30	56138.4	9.84 ks	6.60	Terzan 5 X-3 outburst; Piled up; (10,11)

Table 3.1: List of *Swift/XRT* observations (top) and *Chandra/ACIS* observations (bottom) of Terzan 5 used. References: 1- Wijnands et al. 2012, 2- Heinke et al. 2012, 3- Altamirano et al. 2012c, 4- Wijnands et al. 2012c, 5- Heinke et al. 2006b, 6- Degenaar and Wijnands 2011, 7- Degenaar et al. 2011a, 8- Degenaar and Wijnands 2012, 9- Degenaar et al. 2013a, 10- Homan and Pooley 2012, 11- This work. a- The second count rate is calculated excluding the X-ray burst interval. Reported count rates are not corrected for pile up. MJDs are reported for start of each observation.

3.2.2 *Chandra/ACIS*

We observed Terzan 5 X-3 during outburst with *Chandra/ACIS* in full-frame and FAINT telemetry mode with no grating (Obs. ID: 13708, PI: Pooley). We also used *Chandra* archival data for our analysis of this source, details of which can be found in Table 1. All archival observations were taken in FAINT telemetry mode with the ACIS-S3 CCD at the focus. We analyze *Chandra/ACIS* data in the 0.5-10 keV energy range.

Data was reprocessed using CIAO 4.4 (Fruscione et al., 2006), with CALDB 4.4.8, following the standard CIAO science threads[6]. We used observations during which all sources in the globular cluster were in quiescence. We reprocessed the data, corrected the relative astrometry and ran CIAO *reproject_events*, and then stacked the event files together using CIAO *dmmerge*.

Spectra were then extracted from both the archival and new data using CIAO task *dmextract*. Terzan 5 X-3 was heavily piled up in the new observation (in outburst), and so we extracted a spectrum from the readout streak. Finally, we combined all archival (quiescent data) using FTOOLS *addspec*[7]. Combining the quiescent data resulted in 240 ks of exposure time.

3.2.3 MAXI/GSC

The *MAXI* all sky X-ray monitor's (Matsuoka et al., 2009) *GSC* detector data covers the 2-20 keV energy range, and one-day averaged light curves are publicly provided in four bands: 2-4 keV, 4-10 keV, 10-20 keV and 2-20 keV (Mihara et al., 2011). We noticed two problems with *MAXI/GSC* light curves. Due to the low spatial resolution of *MAXI/GSC* and bright sources in the crowded field of Terzan 5, there is the possibility of background contamination from nearby sources like GX 3+1 and GX 5-1 (Fig. 3.1). Since these two sources

---

[6]http://cxc.harvard.edu/ciao/threads/index.html
[7]We found the results from CIAO's *combine_spectra* and FTOOLS's *addspec* completely identical.

showed stable X-ray brightness with no obvious variations in the *MAXI/GSC* data during Terzan 5 X-3 outburst, the background contamination may lead to a constant enhanced background.

We also noticed that *MAXI/GSC* light curves show periodic behaviour with a period of ≈ 35 days for various well-known stable X-ray sources (e.g., the Crab nebula). This is caused by calibration issues regarding the 70-day precession of the International Space Station's orbit (*MAXI* team 2013, *priv. comm.*). This problem principally affects the 2-4 keV data, with less effect on the 4-10 and 10-20 keV light curves. Thus we ignored the 2-4 keV lightcurves for this research. We also ignored *MAXI/GSC* 10-20 keV band lightcurves, due to the low statistical significance of Terzan 5 X-3's detection there. We decontaminated the *MAXI/GSC* 4-10 keV lightcurve assuming a constant background count rate of 0.023, calculated based on a weighted average of the count rates before the outburst for a period of ~ 120 days, with the addition of a systematic error based on the rms variations in the light curve before the outburst. We used the corrected values of the statistical uncertainties in *MAXI/GSC* data, as the *MAXI* team announced an erratum in the reported statistical uncertainties on April 26, 2013 (*MAXI* team 2013, *priv. comm.*) noting that the corrected uncertainties are a factor of 2 larger than previously reported.

3.2.4   *Swift/BAT*

The *Swift/BAT* telescope data covers 15-150 keV energy range (Barthelmy et al., 2005). We used daily light curves from the *Swift/BAT* transient monitor results provided by the *Swift/BAT* team (Krimm et al., 2013). Data points on these daily light curves are from *Swift/BAT* survey data and are represented in a single band (15-50 keV). These points are the weighted average of all observations performed each day. The Swift/BAT has better angular resolution (20′ vs. 1° FWHM for Swift/BAT vs. MAXI/GSC). Such an improvement in the angular resolution limits the chances of contamination occurring. Although
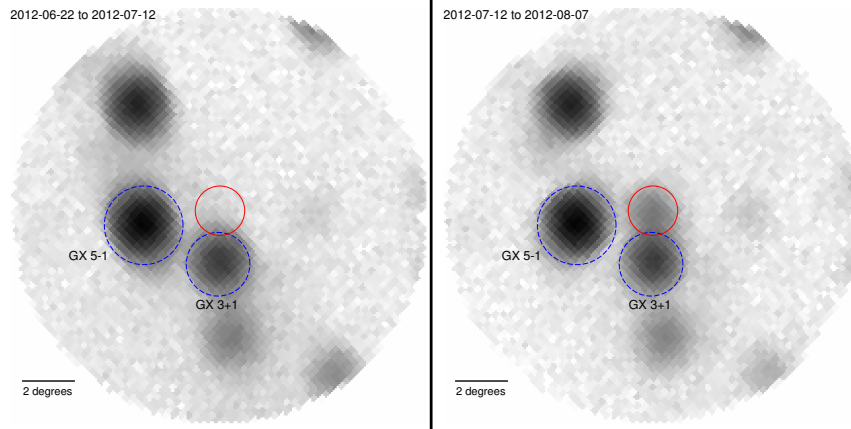
Figure 3.1: *MAXI/GSC* 2-20 keV images of the sky around Terzan 5 (the red circle). Left: before Terzan 5 X-3 outburst. Right: During the outburst. *MAXI/GSC* data for Terzan 5 may suffer contamination from the nearby sources GX 5-1 and GX 3+1 (blue dashed circles).

we cannot rule out some contamination, it seems reasonable that it does not pose a serious problem. As such, it is not surprising that we do not see evidence of contamination of the Swift/BAT data by nearby sources as is identifiable in the MAXI data.

3.3 Analysis and Results

3.3.1 Position

We accurately and precisely located the position of Terzan 5 X-3, using the *Chandra/ACIS* data. We compared the *Chandra/ACIS* observation taken during the outburst and a stacked image of 7 *Chandra/ACIS* observations taken when all Terzan 5 sources were in quiescence (§3.2.2, Table 3.1). We corrected the astrometry in the outburst observation by comparing the positions (using the CIAO *wavdetect* tool) of three other sources in this observation with their astrometrically corrected positions as reported in Heinke et al. (2006b). Using a weighted average of the required shifts ($+0.23''$ for RA and $+0.04''$

for Dec), we find the position of Terzan 5 X-3 to be RA= 17:48:05.41±0.02^s and Dec=−24:46:38.0±0.2″, in agreement (2σ) with the published position of the X-ray source CXOGLB J174805.4-244637 (Heinke et al. 2006b), at RA= 17:48:05.413±0.001^s and Dec=−24:46:37.67±0.02″ (Fig. 3.2).
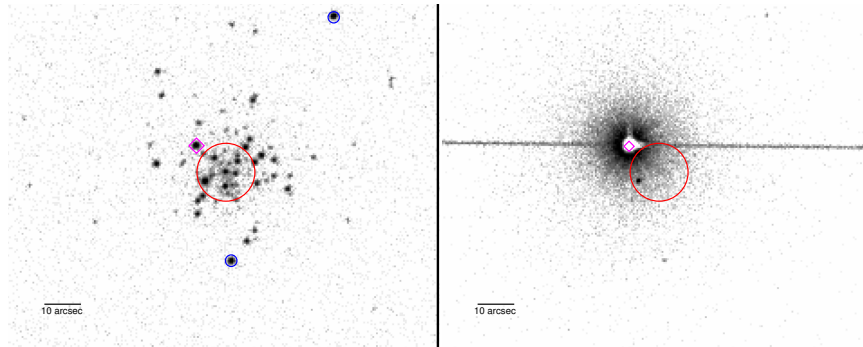
Figure 3.2: *Chandra/ACIS* observations of Terzan 5. Left: Stacked image of observations during quiescence (Bottom of Table 3.1) of all sources; total exposure ≈ 240 ks. Right: Outburst of Terzan 5 X-3 (Obs. ID 13708 with exposure ≈ 10 ks). The red circles and magenta diamond represent the core of Terzan 5 (Harris, 1996) and the position of Terzan 5 X-3, respectively (before astrometric corrections to the outburst image). Blue circles identify additional sources (CXOGLB J174804.7-244709 and CXOGLB J174802.6-244602) used for constraining the hydrogen column density of Terzan 5 (§3.3.3).

3.3.2 Phases of the outburst

We used *MAXI/GSC* and *Swift/BAT* hard X-ray transient monitor light curves to study the evolution of Terzan 5 X-3's outburst in the soft X-ray (4-10 keV, *MAXI/GSC*) and hard X-ray (15-50 keV, *Swift/BAT*) bands. We converted count rates into equivalent fluxes from the Crab Nebula to make these light curves suitable for comparison. For this purpose, we used conversion coefficients given for each instrument[8]: for the *Swift/BAT* hard X-ray transient monitor 1 Crab = 0.22 count cm^{-2} sec^{-1} and for the *MAXI/GSC* 4-10 keV band 1 Crab

---

[8]*MAXI*- http://maxi.riken.jp/top/index.php?cid=000000000036 *Swift/BAT*- http://swift.gsfc.nasa.gov/docs/swift/results/transients

= 1.24 count cm^{-2} sec^{-1}. We plot the light curves for Terzan 5 X-3's outburst as seen by both *MAXI/GSC* and *Swift/BAT*, and their ratio, in Fig. 3.3.

We distinguish four phases of Terzan 5 X-3's outburst. (a) Rise: the hard X-ray brightness of the source increases, the source eventually becoming significantly detected in the soft X-ray as well. (b) Hard state: hard X-ray brightness reaches its peak. (c) Soft state: soft X-ray brightness peaks while hard X-ray brightness drops. (d) Decline: the source briefly gets brighter in the hard X-ray again before turning off. Unfortunately there is insufficient data from the MAXI /GSC during the decline of the outburst. Therefore, we are unable to confirm that Terzan 5 X-3 returns to the hard state during its decline.

We used the soft X-ray (*MAXI/GSC* 4-10 keV, S) and hard X-ray (*Swift/BAT* 15-50 keV, H) lightcurves, to create a color-luminosity diagram (as an analogy to a hardness-intensity diagram, Fender et al. 2004) for the outburst (Fig. 3.4). We defined our color to be (H-S)/(H+S), and defined luminosity as (H+S), converting count rates to luminosities in each band before their summation or subtraction. We converted count rates to luminosities with the assumption of a 5.9 kpc distance and power-law spectra, using power-law index values inferred from *Swift/XRT* data spectral fitting (§3.3.3). We extrapolated the *MAXI/GSC* 4-10 keV band flux to 0.1-12 keV and the *Swift/BAT* 15-50 keV band flux to 12-50 keV, and calculated luminosities in the 0.1-50 keV band. We cannot measure the spectral index above 10 keV, but since in the hard state the spectra are typically reasonably described by a power-law up to 50 keV, and in the soft state the flux above 12 keV is a minor contribution to the total, this is unlikely to have a large effect. In the 0.5-10 keV band, the source was bright for approximately 20 days, reaching a maximum luminosity of 7×10^{37} erg s^{-1} and an average luminosity of 3×10^{37} erg s^{-1} in this time interval. The evolution of the outburst and phases mentioned above can be clearly seen in this color-luminosity diagram (Fig. 3.4). Spectral evolution during the outburst, including at fainter fluxes but with a more limited bandpass, can also

be seen in *Swift/XRT* observations (§3.3.3).

3.3.3 Spectral analysis

Hydrogen column density of Terzan 5

The first step in our spectral analysis is constraining hydrogen column density N_H, which we check by spectral analysis of multiple sources in the cluster. Since the sources are located within 1' of each other, we expect little variation in N_H along the different sightlines. Except for LMXBs observed at high inclination, generally the measured N_H throughout an outburst appears to be stable (Miller et al., 2009), so we assume that Terzan 5 X-3's N_H remains constant. We used *Chandra/ACIS* observations of Terzan 5 taken when all sources were quiescent (Table 3.1). We extracted spectra of three of the brighter faint sources in Terzan 5 (Terzan 5 X-3, CXOGLB J174804.7-244709 and CXOGLB J174802.6-244602; Heinke et al. 2006b, Fig. 3.2) from each observation using CIAO *dmextract* and combined the extracted spectra for each source. We fit these combined spectra, along with the *Chandra* spectrum of Terzan 5 X-3 during the outburst, simultaneously. We used appropriate models based on previous studies of each faint source (Heinke et al., 2006b), confirmed as acceptable fits. For Terzan 5 X-3 during quiescence, and for CXOGLB J 174804.7-244709, we used a NS atmosphere (NSATMOS, Heinke et al. 2006a) plus a power-law (PEGPWRLW). For CXOGLB J 174802.6-244602 we used a power-law. Finally, for Terzan 5 X-3 during outburst, we used a disk model (DISKBB) plus a thermal Comptonization model (COMPTT, Titarchuk 1994). We fit all these spectra simultaneously with a single value of N_H, using the PHABS model in XSPEC, with Anders and Grevesse (1989) abundances, finding $N_H = 1.74^{+0.06}_{-0.08} \times 10^{22}$ cm^{-2}. Individual spectral fits gave consistent results, with differences below the 10% level. This value is consistent with the measurements in Heinke et al. (2003a), Wijnands et al. (2005), Heinke et al. (2006b),

and Degenaar and Wijnands (2011), though not with the lower value of Miller et al. (2011)[9], and is consistent with the $E(B\text{-}V)$ estimates in Valenti et al. (2007) and Massari et al. (2012), using the Güver and Özel (2009) relation to N_H. We note that Miller et al. (2011) fit a simple blackbody plus power-law to the outburst spectrum of IGR J17480-2446 (Terzan 5-X2), which may lead to systematic differences compared to more complex outburst spectral models. We used our best-fit N_H value in the PHABS model, using default abundances, for the rest of the spectral analysis throughout this paper.

For comparison, we also used the same procedure for constraining N_H using the TBABS model (instead of PHABS), with Wilms et al. (2000) abundances, finding an increase in N_H to $2.6 \pm 0.1 \times 10^{22}$ cm^{-2}. The remaining parameters agreed within the errors with the results using our default absorption model, indicating that for our level of analysis only internal consistency is required in the choice of absorption model.

Outburst

The spatial resolution of *Swift/XRT* is such that we must account for possible contamination due to emission form other XRBs in the cluster. To assess these levels, we fit the spectra of pre-outburst observations (using the same extraction region as for the outburst spectra), finding a background level of $L_X \sim 10^{34}$ ergs/s. We used 6 *Swift/XRT* observations taken before the outburst to estimate the combined spectrum from the other cluster sources. Due to the low number of counts per observation, we combined their spectra. We fit the resulting pre-outburst spectrum with an absorbed power-law model (Table 3.2) with N_H fixed to 1.74×10^{22} cm^{-2}, based on the results in §3.3.3.

For our initial spectral analysis, we used an absorbed power-law model to fit Terzan 5 X-3's spectrum, including a second power-law component with

---

[9]Miller et al. (2011) report N$_H$=(1.17±0.04)×10^{22} cm^{-2}, though they do not report the abundance scale they use.

values fixed to the pre-outburst results to model the background (Table 3.2, Fig. 3.5). A simple power-law model provided a good fit to most of the spectra (Table 3.2), while physically motivated complex spectral models could not be well-constrained for the high-quality bright outburst spectra (see below), so we focus on the results from power-law fits. This spectral analysis shows a significant drop of photon index from 2.6 ± 0.7 to 1.4 ± 0.1 during the outburst rise (Fig. 3.5), showing a clear hardening of the spectrum during the rise from quiescence. During the hard state, the photon index shows no significant variations and is ≈ 1.4. After the phase transition to the soft state, the photon index softens to ≈ 1.9, with significant variations and several poor fits.

Several spectral models have been suggested in the literature to model the detailed spectra of transient NS LMXBs in outburst, see e.g., Lin et al. (2007). These models usually contain a soft component for the radiation from the disk and/or boundary layer (i.e., a multi-color black body) and a hard component for the radiation from the hot corona around the accreting object (i.e., Comptonized radiation). We attempted to perform analyses of Terzan 5 X-3's outburst spectra using a variety of complex models with multiple components (e.g., DISKBB + COMPTT, BBODY+COMPTT, BBODY+BKNPOW). We could not obtain strong constraints on the spectral parameters due to the limited energy band available and limited statistical quality of the XRT data. The *Swift/XRT* WT spectra suffered particularly from calibration issues below $\sim$1 keV(§3.2.1). The *Swift/BAT* survey mode hard ($>$15 keV) X-ray spectra had a low signal to noise ratio, which prohibited spectral analysis. We defer further detailed spectral fitting, e.g. to clearly distinguish thermal vs. nonthermal components, to future work.

Thermonuclear burst

During *Swift/XRT* ObsID 32148007, which started at 20:54:00 UT on 2012 July 17 we detected an eightfold count rate increase over $\sim$ three seconds,

starting at $\approx$ 21:06:40, followed by a slower decline over $\sim$1 minute (Fig. 3.6, bottom panel), suggestive of a thermonuclear burst (Altamirano et al., 2012c). Using FTOOLS *xselect*, we divided the data from this observation into time intervals of 4 seconds each. We extracted spectra from each time interval using FTOOLS *xselect* and analyzed the spectra.

During this thermonuclear burst, the count rate reached $\approx$ 160 count s^{-1}. There is a possibility of pileup in *Swift/XRT* observations in windowed timing mode when the count rate exceeds 100 count s^{-1} (Romano et al. 2006). Following the *Swift/XRT* pile-up thread for WT data, we extracted spectra while excluding increasingly large fractions of the central PSF. Doing this, we found that the fitted photon index did not change, and thus we found no significant signs of pileup in this observation during the burst.

We fit an absorbed power-law to the spectrum extracted from a pre-burst interval, and considered this fit as a fixed component of the spectral model for time intervals during the burst (cf., Worpel et al. 2013; our statistics are insufficient to determine whether this assumption is correct, and moderate changes should not affect our conclusions). We fit an absorbed blackbody model (BBODYRAD) to the burst emission, finding decent fits for all intervals, and show the spectral evolution in Fig. 3.6. We find clear evidence of cooling (between 770 - 790 s in Fig. 3.6), while the inferred radius remains essentially constant. This is a clear signature of a thermonuclear burst, and thus of a NS.

We estimated the timescale of this burst using two methods. We fit an exponential model (count rate $\propto e^{-t/\tau_1}$) to the light curve of the burst after the peak, estimating the timescale $\tau_1 \approx 16 \pm 1$s. Following Galloway et al. (2008), we estimated an alternative timescale for thermonuclear bursts $\tau_2 = E_{burst}/F_{peak}$, where E_{burst} is the total fluence during the burst and F_{peak} is flux at the peak, finding $\tau_2 \approx 29$s. Galloway et al. (2008) divide bursts into those with τ_2 longer than 10 s, and those with τ_2 shorter than 10 s. The longer bursts are generally powered by hydrogen burning (with the exception

of "giant" bursts involving photospheric radius expansion, which was not seen here), and the short bursts involve only helium burning, since hydrogen burning proceeds more slowly than helium burning (Fujimoto et al., 1981; van Paradijs et al., 1988; Cornelisse et al., 2003). Our measured burst timescale indicates that hydrogen is being accreted, and thus that the donor star is hydrogen-rich, which requires an orbital period $\gtrsim 1.5$ hr (e.g., Nelson et al. 1986) and excludes a WD donor.

Quiescent behaviour

We used 7 *Chandra/ACIS* observations taken when all sources were quiescent (Table 3.1) to study the behaviour of Terzan 5 X-3 in quiescence before its outburst. We extracted source and background spectra from each observation using CIAO *dmextract*. We used a combination of a power-law (PEGPWRLW) model and a hydrogen atmosphere for a NS (NSATMOS), with absorption (PHABS) set to our preferred cluster value, the NS radius to 10 km, mass to 1.4 $M_{\odot}$, and distance set to 5.9 kpc. This model has been previously used to fit its spectrum in one quiescent observation (Heinke et al., 2006b). To study possible spectral variations, we simultaneously fit spectra from each observation in four different Trials, each with different parameters free (Table 3.3) : I) constraining the NSATMOS and PEGPWRLW components to have the same values between all observations; II) letting only the power-law normalization vary between observations, while constraining the NSATMOS temperature to be the same; III) letting only the NSATMOS temperature vary between observations, while constraining the power-law normalization to be the same; IV) letting both the power-law normalization and the NSATMOS temperature vary between observations. We found no evidence for variation in the power-law photon index Γ between observations if we allowed it to vary. Therefore, we tied its value between observations in each Trial (Fig. 3.7).

Trial I gives a poor fit, with χ^2=116.3 for 76 D.O.F. An F-test confirms the improvement from allowing the power-law flux to vary (Trial I to II), giving an F-statistic of 6.0 and probability of 4×10^{-5} of obtaining such an improvement by chance. Alternatively, allowing the NS temperature to vary (Trial III) also gives an improvement compared to Trial I (F-statistic of 4.2, chance improvement probability of 1×10^{-3}). Letting both components vary is a substantial improvement compared to allowing the NS temperature alone to vary (comparing III to IV, F-statistic=2.27, chance improvement probability of 4.7×10^{-2}), while letting both components vary is not preferred over allowing the power-law

component alone to vary (comparing II to IV, F-statistic=0.89, chance improvement probability 0.50). Thus, we identify clear variation in the non-thermal component, but no evidence for variation in the thermal component.

Rise of the outburst

We fit the *Swift/XRT* spectra from the rise of the outburst with a two-component model including a thermal component (BBODYRAD in XSPEC) and a non-thermal component (PEGPWRLW in XSPEC). We found good fits permitting only the relative normalizations of the thermal and non-thermal components to vary, with a photon index tied between observations ($\Gamma=1.1^{+0.2}_{-0.4}$) and a blackbody radius tied between observations ($R=4.3^{+1.4}_{-1.2}$ km). When the power-law index is left free between observations, the values are consistent, though they are poorly constrained in several spectra. Comparing our two-component model fits (Table 3.4) to our power-law fits (Table 3.2), a clear improvement in the fit is seen. Simultaneous fits to the first five *Swift/XRT* spectra of the outburst (listed in Table 3.4) with an absorbed power-law (with the photon index free between observations) give a reduced χ^2 of 1.32 for 45 degrees of freedom, while fits with an absorbed power-law plus blackbody give a reduced χ^2 of 1.09 for 43 degrees of freedom. An F-test gives an F-statistic of 5.55 and chance improvement probability of 0.007, supporting the addition of the thermal component. Protassov et al. (2002) showed that the F-test is often inaccurate for testing the necessity of adding an additional spectral component. We therefore chose the spectrum with the clearest evidence of a thermal component (ObsID 32148004), which shows a $\Delta\chi^2$ of 6.1 between the power-law and power-law plus thermal spectral fits (going from 12 degrees of freedom to 11). We simulated 1000 data sets using a best-fit absorbed power-law model, and fit them both with a power-law model and with a power-law plus thermal component model. None of our simulations showed a larger $\Delta\chi^2$ than that produced by our model, allowing us to conclude that the probability of incorrectly concluding

that a thermal component is required is less than 99.5%.

This indicates that the hardening during the outburst rise is likely caused by the decreasing relative contribution of a thermal component. With increasing time, and thus with increasing L_x, the fractional contribution of the thermal component decreases, but its kT increases monotonically. In the next section, we suggest that the thermal component is due to low-level accretion onto the surface of the neutron star.

3.4 Discussion

3.4.1 Hardening during the outburst rise

We observed clear evidence of hardening of the spectrum during the outburst rise from $L_X \sim 4 \times 10^{34}$ up to 10^{36} ergs/s. We have evidence that this hardening is due to the relative reduction in strength of a thermal component in the spectrum with increasing brightness. This is the first time that such hardening during the outburst rise has been detected, made possible by our program of *Swift/XRT* globular cluster monitoring allowing early detection of the outburst below $L_X = 10^{35}$ ergs/s. The trend of inferred photon index (for a fit to a power-law model) versus L_X is clear from the data in the rise, and is consistent with the data in the decay (which are not well-sampled below $L_X = 10^{35}$ ergs/s); see Fig. 3.5.

Softening during outburst decays has been seen from other (likely) NS LMXBs, in the L_X range of $10^{34} - 10^{35.5}$ ergs/s, especially when the soft (<2 keV) X-ray energy range is included (Jonker et al., 2003, 2004a; Cackett et al., 2011; Fridriksson et al., 2011; Armas Padilla et al., 2011, 2013c). *RXTE* observations have shown marginal softening during the decay of Aql X-1 down to $L_X = 5 \times 10^{34}$ ergs/s (Maitra and Bailyn, 2004), only in the part of the spectrum below 6 keV. *RXTE* observations of SAX J1808.4-3658 showed almost no spectral changes from $L_X \sim 2 \times 10^{36}$ down to 2×10^{34} ergs/s (Gilfanov et al.,

1998). These apparently contrasting observations are consistent if the softening is due to the increasing importance of the thermal component at lower L_X. Evidence in favor of an increasing relative thermal component can also be seen in *Swift/XRT* spectra of SAX J1808.4-3658 declining from $L_X \sim 10^{36}$ down to 10^{33} ergs/s (Campana et al., 2008). Thus, we interpret the hardening we observe in Terzan 5 X-3's rise as due primarily to the decreasing importance of a thermal component, rather than to the same physics responsible for the softening of black hole LMXBs during their decay, which show a steepening power-law spectrum (e.g., Plotkin et al., 2013).

Comparing the spectra observed from Terzan 5 X-3 to those of other NS LMXBs, we find a common pattern, that below $L_X \sim 1 - 3 \times 10^{35}$ ergs/s a thermal component is often required. For instance, Armas Padilla et al. (2013b) find, using XMM-Newton spectra, that two LMXBs at $L_X = 1 - 10 \times 10^{34}$ ergs/s require a strong thermal component, while this is not critical for another LMXB at $L_X \sim 10^{35}$ ergs/s. Wijnands et al. (2002c), using *Chandra* find that SAX J1747.0-2853, at $L_X \sim 3 \times 10^{35}$ ergs/s, does not need a thermal component. Armas Padilla et al. (2013c) measure a thermal component to comprise $\sim 20\%$ of the 0.5-10 keV luminosity for a transient at $L_X \sim 9 \times 10^{34}$ ergs/s (using XMM), with no evidence (from poorer *Swift/XRT* spectra) for a thermal component above $L_X = 2.6 \times 10^{35}$ ergs/s. Jonker et al. (2003, 2004a) study the return to quiescence of XTE J1709-267, finding a thermal component to comprise $\sim 40\%$ of the flux at $L_X \sim 4 \times 10^{34}$ ergs/s, increasing to $> 90\%$ at 2×10^{33} ergs/s. All these results suggest that there is a physical transition operating around $L_X \sim 10^{35}$ ergs/s which changes the energy spectra.

Such a transition can be provided by the declining optical depth of a hot Comptonizing atmosphere, as seen in numerical calculations of NSs accreting at low rates (Deufel et al., 2001; Popham and Sunyaev, 2001). Deufel et al. 2001 show temperature profiles and emergent spectra for NSs illuminated by high-temperature protons, such as are produced by radiatively inefficient ac-

cretion flows. in their figs. 4 and 5 they show that the emergent spectrum is a featureless Comptonized spectrum extending to ∼100 keV above $L_X \sim 10^{36}$ ergs/s, which develops a clear 0.5 keV thermal component at $\sim 10^{35}$ ergs/s, and loses the Comptonized tail by 10^{33} ergs/s. This transition is a strikingly accurate match to our observations of Terzan 5 X-3's spectral variations, and to other NS transients discussed in the literature. However calculations of Deufel et al. 2001 underpredict the observed hard power-law components seen in many quiescent LMXBs at low L_X ($< 10^{34}$ ergs/s, including Terzan 5 X-3 in quiescence). This may arise from their not including the Comptonizing effects of the overlying accretion flow on the observed spectrum. Popham and Sunyaev (2001) compute solutions for a hot boundary layer, which becomes optically thin for accretion luminosities below $\sim 10^{36}$ ergs/s, suggesting that some additional Comptonization can be performed by the accretion flow.

The temperature of the thermal component increases monotonically with the total X-ray luminosity during the rise (Table 4), as expected if the thermal component during the rise is produced by accretion. A correlation of thermal component temperature with total luminosity has been suggested from comparisons of multiple sources (Armas Padilla et al., 2013c), but this measurement clearly confirms this correlation in a single source. Furthermore, heating of the NS crust by accretion during the outburst will give rise to a rapidly decaying surface temperature at the end of the outburst (e.g., Cackett et al., 2006b). This effect of an accretion-heated crust could be confused with changing thermal emission from low-level accretion onto the NS surface during the outburst decline, but is not an issue during the outburst rise.

3.4.2 Nature of donors in globular cluster X-ray binaries

The detection of a thermonuclear burst during this outburst showed that the accreting object is a NS. Furthermore, the timescale of this thermonuclear burst indicates that the accreted matter contains hydrogen, evidence that the donor is

not a white dwarf. With this information, we are now capable of classifying 15 of the 18 known bright Galactic globular cluster LMXBs as either ultracompact ($P_{orb} < 1$ hour, accreting from a hydrogen-deficient and/or degenerate donor) or not ultracompact (accreting from a nondegenerate, H-rich star). Five are known to be ultracompact by direct detection of their orbital periods, and seven systems are known not to be ultracompact by direct measurement of their orbital periods. On the basis of X-ray burst behaviour indicative of hydrogen burning (Galloway et al., 2008), another three systems can be identified as not ultracompact (Table 3.5). (4U 1722-30, in Terzan 2, has shown some evidence, by its persistent low-luminosity accretion and burst behaviour, in favor of an ultracompact nature; in't Zand et al. 2007.) Thus, the fraction of observed bright globular cluster LMXBs that are ultracompact appears to be between 28-44% (for 5 or 8 of 18). This fraction is believed to be higher than in the rest of the Galaxy (Deutsch et al., 2000), but uncertainties in selection effects mean that we cannot confidently extrapolate the true underlying fraction of ultracompact systems and make clear comparisons to binary population synthesis models (e.g., Ivanova et al., 2008).

3.4.3   Quiescent counterpart

We have identified the quiescent counterpart to Terzan 5 -X3 with the brightest previously suggested candidate quiescent LMXB in the cluster, CXOGLB J174805.4-244637 (Heinke et al., 2006b). Our spectral analysis reveals evidence for a variable power-law contribution to the quiescent spectrum over timescales of years, but exhibits no evidence for changes to the thermal component. It is fascinating to see clearly here that the quiescent spectral properties appear to lie on a continuum with the outburst properties, with increasing hardening from quiescence, through the early rise, up to the hard state at $L_X > 10^{36}$ ergs/s (Fig. 3.5).

Chandra quiescent X-ray counterpart searches have now been performed for

nine transient cluster LMXBs, of which the three with the faintest outbursts have been identified with very faint ($L_X < 10^{32}$ ergs/s) quiescent counterparts (M15 X-3, Heinke et al. 2009a; NGC 6440 X-2, Heinke et al. 2010; IGR J17361-4441 in NGC 6388, Pooley et al. 2011b), two have spectrally hard counterparts with $L_X \sim 10^{32-33}$ ergs/s (EXO 1745-248 in Terzan 5, Wijnands et al. 2005; IGR J18245-2452 in M28, Papitto et al. 2013; Linares et al. 2014), and four have spectrally soft counterparts with $L_X \sim 10^{32-33}$ ergs/s (SAX J1748.9-2021 in NGC 6440, in't Zand et al. 2001; X1732-304 in Terzan 1, Cackett et al. 2006a; IGR J17480-2446 in Terzan 5, Degenaar et al. 2011a; and Terzan 5 X-3). These identifications support the idea that the faint soft X-ray sources identified as candidate quiescent LMXBs in globular clusters are indeed transient LMXBs, between (relatively bright) outbursts (Heinke et al., 2003d; Wijnands et al., 2013). The brightest of the faint soft X-ray sources should experience relatively high long-term average mass accretion rates, which will cause relatively large amounts of deep crustal heating and keep their cores warm. Such high mass accretion rates suggest frequent outbursts, and thus it is comforting that we have identified the brightest of the faint soft X-ray sources in the clusters NGC 6440, Terzan 5, and Terzan 1 with observed transients. The suggestion that roughly half the quiescent LMXBs in each cluster are easily identifiable in short *Chandra* observations by showing soft, primarily thermal X-ray spectra and X-ray luminosities between 10^{32-33} ergs/s (Heinke et al., 2005a) continues to seem reasonable, though it remains unproven.

From the quiescent NS thermal bolometric luminosity ($L_{NS,(0.01-10keV)} = 1.5 \times 10^{33}$ ergs/s, kT=118 eV at the surface) of Terzan 5 X-3, and its outburst properties, we can make some general statements about its outburst history or neutrino cooling properties, assuming that the quiescent thermal flux is due to heat deposited in the core during multiple accretion episodes (Brown et al., 1998). We estimate the total mass transfer rate onto the NS during this outburst by converting the daily *MAXI/GSC* 4-10 keV flux estimates (in

Crab units) into 0.1-12 keV fluxes (assuming a power-law with photon index set by the nearest *Swift/XRT* observations), converting the daily *Swift/BAT* flux estimates into 12-50 keV fluxes (using the same power-law photon index as for the *MAXI* data), adding these together, and assuming a 1.4 $M_\odot$, 10 km NS. This gives us a total energy release over the outburst of 9×10^{43} ergs, and a total mass transfer of 2.4×10^{-10} $M_\odot$.

If we assume "standard" modified Urca cooling (Yakovlev and Pethick, 2004; Wijnands et al., 2013), then we can estimate (using the quiescent NS luminosity) a mass transfer rate onto the NS of $\dot{M} \sim 3 \times 10^{-11}$ $M_\odot$/year (though this value might vary depending on the choice of crustal composition, e.g. whether a thick light-element layer is present; Page et al. 2004). Assuming this outburst is typical, we derive an average interval of ~ 8 years between outbursts. If the average interval between outbursts were much longer than 10 years, then Terzan 5 X-3 would be brighter in quiescence than expected under even the slowest cooling processes. One could attribute its quiescent thermal luminosity to continued accretion, but our analysis of the quiescent observations identifies no evidence for variability in the thermal component, arguing against this explanation. All Terzan 5 X-ray outbursts since 1996 have been identified with their quiescent counterpart with arcsecond precision, except one in 2002 (Wijnands et al., 2002b). The 2002 outburst had an average luminosity of $L_X \sim 2 \times 10^{37}$ erg s^{-1}, peak $L_X \sim 4 \times 10^{37}$ erg s^{-1}, and lasted for ~ 30 days (Degenaar and Wijnands, 2012). The 2012 outburst of Terzan 5 X-3 had a similar average luminosity of $L_X \sim 2 \times 10^{37}$ erg s^{-1}, peak $L_X = 7 \times 10^{37}$ erg s^{-1}, and lasted for 30 days above $L_X \sim 10^{36}$ ergs s^{-1} (comparable to the RXTE/ASM detection limit for the 2002 outburst). We therefore suggest that the 2002 X-ray outburst is likely to have also been produced by Terzan 5 X-3. This would nicely fit the ~ 8 year recurrence time we inferred above.
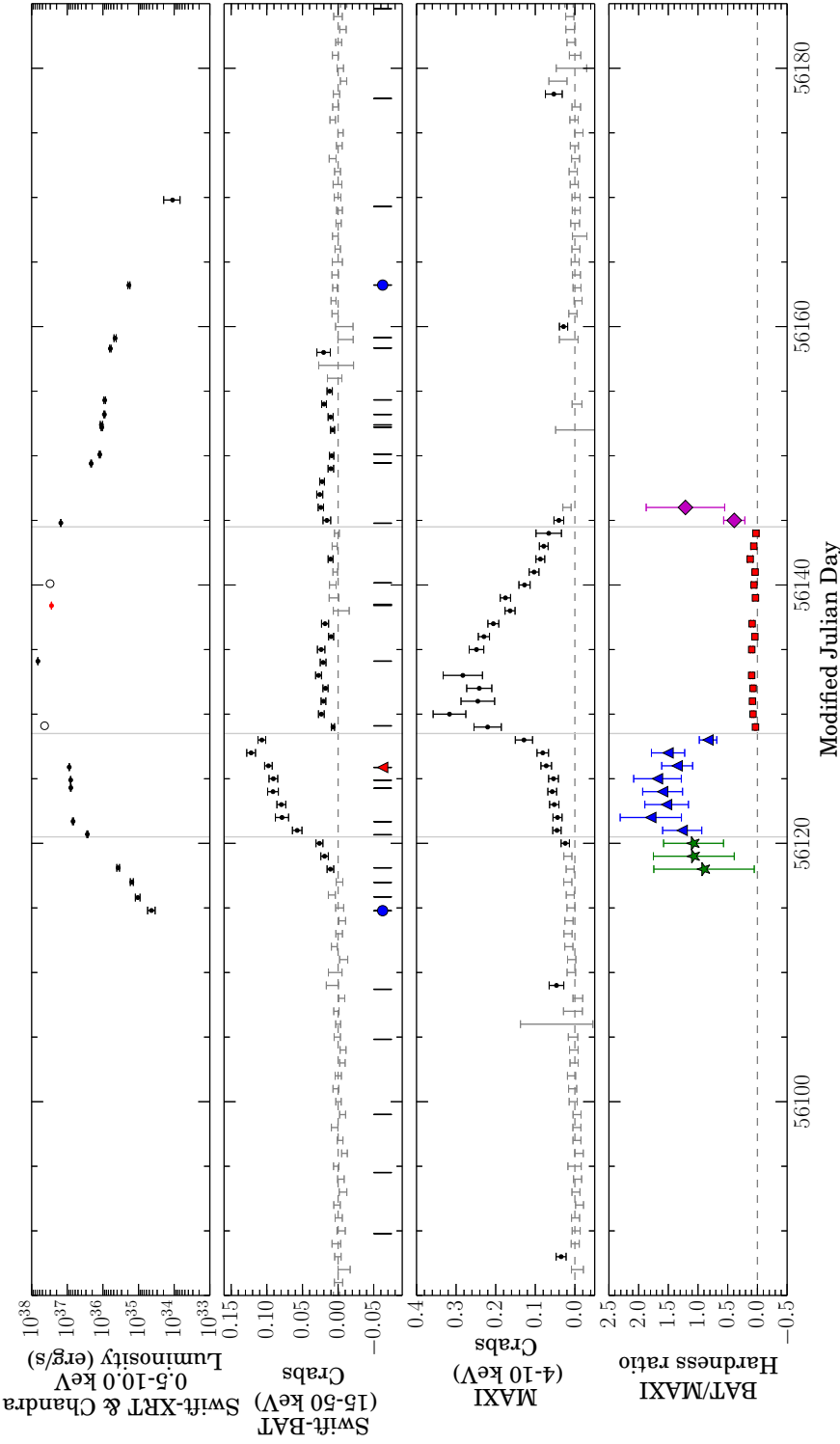
Figure 3.3: Evolution of Terzan 5 X-3 outburst. From the top, First panel: Luminosities from spectral fitting of *Swift*/XRT & *Chandra*/ACIS pointed observations (§3.3.3). Empty circles represent observations where these fits were poor ($\chi^2_\nu > 2$). The red datapoint represents *Chandra*/ACIS observation. Second panel: *Swift*/BAT lightcurve in the 15-50 keV band. Third panel: *MAXI*/GSC background-subtracted lightcurve in the 4-10 keV band. Fourth panel: Hardness ratio (H/S after conversion to Crab units) of the two light curves (*Swift*/BAT/*MAXI*/GSC). Black data points in the upper two panels represent significant detections ($> 2\sigma$) in each band, while grey bars show times when Terzan 5 X-3 was not significantly detected. Vertical lines at the bottom of the first panel represent times of pointed *Swift*/XRT and *Chandra*/ACIS observations. The first and last detection of the outburst in *Swift*/XRT data is represented by blue circles. The red triangle identifies the time of the detected thermonuclear burst (§3.3.3). Colors and shapes in the bottom panel indicate the different phases of outburst; a) green stars, rise, b) blue triangles, hard state, c) red squares, soft state, d) magenta diamonds, decline. Both *Swift*/BAT and *MAXI*/GSC lightcurves are in Crab units and error bars are 1σ uncertainties. Vertical lines in panels show approximate bounry of introduced phases. Note that in the fourth panel symbol size is larger than the errorbars in the soft state. All daily averages are plotted at the beginning of each day.

70
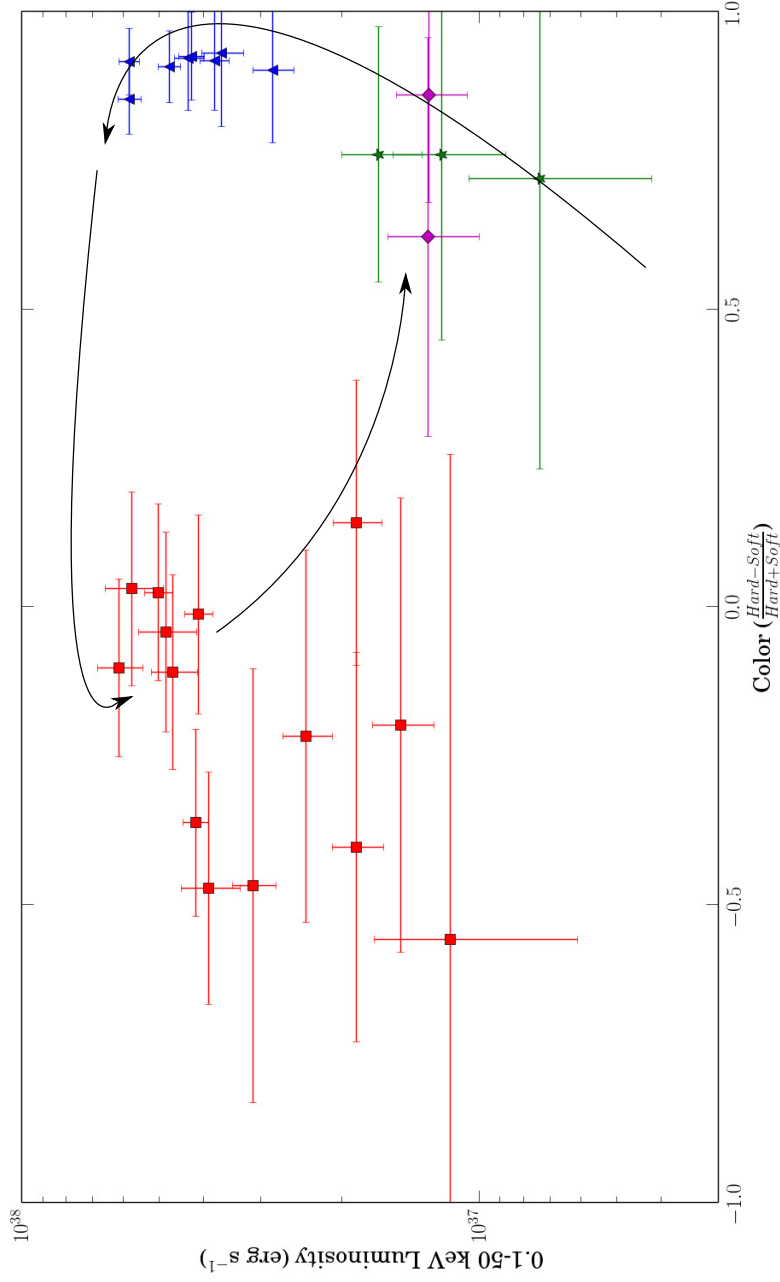
Figure 3.4: Color-luminosity diagram of Terzan 5 X-3 outburst, using the soft X-ray (*MAXI/GSC* 4-10 keV, S) and hard X-ray (*Swift/BAT* 15-50 keV, H) light curves, each in ergs s^{-1} (§3.3.2). color is (H-S)/(H+S), while luminosity is (H+S). colors and shapes of points indicate the phases of outburst (as in Fig. 3.3); a) green stars, rise, b) blue triangles, hard state, c) red squares, soft state, d) magenta diamonds, decline. Arrows represent the chronological order of data points. Error bars indicate 1σ uncertainties.

Obs. ID	MJD	Photon index	Flux	L_X	χ^2_ν/D.O.F(nhp)
32148002-91445005	55966-56108	$2.4^{+0.5}_{-0.4}$	$2.4^{+0.7}_{-0.6}$	$1.0^{+0.3}_{-0.2}$	0.68/7(0.69)
91445006	56114.8	2.6±0.7	10^{+5}_{-3}	4^{+2}_{-1}	0.83/6(0.54)
32148003	56115.8	2.5±0.4	25^{+7}_{-5}	10^{+3}_{-2}	0.85/5(0.51)
32148004	56117.0	2.3±0.3	37±6	15±2	1.86/9(0.052)
32148005	56118.1	1.9±0.4	90±12	37±5	0.54/6(0.78)
32148006	56120.7	1.4±0.1	658±32	273±13	1.58/19(0.05)
526511000	56121.7	1.4±0.1	1658±91	688± 38	1.20/14(0.27)
91445008	56124.3	1.46±0.08	1920±63	797± 26	0.69/25(0.87)
526892000	56124.9	1.39±0.06	1936±46	803± 19	1.56/34(0.03)
32148007	56125.9	1.40±0.04	2125±40	882± 17	1.05/37(0.38)
91445009^a	56129.1	1.8±?	10440±?	4333±?	$3.94/56(1.9\times10^{-21})$
91445010	56134.1	1.62±0.05	16070±330	6669±137	0.77/36(0.84)
13708^a(CXO)	56138.4	1.68±0.03	6680±80	2772±33	$1.76/102(3.4\times10^{-6})$
91445011^a	56140.1	1.8±?	7330±?	3042±?	$2.10/80(3.4\times10^{-6})$
91445012	56144.8	2.11±0.03	3651±70	1515±29	1.12/38(0.27)
91445013	56149.4	2.07±0.07	514±20	213± 8	1.10/58(0.28)
32148008	56150.1	1.7±0.1	295±16	122± 7	0.81/45(0.81)
32148011	56152.2	1.8±0.1	260±16	108±7	0.70/37(0.91)
530808000	56152.4	1.9±0.2	266±30	110± 12	1.12/10(0.34)
32148010^a	56153.2	1.8±0.1	219±13	91±5	$1.79/44(9.5\times10^{-4})$
91445014	56154.3	1.9±0.2	215±18	89±7	1.06/23(0.38)
32148012	56158.3	2.0±0.1	149±11	62±5	1.06/33(0.37)
91445015	56159.1	1.8±0.3	110±13	46±5	0.97/10(0.47)
91445016	56163.2	2.0±0.2	45±5	19±2	1.49/16(0.09)
32148013	56169.3	$2.4^{+1.5}_{-1.2}$	$2.7^{+4.8}_{-1.5}$	$1.1^{+1.9}_{-0.6}$	-

Table 3.2: *Swift/XRT* and *Chandra/ACIS* observations fit to an absorbed power-law model. Unabsorbed flux in units of 10^{-12} erg s^{-1} cm^{-2} and Luminosity in 10^{34} erg s^{-1}, both in 0.5 - 10 keV. all the flux and luminosity values are background-subtracted. "a" indicates spectra which are not well-described by a power-law (null hypothesis probability is $< 10^{-2}$); if $\chi^2 > 2$, no errors are calculated (indicated by "?"). The first row shows a spectral fit to a merged spectrum of 6 *Swift/XRT* observations of Terzan 5 before the outburst of Terzan 5 X-3. For Obs.ID 32148013, due to low counts, we used *cstat* statistics in the fitting. Reported uncertainties are 90% intervals.
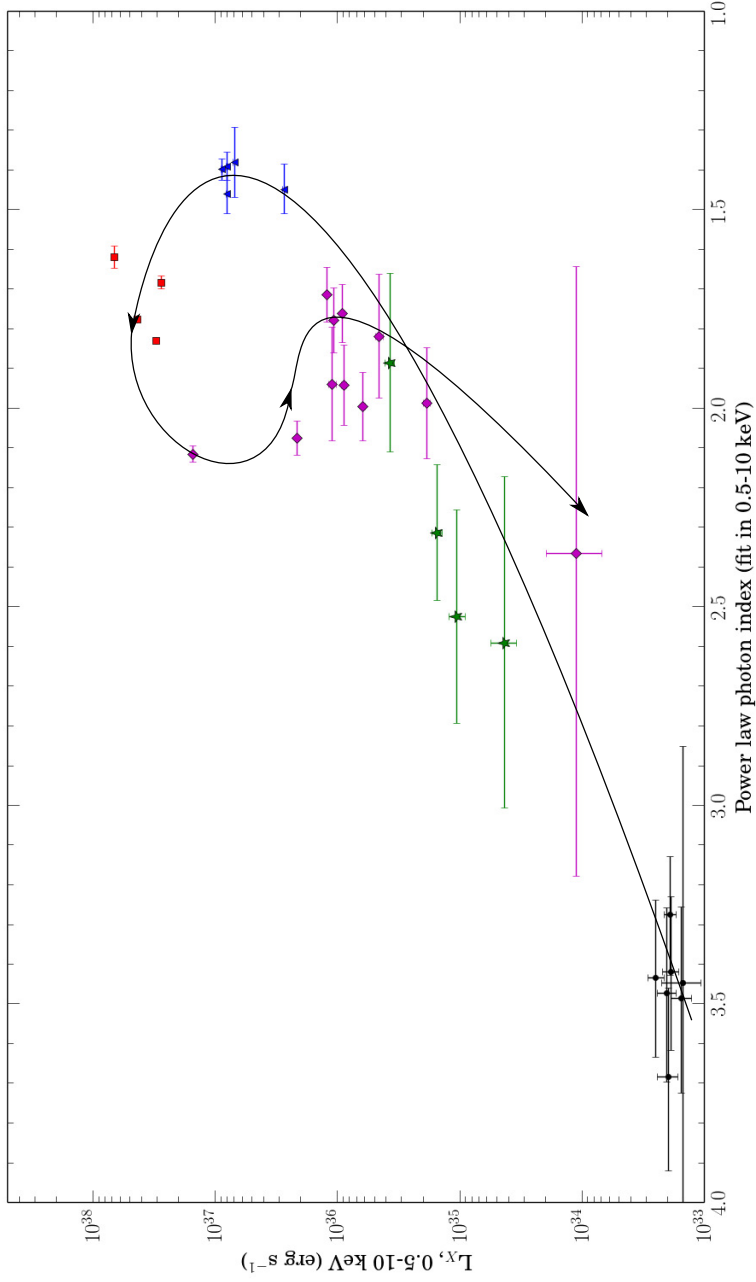
Figure 3.5: Luminosity versus power-law photon index of Terzan5 - X3 during the outburst, using *Swift/XRT* and one *Chandra/ACIS* outburst observations, plus two quiescent *Chandra/ACIS* observations. colors and shapes of points indicate the phases of outburst (as in Fig. 3.3); a) green stars, rise, b) blue triangles, hard state, c) red squares, soft state, d) magenta diamonds, return to hard state. The black circles represent *Chandra/ACIS* observations in quiescence, covering the range of observed hardness in the quiescent state. Arrows represent the chronological order of data points. Error bars indicate 1-σ uncertainties.
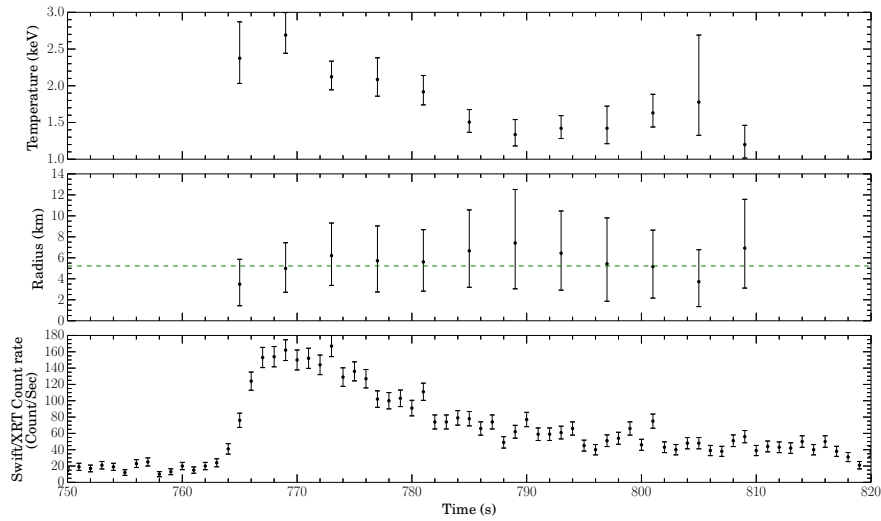
Figure 3.6: Spectral evolution during the thermonuclear burst of Terzan 5 X-3, using blackbody fits. The first and second panels show the variation in temperature and radius respectively. The third panel is the 0.5-10 keV light curve of the burst. The significant drop of temperature around 770 - 790 s shows evidence for cooling during the thermonuclear burst. The green line in the second panel represents the weighted average radius. Error bars are 1-σ uncertainties. Time bins in the top two panels are 4s long.
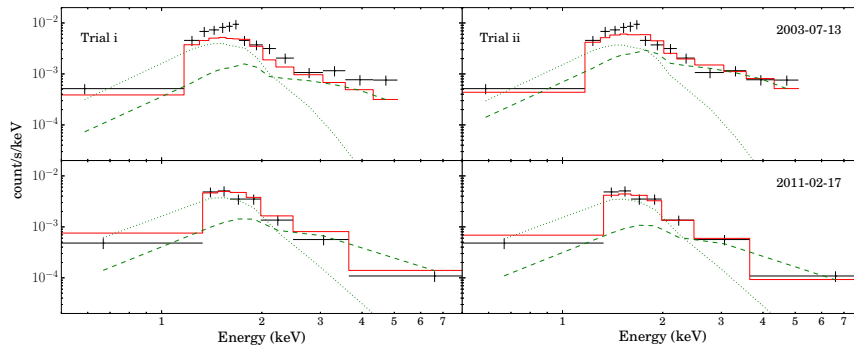
Figure 3.7: Extracted spectra from two of the *Chandra/ACIS* observations of Terzan 5 X-3, compared to the fitted model (NSATMOS + PEGPWRLW in XSPEC) from Trials I and II (Table 3.3). The dotted line indicates the contribution of the NSATMOS, while the dashed line indicates the contribution from the power-law component, and the solid line is their sum. Spectral variations are clear. Comparing Trial II to I fitting improvement can be seen.

Trial	ObsID	$\log T$ (K)	$F_{X,NS}$ (0.5-10 keV) (10^{-13} erg cm^{-2} s^{-1})	Γ	$F_{X,PL}$ (0.5-10 keV) (10^{-13} erg cm^{-2} s^{-1})	$L_{X,total}$ (0.5-10 keV) (10^{33} erg s^{-1})	χ^2_ν/D.O.F(nhp)
I	all	$6.143^{+0.015}_{-0.011}$	$2.4^{+0.3}_{-0.2}$	1.9 ± 0.4	$1.1^{+0.3}_{-0.1}$	$1.4^{+0.2}_{-0.1}$	$1.53/76(0.002)$
II	03798	$6.138^{+0.012}_{-0.018}$	$2.4^{+0.3}_{-0.5}$	2.1 ± 0.4	$1.9^{+0.6}_{-0.4}$	1.8 ± 0.3	$1.09/70(0.27)$
	10059	t	t	t	$1.3^{+0.5}_{-0.3}$	1.5 ± 0.2	t
	13225	t	t	t	$0.8^{+0.4}_{-0.3}$	1.3 ± 0.2	t
	13252	t	t	t	$1.2^{+0.5}_{-0.3}$	1.5 ± 0.2	t
	13705	t	t	t	0.7 ± 0.6	1.3 ± 0.3	t
	14339	t	t	t	$0.8^{+0.5}_{-0.3}$	1.3 ± 0.2	t
	13706	t	t	t	$1.4^{+0.4}_{-0.3}$	1.6 ± 0.2	t
III	03798	$6.172^{+0.001}_{-0.015}$	$3.3^{+0.4}_{-0.5}$	1.9 ± 0.4	$1.0^{+0.3}_{-0.2}$	1.8 ± 0.2	$1.22/70(0.099)$
	10059	$6.149^{+0.014}_{-0.019}$	$2.7^{+0.3}_{-0.5}$	t	t	1.5 ± 0.2	t
	13225	$6.120^{+0.019}_{-0.029}$	1.9 ± 0.5	t	t	1.2 ± 0.2	t
	13252	$6.144^{+0.014}_{-0.019}$	$2.4^{+0.3}_{-0.5}$	t	t	1.4 ± 0.2	t
	13705	$6.115^{+0.025}_{-0.042}$	$1.9^{+0.5}_{-0.7}$	t	t	1.2 ± 0.3	t
	14339	$6.131^{+0.017}_{-0.023}$	$2.2^{+0.2}_{-0.5}$	t	t	1.3 ± 0.2	t
	13706	$6.155^{+0.012}_{-0.017}$	$2.7^{+0.3}_{-0.5}$	t	t	1.5 ± 0.2	t
IV	03798	$6.161^{+0.015}_{-0.021}$	$3.0^{+0.3}_{-0.6}$	1.7 ± 0.4	1.5 ± 0.4	$1.9^{+0.2}_{-0.3}$	$1.10/64(0.27)$
	10059	$6.148^{+0.016}_{-0.021}$	$2.7^{+0.6}_{-0.5}$	t	$1.1^{+0.4}_{-0.3}$	$1.6^{+0.3}_{-0.2}$	t
	13225	$6.134^{+0.015}_{-0.021}$	$2.2^{+0.2}_{-0.5}$	t	$0.7^{+0.3}_{-0.2}$	1.2 ± 0.2	t
	13252	$6.146^{+0.015}_{-0.021}$	$2.7^{+0.3}_{-0.5}$	t	$1.0^{+0.4}_{-0.3}$	1.5 ± 0.2	t
	13705	$6.121^{+0.025}_{-0.043}$	1.7 ± 1.0	t	1.3 ± 0.9	1.2 ± 0.5	t
	14339	$6.142^{+0.014}_{-0.019}$	$2.4^{+0.3}_{-0.5}$	t	$0.7^{+0.4}_{-0.3}$	1.3 ± 0.2	t
	13706	$6.154^{+0.014}_{-0.021}$	$2.7^{+0.3}_{-0.5}$	t	$1.1^{+0.3}_{-0.2}$	1.6 ± 0.2	t

Table 3.3: Spectral fitting of 7 *Chandra/ACIS* observations of Terzan 5 X-3 during quiescence (see Table 3.1), using PHABS(PEGPWRLW+NSATMOS) in XSPEC. In Trial I both components are constrained to have the same values between observations. In Trials II and III one of the components may vary between observations, while in the 4th Trial both components are free. We use a "t" whenever values of a parameter are tied between observations. kT is the NS surface temperature in the star's frame, Γ is the power-law photon index, $F_{X,NS}$ is the unabsorbed flux from the NS atmosphere component, and $F_{X,PL}$ is the unabsorbed flux from the power-law component. Uncertainties are 90% confidence intervals. nhp is the null hypothesis probability (otherwise known as the p-value).

Obs. ID	MJD	kT (keV)	$F_{X,BB}$ (0.5-10 keV) (10^{-12} erg s^{-1} cm^{-2})	$F_{X,PL}$ (0.5-10 keV) (10^{-12} erg s^{-1} cm^{-2})	$F_{X,PL}/F_{X,total}$	$L_{X,total}$(0.5-10 keV) (10^{34} erg s^{-1})	χ^2_ν/D.O.F
91445006	56114.8	0.31 ± 0.03	5 ± 2	5 ± 2	$50\pm20\%$	4 ± 1	0.53/6
32148003	56115.8	0.36 ± 0.03	9 ± 3	13 ± 4	$59^{+15}_{-16}\%$	9 ± 2	0.68/5
32148004	56117	0.41 ± 0.02	15^{+4}_{-3}	17 ± 6	$53^{+12}_{-16}\%$	13 ± 3	1.19/9
32148005	56118.1	$0.44^{+0.05}_{-0.07}$	20 ± 10	70 ± 20	$78^{+12}_{-15}\%$	37 ± 9	0.55/6
32148006	56120.7	0.67 ± 0.06	110 ± 40	500^{+60}_{-70}	$82^{+7}_{-8}\%$	250 ± 30	1.39/19

Table 3.4: Results of spectral analyses for the rise of the outburst with a two-component model: thermal (BBODYRAD in XSPEC) plus non-thermal (PEGPWRLW in XSPEC). $F_{X,BB}$ and $F_{X,PL}$ are the blackbody and power-law unabsorbed fluxes, respectively. The power-law photon index was tied between spectra, and found to be $1.1^{+0.2}_{-0.4}$. The thermal component normalization (which is proportional to blackbody radius) is assumed constant, and tied between observations. Uncertainties are 90% confidence intervals. χ^2_ν and degrees of freedom in this table are found by fitting each dataset individually based on values found in simultaneous fit.

LMXB	globular cluster	State	P_{orb}	nature	notes	references
4U 1820-30	NGC 6624	P	11 min	U	X	(1)
4U 0513-40	NGC 1851	P	17 min	U	UV	(2)
X1850-087	NGC 6712	P	20.6^a min	U	UV	(3)
M15 X-2	M 15	P	22.6 min	U	UV	(4)
NGC 6440 X-2	NGC 6440	T	57.3 min	U	XP	(5)
XB 1832-330	NGC 6652	P	2.1 hrs	N	O	(6)
4U 1746-37	NGC 6441	P	5.16 hrs	N	X	(7)
SAX J1748.9-2021	NGC 6440	T	8.7 hrs	N	XP	(8)
IGR J18245-2452	M28	T	11.0 hrs	N	XP	(9)
GRS 1747-312	Terzan 6	T	12.36 hrs	N	X	(10)
AC 211	M 15	P	17.1 hrs	N	UV	(11)
Terzan 5 X-2	Terzan 5	T	21.27 hrs	N	XP	(12,13)
Rapid Burster	Liller 1	T	?	N	B	(14)
EXO 1745-248	Terzan 5	T	?	N	B	(14)
Terzan 5 X-3	Terzan 5	T	?	N	B	(15)
XB 1732-304	Terzan 1	T	?	?	?	(16)
4U 1722-30	Terzan 2	P	?	U?	B	(17)
IGR J17361-4441	NGC 6388	T	?	?	?	(18)
LMXBs with no observed outbursts						
47 Tuc W37	47 Tuc	Q	3.09 hrs	N	X	(19)
47 Tuc X5	47 Tuc	Q	8.67 hrs	N	X	(20)
ω Cen qLMXB	ω Cen	Q	?	N	Hα	(21)

Table 3.5: Orbital periods, or other classification, of the 18 Galactic globular cluster LMXBs that are persistently bright or have shown luminous outbursts, plus three quiescent globular cluster LMXBs. X-ray bursts have been detected from all the bright LMXBs except for AC 211 in M15 and IGR J17361-4441 in NGC 6388. State: P=persistent (or active for >30 years), T=transient, Q=quiescent (so far). Nature: U=ultracompact, N=normal. Notes: X=period from X-ray photometry, UV=period from UV photometry, N=normal. Notes: X=period from X-ray photometry, XP=period from X-ray pulsations, O=period from optical photometry, B=nature of donor inferred from UV photometry, XP=period from X-ray pulsations, O=period from optical photometry, B=nature of donor inferred from properties of X-ray bursts, Hα=hydrogen seen in optical counterpart spectrum. Notes represent method of measuring P_{orb} or determining donor natures. References: 1- Stella et al. 1987, 2- Zurek et al. 2009, 3- Homer et al. 1996, 4- Dieball et al. 2005, 5- Altamirano et al. 2010, 6- Engel et al. 2012, 7- Bałucińska-Church et al. 2004, 8- Altamirano et al. 2008, 9- Papitto et al. 2013, 10- in't Zand et al. 2003, 11- Ilovaisky et al. 1993, 12- Strohmayer et al. 2010, 13- Papitto et al. 2011, 14- Galloway et al. 2008, 15- this work, 16-Guainazzi et al. 1999, 17- in't Zand et al. 2007, 18- Bozzo et al. 2011, 19-Heinke et al. 2005a, 20- Heinke et al. 2003c, 21- Haggard et al. 2004. a- Or the alias period of 13 minutes.

Chapter 4

Limits on thermal variations in a dozen quiescent neutron stars over a decade

Arash Bahramian[1], Craig O. Heinke[1,2], Nathalie Degenaar[3], Laura Chomiuk[4], Rudy Wijnands[5], Jay Strader[4], Wynn C. G. Ho[6], David Pooley[7,8]

[1] Dept. of Physics, CCIS 4-183, University of Alberta, Edmonton, AB T6G 2E1, Canada. [2] Humboldt Fellow, Max Planck Institut für Radioastronomie, Auf dem Hügel 69, 53121 Bonn, Germany. [3] Institute of Astronomy, University of Cambridge, Madingley Road, Cambridge CB3 OHA, UK. [4] Department of Physics and Astronomy, Michigan State University, East Lansing, MI 48824, USA. [5] Anton Pannekoek Institute for Astronomy, University of Amsterdam, Postbus 94249, NL-1090 GE Amsterdam, The Netherlands. [6] Mathematical Sciences and STAG Research Centre, University of Southampton, Southampton, SO17 1BJ, United Kingdom. [7] Eureka Scientific, 2452 Delmer Street, Suite 100, Oakland, CA 94602-3017, USA. [8] Sam Houston State University, Department of Physics, Farrington Building, Suite 204, Huntsville, Texas 77341, USA.

Abstract

In quiescent low-mass X-ray binaries (qLMXBs) containing neutron stars, the origin of the thermal X-ray component may be either release of heat from the core of the neutron star, or continuing low-level accretion. In general, heat from the core should be stable on timescales $< 10^4$ years, while continuing accretion may produce variations on a range of timescales. While some quiescent neutron stars (e.g. Cen X-4, Aql X-1) have shown variations in their thermal components on a range of timescales, several others, particularly those in globular clusters with no detectable nonthermal hard X-rays (fit with a powerlaw), have shown no measurable variations. Here, we constrain the spectral variations of 12 low mass X-ray binaries in 3 globular clusters over ~ 10 years. We find no evidence of variations in 10 cases, with limits on temperature variations below 11% for the 7 qLMXBs without powerlaw components, and limits on variations below 20% for 3 other qLMXBs that do show non-thermal emission. However, in 2 qLMXBs showing powerlaw components in their spectra (NGC 6440 CX 1 & Terzan 5 CX 12) we find marginal evidence for a 10% decline in temperature, suggesting the presence of continuing low-level accretion. This work adds to the evidence that the thermal X-ray component in quiescent neutron stars without powerlaw components can be explained by heat deposited in the core during outbursts. Finally, we also investigate the correlation between hydrogen column density (N_H) and optical extinction (A_V) using our sample and current models of interstellar X-ray absorption, finding $N_H(\text{cm}^{-2}) = (2.81 \pm 0.13) \times 10^{21} A_V$.

4.1 Introduction

Transient low-mass X-ray binaries (LMXBs) show occasional outbursts, separated by periods of quiescence (typically months to years) in which their X-ray emission dramatically drops, to $L_X = 10^{31}$–10^{33} erg s^{-1}, and there is little or no accretion occurring. The X-ray spectra of quiescent LMXBs (qLMXBs) containing a neutron star (NS) consist of a soft blackbody-like component (if fit

with a blackbody, giving typical temperatures of 0.2-0.3 keV) and sometimes an additional harder component, typically fit with a powerlaw, with photon-index between 1 and 2 (e.g. Campana et al., 1998; Rutledge et al., 1999). The origin of the powerlaw component in these systems may be continuing low level accretion onto the NS, an accretion shock between infalling matter and the NS's magnetosphere or a pulsar wind, or synchrotron radiation from a pulsar wind nebula (e.g. Campana et al., 1998; Bogdanov et al., 2005). Recent X-ray observations support boundary-layer emission from accretion onto the NS as the likely origin of the hard powerlaw component at least in some sources (e.g. Cen X-4 and PSR J1023+0038, Chakrabarty et al. 2014; D'Angelo et al. 2015; Archibald et al. 2015; Wijnands et al. 2015).

The blackbody-like component can be well-described by NS hydrogen atmosphere models, with an implied radius consistent with theoretically predicted NS radii (e.g. Rajagopal and Romani, 1996; Zavlin et al., 1996; Rutledge et al., 1999, 2001). The soft component has been widely interpreted as the slow (10^4 years) release of heat from the core of the NS, deposited through deep crustal heating during previous episodes of accretion (Brown et al., 1998). A nearly identical soft spectrum can also be created in the upper layers of the NS atmosphere by low-level accretion (Zampieri et al., 1995; Zane et al., 2000), though the most detailed model predicts, in addition, an optically thin high-temperature bremsstrahlung component (Deufel et al., 2001), which may be identified with the powerlaw component (e.g. Bahramian et al., 2014). However, low-level accretion at sufficiently high rates (corresponding to $L \sim 10^{33}$ erg/s) could maintain metals in the atmosphere at abundances sufficient to soften the spectrum, leading to an overestimate of R (Rutledge et al., 2002b). The question of the origin of the thermal component in qLMXBs is of intense interest, since fitting the thermal spectra of qLMXBs in globular clusters is often used to measure the radius of NSs and place constraints on the dense matter equation of state (Rutledge et al. 2002a; Heinke et al. 2006a; Webb and Barret

2007; Steiner et al. 2010, 2013; Guillot et al. 2011; Servillat et al. 2012; Guillot et al. 2013; Guillot and Rutledge 2014; Lattimer and Steiner 2014; Heinke et al. 2014; Özel et al. 2016; see also Miller et al. 2013). Confirmation that thermal spectra of qLMXBs (especially those without powerlaw components) are not produced by accretion would eliminate the possibility that metals remain in the atmosphere, and thus eliminate a systematic uncertainty in this method of constraining the NS radius.

At low accretion rates, the NS's magnetic field is expected to exercise a propeller effect, which retards the accretion of material onto the NS surface (Illarionov and Sunyaev, 1975). The mechanism is that ionized disc material will become attached to the magnetic field lines when the magnetospheric pressure exceeds the gas pressure; if this boundary (the edge of the magnetosphere) occurs at a radius larger than the corotation radius, the material is accelerated to velocities higher than the Keplerian orbital velocity, throwing it away, and possibly out of the system. On the other hand, simulations of low-level accretion onto a magnetic propeller predict some material will reach the neutron star (Romanova et al., 2002; Kulkarni and Romanova, 2008; D'Angelo and Spruit, 2010, 2012). Pulsations have recently been identified from two (relatively bright) qLMXBs, the transitional pulsars PSR J1023+0038 at $L_X=3 \times 10^{33}$ erg/s, and XSS J12270-4859 at $L_X=5 \times 10^{33}$ erg/s, proving that matter accretes onto the surface even though it seems to be in the propeller regime (Archibald et al., 2015; Papitto et al., 2015). Detections of pulsations at low accretion rates from X-ray pulsars (with known magnetic fields) in high-mass X-ray binaries also suggest continued accretion in the propeller regime (e.g. Negueruela et al., 2000; Reig et al., 2014). Note that pulsations have not yet been detected from quiescent LMXBs other than transitional MSPs (D'Angelo et al. 2015; Elshamouty et al., in prep.).

Thus, there is evidence that continued accretion can produce an X-ray spectrum consistent with the soft component in qLMXBs, by heating the NS surface

(Zampieri et al., 1995; Zane et al., 2000; Deufel et al., 2001) and that continued accretion can continue at very low accretion rates. Testing for variability is a promising method to constrain whether thermal emission from qLMXBs is driven by accretion. X-ray emission driven by heat emerging from the core should be stable on timescales $\sim 10^4$ years (Colpi et al., 2001; Wijnands et al., 2013). For NSs that have undergone recent episodes of accretion, decays of the thermal component are seen (e.g. Wijnands et al., 2002a; Cackett et al., 2008; Degenaar et al., 2011b; Fridriksson et al., 2011), attributed to heat leaking from shallower levels in the crust, where it was deposited during the outburst (Ushomirsky and Rutledge, 2001; Rutledge et al., 2002c). This variation should be a monotonic decline on a time scale of years/decades. Possibilities for variations of the thermal component without accretion, based on changes in the chemical composition of the envelope, have been advanced (Brown et al., 2002; Chang and Bildsten, 2004), but these do not predict significant changes on timescales of years without intervening outbursts. Alternatively, if the thermal component is caused by continuous accretion onto a NS, the temperature may vary in either direction, on a range of timescales.

Strong evidence for variability of the thermal component of some qLMXBs during quiescence has been reported for the transients Aquila X-1 (Rutledge et al., 2002b; Cackett et al., 2011), Cen X-4 (Campana et al., 1997, 2004; Cackett et al., 2010), XTE J1701-462 (Fridriksson et al., 2010), and MAXI J0556-332 (Homan et al., 2014). Each of the transient qLMXBs that showed strong variation in the thermal component also showed a relatively strong powerlaw component, typically making up $\sim$50% of the 0.5-10 keV flux (e.g. Rutledge et al., 2002b; Cackett et al., 2010; Homan et al., 2014). So far, this is consistent with the suggestion (Heinke et al., 2003d) that continued accretion is responsible for both the powerlaw component (at least for $L_X \gtrsim 10^{33}$ erg/s, Jonker et al. 2004a) and variability.

Globular clusters (GCs) are highly efficient factories for producing X-ray

sources ($\sim$100 times more efficient than the rest of the Galaxy, per unit mass; Katz, 1975; Clark, 1975).The densest and most massive globular clusters have been shown by Chandra to contain multiple soft X-ray sources with L_X in the 10^{32}–10^{33} erg/s range, whose spectra strongly indicate that they are qLMXBs (Grindlay et al., 2001; Pooley et al., 2002; Heinke et al., 2003a,b; Pooley et al., 2003; Maxwell et al., 2012). These can be discriminated from other sources (spectrally harder cataclysmic variables, chromospherically active binaries, and millisecond radio pulsars) through spectral fitting (e.g. Rutledge et al., 2002a), or through X-ray colours and luminosities (Heinke et al., 2003d; Pooley and Hut, 2006). The majority of the candidate qLMXBs show no evidence for powerlaw components in their spectra (Heinke et al., 2003d). This may be a selection effect, since it is easier to discriminate qLMXBs from other sources if they show purely thermal spectra. Deep Chandra observations of globular clusters identify a significant population of candidate qLMXBs with strong powerlaw components, which require high-quality X-ray spectra to confidently identify the thermal components (Heinke et al., 2005a), and half of the transient cluster LMXBs followed up with Chandra are too faint, or too dominated by a powerlaw component, for detection of a thermal component (e.g. Wijnands et al., 2005; Heinke et al., 2010; Linares et al., 2014).

Several qLMXBs in globular clusters with thermal components have been examined to search for variations between observations. Several show flux variations, but spectral analyses have permitted these variations to be driven only by changes in the normalization of the powerlaw component (Heinke et al., 2005a; Cackett et al., 2005; Bahramian et al., 2014), or of obscuring material– the latter especially in edge-on systems (e.g. Nowak et al., 2002; Heinke et al., 2003c; Wijnands et al., 2003). A few qLMXBs without detectable powerlaw components have repeated deep observations with *Chandra*, permitting sensitive measurements for variability; these include (with 90% confidence variability limits) 47 Tuc X7, $\Delta T/T <$1.0% over 2 years (Heinke et al., 2006a); NGC 6397

U18, $\Delta T/T$ <1.4% over 10 years (Guillot et al., 2011; Heinke et al., 2014); M28 source 26 (no variation found, Servillat et al., 2012) and ω Cen, $\Delta T/T$ <2.1% over 12 years (Heinke et al., 2014).

We are interested in whether this lack of variability is the norm in thermal components of globular cluster qLMXBs, and whether (if it is observed anywhere) there is a correlation with the presence of powerlaw components. Strong evidence that globular cluster qLMXBs without powerlaw components are not variable would increase confidence in the assumptions used to derive radius measurements for their NSs and obtain constraints on the dense matter equation of state. We choose to focus on qLMXBs in globular clusters, since globular clusters are the only places where we can find and study large populations of qLMXBs in single Chandra pointings (and with relatively low optical extinction, compared to many qLMXBs in the Galactic Plane) and distances to qLMXBs in globular clusters are known better than to the ones in the field.

In this paper, we analyze a sample of 12 qLMXBs in 3 globular clusters, NGC 6266 (M 62), NGC 6440, and Terzan 5, searching for variations over multiple observations spanning roughly a decade. Each of these dense globular clusters have at least 4 candidate qLMXBs, and multiple *Chandra/ACIS* observations. When this work was in an advanced state, Walsh et al. (2015) reported on the analysis of 9 similar sources in Terzan 5 and NGC 6440 as considered here, though using fewer Terzan 5 observations, and not including NGC 6266. We directly compare our results with those of Walsh et al., finding general agreement. In §4.2, we describe our data reduction and analysis methods. In §4.3, we show the results of our analysis, and in §4.4, we discuss the implications.

4.2 Data reduction and Analysis

All datasets were obtained using ACIS-S in Faint, Timed Exposure mode. The data covers a time span of 9 to 12 years for the GCs in our sample (Table 4.1). We used CIAO 4.6 (Fruscione et al., 2006) and CALDB 4.6.2 for data reprocessing following standard CIAO science threads[1]. We chose known (and candidate) LMXBs with more than ~ 60 photons (per epoch) for spectral analysis, resulting in a total sample of 12 sources. These targets are tabulated in Table 4.2. We performed spectral extraction using the task *specextract* and performed spectral analysis in the 0.3-10 keV energy range using HEASOFT 6.16 and XSPEC 12.8.2 (Arnaud, 1996). We combined (using the CIAO *dmmerge* tool) spectra from observations which occurred within a month for our targets in Terzan 5, to improve the spectral quality. We grouped each spectrum by 15 counts per bin, and used chi-squared statistics for analysis. Details of the spectral extractions and analyses for each cluster are discussed in §4.3. All uncertainties reported in this paper are 90% confidence.

We fit the spectra with an absorbed neutron star atmosphere, plus a powerlaw (if needed). We used the NSATMOS (Heinke et al., 2006a) NS atmosphere model, with the NS mass and radius frozen to the canonical values of 1.4 $M_\odot$ and 10 km, the normalization fixed to 1 (implying radiation from the entire surface), and the distance fixed to the estimated distance of the cluster (see §4.3). In cases where this single-component model does not produce a good fit, leaving significant residuals at high energies($\geq$3 keV), a powerlaw component (PEGPWRLW, with normalization set to represent flux in the 0.5-10 keV range) was added to the model. In cases where it was unclear whether the fit was improved by adding a second component, we checked this by an F-test. We set the powerlaw photon index (Γ) as a free parameter when fitting datasets where the data quality above 3 keV is high enough to constrain this quantity.

---

[1]http://cxc.harvard.edu/ciao/threads/index.html

However, in datasets where the data quality is not sufficient to do this, we fixed the photon index to 1.5, which is a typical value from LMXBs in quiescence (Campana et al., 1998, 2004; Fridriksson et al., 2011; Degenaar et al., 2011b; Chakrabarty et al., 2014).

We fit all spectra available for each source simultaneously. We tied the N_H and powerlaw photon index to a single value for each source, and let the NS temperature and powerlaw flux vary between observations. There is good evidence that N_H does not vary during the spectral evolution of most LMXBs (Miller et al., 2009). Although correlated variations in N_H and powerlaw photon index have been proposed to explain spectral variability in Aql X-1 in quiescence (Campana and Stella, 2003), such a model requires the powerlaw to dominate over the thermal component of the spectrum, and forces the photon index to (unreasonably) high values (≥ 2.5). Fitting individual high-quality spectra of Aql X-1 (Cackett et al., 2011), SAX J1808.4-3658 (Heinke et al., 2009b), and Terzan 5 X-3 (Bahramian et al., 2014) in quiescence gives consistent values (within the errors) between epochs for both N_H and the powerlaw photon index. Deep observations of Cen X-4 do show evidence for powerlaw photon index changes (Cackett et al., 2010), changing from ~ 1.7 in all observations where $L_X < 2 \times 10^{32}$ erg/s, to ~ 1.4 at higher L_X values (Chakrabarty et al., 2014). Fridriksson et al. (2010) also find evidence for variation in the powerlaw photon index in XTE J1701-462, but only when L_X reaches $> 2 \times 10^{34}$ erg/s, well above the range discussed here. Summarizing these observations, when the total L_X does not vary by a large factor, the powerlaw photon index appears to remain roughly constant. As we will see below, our observations do not reveal large swings in L_X, so we feel that keeping a fixed powerlaw index is justified.

As we are looking for relative variations in kT, to estimate the uncertainties in the NS temperature and powerlaw flux, after initially fitting the N_H we then froze N_H to its best-fit value. In cases where the source shows significantly

higher N_H value than the average of the cluster, we investigated the possibility of intrinsic absorption leading to variations in N_H (§4.3).

We also search for signs of temporal variations during each observation for all sources. (Due to the limited signal, we explore only total flux variations.) We extracted background-subtracted lightcurves in 0.3-7 keV band for each source using CIAO task *dmextract*. Due to the faint nature of the sources in our study, we binned each lightcurve by 1000 s. We used the FTools task *lcstats* to perform chi-squared and Kolmogorov-Smirnov (KS) tests for variations. Since we ran these tests on 80 lightcurves (all sources in our sample in all observations used[2]), we require a false-alarm probability below 5%/80=0.06% to identify variability at 95% confidence (Note that null-results from a test do not prove the source did not vary).

4.3 Results

4.3.1 Hydrogen column density

We constrained the hydrogen column density (N_H) for each GC using our sample of LMXBs. In our primary analysis in this paper, we forced the N_H to a single value for all observations of each source. We used the Tuebingen-Boulder ISM absorption model (TBABS) with Wilms et al. (2000) abundances and Balucinska-Church and McCammon (1992) cross sections. (We tested the Verner et al. (1996) cross sections, and found no difference in our results). We also tried using the abundances of Anders and Grevesse (1989) for comparison (see below). After constraining N_H values for each target, we calculated the mean value for sources in each cluster. (We excluded Terzan 5 CX 9 from this analysis due to possible intrinsic absorption–see §4.3.4.) We compare these values with those produced by adopting reddening values, E(B–V), from the

---

[2]We excluded one of Terzan 5 observations (Obs.ID 13705) from this investigation due to its short exposure (14 ks).

Target	Obs. ID	Date	Exposure (ks)
NGC 6266	02677	2002-05-12	62
	15761	2014-05-05	82
NGC 6440	00947	2000-07-04	23
	03799	2003-06-27	24
	10060	2009-07-28	49
Terzan 5	03798	2003-07-13	40
	10059	2009-07-15	36
	13225	2011-02-17	30
	13252	2011-04-29	40
	13705	2011-09-05	14^A
	14339	2011-09-08	34^A
	13706	2012-05-13	46
	14475	2012-09-17	30
	14476	2012-10-28	29
	14477	2013-02-05	29^B
	14625	2013-02-22	49^B
	15615	2013-02-23	84^B
	14478	2013-07-16	29
	14479	2014-07-15	29^C
	16638	2014-07-17	72^C
	15750	2014-07-20	23^C

Table 4.1: Chandra ACIS observations used in this study. A, B, C: We merged spectra extracted from all observations marked A (and merged those marked B, etc.), as they occurred close in time.

Source	CXOGlb J	L_X
		(10^{32}erg s^{-1}, 0.5-10 keV)
NGC 6266 CX4	170113.09–300655.43	4.5±0.3
NGC 6266 CX5	170113.10–300642.33	4.2±0.3
NGC 6266 CX6	170113.76–300632.48	3.9±0.3
NGC 6266 CX16	170112.58–300622.38	1.0±0.2
NGC 6440 CX1	–	10±1
NGC 6440 CX2	–	14±1
NGC 6440 CX3	–	8±1
NGC 6440 CX5	–	7.4±0.8
Terzan 5 CX9	174804.8–244644	9.0±0.9
Terzan 5 CX12	174806.2–244642	7.0±0.8
Terzan 5 CX18	174805.2–244651	6.3±0.6
Terzan 5 CX21	174804.2–244625	4.4±0.5

Table 4.2: Candidate LMXBs studied in this paper. Luminosities are based on latest epoch used for each GC and are measured in this study. Reported uncertainties for luminosities are 90% confidence and do not include uncertainties in distance. References for source identification: This work (NGC 6266), Pooley et al. 2002 (NGC 6440), (3) Heinke et al. 2006b (Terzan 5).

Harris catalog (Harris, 1996, 2010 revision) and the relation between N_H and optical extinction (A_V) from Güver and Özel 2009):

$$N_H(\text{cm}^{-2}) = (2.21 \pm 0.09) \times 10^{21} A_V \qquad (4.1)$$

(Table 4.3). The N_H values calculated from A_V using the relation of Güver and Özel (2009) agree nicely with fits to the X-ray spectra using the Anders and Grevesse (1989) abundances–which makes sense, as Güver and Özel (2009) used N_H estimates from the literature on X-ray studies of supernova remnants, most of which used Anders and Grevesse (1989) abundances. However, N_H values measured from spectral fitting using Wilms et al. (2000) abundances are ~27 % higher than predicted using Güver and Özel (2009). This makes sense, because the Wilms et al. (2000) abundances are typically ~30% lower for X-ray relevant elements. We therefore introduce a new relation between N_H and A_V,

designed specifically for use with the Wilms et al. (2000) abundances,

$$N_H(\text{cm}^{-2}) = (2.81 \pm 0.13) \times 10^{21} A_V \qquad (4.2)$$

where the error is the 1-σ scatter we measure in the relation from the fit. We derived this equation from fitting a linear model to N_H values measured for 11 out of 12 sources in our sample (we excluded Terzan 5 CX 9 due to possible presence of enhanced absorption). We also investigated the effects of including dust scattering for point sources by adding a scattering model (Predehl et al., 2003) to our spectral model, with A_V fixed to $0.117 \times N_H/(10^{22} \text{ cm}^{-2})$. We found that dust scattering causes a slight decrease of $\approx 1\%$ in the N_H values, and thus increases the A_V-to-N_H conversion factor to 2.84×10^{21} cm^{-2}. As this work was being finalized, Foight et al. (2015) published their investigation of the A_V-to-N_H correlation using optical vs. X-ray studies of supernova remnants, also using Wilms et al. (2000) abundances, which found the conversion factor to be $2.87 \pm 0.12 \times 10^{21}$ cm^{-2}. This is in complete agreement with our results.

4.3.2   NGC 6266

NGC 6266 (M 62) is a massive dense globular cluster. At least 26 X-ray sources can be identified in *Chandra* images of the cluster, of which 5 have been suggested to be qLMXBs on the basis of their soft spectra and X-ray luminosities (Pooley et al., 2003; Heinke et al., 2003d). One of these (the brightest, and with the hardest X-ray spectrum; reasonably fit by an absorbed powerlaw of photon index 2.5±0.1) shows strong evidence (from its radio/X-ray flux ratio) for containing a black hole (Chomiuk et al., 2013). We use two deep *Chandra/ACIS* observations (Table 4.1) to study the other 4 soft candidate qLMXBs, which we name CX 4, CX 5, CX 6, and CX 16 (ordering the detected sources by *Chandra* countrates). In the 2002 observation, the cluster core is 2.5 arcminutes off-axis, and the sources have visibly elongated point-spread functions. To address this

GC	E(B−V) (mag)	A_V (mag)	Calculated N_H (Guver09) ($\times 10^{21}$ cm^{-2})	Measured N_H (Anders89) ($\times 10^{21}$ cm^{-2})	Measured N_H (Wilms00) ($\times 10^{21}$ cm^{-2})	Discrepancy (%)
NGC 6266	0.47	1.46	3.2±0.2	3.2±0.4	4.1±0.4	22±9
NGC 6440	1.07	3.32	7.3±0.5	7.2±0.6	10±1	27±9
Terzan 5	2.61	8.09	18±1	17±2	26±2	31±9

Table 4.3: Comparing N_H for GCs based on different assumptions. Calculated N_H is calculated based on relation between A_V and N_H provided by Güver and Özel (2009). The uncertainties reported for calculated N_H values based on Güver and Özel (2009) are only statistical uncertainties from the correlation. Measured N_H values are based on X-ray spectroscopy of the sources in our sample (average and uncertainty calculated for each GC; see text) with two different assumptions for the abundances of elements (Anders and Grevesse 1989 and Wilms et al. 2000). E(B−V) values are obtained from the Harris Catalog (Harris, 1996); to obtain A_V, we assumed R_V=3.1. Discrepancy is calculated between the measured N_H using Wilms et al. (2000) abundances and the calculated values based on the relation of Güver and Özel (2009). All uncertainties are 90% confidence.

issue, we used elliptical extraction regions of the same size for all sources. The 2014 observation was performed on-axis, so we used circular extraction regions. We show images of these observations and extraction regions in Fig. 4.1. We ran *wavdetect* to determine accurate positions and brightnesses of these X-ray sources, and corrected the astrometry by applying coordinate shifts to match the radio and X-ray positions of M62 CX1.

We assumed a distance of 6.8 kpc, and a reddening of E(B–V)=0.47 mag, for NGC 6266 in our analysis (Harris, 1996, 2010 revision). Assuming R_V=3.1, this reddening gives A_V=1.46 mag. The A_V/N_H relation of Güver and Özel (2009) which is based on Anders and Grevesse (1989) abundances, predicts N_H=3.2×10^{21} cm^{-2} for this cluster based on Anders and Grevesse (1989) abundances; in §4.3.1, we use N_H values measured from our spectral analysis of X-ray observations to derive a new relationship between N_H and A_V, N_H=2.8×$10^{21}A_V$, specifically for use with the Wilms et al. (2000) abundances.

Due to the relatively low interstellar absorption and reasonable fluxes of our targets, the spectra from this cluster are of high quality (Fig. 4.2, top left). We found no evidence of temperature variations in these objects (Table 4.4). For three of our targets (CX4, CX5 & CX6) we constrain temperature variations to less than 5%. For CX16 this limit is < 10% due to its faintness.

NGC 6266 CX4 is the only candidate qLMXB in NGC 6266 that shows evidence for a powerlaw component (Table 4.4). To constrain the contribution from the powerlaw, we fixed the photon index to 1.5 due to the limited spectral quality at higher energies. We notice that there is a hint of a faint source $\sim 1''$ from CX4 (southwest of CX4, visible when the image is over-binned). To address this, we performed a second set of spectral analyses with a smaller source extraction region excluding the region of the possible nearby source, but we found no significant spectral changes suggesting the non-thermal emission is therefore intrinsic to CX4 (Table 4.4 contains fits performed with the standard extraction regions).
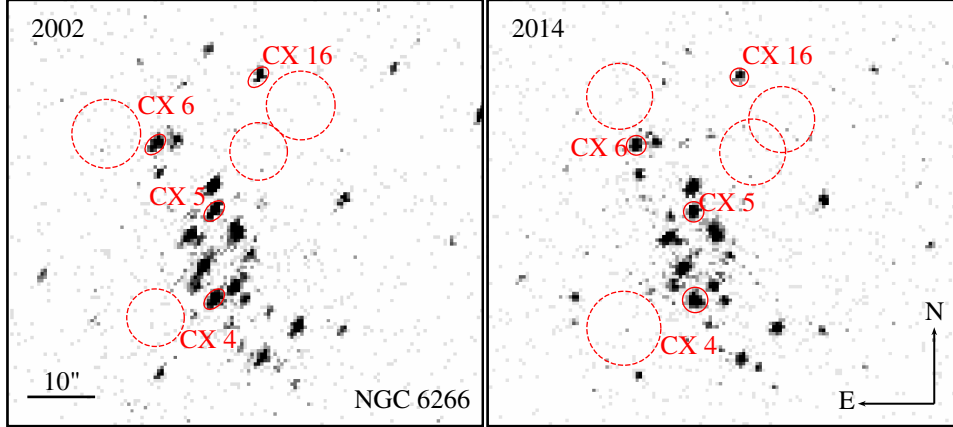
Figure 4.1: X-ray (0.3-7 keV) images of NGC 6266 as seen by Chandra-ACIS in 2002 (left) and 2014 (right). Source extraction regions are represented by solid circles/ellipses, and background extraction regions are represented by dashed circles. In the 2002 observation, the centre of NGC 6266 was located 2.5 arcminutes off-axis. To account for the distortion of the point-spread function this offset induced, we used elliptical extraction regions for that observation.

We searched for short (∼1000 s) timescale temporal variations in each observation by performing chi-squared and KS tests, and found no evidence of variation for any of our targets in NGC 6266. No source shows probability of constancy less than 0.06% which is the 95% confidence range when considering all trials (80, for all sources in this study).

4.3.3 NGC 6440

NGC 6440 is a moderately extinguished GC near the Galactic center. There are at least 25 X-ray sources identified in this cluster, of which two are known transient LMXBs (NGC 6440 CX 1 = SAX J1748.9-2021, in't Zand et al. 1999, 2001; Pooley et al. 2002; Bozzo et al. 2015; NGC 6440 X-2, Altamirano et al. 2010; Heinke et al. 2010). This cluster is 8.5 kpc away and has a reddening of E(B-V)=1.07 (Harris, 1996). We used three long *Chandra/ACIS* observations of this cluster, obtained in 2000, 2003, and 2009. We study the four brightest identified qLMXB candidates in or near the core of this cluster, CX 1, CX 2 (not to be confused with the AMXP denoted as NGC 6440 X-2, which is not

Source	N_H (10^{21} cm^{-2})	Year	logT (K)	% Variation	% Powerlaw flux fraction (0.5-10 keV)
NGC 6266 CX 4	3.9±0.4	2002	6.057±0.007	–	8±7
Powerlaw Γ=(1.5)		2014	6.056±0.006	< 3.2	12±5
χ^2_ν/d.o.f = 0.87/56					
NGC 6266 CX 5	3.9±0.4	2002	6.055±0.007	–	< 9
Powerlaw Γ=(1.5)		2014	6.062±0.006	< 4.7	< 7
χ^2_ν/d.o.f = 0.87/52					
NGC 6266 CX 6	4.2±0.4	2002	6.056±0.006	–	< 9
Powerlaw Γ=(1.5)		2014	$6.053^{+0.006}_{-0.007}$	< 3.6	< 7
χ^2_ν/d.o.f = 0.64/49					
NGC 6266 CX 16	4.3±0.6	2002	5.96±0.01	–	< 23
Powerlaw Γ=(1.5)		2014	5.94±0.01	< 9	< 15
χ^2_ν/d.o.f = 1.21/14					

Table 4.4: NGC 6266: Results of spectral analysis using an absorbed NS atmosphere (TBABS*NSATMOS), plus a powerlaw added when needed. All uncertainties are 90% confidence. Temperature variations are calculated from the first observation in 2002. Powerlaw fractions are fractions of the total 0.5-10 keV flux.
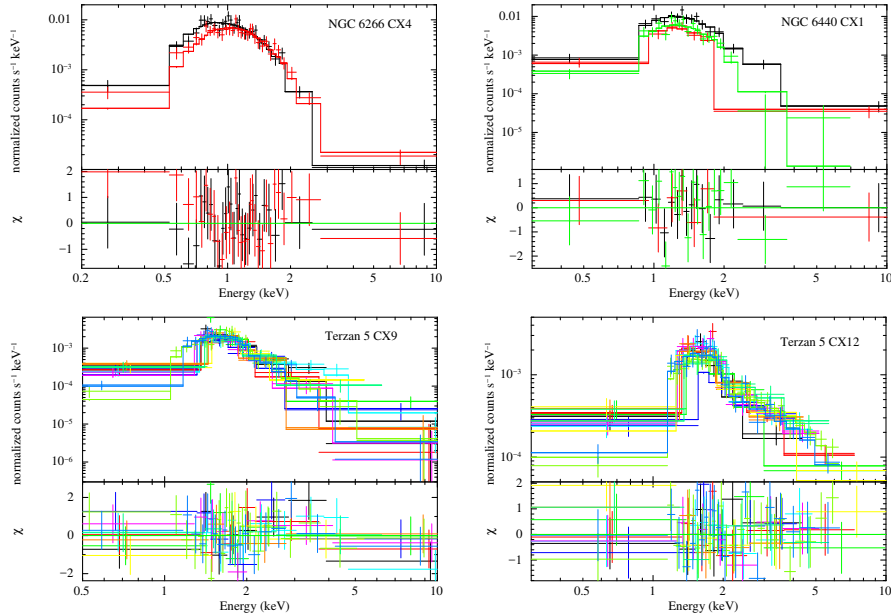
Figure 4.2: Examples of extracted spectra; top panels show data (crosses) and model (line). Different colours represent different epochs. Note that in addition to changes in the source, changes in the detector may alter the observed spectrum (these changes are included in the model). Top left: NGC 6266 CX4 (see §4.3.2). Only two *Chandra/ACIS* epochs are available, but the spectral quality is high. Top right: NGC 6440 CX1 (see §4.3.3). The black (2000) spectrum is brighter at all energies, particularly at higher energies; we attribute this to a difference in the powerlaw component, and possibly the thermal component. Bottom left & right: Terzan 5 CX9 & Terzan 5 CX12 respectively, including spectra from 11 epochs (see §4.3.4). The spectral fit for CX9 shown here uses a hydrogen atmosphere model. Note that there are still clear waves in the residuals (down at 2 keV, up at 3, down again at 5 keV), indicating problems with the fit (though the χ^2 is formally acceptable, 87.42 for 87 dof). These residual patterns are not completely eliminated in a helium atmosphere model, though they are reduced. CX12 shows evidence for a strong powerlaw component in this fit, as well as evidence for variation in soft X-rays (particularly in the 4th observation, taken in April 2011, colored dark blue here).

detected in deep quiescence, e.g. Heinke et al. 2010), CX 3, and CX 5, which were identified as likely qLMXBs by Pooley et al. (2002).

The *Chandra/ACIS* observation of NGC 6440 in 2009 occurred while NGC 6440 X-2 was in outburst (Heinke et al., 2010) and the image is severely piled-up in the vicinity of this source. However, we were nevertheless able to use this observation for spectral analysis of qLMXBs, as NGC 6440 X-2 is located further away from the core of the cluster ($\sim 12''$) and the outburst was relatively faint (peaking at $\sim 1 \times 10^{36}$ erg s^{-1}). We addressed the contamination from the X-2 outburst on affected sources (CX 1, CX 2 & CX 3) by extracting background spectra from multiple regions at the same angular distance as the target from X-2. Our targets and chosen extraction regions are shown in Fig. 4.3.

Two of the sources in this cluster (CX 1 and CX 3) show excesses at high energies to the NSATMOS fits, so we added a powerlaw component to their spectral models. In both cases, we froze the powerlaw photon index to the value found in the best fit to all three observations. We also note that there is a hint for the presence of a very faint source near CX 3 ($\sim$10 times fainter than CX 3, south of it, visible when the image is over-binned), however it does not affect the spectrum. The results of our spectral analyses for NGC 6440 are tabulated in Table 4.5. Walsh et al. (2015) measure powerlaw contributions consistent with our results for CX 2 and CX 3 in both 2003 and 2009 observations; We note that our extraction regions might differ from the ones chosen by Walsh et al. (2015) as they do not discuss their choice of extraction regions. This is specially important due to the large and spatially varying background from the outburst of NGC 6440 X-2.

From our sample, CX 2 and CX 3 show no evidence of variation in the NS temperature. This is in general accord with the results of Walsh et al. (2015). These authors include a short (4 ks) *Chandra/ACIS* observation of NGC 6440, 12 days after our 3rd observation, and find that the flux increases

in this observation for CX 5. If the spectrum is assumed to consist of only a NS atmosphere model, then the NS temperature must have increased in CX 5. However, Walsh et al. (2015) note that, since CX 5's spectrum may contain a powerlaw in this observation, the variability cannot be conclusively attributed to changes in the NS temperature. We find no evidence for variation in the spectrum of CX 5 between 2000 and 2009. We also detect the presence of a weak powerlaw component in the 2000 epoch at 1.7 σ.

We found possible evidence for thermal variations in CX 1 in quiescence (Fig. 4.2, top right). We significantly detect a powerlaw with photon index 1.7±2 in the 2000 observation, but not in the 2003 or 2009 observations. Fixing this powerlaw index to the best-fit index, our best fit finds a $-10^{+7}_{-6}\%$ change in temperature from 2000 to 2003, with the 2009 observation consistent with the 2003 observation (Table 4.5). This marginal evidence for variation suggests the presence of continuing accretion during the 2000 observation (plausible considering that CX 1 erupted into outburst two years before, and one year after, the 2000 observation, in't Zand et al. 2001).

Cackett et al. (2005) investigated the spectral variations of CX 1 using the first two *Chandra/ACIS* observations of NGC 6440, but they argued that the observed spectral variations were likely due to changes in the powerlaw component exclusively. Cackett et al's best fit uses a powerlaw component with photon index 2.5(±1.0), which explains the difference with our best fit (photon index 1.7±2); a softer powerlaw can explain flux differences in the soft X-rays, whereas our harder value of photon index require changes in the thermal component to explain. Walsh et al. (2015) also fit the spectra of CX1 in these 3 observations (adding the short 2009 observation mentioned above) using C-stats in Xspec, find a different value from Cackett et al. (2005) and basically agree with our results–the powerlaw photon index is measured at 1.6±1.0, and the 2000 data indicate a slightly higher NS temperature compared to the 2003 data, at 1σ confidence (though not at 99% confidence). Walsh et al. also
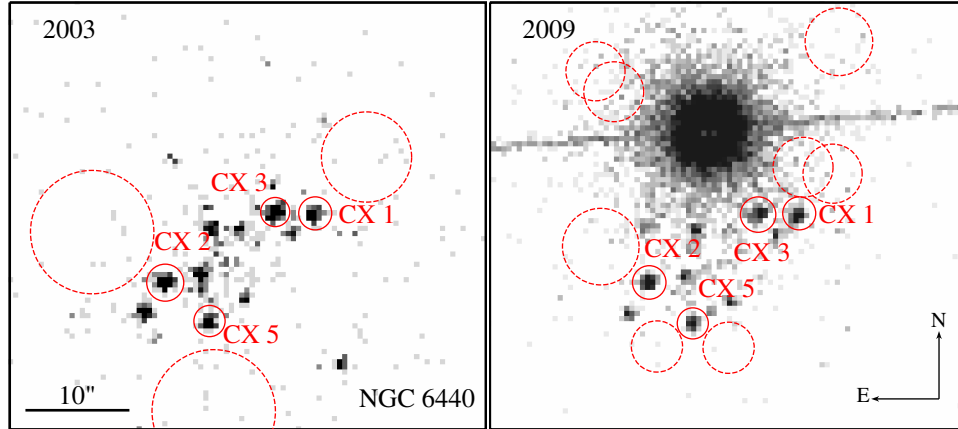
Figure 4.3: NGC 6440 as seen by Chandra-ACIS in the 0.3-7 keV band in 2003 (left) and 2009 (right). Solid circles represent the source extraction regions and dashed circles show the selected background regions. In the 2009 observation, the image is contaminated by an outburst from NGC 6440 X-2 (Heinke et al., 2010). We address this contamination for affected sources by choosing multiple background extraction regions at the same distance from X-2 as the target.

conclude (from χ^2 fitting) that it is not clear whether the variation in CX1 was due exclusively to changes in the powerlaw component, exclusively to changes in the thermal component, or to changes in both. We agree with Walsh et al. that it is not clear whether the thermal component varied between the 2000 observation and later observations.

Searching for short ($\sim 1000s$) timescale variations in each observation for all sources, we found no evidence of variation. No source shows probability of constancy less than 0.06% which is the 95% confidence range when considering all trials (80, for all sources in this study).

4.3.4 Terzan 5

Terzan 5 is a massive, highly extincted GC near the Galactic center. It is located at a distance of 5.9±0.5 kpc (Valenti et al., 2007) and it harbours more than 40 X-ray sources (Heinke et al., 2006b). There are three known transient LMXBs in this cluster, the most in any Galactic GC (Bahramian et al., 2014).

Source	N_H (10^{22} cm^{-2})	Year	logT (K)	% Variation	% Powerlaw flux fraction (0.5-10 keV)
NGC 6440 CX1	1.1±0.1	2000	6.16±0.01	10^{+7}_{-6}	26±10
Powerlaw Γ=(1.7)		2003	$6.12^{+0.01}_{-0.02}$	–	< 10
χ^2_ν/d.o.f = 0.84/37		2009	6.14±0.01	< 11	< 8
NGC 6440 CX2	1.1±0.1	2000	6.16±0.01	–	< 6
Powerlaw Γ=(1.5)		2003	6.179±0.009	< 9	< 9
χ^2_ν/d.o.f = 0.87/47		2009	6.172±0.007	< 7	< 7
NGC 6440 CX3	0.9±0.1	2000	$6.08^{+0.02}_{-0.03}$	–	35±17
Powerlaw Γ=(2)		2003	6.10±0.02	< 17	33±14
χ^2_ν/d.o.f = 0.57/35		2009	6.10±0.02	< 17	19±15
NGC 6440 CX5	1.0±0.1	2000	6.09±0.01	–	18±15
Powerlaw Γ=(1.5)		2003	$6.10^{+0.02}_{-0.01}$	< 10	< 10
χ^2_ν/d.o.f = 1.00/25		2009	6.11±0.01	< 10	< 7

Table 4.5: Spectral analysis of qLMXBs in NGC 6440. We fit the spectra with an absorbed NS atmosphere (TBABS*NSATMOS), and included a powerlaw component when necessary. All uncertainties are 90% confidence. Temperature variations are calculated based on the coldest measured temperature for each source. Powerlaw fractions are fractions of the total 0.5-10 keV flux. In cases where the spectral quality allows us to constrain the powerlaw photon index (CX1 and CX3), we tied the index between observations and searched for the best-fit value, then froze the index to that best-fit value; otherwise we fixed the index to 1.5. The photon index used is listed in column 1.

Terzan 5 has shown numerous outbursts (an overview up to 2012 is given in Degenaar and Wijnands 2012), several of which were not accurately localized (the most recent detected outburst without accurate localization being in 2002). It is therefore quite possible that other sources have been in outburst in the recent past.

We use all available *Chandra/ACIS* observations of this GC in which all sources are quiescent to study the brighter thermally-dominated qLMXBs without observed outbursts. We start with the sample of candidate qLMXBs from Heinke et al. (2006a), which identified thermally-dominated qLMXBs by spectral fitting, or by hardness ratio plus inferred X-ray luminosity. Analyses of the quiescent behaviour of the outbursting sources Ter 5 X-1 (EXO 1745-248), X-2 (IGR J17480-2446), and X-3 (Swift J174805.3-244637) have been reported in Degenaar and Wijnands 2011; Degenaar et al. 2011a, 2013a; Bahramian et al. 2014; Degenaar et al. 2015, so we exclude those sources here.

For the purpose of imaging and source detection, we merge all available observations following CIAO threads[3]. We corrected relative astrometry in all frames by matching the coordinates of 6 bright sources. We ran *reproject_aspect* to create a new reprojected aspect solution for each observation. Then we applied these aspect solutions to the event files by running *reproject_events*, and finally we combined the reprojected event files by running *reproject_obs*.

We selected the candidate qLMXBs which had sufficient counts for spectral analysis in each epoch (≥ 60; i.e. more than 4 spectral bins of 15 counts), leaving us with a sample of four thermally-dominated qLMXBs, identified as CX9, CX12, CX18, and CX21 in Heinke et al. (2006a). We used the merged image to choose source and background spectral extraction regions. This is important since in cases like CX9 and CX18, the vicinity of the source is complex and there can be multiple sources of contamination. In cases where the vicinity of the source is complex/crowded, we extracted background spectra from annuli

---

[3]http://cxc.harvard.edu/ciao/threads/combine/

around the targets, excluding detected sources. The combined image of Terzan 5, with our extraction regions, is presented in Fig. 4.4.

We combined spectra from observations which occurred less than a month apart (using *combine_spectra*), to obtain better statistics. Investigating these observations individually, no spectral variation was detected. These observations are marked in Table 4.1. All our targets in Terzan 5 show a high energy excess suggesting the presence of a powerlaw component in their spectra with average fraction of $\sim$10% of the total flux for CX9, CX18, and CX21 and an average fraction of $\sim$33% for CX 12. Comparing these with our targets in NGC 6266 and NGC 6440, where the powerlaw component is mostly detected when flux fraction is $\geq$10%, suggests that our detection of a powerlaw component in all our targets in Terzan 5 might be due to the greater depth of these observations, combined with our relatively higher sensitivity to hard vs. soft photons in this heavily absorbed cluster. We froze the powerlaw photon index to 1.5 for CX9, CX18 and CX21, due to a lack of sufficient signal to constrain it. For CX12 we freeze it to the value of 1.8, obtained from the best fit to all observations.

The values of N_H for CX12, CX18 and CX21 are all in agreement with the value of 2.6$\pm$0.1 $\times$ 10^{22} cm^{-2} from previous studies (see §4.3.1)[4]. However, CX9 has a hydrogen column density of 3.1$\pm$0.2 $\times$ 10^{22} cm^{-2}, higher than the measured value for the cluster. We investigate the high-resolution reddening map of Terzan 5 (Massari et al. 2012, available online from Cosmic-Lab [5]), and find no significant difference ($<$1.5%) in reddening between the direction of CX9 and the rest of the sources in our sample. This suggests that the inferred high N_H value may be caused by intrinsic absorption in the system. Spectra of

---

[4]In many previous studies, abundances from Anders and Grevesse (1989) have been used for absorption models. Using these abundances, Bahramian et al. (2014) find $N_H = 1.74^{+0.06}_{-0.08} \times 10^{22}$ cm^{-2}. However in the same paper they show that using Wilms et al. (2000) abundances gives an equivalent value of 2.6$\pm$0.1 $\times$ 10^{22} cm^{-2}.

[5]http://www.cosmic-lab.eu/tred/tred.php

| | Terzan 5 CX9 | | |
| | Hydrogen | | Helium |
Parameter	Trial 1	Trial 2	Trial 3
N_H (10^{22}cm^{-2})	3.1±0.2	(2.6)	2.9±0.2
logT (K)	6.12±0.01	6.21±0.06	6.10±0.01
NS R (km)	(10)	7±1	(10)
PL flux ^{A}	1.1±0.3	1.3±0.3	0.9±0.3
χ^2_ν/d.o.f	1.11/102	1.24/102	1.07/102
NHP	0.20	0.05	0.29

Table 4.6: Tests of hydrogen (NSATMOS) and helium (NSX) atmosphere models for Terzan 5 CX9. Two trials use hydrogen atmospheres: in trial 1, N_H is free, while the NS radius is fixed to 10 km. In trial 2, N_H is fixed to the average value for Terzan 5, and the NS radius is free. Trial 3 is the same as trial 1, except using a helium atmosphere. Since we didn't find any sign of variation in our initial fits, all values are tied between epochs. The neutron star mass is assumed to be 1.4 M⊙ in each case. Uncertainties are 90% confidence, and values in parentheses are frozen. A: powerlaw fluxes are in units of 10^{-14}erg s^{-1} cm^{-2}, in the 0.5-10 keV range. NHP is null hypothesis probability.

CX9 are shown in Fig. 4.2 (bottom left).

We also performed spectral fits on CX9 by replacing the non-magnetic hydrogen atmosphere model (NSATMOS) with a non-magnetic helium atmosphere model (NSX in Xspec, Ho and Heinke 2009). This fit gives a slightly better χ^2 compared to the hydrogen atmosphere model (χ^2 decreased from 114 to 109, where both cases have 102 degrees of freedom), and also a lower absorption value of $N_H = 2.9 \pm 0.2 \times 10^{22}$ cm^{-2}, consistent with the rest of the cluster (Table 4.6). These results indicate that a helium atmosphere is a possible explanation for the unusual aspects of CX9's spectrum (see §4.4). Note that there are still clear waves in the residuals (down at 2 keV, up at 3, down again at 5 keV), indicating problems with the fit (though the χ^2 is formally acceptable, 87.42 for 87 dof). These residual patterns are not completely eliminated in a helium atmosphere model, though they are reduced.

We found no evidence regarding spectral variations between observations in CX 9, CX 18 and CX 21. However CX 12 shows marginal evidence of variation over time (Table 4.7). Our main fit, in which only the NS temperature and

powerlaw flux are free among observations, suggests that these variations are caused by changes in the temperature of the NS, particularly a decrease in the 2011-4 epoch, and to a lesser degree in the two 2013 observations. However, the substantial powerlaw component, which is particularly strong in the epochs with the coldest NS temperature measurements, suggests that subtle changes in the powerlaw (both flux and index) might cause the variations (Fig. 4.2, bottom right). We note that thermal variations are only suggested in 2 epochs (2011-4 and 2013-2) out of 11. However we get an acceptable chi-squared when fitting the temperatures to a straight line. Thus we agree with Walsh et al. (2015) that these variations are not statistically significant.

To investigate the origin of CX12's spectral variations more carefully, we perform fits letting different pairs of model parameters vary; kT and PL flux (Fit 1), N_H and PL flux (Fit 2), or PL Γ and PL flux (Fit 3; see Table 4.8). In fit 1, variations in both kT and the PL flux are seen, and the fit is reasonable. However, the variations in kT appear to be anticorrelated with the variations in PL flux, which is unlike, for instance, the behaviour of Cen X-4 (Cackett et al., 2010). It should be noted that the signature of variation comes mainly from two data points (epochs 2011/4 and 2013/2). Performing a chi-squared test of constancy on temperature measured in all epochs gives a null hypothesis probability of 0.55, providing little evidence for variation. Compared to fit 1, fit 3 shows an increase of 14 in χ^2 (107 compared to 93, both fits have 96 degrees of freedom, giving a relative likelihood of 9×10^{-4} for fit 3 compared to fit 1 based on Akaike information criterion), indicating that changes in the powerlaw alone (both index and flux) are insufficient to drive the variations. However, fit 2, varying N_H and PL flux, gave a similar fit quality to fit 1 ($\chi^2 = 92.6$ compared to $\chi^2 = 93.4$, both with 96 degrees of freedom). Thus, the variations may plausibly be caused by changes in the NS temperature, or changes in intrinsic absorption, along with changes in the PL flux. Since we do not have independent evidence of the inclination of CX12, it is quite possible

that this system is nearly edge-on, and that we suffer varying obscuration levels at different times.

We performed chi-squared and KS tests on individual lightcurves extracted from each observation for our target sources (excluding observation 13705, due to its short exposure). We found evidence of short ($\sim$1000 s) timescale variations in Terzan 5 CX 21's lightcurve, in observation 14475 (Sept. 2012, Fig. 4.5). A KS test gives probability of constancy $= 4.6 \times 10^{-4}$ for this lightcurve, which is slightly higher than 95% confidence, when accounting for the number of trials (80, for all sources in this study). Note that although there is evidence for presence of the PL in this epoch, the PL flux fraction is rather small (13^{+16}_{-11} %), suggesting that the thermal fraction is also likely to vary. It is also possible that variations observed for this source are due to eclipse in the system, however we do not find evidence for eclipse in other epochs. No other source shows KS probability of constancy less than 0.06% (95% confidence).
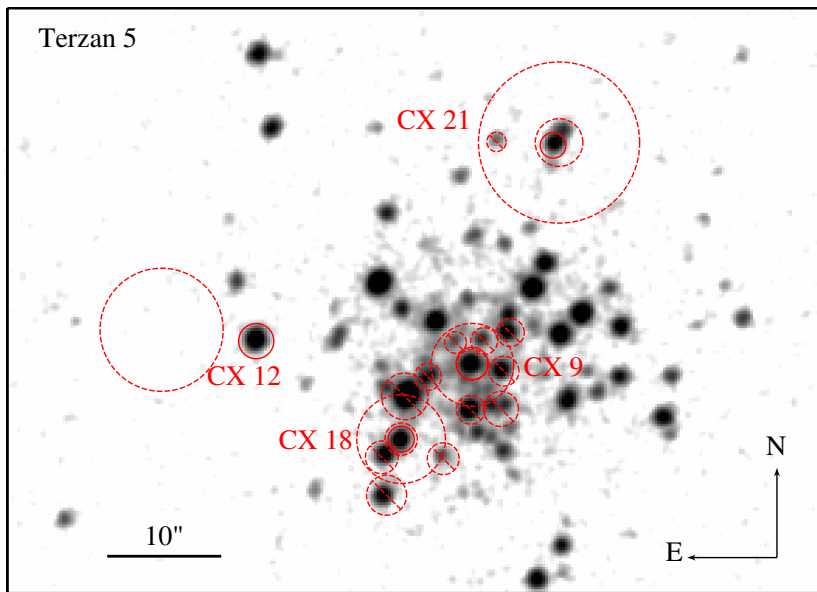
Figure 4.4: Stacked and smoothed *Chandra/ACIS* image of Terzan 5 in 0.3-7 keV band (total ∼620 ks). Source extraction regions for our targets are shown with red solid circles, and regions for background regions are represented by dashed circles/annuli. For targets in complex regions, we extracted background from annuli. Dashed circles with slashes represent excluded regions in background extraction (i.e. contaminating sources).

Source	Epoch	logT (K)	% Variation	% Powerlaw flux fraction (0.5-10 keV)
Terzan 5 CX 9	2003	$6.13^{+0.01}_{-0.02}$	<15	7^{+7}_{-6}
Powerlaw $\Gamma=(1.5)$	2009	6.11 ± 0.02	<12	<14
$N_H = 3.1 \pm 0.2 \times 10^{22}$	2011-2	6.12 ± 0.02	<15	12^{+10}_{-8}
$\chi^2_\nu/d.o.f = 1.00/87$	2011-4	6.11 ± 0.02	<12	8^{+9}_{-7}
	2011-9	6.10 ± 0.02	$-$	22^{+11}_{-9}
	2012-5	$6.12^{+0.01}_{-0.02}$	<12	<8
	2012-9	6.11 ± 0.02	<12	11^{+10}_{-8}
	2012-10	6.13 ± 0.02	<17	<8
	2013-2	$6.125^{+0.007}_{-0.008}$	<13	4^{+3}_{-2}
	2013-7	6.12 ± 0.02	<15	10^{+10}_{-8}
	2014	$6.128^{+0.008}_{-0.009}$	<14	<5
Terzan 5 CX 12	2003	6.09 ± 0.02	23^{+31}_{-16}	14^{+10}_{-8}
Powerlaw $\Gamma=1.8\pm0.3$	2009	$6.08^{+0.02}_{-0.03}$	20^{+31}_{-18}	27^{+13}_{-10}
$N_H = 2.6 \pm 0.2 \times 10^{22}$	2011-2	$6.07^{+0.02}_{-0.03}$	<48	29^{+16}_{-13}
$\chi^2_\nu/d.o.f = 0.97/96$	2011-4	$6.00^{+0.04}_{-0.08}$	$-$	52^{+27}_{-18}
	2011-9	$6.09^{+0.02}_{-0.03}$	23^{+32}_{-18}	28^{+11}_{-9}

2012-5	$6.09^{+0.02}_{-0.02}$	23^{+32}_{-16}	27^{+11}_{-9}
2012-9	$6.07^{+0.03}_{-0.04}$	<51	34^{+17}_{-13}
2012-10	$6.08^{+0.02}_{-0.03}$	20^{+31}_{-18}	29^{+16}_{-13}
2013-2	$6.04^{+0.02}_{-0.02}$	<38	44^{+8}_{-7}
2013-7	$6.05^{+0.03}_{-0.06}$	<44	49^{+22}_{-16}
2014	$6.07^{+0.02}_{-0.01}$	17^{+31}_{-12}	29^{+7}_{-6}
Terzan 5 CX 18			
Powerlaw $\Gamma=(1.5)$			
$N_H = 2.7 \pm 0.2 \times 10^{22}$			
$\chi^2_\nu/\text{d.o.f} = 1.12/51$			
2003	6.09 ± 0.02	<17	13^{+11}_{-8}
2009	6.09 ± 0.02	<17	<13
2011-2	6.10 ± 0.02	<20	<7
2011-4	6.08 ± 0.02	<15	<14
2011-9	6.08 ± 0.02	<15	7^{+8}_{-6}
2012-5	6.07 ± 0.02	<12	7^{+9}_{-7}
2012-9	$6.07^{+0.02}_{-0.03}$	–	<13
2012-10	$6.09^{+0.02}_{-0.03}$	<17	<13
2013-2	6.08 ± 0.01	<12	12 ± 1
2013-7	$6.07^{+0.02}_{-0.03}$	<12	10^{+14}_{-10}
2014	6.09 ± 0.01	<15	7 ± 1

Terzan 5 CX 21	2003	$6.04^{+0.02}_{-0.03}$	<15	16^{+16}_{-12}
Powerlaw Γ=(1.5)	2009	$6.06^{+0.02}_{-0.03}$	<20	10^{+12}_{-9}
$N_H = 2.4 \pm 0.2 \times 10^{22}$	2011-2	$6.07^{+0.02}_{-0.03}$	<23	<12
$\chi^2_\nu/\mathrm{d.o.f} = 0.92/36$	2011-4	6.03 ± 0.03	–	17^{+16}_{-11}
	2011-9	6.08 ± 0.02	<26	<10
	2012-5	6.04 ± 0.02	<15	<15
	2012-9	$6.04^{+0.02}_{-0.04}$	<15	13^{+16}_{-11}
	2012-10	$6.05^{+0.02}_{-0.03}$	<17	11^{+14}_{-10}
	2013-2	6.04 ± 0.01	<12	11^{+5}_{-4}
	2013-7	6.06 ± 0.02	<20	<7
	2014	6.05 ± 0.01	<15	<16

Table 4.7: Spectral analyses of Terzan 5 targets with an absorbed NS atmosphere + powerlaw. All uncertainties are 90% confidence. Temperature variations are calculated based on the coldest measured temperature for each source. The "Epoch" values give the year and month, in cases where multiple observations per year were performed. Powerlaw fractions are fractions of the total unabsorbed 0.5-10 keV flux. All targets in Terzan 5 show significant evidence for the presence of a powerlaw component in their spectrum. In cases where the spectral quality allows us to constrain the powerlaw photon index (CX 12), we tied the index between observations and searched for the best-fit value, then froze the index to that best-fit value; otherwise we fixed the index to 1.5. The photon index used is listed in column 1. N_H values are in units of cm^{-2}.
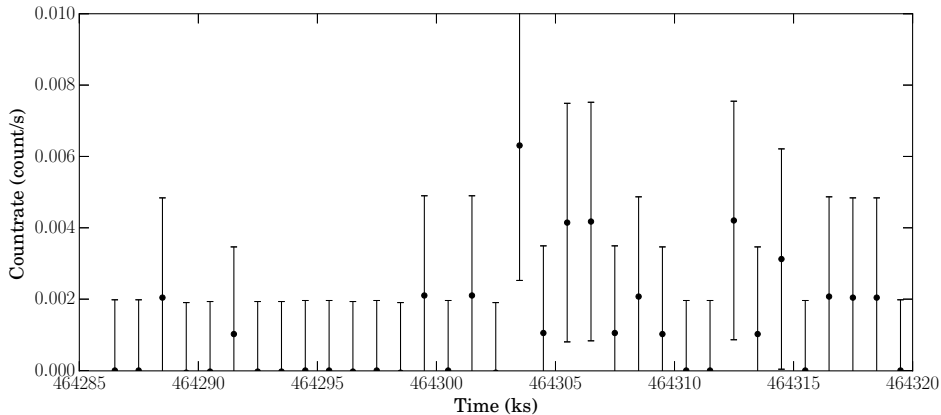
Figure 4.5: Binned lightcurve of Terzan 5 CX 21 from observation 14475 (Sept. 2012). A KS test gives probability of constancy = 4.6×10^{-4} for this lightcurve, which is slightly higher than 95% confidence, when accounting for the number of trials. It is possible that this variation may be due to eclipse. However we do not find strong evidence for eclipse in other epochs of this source.

4.4 Discussion

4.4.1 Terzan 5 CX9: a NS with a helium atmosphere?

Terzan 5 CX 9 shows an unusual spectral shape compared to other qLMXBs, with significantly lower flux at low energies (between 0.1 and 1 keV), compared to similar sources. This could be due to a higher amount of absorption. Investigating the reddening map of this cluster, we can rule out differential reddening. However, there could be additional intrinsic absorption, for instance if we are looking at the system edge-on.

Another possibility is that this NS may have an atmosphere composed of helium. Ultracompact X-ray binaries (with a white dwarf donor star, possessing no hydrogen) are fairly common among bright LMXBs in globular clusters (e.g. Zurek et al., 2009). Helium white dwarf donors might thus be expected to lead to helium atmospheres on the NSs; there is evidence for low hydrogen content in X-ray bursts from some bright ultracompact X-ray binaries (Cumming, 2003; Galloway et al., 2008). The X-ray spectra of helium atmospheres are similar

Terzan 5 CX12

Epoche	Fit 1 Constant N_H & Γ logT (K)	PL flux (10^{-14}erg s^{-1} cm^{-2})	Fit 2 Constant T_{NS} & Γ N_H (10^{22}cm^{-2})	PL flux (10^{-14}erg s^{-1} cm^{-2})	Fit 3 Constant N_H & T_{NS} Γ	PL flux (10^{-14}erg s^{-1} cm^{-2})
2003	6.09 ± 0.02	2 ± 1	$2.5^{+0.3}_{-0.2}$	2 ± 1	$3.1^{+0.8}_{-0.7}$	7^{+6}_{-3}
2009	$6.08^{+0.02}_{-0.03}$	5 ± 2	$2.5^{+0.3}_{-0.2}$	5 ± 1	2.4 ± 0.7	7^{+4}_{-2}
2011-2	$6.07^{+0.02}_{-0.03}$	4 ± 2	$2.7^{+0.5}_{-0.3}$	4 ± 2	2.3 ± 0.7	6^{+3}_{-2}
2011-4	$6.00^{+0.04}_{-0.08}$	6 ± 2	$3.5^{+0.6}_{-0.4}$	5 ± 2	$1.3^{+0.6}_{-0.7}$	4 ± 1
2011-9	$6.09^{+0.02}_{-0.03}$	5 ± 2	$2.5^{+0.3}_{-0.2}$	5 ± 1	2.4 ± 0.6	8^{+3}_{-2}
2012-5	$6.09^{+0.02}_{-0.02}$	5 ± 1	$2.4^{+0.3}_{-0.2}$	5 ± 1	2.4 ± 0.6	8^{+4}_{-2}
2012-9	$6.07^{+0.03}_{-0.04}$	6 ± 2	$2.5^{+0.5}_{-0.3}$	5 ± 2	1.8 ± 0.8	6^{+3}_{-2}
2012-10	$6.08^{+0.02}_{-0.03}$	5 ± 2	$2.3^{+0.4}_{-0.3}$	5 ± 2	2 ± 1	7^{+5}_{-2}
2013-2	$6.04^{+0.02}_{-0.02}$	7 ± 2	$3.0^{+0.3}_{-0.2}$	6 ± 1	1.6 ± 0.3	6 ± 1
2013-7	$6.05^{+0.03}_{-0.06}$	8 ± 2	$2.8^{+0.6}_{-0.4}$	8 ± 2	1.8 ± 0.5	8 ± 2
2014	$6.07^{+0.02}_{-0.01}$	5 ± 1	$2.6^{+0.2}_{-0.2}$	5 ± 1	2.2 ± 0.4	6 ± 1
χ^2_ν/d.o.f	0.97/96		0.96/96		1.12/96	
NHP	0.55		0.58		0.20	

Table 4.8: Testing three possibilities to explain the spectral variations in Terzan 5 CX12. Fit 1: Fixing N_H and the powerlaw photon index to their best-fit value across all spectra ($N_H = 2.6 \times 10^{22}$cm^{-2}, $\Gamma = 1.8$), while letting the NS temperature and powerlaw flux to vary between epochs. Fit 2: Allowing N_H and powerlaw flux to vary across epochs, while fixing the NS temperature and powerlaw photon-index ($\log T = 6.08$, $\Gamma = 1.7$). Fit 3: Only photon index and powerlaw flux are allowed to vary between epochs, with N_H and the NS temperature frozen ($N_H = 2.5 \times 10^{22}$cm^{-2}, $\log T = 6.05$). powerlaw fluxes are given in 0.5-10 keV band. The NS mass and radius are frozen to their canonical values of 1.4 $M_\odot$ and 10 km in all cases. All uncertainties are 90% confidence. NHP is null hypothesis probability.

to hydrogen atmospheres, but slightly harder (Romani, 1987; Ho and Heinke, 2009). An observed spectrum will thus give different parameter values for He vs. H atmospheres, and several papers have considered the importance of atmosphere composition for attempts to constrain the NS mass and radius (Servillat et al., 2012; Catuneanu et al., 2013; Lattimer and Steiner, 2014; Heinke et al., 2014). For relatively low-count spectra such as CX9, which parameter is different from other NS qLMXBs–e.g., atmospheric composition (H or He), vs. N_H–may not be possible to differentiate. No helium atmosphere has yet been confidently identified on a NS, so any evidence in favor of a helium atmosphere is intriguing.

4.4.2 Possible continuous accretion for NGC 6440 CX1 & Terzan 5 CX12

NGC 6440 CX 1 is the brightest X-ray source in the cluster. It has shown multiple X-ray outbursts over the last 20 years (1998, 2001, 2005, 2010, 2015; in't Zand et al. 1999, 2001; Markwardt and Swank 2005; Patruno et al. 2010; Homan et al. 2015). In quiescence, it shows a mostly thermal spectrum although there are signs of variations in the spectrum over the course of years. In the 2000 observation, we find that the spectrum requires a powerlaw component for a good fit, but in later observations this component is not required. Cackett et al. (2005) argued that the changing normalization of the powerlaw component, with photon index∼2.5, was the main source of spectral variation. However, we suggest that the unusually high photon index used there led to the overestimation of the powerlaw's contribution. Walsh et al. (2015) also fit the spectra of CX 1 with similar models. They find that formally, either the powerlaw or thermal component can be the source of variation, and we agree with that finding. However, when we hold the NS temperature constant across the epochs while allowing the powerlaw normalization to vary (with photon

index tied to a single value across epochs), the best-fit value of the powerlaw photon index will increase to 2.7±0.5 (compared to 1.7±2 when the NS temperature also varies). This agrees with Walsh et al.'s fit results when assuming NS temperature fixed (the first fit in their Table 4), where they find a photon index of 3.1±0.5. The anomalously high photon index required for such a fit strongly argues that the thermal component may also be varying.

Terzan 5 CX12 is well-fit by an absorbed two-component (thermal+powerlaw) model, with an N_H column typical of sources in the cluster ($2.6\pm0.1\times10^{22}$ cm^{-2}). CX12 shows hints of spectral variations, concentrated at low energies (< 2 keV; see Figure 2, lower right). Thus it's unlikely that the powerlaw component is responsible for these variations. Intrinsic absorption (e.g. an edge-on system, where an uneven accretion disk occasionally blocks the line of sight), or continuing thermal variation due to accretion are possible origins of these variations.

4.4.3   Variability of thermal component in qLMXBs

In our sample of 12 globular cluster qLMXBs, NGC 6440 CX1 and Terzan 5 CX12 are the only sources that show evidence of variations in the thermal component over timescales of years. In both cases, the thermal component appears to be the most plausible origin of the variations, but in neither case can thermal variations be proven. For NGC 6440 CX1, the best-fit thermal variation is only a 10% temperature change, while for Terzan 5 CX12 one observation appears to have a 20% drop.

Terzan 5 CX 21 shows evidence of variability on timescales of hours (within observations), although we did not detect variations on longer timescales (between observations). This variability may be due to variations in the (dominant) thermal component in quiescence. Alternatively, it may be caused by eclipses by the companion, if the system is at a high inclination angle.

A crucial result of our analysis is that we have assembled an additional 7

qLMXBs (in addition to 4 others previously reported, see Introduction) with multiple high-quality X-ray spectra showing little or no evidence for a powerlaw component; NGC 6266 CX4, CX5, CX6, and CX16, and NGC 6440 CX1 (considering only the 2003 and 2009 observations), CX2, and CX5. None of these objects show evidence for a powerlaw component comprising more than 12% of the 0.5-10 keV flux (except for the 2000 observation of CX1, which we exclude here). The upper limits on a powerlaw (assuming a photon index of 1.5) are, in four cases, <10% of the 0.5-10 keV flux, and <17% or <23% in two others. Using *Chandra* observations spaced over 9-12 years (6 for NGC 6440 CX1), we can constrain the thermal emission from these NS to not have varied by more than 10% in any of these sources. Combined with the literature constraints on 4 other sources discussed in §1 (and in agreement with the recent work of Walsh et al. 2015), this provides increasing evidence that the thermal X-ray spectral components of NS qLMXBs without powerlaw components to their spectra are not powered by continuing accretion. (Of course, a clear detection of intrinsic variation of the thermal component in a source without a powerlaw component would disprove this hypothesis.) This contrasts with recent works that indicate that in some NS qLMXBs with powerlaw components, the powerlaw, as well as some of the thermal component, is powered by continuing, variable, accretion onto the NS surface (Cackett et al., 2010; Bahramian et al., 2014; Chakrabarty et al., 2014; D'Angelo et al., 2015; Wijnands et al., 2015).

This evidence against continuing accretion for those qLMXBs without powerlaw components also supports the use of these qLMXB spectra to obtain constraints on the mass and radius (and thus on the equation of state) of NSs, since a lack of accretion indicates that the atmosphere will not be contaminated by heavy elements.

Chapter 5

The ultracompact nature of the black hole candidate X-ray binary 47 Tuc X9

Arash Bahramian[1], Craig O. Heinke[1], Vlad Tudor[2], James C.A. Miller-Jones[2], Slavko Bogdanov[3], Thomas J. Maccarone[4], Christian Knigge[5], Gregory R. Sivakoff[1], Laura Chomiuk[6], Jay Strader[6], Javier A. Garcia[7], Timothy Kallman[8]

[1] Dept. of Physics, CCIS 4-183, University of Alberta, Edmonton, AB T6G 2E1, Canada. [2] International Centre for Radio Astronomy Research - Curtin University, GPO Box U1987, Perth, WA 6845, Australia. [3] Columbia Astrophysics Laboratory, Columbia University, New York, NY, USA. [4] Dept. of Physics, Texas Tech University, Lubbock, TX, USA. [5] School of Physics and Astronomy, University of Southampton, Southampton, UK. [6] Dept. of Physics and Astronomy, Michigan State University, East Lansing, MI, USA. [7] Harvard-Smithsonian Center for Astrophysics, Cambridge, MA, USA. [8] NASA Goddard Space Flight Center, Greenbelt, MD, USA.

Abstract

47 Tuc X9 is a low mass X-ray binary (LMXB) in the globular cluster 47 Tucanae, which was previously thought to be a cataclysmic variable. However, Miller-Jones et al. (2015) recently identified a radio counterpart to X9 (inferring a radio/X-ray ratio consistent with black hole LMXBs), and suggested that the donor star might be a white dwarf. We report simultaneous observations of X9 performed by *Chandra*, *NuSTAR* and ATCA. Our X-ray spectral fitting provides evidence for photo-ionized gas having a high oxygen abundance in this system, which indicates a C/O white dwarf donor. We also identify reflection features in the hard X-ray spectrum. We identify a likely ~ 6.8 day regular modulation in the X-ray brightness by a factor of 10, in archival *Chandra*, *Swift*, and *ROSAT* data, presumably indicating precession of the disk. The simultaneous radio/X-ray flux ratio is consistent with either a black hole primary, or a neutron star primary, if the neutron star is a transitional millisecond pulsar. Considering the lack of transitional millisecond pulsar features in the X-ray lightcurve, and the strong evidence in favor of a white dwarf donor, we suggest that this is likely the first ultracompact black hole X-ray binary identified in our galaxy.

5.1   Introduction

Low mass X-ray binaries (LMXBs) are systems in which a compact object (white dwarf, neutron star or black hole) accretes matter from a companion (typically a main sequence star) through Roche-lobe overflow or wind-fed accretion (from a red giant). It has been long noticed that the population of LMXBs per unit mass in globular clusters (GCs) is orders of magnitude higher than of the Galactic field (Katz, 1975). This overabundance has been associated with the high stellar density in GCs. While in the Galactic field, most LMXBs are formed through binary evolution of primordial binaries, it has been shown that in GCs, the dominant channel to form LMXBs is through encounters. These

scenarios include tidal capture by a neutron star (NS) or black hole (BH), exchange of a compact object into a primordial binary, or collision of a compact object with a red giant (Clark, 1975; Fabian et al., 1975).

Hundreds to thousands of stellar mass BHs form in GCs through stellar evolution. A fraction of these BHs will have sufficient natal kicks to leave the cluster after birth, while the rest will sink towards the center of the cluster and form a dense sub-cluster. It was previously thought the core-collapse of this sub-cluster will result in total evaporation from the GC and thus no BHs will be left in the cluster (Kulkarni et al., 1993; Sigurdsson and Hernquist, 1993). This was consistent with observations of LMXBs in GCs as all the LMXBs found in GCs at the time were shown to be NS-LMXBs (e.g., Verbunt and Lewin, 2006).

However our understanding of the BH-LMXB population in GCs has changed significantly over the past few years, with the discovery of highly luminous BH-LMXB candidates in extragalactic GCs (e.g., Maccarone et al., 2007; Maccarone and Peacock, 2011), as well as quiescent BH-LMXB candidates in Galactic GCs (Strader et al., 2012; Chomiuk et al., 2013; Miller-Jones et al., 2015). Additionally, on the theoretical front recent, more detailed simulations have found that a substantial fraction of BHs may remain in GCs up to the present day (Sippel and Hurley, 2013; Morscher et al., 2013, 2015).

X-ray spectroscopy can help distinguish between some types of faint/quiescent X-ray sources in GCs. While cataclysmic variables (CVs) — systems with a white dwarf (WD) accreting from a main-sequence or sub-giant star — tend to show a hard X-ray spectrum dominated by hot bremsstrahlung emission, NS-LMXBs (in quiescence) often show a softer spectrum, dominated by blackbody-like emission from the NS surface (Rutledge et al., 1999, 2002c; Grindlay et al., 2001; Heinke et al., 2003d).

X-ray spectra of quiescent LMXBs also often show a non-thermal component, fit with a power law with photon index between 1 and 2, which could

be produced by continuous low-level accretion (e.g., Campana et al., 1998). In quiescent BH-LMXBs, the X-ray emission is thought to be from a radiatively inefficient accretion flow (RIAF) and/or possibly synchrotron emission from the jet (Plotkin et al., 2013), while the non-thermal component in quiescent NS-LMXBs may be associated either with accretion or with magnetospheric or shock emission related to a turned-on radio pulsar wind (Campana et al., 1998; Jonker et al., 2004b; Wijnands et al., 2015). The non-thermal component has similar properties in NS and BH LMXBs in quiescence, so it can be difficult to distinguish between BH LMXBs and NS LMXBs lacking a strong blackbody-like component. A chief diagnostic method to find BH-LMXBs have been based on the ratio of radio/X-ray luminosities of the system (Maccarone, 2005). BH-XRBs show compact partially-absorbed jet emission in quiescence (and in the hard state during outbursts), making them brighter in radio compared to NS-LMXBs with similar X-ray luminosities (Gallo et al., 2003; Fender et al., 2003).

In LMXBs, if the companion is a compact hydrogen-deficient star (e.g., a WD), then the orbital period is short ($P_{orb} <$ 80 min), and the system is an ultra-compact X-ray binary (UCXB). The depletion of hydrogen in UCXBs leads to high abundances of either helium or carbon and oxygen (C/O). For UCXBs with C/O WDs, the overabundance of carbon and oxygen can produce observable diagnostics in far-UV and X-ray spectra (Nelemans et al., 2010).

47 Tucanae (47 Tuc) is a dense, massive ($6.5 \times 10^5 M_\odot$, Kimmig et al., 2015) Galactic GC at a distance of 4.53±0.01 kpc (Woodley et al., 2012). Low extinction ($E(B - V) = 0.04$, Salaris et al., 2007) makes this cluster easy to study. 47 Tuc harbours $\sim$ 230 X-ray sources (Heinke et al., 2005b), including 23 radio millisecond pulsars (Freire et al., 2003; Pan et al., 2016), and many CVs and chromospherically active binaries (Grindlay et al., 2001; Edmonds et al., 2003a,b). As the cluster has a very high stellar encounter rate (Bahramian et al., 2013), it should produce many XRBs. Indeed, five

quiescent NS LMXBs, all with prominent thermal blackbody-like components in their X-ray spectra (two also have strong nonthermal components), have been identified and studied in 47 Tuc (Heinke et al., 2003c, 2005a, 2006a; Bogdanov et al., 2016).

47 Tuc X9 is the brightest ($\gtrsim 10^{33}$ erg s^{-1}) X-ray source in the core of 47 Tuc with a hard spectrum (Grindlay et al., 2001; Heinke et al., 2005b). X-ray emission from 47 Tuc was first noticed in observations by *Einstein* and the source was identified as 1E 0021.8-7221 (Hertz and Grindlay, 1983; Grindlay et al., 1984). Later *ROSAT* observations found 9 X-ray sources within the cluster, and identified X9 as the counterpart for 1E 0021.8-7221 (Verbunt and Hasinger, 1998). In both *Einstein* and *ROSAT* observations, X9 has shown clear variability. The first *Chandra* study of X9 (aka W42) in 2000 suggested the presence of a 218 s modulation in the light curve, which if verified would mark X9 as an intermediate polar CV[1] (Grindlay et al., 2001). Spectral analyses of the *Chandra* X-ray data showed a complex spectrum with a very hard nonthermal component, and extremely strong oxygen spectral lines (Heinke et al., 2005b).

A variable blue star in the cluster was discovered and identified as a likely CV, and the counterpart of 1E 0021.8-7221, by Paresce et al. (1992). The relatively high X-ray luminosity, low optical/X-ray ratio, and hints of a 120-s periodicity in Einstein data (Auriere et al., 1989), inspired the suggestion that X9 was an intermediate polar (Paresce et al., 1992). V1 was identified as the likely counterpart for X9 by Verbunt and Hasinger (1998) (who argued, presciently, that X9 was likely a low-mass X-ray binary). The association of V1 and X9 was later confirmed by *Chandra* observations (Grindlay et al., 2001). V1 showed rapid ($\sim$hours) X-ray and optical/UV variability, with a hint of a $\sim$6-hour periodicity in the UV flux (Paresce et al., 1992). Time series analysis of *V*

---

[1]a CV with a magnetic WD accretor; in these systems both orbital period and WD spin period can be detected in the light curve.

and *I* light curves by Edmonds et al. (2003b) indicated a marginal 3.5 hour (or 7 hour, if due to ellipsoidal variations) periodicity. *HST* far-UV-spectroscopy of X9 showed strong, double-peaked C IV emission lines, confirming the presence of an accretion disk and/or disk wind in the system (Knigge et al., 2008).

Recently Miller-Jones et al. (2015) reported on deep radio observations of 47 Tuc that detected a radio counterpart for X9. The ratio of radio/X-ray luminosity for X9 is strongly inconsistent with a CV, and more consistent with a BH LMXB, or possibly a transitional millisecond pulsar (tMSP – deemed unlikely from the X-ray spectral and variability properties). Based on the X-ray brightness (and thus accretion rate) and lack of Hα emission in the system, they suggest the system might be a UCXB. They further inferred an orbital period of ~ 25 min, from a correlation between quiescent X-ray luminosity and time-averaged mass transfer rate from the companion, and calculations of the time-averaged mass transfer rate at different orbital periods in ultracompact X-ray binaries.

In this work we study the X-ray properties of X9 as observed by *Chandra* and *NuSTAR* and the radio/X-ray flux ratio from simultaneous radio observations. We describe the data used in this work, with description of reduction and analysis methods, in Section 5.2. In Section 5.3, we present results and in Section 5.4, we will discuss implications of these findings.

5.2   Data and Analysis

We obtained simultaneous radio and X-ray observations of X9 with the Australian Telescope Compact Array (*ATCA*), *Chandra* using the ACIS-S detector, and *NuSTAR* on February 2nd, 2015 (MJD = 57055; *ATCA* from 0:500 to 17:00 UT on Feb. 2, *Chandra* from 14:25 on Feb. 2nd, to 03:20 on Feb. 3rd, and *NuSTAR* from 11:51 on Feb. 2nd to 00:46 on Feb. 5th, all UT). We also analyzed *Chandra* observations in late 2014 (described in Bogdanov et al., 2016) and

archival *Chandra/ACIS*, *Chandra/HRC*, *Swift/XRT*, *ROSAT/HRI*, and *Einstein* data to study variability of X9 over long time scales ($\sim$ days to years).

5.2.1 *Chandra/ACIS*

Archival *Chandra/ACIS* data were obtained in 2000 (with the ACIS-I3 chip) and 2002 (with ACIS-S3) in faint mode. Our 2014–15 campaign (PI: Bogdanov) included 6 observations between September 2014 and February 2015 (Table 5.1). All observations in this campaign were performed in Very Faint mode on ACIS-S3. We focus our spectral analysis upon the 2015 *Chandra* observation; detailed analysis of other archival *Chandra* spectra is deferred to future papers.

We used `CIAO` 4.7 with `CalDB` 4.6.8 (Fruscione et al., 2006) for data reprocessing and analysis. We reprocessed all *Chandra* data with `chandra_repro` and extracted source and background spectra using `specextract`. We chose an extraction radius of 1.8″ for the source region. 47 Tuc X9 is near the crowded center of the cluster. Thus, for background regions, we used an annulus with inner and outer radii of 2.7″ and 7.4″ around the source, excluding detected sources (Fig. 5.1). We binned all final spectra to have a minimum number of counts per bin; depending on exposure and data quality, either by 50 or 20 counts per bin. Finally we used XSPEC 12.8.2 (Arnaud, 1996) for spectral analysis, and performed spectral fitting in the 0.4-10 keV band.

5.2.2 *NuSTAR*

NuSTAR has a relatively large point-spread function, with a half-power diameter of $\sim 1'$ (Harrison et al., 2013), which encloses a substantial fraction of the core of 47 Tuc. 47 Tuc X9 is easily the brightest X-ray source above 2 keV within the half-mass radius of 47 Tuc (Heinke et al., 2005b). The cataclysmic variable AKO 9 (Knigge et al., 2003) is the only other source detected above 6

Obs. ID	Date	Exposure (ks)
Chandra/ACIS		
00953	2000-03-16	32
00955	2000-03-16	32
02735	2002-09-29	65
02736	2002-09-30	65
02737	2002-10-02	65
02738	2002-10-11	69
16527	2014-09-05	41
15747	2014-09-09	50
16529	2014-09-21	25
17420	2014-09-30	09
15748	2014-10-02	16
16528	2015-02-02	40
NuSTAR		
80001084002	2015-02-02	17
80001084004	2015-02-03	76
Chandra/HRC		
5542	2005-12-19	50
5543	2005-12-20	51
5544	2005-12-21	50
5545	2005-12-23	52
5546	2005-12-27	48
6230	2005-12-28	45
6231	2005-12-29	47
6232	2005-12-31	44
6233	2006-01-02	97
6235	2006-01-04	50
6236	2006-01-05	52
6237	2005-12-24	50
6238	2005-12-25	48
6239	2006-01-06	50
6240	2006-01-08	49

Table 5.1: *Chandra* and *NuSTAR* observations used in this study.
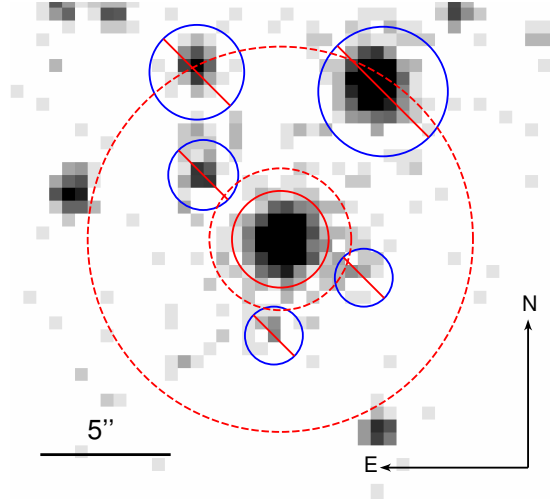
Figure 5.1: *Chandra* image of the vicinity of X9 in the core of 47 Tuc. Red circles represent nominal source (solid red circle) and background (dashed red circle) regions for spectral extractions. X-ray sources present in the background were excluded from extraction region (blue circles).

keV in this *Chandra* observation. However, AKO 9 is ~ 20 times fainter than X9 in the 6-10 keV band (Fig. 5.2, middle and right panels). This makes X9 the principal source of X-rays above 6.0 keV in the cluster, and ensures that *NuSTAR* spectra above 6 keV are minimally affected by confusion.

Our *NuSTAR* observation of 47 Tuc was performed between February 2nd and 5th, 2015. This observation was simultaneous with *Chandra* ObsID 16528 and our *ATCA* radio observation. Our *NuSTAR* observation was performed in two segments with a gap from Feb. 2nd, 21:11 to 3rd, 8:46 UT.

X9 is clearly detected in our *NuSTAR* observations (Fig. 5.2, left panel). The suggested extraction radius for weak sources in *NuSTAR* data is $30''$ (see *NuSTAR* observatory guide[2]). We used this radius for all *NuSTAR* spectral extractions (source and background). We use the 6–79 keV band for all *NuSTAR* data analysis of X9.

We used the `nustardas` package released with `heasoft` 16.6 for data repro-

---

[2]https://heasarc.gsfc.nasa.gov/docs/nustar/nustar_obsguide.pdf
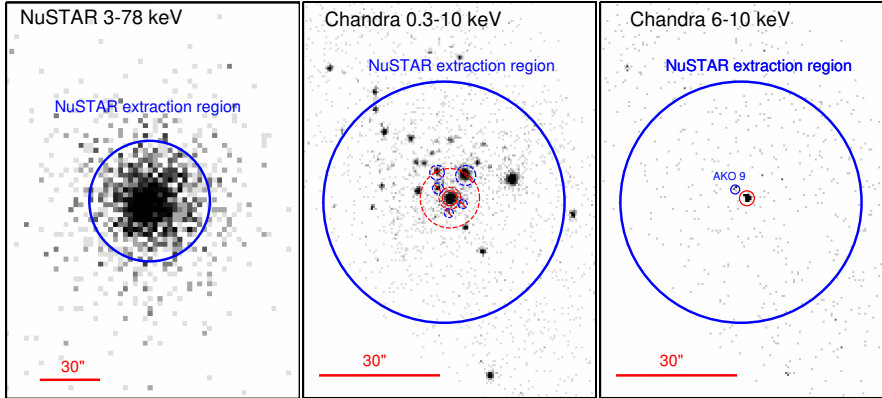
Figure 5.2: X-ray image of X9 in 47 Tuc as observed by *NuSTAR* (left) and *Chandra/ACIS* (center & right). X9 is the only significant source above 6 keV in *Chandra* observations and thus is the major contributor in *NuSTAR* data of the cluster. The solid blue circle represents our spectral extraction region for X9 in *NuSTAR* data.

cessing and analysis. We processed the observations by running `nupipeline` and proceeded to extract spectra and light curves from both modules (FPMA & FPMB) using `nuproducts`. After grouping the spectra by counts (20 per bin for the shorter segment and 40 for the longer segment) we used XSPEC for spectral analysis.

5.2.3 Chandra/HRC

The 47 Tuc *Chandra/HRC* campaign (PI: Rutledge, Cameron et al. 2007) contains 15×50 ks observations performed over a period of 20 days. These provided us with a unique opportunity to study variations of X9 on time-scales of days. We combined these observations using `reproject_obs` and extracted X9's light curve from a circle with a radius of $2''$, running `dmextract` (in CIAO software package) with background subtraction and assuming Gehrels uncertainties (Gehrels, 1986). Finally, we binned the light curve into intervals of 10 ks.

5.2.4 *Swift/XRT*, *ROSAT/HRI*, and *Einstein*

As X9 shows strong variability in X-rays, we also investigated available archival data from *Swift/XRT*, *ROSAT/HRI*, and *Einstein* to study the extent of these variations across a wide range of timescales.

Since 2014, *Swift* has observed 47 Tuc frequently with long ($\sim$ 4000 s) exposures as part of a GC monitoring program[3] (Linares & Chenevez, in prep.). Unlike typical *Swift/XRT* exposures ($\sim$ 1000 – 2000 s), these exposures are adequate to constrain the brightness of sources at a few $\times 10^{33}$ erg s^{-1} at a distance of 4.5 kpc (like X9). Thus we analyze these datasets to look for variability and possible brightening (e.g., due to enhanced accretion) from X9.

However, due to the relatively low resolution and large point-spread function of *Swift/XRT*, the X-ray sources in 47 Tuc blend together in these observations. We chose to extract events in the 4–10 keV band, in which X9 is the dominant source, as a trade-off between signal/noise ratio and dominance of X9's flux over the rest of the cluster. After measuring background-subtracted count rates in the 4–10 keV band for each observation and subtracting contamination from other cluster sources in the *Swift/XRT* extraction region (based on their flux in the 4–10 keV band *Chandra* image), we converted these count rates to flux by folding the best fit spectral model found for our 2015 *Chandra/ACIS* + *NuSTAR* spectrum (see § 5.3.2) through the *Swift/XRT* response matrix (using XSPEC) and finding equivalent flux values for each measured count rate. Ultimately we converted flux values to luminosity in the 0.5–10 keV band, assuming a distance of 4.53 kpc to 47 Tuc.

There are also archival *ROSAT/HRI* data available for 47 Tuc, with spatial resolution capable of marginally resolving the core of 47 Tuc. Detailed analyses of these data, attributing counts to each of the brightest core sources, have been reported by Verbunt and Hasinger (1998). We use the corresponding

---

[3]http://www.iac.es/proyecto/SwiftGloClu/

count rates (Verbunt and Hasinger, 1998, Figure 3) in our analysis. Similar to our procedure for *Swift* data, we used the best fit spectral model folded to *ROSAT/HRI* to convert count rates to flux and luminosity.

Among the instruments on board of *Einstein*, there were the High Resolution Imager (*HRI*) sensitive in the 0.15–3.0 keV band with a spatial resolution of $\sim 2''$ and the Imaging Proportional Counter (*IPC*) sensitive in the 0.4–4.0 keV band with a resolution of $\sim 1'$. Although *HRI* had a high angular resolution, it had a low effective area ($5 - 20$ cm^2). In contrast, *IPC* had a relatively large effective area (100 cm^2). *Einstein* observed 47 Tuc in 1979 8 times (5 HRI observations followed with 3 IPC observations) and 1E 0021.8-7221 is clearly detected in all observations (Hertz and Grindlay, 1983; Auriere et al., 1989).

5.2.5   ATCA

Since the existing radio and X-ray data on 47 Tuc X9 were taken several years apart (Miller-Jones et al., 2015) and X-ray binaries in quiescence can be highly variable (Bernardini and Cackett, 2014), we obtained ATCA data simultaneous with the scheduled *Chandra* observations in 2015 February, under project code C3012. The ATCA data were taken from 0505–1705 UT on 2015 February 2, with the array in an extended 6 km configuration. Using the Compact Array Broadband Backend (CABB; Wilson et al., 2011) we observed simultaneously in two frequency bands, each of bandwidth 2048 MHz, centred at 5.5 and 9.0 GHz. 90 min of data were lost to bad weather, leaving us a total of 523 min on source.

We used B1934-638 to set both the amplitude scale and to determine the instrumental frequency response. The starting elevation of the target was 52°, and decreased with time. For the first 10 hr of observations, we were able to use the same nearby compact source, B2353-686, to determine the time-variable complex gains as used by Miller-Jones et al. (2015). However, that source set below the elevation limit of the telescope at 1445 UT, after which we switched to the more distant but higher-elevation complex gain calibrator J0047-7530

to enable continued observations of 47 Tuc. We reduced the data according to standard procedures within the Multichannel Image Reconstruction, Image Analysis and Display (MIRIAD) software package (Sault et al., 1995), and then exported the calibrated, frequency-averaged data to the Common Astronomy Software Application (CASA McMullin et al., 2007) for imaging. We detected X9 in both frequency bands, and used the CASA task IMFIT to fit a point source to the target in the image plane. This gave measured flux densities of 27.6 ± 7.2 and $38.5 \pm 9.7 \,\mu\mathrm{Jy}\,\mathrm{bm}^{-1}$ at 5.5 and 9.0 GHz respectively, giving a measured spectral index (defined such that flux density S_ν scales with frequency ν as $S_\nu \propto \nu^\alpha$ of $\alpha = 0.7 \pm 0.8$).

5.3 Results

5.3.1 Periodic variability

Einstein observations of 47 Tuc in the 1980s indicated that 1E 0021.8-7221 (the only detected X-ray source in the cluster at the time) shows strong variations. Auriere et al. (1989) report a variable absorbed flux of $2.2 - 6.4 \times 10^{-12}$ erg cm^{-2} s^{-1} in the 0.4–2.0 keV band. Assuming a distance of 4.53 kpc and extrapolating these luminosities to the 0.5–10 keV band using the power-law model reported by Auriere et al. (1989), with a photon index of 2, we find a luminosity range of $6.3 - 21.5 \times 10^{33}$ erg s^{-1} for *Einstein/HRI* and *Einstein/IPC* data points.

In *ROSAT/HRI* observations of 47 Tuc between 1992 and 1996 (Verbunt and Hasinger, 1998), X9 shows a variable brightness between 1.5 and 6.1×10^{33} erg s^{-1} (extrapolated to the 0.5–10 keV band). Similar variations can be seen in *Chandra/ACIS* campaigns in 2000, 2002, and 2014–2015, as well as recent deep *Swift/XRT* observations of the cluster (Fig. 5.3).

The *Chandra/HRC* lightcurve of X9 shows periodic variations between 8.4×10^{32} erg s^{-1} and 6.6×10^{33} erg s^{-1} on timescales of a few days (Fig. 5.3). We used a generalized Lomb-Scargle periodogram algorithm (Lomb, 1976; Scargle, 1982)
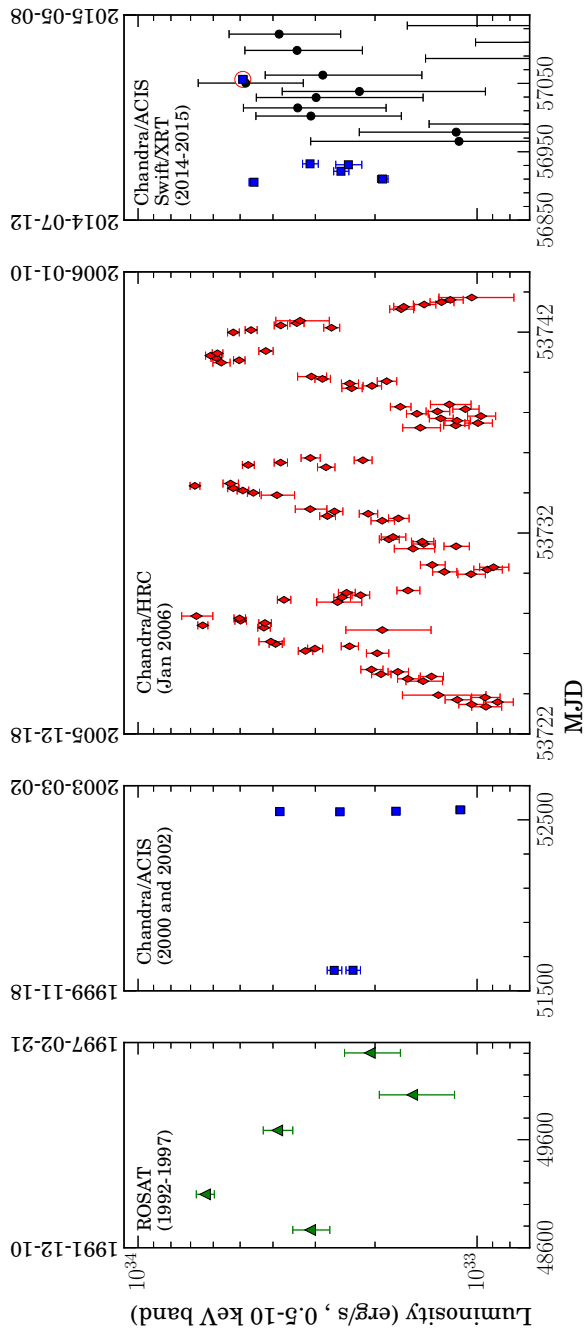
Figure 5.3: Lightcurve of 47 Tuc X9 as seen by various telescopes since 1991. Note that each panel has a different timescale. Green triangles show *ROSAT/HRI* observations performed in the 1990s (Verbunt and Hasinger, 1998), blue squares represent *Chandra/ACIS* campaigns in 2000 (Grindlay et al., 2001), 2002 (Heinke et al., 2005b) and 2014-2015 (Bogdanov et al., 2016, this work). Red diamonds show *Chandra/HRC* observations between December 2005 and January 2006 (Cameron et al., 2007) and black circles show *Swift/XRT* observations (Linares & Chenevez in prep.). The *Chandra/ACIS* observation performed simultaneously with *NuSTAR* and ATCA is indicated with a red circle around the blue square.
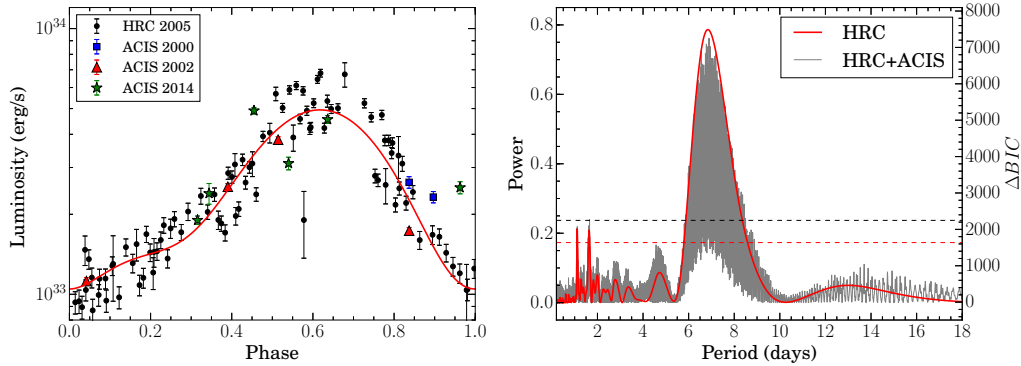
Figure 5.4: *Left:* Folded X-ray lightcurve of X9 and a second order Fourier fit with a period of 6.89 days for *HRC+ACIS* data. The folded lightcurve of X9 shows non-sinusoidal behavior with a slower rise and a faster drop. *Right:* Result of a periodicity search using the Lomb-Scargle method for just *HRC* data (red line) and for *HRC+ACIS* data (gray line). The straight red and gray dashed lines indicate the 95% confidence thresholds calculated using bootstrap resampling. Note that the uncertainties found with this method for X9 might be overestimated due to the complex profile of oscillations.

implemented in the Python package `AstroML`[4] (Vanderplas et al., 2012; Ivezić et al., 2014) to constrain the period of the variabilty observed in *Chandra/HRC* data. We found a period of $6.8^{+1.8}_{-1.0}$ days for *HRC* data (Fig. 5.4, right; red line).

The uncertainties reported for the period here are calculated based on bootstrap resampling. We note that these values might be over-estimated due to the complex profile of this light curve. A two-term Fourier fit describes the light curve significantly better than a single-term fit, with an F-test probability of chance improvement of 7×10^{-11} % for *HRC* data[5]. The two-term Fourier fit shows the rise towards the peak is slower than the fall (Fig. 5.4, left).

The periodicity is only clearly visible in the *Chandra/HRC* data. However, we also searched for indications of this variability in *Chandra/ACIS* data. We performed a period search using the Lomb-Scargle method with both *Chandra/HRC* and *Chandra/ACIS* data points. Adding the *ACIS* data points adds

---

[4]http://www.astroml.org/

[5]Since an F-test for the third order Fourier term provides a chance probability of 4.5%, thus we prefer the two-term model.

aliasing to the periodogram (Fig. 5.4, right; gray line). The optimum period in this case is found to be $6.9^{+1.6}_{-1.0}$ days. The Fourier fit and folded light curve indicate that the periodicity is likely present in *Chandra/ACIS* data as well (Fig. 5.4, left).

One *ROSAT/HRI* observation of 47 Tuc in 1993 shows X9 at a luminosity of $6.1 \pm 0.4 \times 10^{33}$ erg s^{-1}, which in comparison with later *ROSAT/HRI* and *Chandra/ACIS* observations was thought to be caused by an enhanced activity like a flare or outburst (Verbunt and Hasinger, 1998). However, *Chandra/HRC* data shows that X9 reaches a peak luminosity of $\sim 6.3 \pm 0.2 \times 10^{33}$ erg s^{-1} periodically, and thus this level of brightness for X9 is not unusual.

The peak luminosities observed by *Chandra/HRC* or *ROSAT/HRI* are $\sim$3.5 times fainter than the peak luminosity observed by *Einstein* HRI observations in 1979 ($\sim 2.15 \times 10^{34}$ erg s^{-1} extrapolated to the 0.5 – 10 keV band). We note that due to the poor spatial resolution of *Einstein/IPC* (3′), the IPC data analyzed by Auriere et al. (1989) contains the entire half-mass radius of the cluster, and may be the sum of flux from multiple sources. However, the peak of the lightcurve was recorded by the *Einstein/HRI*, which has superior spatial resolution ($\sim$ 2″), and localized the brightest *Einstein* source to only 1.4″ away from X9.

The peak of the combined *Einstein* lightcurve, at $\sim 2 \times 10^{34}$ erg s^{-1}, was also well above the typical cluster luminosity, $\sim 5.7 \times 10^{33}$ erg s^{-1} for all sources besides X9 (Heinke et al., 2005b), and above the maximum cluster luminosity when X9 was at its peak ($\sim 1.2 \times 10^{34}$ erg s^{-1}). However, the *Einstein/IPC* data show a decline in luminosity down to fluxes consistent with the rest of the cluster plus X9 in its lower state, on timescales typical of X9's variations (Fig. 5.5). The excellent match of the X-ray position, minimum flux, and decay timescale suggest that the bright state recorded by *Einstein/HRI* was due to X9, reaching a peak luminosity roughly twice the maximum luminosity seen by *ROSAT*, *Chandra* or *Swift* later.
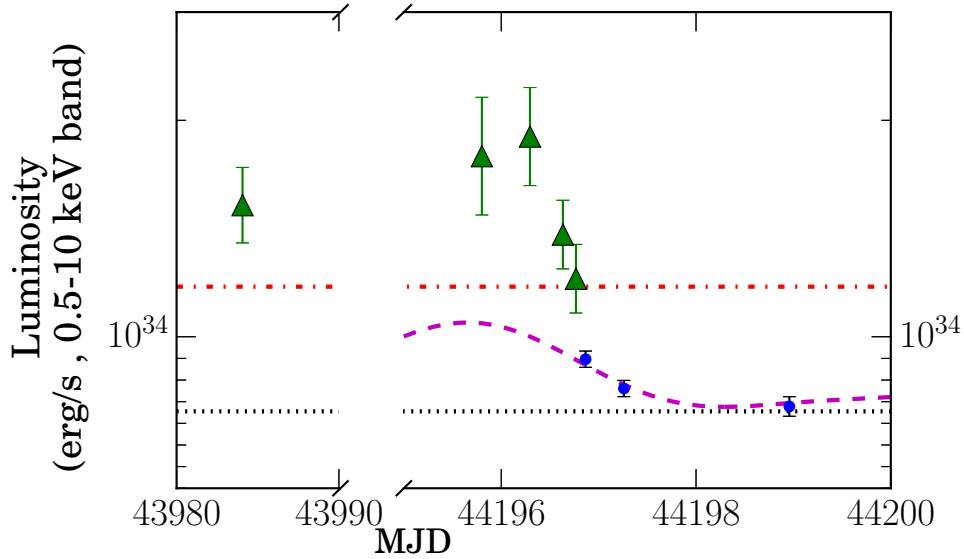
Figure 5.5: *Einstein/HRI* (green triangles) and *Einstein/IPC* (blue dots) observations of 47 Tuc in 1979 as reported by Auriere et al. (1989). Black dotted line shows the cumulative luminosity of X-ray sources in 47 Tuc's half-mass radius with X9 at minimum luminosity, and the red dash-dotted line shows the cumulative luminosity of the cluster with X9 at the maximum luminosity observed by *Chandra/HRC*. The dashed magenta line shows a projection of our Fourier fit to *Chandra/HRC* data (with an arbitrary shift applied in time fit to the data by eye). *HRI* data points above the periodic profile and maximum observed luminosity indicate that an X-ray source in 47 Tuc was showing enhanced activity during *Einstein/HRI* observations.

5.3.2 X-ray Spectroscopy

We tried to constrain the broadband spectral shape through joint *Chandra* and *NuSTAR* spectral fitting. We used XSPEC 12.8.2 in all our spectral analysis and assumed Wilms et al. (2000) abundances and Verner et al. (1996) cross-sections. Foreground reddening in the direction of 47 Tuc is $E(B - V) = 0.04$ (Salaris et al., 2007). Assuming $R_V = 3.1$ and using the observed correlation between extinction (A_V) and hydrogen column density N_H for Wilms abundances (Bahramian et al., 2015; Foight et al., 2015), we get a hydrogen column density of 3.5×10^{20} cm^{-2}. We assumed this as the hydrogen column density towards 47 Tuc throughout this paper. (Since it is quite small, variations in N_H due to differential extinction would lead to correspondingly small variations in spectral fits.) For all spectral analyses, we considered 0.4–10 keV band data from *Chandra/ACIS* and 6.0–79 keV data for *NuSTAR*. Our *NuSTAR* spectra contain data from two observations (Table 5.1) and two modules (FPMA & FPMB). We fit all these spectra jointly (instead of combining the spectra). Due to the brightness of X9, we also accounted for the effects of pileup on *ACIS* data by including the `pileup` model in XSPEC in all *Chandra* spectral fittings, even though the 2014–15 *Chandra/ACIS* campaign used a 1/8 subarray mode to reduce pileup. Due to possible differences in detector responses between *NuSTAR* and *Chandra/ACIS*, in all our models we include a variable coefficient representing the *NuSTAR/Chandra* relative normalization ratio.

The X-ray spectrum of X9 (Fig. 5.6) contains a strong line complex around 0.7 keV, attributed to O VIII by Heinke et al. (2005b), and an extended hard energy tail. We see no evidence of a Kα iron line. Our initial model for fitting the spectrum was an absorbed collisionally-ionized gas model (`mekal` model in XSPEC, e.g., Mewe et al., 1985, 1986), plus a cut-off power law (`constant*pileup*tbabs*(mekal+cutoffpl)`)[6]. However, this model failed

---

[6]Note that the constant factor in the model represents the *NuSTAR/Chandra* normalization ratio.

to adequately describe the spectra ($\chi^2_\nu = 1.56$ for 185 d.o.f). Particularly it failed to fit some of the stronger oxygen features below 1 keV. We discuss fit improvements for these features in detail below.

Comptonization and reflection

In addition to the low energy features, our initial fit (`constant*pileup*tbabs*(mekal+ cutoffpl)`) shows a significant trend of residuals as a "bump" in 10–30 keV region (Fig. 5.6, top-left). Thus we test other appropriate models by replacing the power law component with them. To compare how models fit the harder part of the spectrum, in this section we report statistics in the 1–79 keV band for each model. Our initial power-law-only model yielded a χ^2_ν of 1.37 for 171 d.o.f. Replacing the power-law with a Comptonization model (e.g., `compTT`; Titarchuk, 1994) does not improve the fit (χ^2_ν of 1.39 for 170 d.o.f).

It is possible that the observed bump is caused by reflected emission. Using a reflected power law from neutral matter (`pexrav`; Magdziarz and Zdziarski, 1995) improved the fit significantly ($\chi^2_\nu = 0.98$ for 168 d.o.f, Fig. 5.6, top-right). A reflected power-law from ionized matter (`pexriv`) gives similar results ($\chi^2_\nu = 0.99$ for 166 d.o.f) but leaves the disk temperature and ionization parameter ($\xi = 4\pi F_{ion}/n$, where F_{ion} is irradiating flux in the 5–20 keV band and n is density of the reflector) mostly unconstrained ($\xi < 100$ erg cm s^{-1}). We also tried fitting the hard component of the spectrum using a Compton-scattering model convolved with a reflection model (e.g., `reflect*comptt`). This model also addresses the reflection bump well ($\chi^2_\nu = 1.00$ for 167 d.o.f). The details of our spectral fitting with these models are tabulated in Table 5.2.

The general improvement achieved by adding effects of reflection to the model, and the fact that the reflection scale parameter in all cases is non-zero (and above 0.5), give strong evidence for the significance of reflection in this system.

All three models containing reflection fit the spectrum well. However, as

	Without reflection		With reflection		
	Powerlaw	CompTT	Pexrav	Pexriv	Reflect×CompTT
photon index	1.01 ± 0.07	–	1.2 ± 0.1	$1.17^{+0.1}_{-0.03}$	–
E_{fold} (keV)	> 85	–	56^{+22}_{-14}	62^{+63}_{-15}	–
T_0 (keV)	–	< 0.3	–	–	0.35 ± 0.04
T_e (keV)	–	> 161	–	–	62^{+234}_{-31}
τ	–	$1.8^{+1.3}_{-0.8}$	–	–	$0.9^{+2.7}_{-0.8}$
Reflect scale	–	–	$1.3^{+2.0}_{-0.4}$	$1.1^{+1.0}_{-0.3}$	$5.5^{+4.4}_{-1.8}$
Fe abund.	–	–	< 0.3	< 0.3	< 0.3
$\theta°$	–	–	< 68	< 45	< 60
T_{disk} (keV)	–	–	–	$0.001\pm?$ [a]	–
ξ (erg cm/s)	–	–	–	< 270	–
$C_{NU/CX}$	1.03 ± 0.09	$1.07^{+0.09}_{-0.07}$	0.90 ± 0.09	$0.88^{+0.1}_{-0.09}$	$0.87^{+0.13}_{-0.06}$
χ^2_ν/d.o.f	1.37/171	1.39/170	0.98/168	0.99/166	1.00/167
N.H.P (%)	0.06	0.05	54.2	52.4	47.2

Table 5.2: Best-fit parameter values for hard spectral components, fit in the 1-79 keV band. T_0 is temperature of the incident photons, T_e is the electron temperature and τ is optical depth in Comptonization models. We assume a disk geometry for the Comptonization component. Reflection scale indicates the relative scale of the reflected emission compared to the source. E_{fold} is the folding energy for exponential cut-off in the power law tail. Iron abundance is indicated as a fraction of solar abundance. The inclination angle is denoted by θ and ξ represents the ionization parameter. $C_{NU/CX}$ shows the relative *NuSTAR* to *Chandra/ACIS* normalization factor. N.H.P. indicates the null hypothesis probability. [a]- The disk temperature in Pexriv model is not constrained and the value stated here is just from the best fit.

the ionization parameter in Pexriv is loosely constrained and is consistent with zero (i.e., suggesting insignificance of ionized matter in the reflection), we prefer Pexrav to Pexriv. As the physically motivated model (in this case) requires an unusually high reflection scale parameter, indicating significant obscuration of the emission source (which seems inconsistent with the constraints on the inclination angle in the reflection component), we use Pexrav for the rest of our analysis.

Collisionally-ionized gas models

After addressing the hard component of the spectrum, we focused on the features in the soft end while fitting the whole band (0.4–79.0 keV). Our model with a single Mekal model and pexrav (`constant*pileup*tbabs*(mekal+pexrav)`) failed to describe the strong emission features below 1 keV ($\chi^2_\nu = 1.34$ for 183 d.o.f) leaving significant residuals below 1 keV. Adding a second mekal component did not improve the fit. As the features we are trying to fit are dependent on the abundances of elements in the system, we test our model with 47 Tuc abundances of elements (following Heinke et al. 2005b, assuming abundances of 0.6 solar for C,N, and O, and 0.4 solar for elements Ne through Ca, and 0.2 for Fe and Ni, see also Carney 1996; Salaris and Weiss 1998). To do so, we replace the Mekal component in our model with VMekal, which allows for adjustable abundances of elements. This model provides a slightly better fit with a $\chi^2_\nu = 1.23$ for 183 d.o.f (Fig. 5.6, middle-left). Adding a second vmekal component did not improve the fit.

The major features that the models above fail to describe mainly consist of strong spectral lines, from O VII and VIII between 0.6 and 0.8 keV. Additionally, in our *Chandra/ACIS* spectrum, there is a bump at ~ 0.3 keV that is not fit well when our band is extended to 0.3 keV. This bump could be due to carbon lines or uncertainties in the *ACIS* response matrix. The former is particularly plausible as Knigge et al. (2008) identify strong carbon lines in the FUV spectrum of X9. This significant underestimation of oxygen emission in our models suggests that the abundance of oxygen (and possibly carbon) in this system is higher than the measured values for either 47 Tuc or solar abundances. Miller-Jones et al. (2015) suggest that X9 might be a UCXB (based on mass transfer rate). This is consistent with a high abundance of oxygen, as carbon and oxygen can be dominant species in UCXBs where the donor is a C/O WD. We attempt a first test of this scenario by using the abundances calculated by Koliopanos et al. (2013) for a C/O UCXB system.

Although a model with a single VMekal component with UCXB abundances fails to describe the features below 1 keV ($\chi^2_\nu = 1.35$ for 183 d.o.f), adding a second VMekal component gives a slightly better fit with $\chi^2_\nu = 1.22$ for 181 d.o.f. (Table 5.3 and Fig. 5.6, middle-right), and thus adds more evidence for the presence of a C/O white dwarf companion in this system.

Reflection models for UCXBs

Our spectral analysis in Sections the two sections above provides evidence for reflection, and indicates an ultra-compact nature for the system, with a high abundance of oxygen. Thus it is possible that the strength of oxygen lines is due to reflection from a hot oxygen-rich disk. Thus we test this scenario by fitting the spectrum with a reflection model appropriate for oxygen-rich UCXBs. For this purpose we used $Xillver_{CO}$ (Madej et al., 2014), which is a reflection model for accretion disks in oxygen-rich UCXBs. $Xillver_{CO}$ is based on the Xillver reflection model (García and Kallman, 2010; García et al., 2011, 2013).

$Xillver_{CO}$ contains only the *reflected* emission from a disk plus a power law continuum (and not the emission from these components themselves). Thus to include all the components, our model became

`constant*pileup*tbabs*(diskbb+cutoffpl+xillverCO)`. In this model we tied the disk temperature between $Xillver_{CO}$ and diskbb, and tied the photon index and cut-off energy between $Xillver_{CO}$ and the cutoff power law. This model gives a moderately good fit with $\chi^2_\nu = 1.30$ for 181 d.o.f. However it shows clear residuals in fitting the oxygen features and the reflection bump (Fig. 5.6, bottom-left).

Photo-ionized gas models

None of the models tested in the Sections above seem to be able to entirely address the oxygen features. Specifically, most of these models seem to underestimate the relative amplitude of O VIII compared to O VII. This could be

due to a significant increase in the ionization state of oxygen due to photo-ionization. To investigate this, we used XSTAR (Kallman and Bautista, 2001) to simulate a model spectrum of photo-ionized oxygen in a system with a size scale applicable to X9.

For our simulations we assumed an oxygen-rich diffuse gas region[7], illuminated by a source (possibly the inner accretion flow) with an X-ray luminosity of $\sim 10^{33}$ erg s^{-1} (a typical luminosity level for X9). For the illuminating source we assumed a power law spectrum obtained from the best power law fit to the *Chandra/ACIS* spectrum in the 1–10 keV band. For the simulation, we assumed a hydrogen column density of 10^{22} cm^{-2} and a constant gas density of 10^{10} cm^{-3}. The variables in our grid model were temperature (10^4 to 10^7 k) and ionization parameter[8] ($\log \xi$ from -4 to 4). Our simulations were parallelized using PVM_XSTAR (Noble et al., 2009). Finally we produced an XSPEC table model using the XSTAR task `xstar2table` and performed spectral fitting with this model. From here on, we refer to this model as the photo-ionization model (`phoionize`).

We used a slightly different version of XSTAR (B.O.8) compared to the regular XSTAR release (B.N.24). The main difference between the two versions is the effects of bound-bound radiative excitation which, is turned on in the B.O.8 release. This is especially important as the oxygen Lα line can also be emitted by bound-bound radiative excitation of the upper level by continuum photons. Thus the B.O.8 release produces the helium-like oxygen line at a different energy as it pumps the resonance line, while the regular version makes a stronger intercombination line via recombination. Reproducing our models using the B.N.24 yielded a slightly inferior fit. This result indicates the importance of

---

[7]Currently we are unable to consider effects of carbon in our simulatuons, due to a complication in the current release of XSTAR.

[8]Note that this ionization parameter is defined as $\xi = L/nR^2$ where L is luminosity, n is density and R is the distance between the illuminating source and the illuminated gas, such that L/R^2 is the illuminating flux of the region.

bound-bound radiative excitation in production of these lines in the emitting region.

We used our XSTAR models to fit the joint *Chandra* and *NuSTAR* spectra. To do so, our full model became `constant*pileup*tbabs*(phoionize+pexrav)`. This model fit the spectra exceptionally well ($\chi^2_\nu = 1.02$ for 181 d.o.f, Table 5.3), almost completely removing residuals around the oxygen features (Fig. 5.6, bottom right). Our best fit using this model gives a gas temperature of $0.20^{+0.08}_{-0.10}$ keV and an ionization parameter ($\log \xi$) value of $0.6^{+0.8}_{-0.1}$. In our best fit, the Fe abundance in Pexrav is also found to be < 0.3 of the solar value. Koliopanos et al. (2013) suggest that strength of Fe Kα line (and thus the measured abundance of Fe) should be suppressed in systems with high carbon and oxygen abundances. However, Madej et al. (2014) indicate that this is only the case in systems with completely neutral gas.

Although our photo-ionized model provides a very good fit, there is a single spectral bin around ~ 0.8 keV that shows a significant residual (Fig. 5.6, bottom right). As this spectral bin is located in a region where the dominant component changes, it is unclear if this residual is due to incomplete modeling of the underlying continuum or caused by a spectral feature.

The superiority of this fit compared to the collisional models discussed in the previous section is a strong indicator of the extreme overabundance of oxygen and the fact that photo-ionization in this system must be considered. We discuss the implications of this finding in Section 5.4.2.

Our spectral analysis presented above is a first glance at a complex system. We note that in other *Chandra* datasets, due to the strong presence of oxygen features, Mekal with UCXB abundances or our photo-ionized model fits the spectra significantly better than models with solar abundances. We found our model fits most of the *Chandra* spectra reasonably well, however we noticed significant residual trends in a few data sets. We leave extensive spectral modeling and an in-depth study of the spectral evolution in the system to a later

	VMekal			Xillver$_{CO}$	Phoionize
	Solar	47 Tuc	UCXB	UCXB	Oxygen
T1 (keV)	0.16 ± 0.01	$0.17^{+0.01}_{-0.02}$	0.26 ± 0.05	0.11 ± 0.01	$0.20^{+0.08}_{-0.10}$
T2 (keV)	–	–	< 0.3	–	–
$\log(\xi)$	–	–	–	–	$0.6^{+0.8}_{-0.1}$
Photon index	1.04 ± 0.08	1.07 ± 0.08	1.05 ± 0.08	$1.2^{+0.3}_{-0.2}$	$1.12^{+0.08}_{-0.07}$
E_{fold} (keV)	35^{+13}_{-7}	47^{+14}_{-9}	38^{+12}_{-7}	201 ± 15	51^{+18}_{-11}
Reflect scale	$1.3^{+3.0}_{-0.5}$	$1.1^{+1.5}_{-0.4}$	$1.2^{+2.0}_{-0.4}$	–	$1.1^{+1.5}_{-0.3}$
θ (deg)	< 78	< 68	< 72	< 54	< 66
$C_{NU/CX}$	$0.96^{+0.09}_{-0.08}$	$0.90^{+0.09}_{-0.08}$	0.93 ± 0.08	$1.00^{+0.06}_{-0.07}$	0.89 ± 0.09
χ^2_ν/d.o.f	1.33/183	1.23/183	1.22/181	1.30/181	1.02/181
N.H.P (%)	0.15	1.8	2.1	0.43	41.6

Table 5.3: Best-fit parameter values for our models fitting the entire 0.4-79 keV band spectrum. The VMekal models are two-VMekal+pexrav models with abundance of elements based on values for solar (Wilms et al., 2000), 47 Tuc (Heinke et al., 2005b; Salaris and Weiss, 1998; Carney, 1996), and UCXB abundances (Koliopanos et al., 2013). Phoionize is the oxygen photo-ionization model produced using XSTAR (see text). T1 and T2 are temperature of each Mekal/VMekal component. Adding a second VMekal component only improved the fit in the case with UCXB abundances. In the case of Phoionize, T1 is the temperature of the photo-ionized region. E_{fold} represents the exponential cut-off energy in Pexrav and θ the inclination angle. Note that the iron abundance parameter in Pexrav is set to the value assumed for VMekal in each case. For Phoionize, this parameter was set free and was found to be < 0.3 of the solar value.

paper (Bahramian et al., in prep.).

5.4 Discussion

5.4.1 Origin of the super-orbital periodicity

The overabundance of oxygen in this component indicates a WD companion, and thus an orbital period < 80 min. The limits on optical flux from a companion star rule out a main-sequence star that could fill its Roche lobe for periods longer than 3.5 hours (Knigge et al., 2008). Thus, the 6.8 day periodic X-ray variability must have a super-orbital origin.

Super-orbital modulations have been observed in multiple XRBs (e.g., see
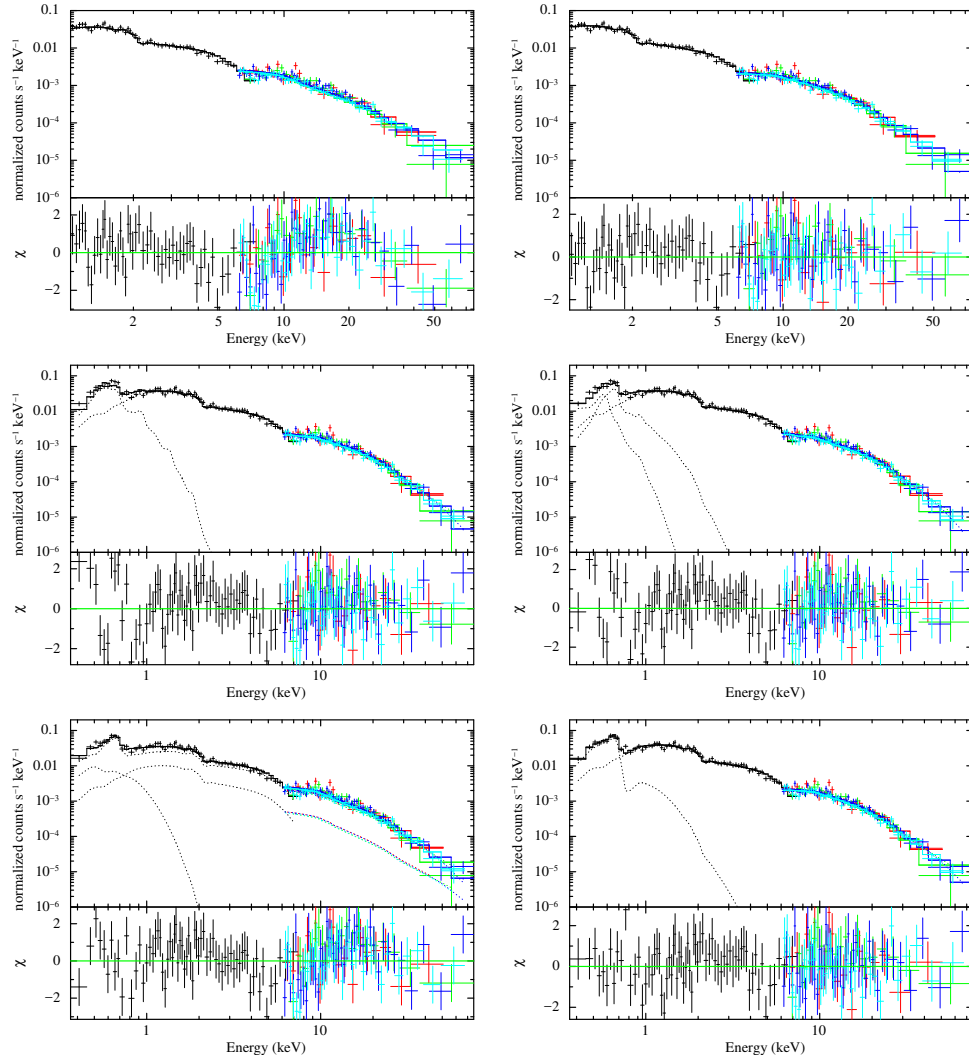
Figure 5.6: X-ray spectrum of 47 Tuc X9 as seen by *Chandra* (black) and *NuSTAR* (colored, red & blue from FPMA, green and cyan from FPMB) on February 2015 and models used to fit the spectra. The top panels show two of the fits performed in the 1-79 keV band to address the reflection bump above 10 keV, and the middle and bottom panels show attempts to address the oxygen features below 1 keV. The models represented here are: a cut-off power law (top-left), pexrav (top-right), a single vmekal + pexrav with 47 Tuc cluster abundances (mid-left), two vmekals+pexrav with ucxb abundances (mid-right), ucxb reflection model (bottom-left) and oxygen photo-ionization+pexrav (bottom-right). In the top panels, the reflection bump above 10 keV is clearly addressed by pexrav. Oxygen photo-ionization is the only model properly fitting the oxygen features below 1 keV.

Charles et al. 2008 for a review). It is thought that these modulations can be produced by mechanisms like precession, tilting, or warping of the accretion disk (among other possible scenarios like state changes or superhumps).

Among the systems showing super-orbital modulation, 4U 1916-053 is a persistent UCXB with an orbital period of 50 min (Walter et al., 1982; Nelemans and Jonker, 2010). Strong helium and nitrogen lines in the spectrum indicate a He WD companion (Nelemans et al., 2006), while X-ray bursts indicate a neutron star accretor (Becker et al., 1977). 4U 1916-053 shows an orbital modulation of period 5 days, presumably related to the "superhump" phenomenon (Patterson et al., 2005). Charles et al. (2008) suggest that the 5-day modulation in this system is caused by precession and/or warping of the accretion disk. Given the similarities between 4U 1916-053 and 47 Tuc X9, it is possible that similar mechanisms are responsible for the 6.7 day modulation observed in X9.

5.4.2   X9 as an ultra-compact X-ray binary

Based on the X-ray luminosity of X9 ($L_X \sim$ a few $\times 10^{33}$ erg s^{-1}) and the inferred mass transfer rate, Miller-Jones et al. (2015) suggest the system might be a UCXB with an orbital period of ~ 25 min. Knigge et al. (2008) reported the presence of strong carbon lines in the UV spectrum of X9, indicating the presence of carbon in the accretion flow, and absence of helium lines (hinting at the possibility of a C/O WD donor).

Heinke et al. (2005b) showed that in X-rays, X9's spectrum contains strong oxygen lines below 1 keV. As we tried to model the spectrum with various models (collisional gas, reflection in UCXBs, and oxygen photo-ionization; Section 5.3.2), we find the oxygen photo-ionization model provides a clearly better fit compared to the rest of the models. The superior goodness of this fit indicates the significance of photo-ionization in production of these oxygen lines, and thus points to the presence of overabundant oxygen possibly in the form of a

diffuse region around the inner accretion disk. Clear evidence of photo-ionized oxygen excess provides additional evidence for a C/O WD companion in this system.

5.4.3 Nature of the compact accretor

Our radio observation of X9 provided measured flux densities of 27.6 ± 7.2 and $38.5 \pm 9.7\,\mu\mathrm{Jy\,bm^{-1}}$ at 5.5 and 9.0 GHz respectively. Comparing with previous observations in 2010 and 2013 Miller-Jones et al. (2015), the 9-GHz radio emission has not changed markedly since the prior observations, although the 5.5 GHz emission appears to have dropped by a factor of 1.5 ± 0.4. As discussed in Miller-Jones et al. (2015), the radio flux of X9 is significantly higher than the values reported for any CV, making a CV nature for X9 an unlikely scenario.

With our simultaneous X-ray and radio measurements of X9, we plot X9 on the L_R–L_X plane (Fig. 5.7). Compared to Miller-Jones et al. (2015), we find a lower 5.5 GHz luminosity, but a higher X-ray luminosity.[9] This places X9 closer to the position of the transitional MSPs (tMSPs) and NS-XRBs.

The position of X9 on the L_R–L_X plot suggests either a NS or a BH as possibilities for the accreting object. Although it is possible for the system to be a quiescent tMSP, the X-ray behavior of X9 is significantly different than the other discovered tMSPs. Specifically, quiescent tMSPs show rapid ($\sim$ minutes) switching between two relatively stable luminosity levels around 10^{33} and 10^{34} erg s^{-1} (Papitto et al., 2013; de Martino et al., 2013; Linares et al., 2014; Tendulkar et al., 2014; Bogdanov and Halpern, 2015). However this is not the case for X9 as the source shows a slow (6 day), apparently periodic, variation.

An alternative scenario is that we are viewing the system at a very high inclination angle, where the outer disk obscures the inner parts of the accretion

---

[9]Note that the observations reported in Miller-Jones et al. (2015) were not simultaneous.
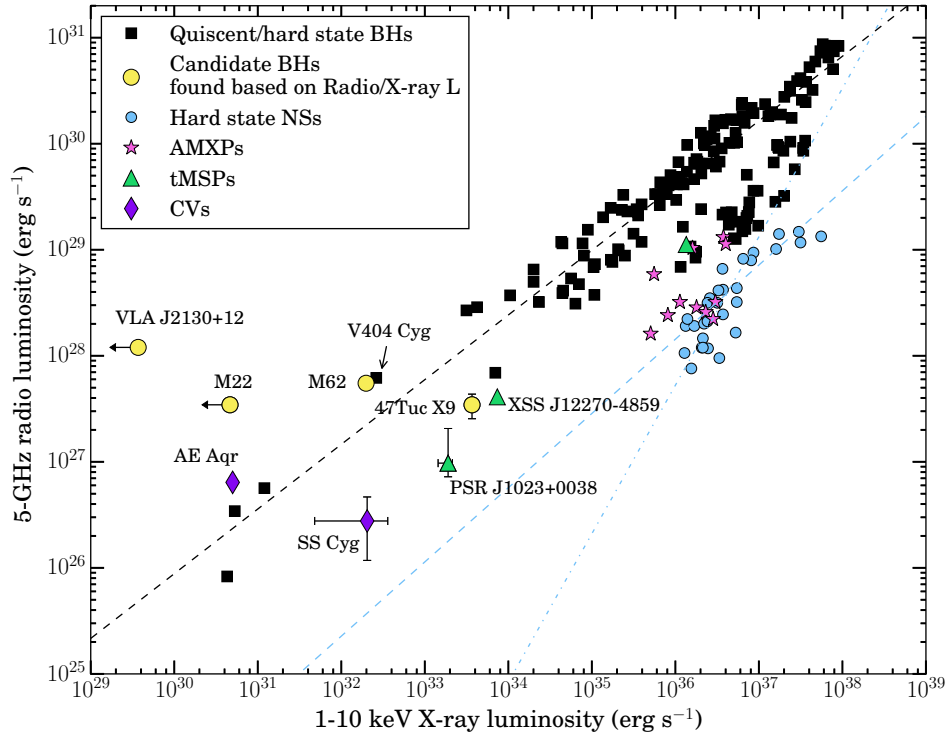
Figure 5.7: Radio/X-ray luminosity correlation for X-ray binaries and stellar mass black holes. Orignial plot from Tetarenko et al. (2016b). X9 falls below the correlation line for BH-LMXBs.

disk, so that the observed flux is significantly lower than the true flux. We found clear evidence for reflected emission in the X-ray spectrum of X9. To our knowledge, this is the lowest-luminosity X-ray binary (non-CV) system to show reflection. Clear detection of reflection from a faint ($< 10^{34}$ erg s^{-1}) system and the ionized emission possibly associated with an accretion disk corona in the system, dominating the continuum below 1 keV, suggests that the inner accretion disk might be heavily obscured and thus the true X-ray luminosity could be higher. In this scenario, a NS nature for the compact object is preferred by the radio/X-ray flux ratio.

Chapter 6

Revealing a new symbiotic X-ray binary with Gemini NIFS

Arash Bahramian[1], Jeanette C. Gladstone[1], Craig O. Heinke[1], Rudy Wijnands[2], Ramanpreet Kaur[3], Diego Altamirano[4]

[1] Dept. of Physics, University of Alberta, CCIS 4-183, Edmonton, AB T6G 2E1, Canada. [2] Astronomical Institute 'Anton Pannekoek', University of Amsterdam, Science Park 904, 1098 XH Amsterdam, the Netherlands. [3] Physics Department, Suffolk University, 41 Temple Street, Boston MA 02114, USA. [4] Physics & Astronomy, University of Southampton, Southampton, Hampshire SO17 1BJ, UK.

Abstract

We use K-band spectroscopy of the counterpart to the rapidly variable X-ray transient XMMU J174445.5-295044 to identify it as a new symbiotic X-ray binary. XMMU J174445.5-295044 has shown a hard X-ray spectrum (we verify its association with an Integral/IBIS 18-40 keV detection in 2013 using a short Swift/XRT observation), high and varying N_H, and rapid flares on timescales down to minutes, suggesting wind accretion onto a compact star. We observed its near-IR counterpart using the Near-infrared Integral Field Spectrograph (NIFS) at Gemini-North, and classify the companion as $\sim$ M2 III. We infer a distance of $3.1^{+1.8}_{-1.1}$ kpc (conservative 1σ errors), and therefore calculate that the observed X-ray luminosity (2-10 keV) has reached to at least 4×10^{34} ergs/s. We therefore conclude that the source is a symbiotic X-ray binary containing a neutron star (or, less likely, black hole) accreting from the wind of a giant.

6.1 Introduction

Symbiotic binaries transfer mass via the winds of cold (usually late K or M) giants onto compact objects: white dwarfs, neutron stars or black holes (Kenyon, 1986), with orbital periods typically in the 100s to 1000s of days (Belczyński et al., 2000). They were first identified by the presence of high-ionization emission lines in optical spectra of otherwise cold giants, indicating the presence of two components of vastly different temperatures. ROSAT X-ray studies of symbiotic binaries distinguished three classes (α, β, γ) by the X-ray spectral shape (Murset et al., 1997), with higher energy X-ray measurements adding two further classes showing highly-absorbed spectra (Luna et al., 2013). A small but rapidly increasing number of symbiotic systems have been identified as containing a neutron star as an accretor, through the measurement of pulsations and/or hard X-ray emission above 20 keV, and are known as symbiotic X-ray binaries (Masetti et al., 2006).

Only seven symbiotic X-ray binaries have been positively identified so far;

GX 1+4, (Davidsen et al., 1977); 4U 1700+24, (Masetti et al., 2002); 4U 1954+319, (Masetti et al., 2006); Sct X-1, (Kaplan et al., 2007); IGR J16194-2810, (Masetti et al., 2007); IGR J16358-4726, (Nespoli et al., 2010); and XTE J1743-363, (Bozzo et al., 2013). Several other likely candidate systems have also been proposed (e.g. Nucita et al. 2007, Masetti et al. 2011, Hynes et al. 2014). The identification and characterization of a symbiotic X-ray binary requires clear information on the nature of the accretor (e.g. from pulsations or unusual luminosities) and the donor (e.g. from spectroscopy).

Heinke et al. (2009c) identified XMMU J174445.5-295044 as a rapidly variable (timescales down to 100s of seconds) Galactic transient, using nine *XMM-Newton*, *Chandra*, and *Suzaku* observations. It showed 2-10 keV X-ray fluxes up to $> 3 \times 10^{-11}$ erg cm^{-2} s^{-1}, and variations in N_H, from 8×10^{22} up to 15×10^{22} cm^{-2}. The rapid variations and variable N_H suggested accretion from a clumpy wind, rather than an accretion disk. Heinke et al. (2009c) also identified a bright near-infrared (NIR) counterpart (2MASS J17444541-2950446) within the 2" XMM error circle. Heinke et al. (2009c) calculated the probability of a star of this brightness in K_S appearing in the X-ray error circle as only 2%, indicating that it is almost certainly the true counterpart. This star appears highly obscured and shows infrared colors typical of late-type stars, which Heinke et al. suggested indicates that XMMU J174445.5-295044 is a symbiotic star or symbiotic X-ray binary.

The *INTEGRAL* Galactic bulge monitoring program (Kuulkers et al., 2007) reported an X-ray transient detected by the JEM-X monitor on March 23, 2012 (Chenevez et al., 2012), at 17:44:48, -29:51:00, with an uncertainty of 1.3′ at 95% confidence, consistent with XMMU J174445.5-295044. The 10-25 keV flux of $1.5 \pm 0.3 \times 10^{-10}$ erg cm^{-2} s^{-1} is larger than previously reported for XMMU J174445.5-295044, but the high estimated N_H (not specified, but the JEM-X source was undetected below 10 keV, indicating $N_H > 10^{23}$ cm^{-2}) suggests that this is likely the same source, as it is known to exhibit similarly large

intrinsic extinction (Heinke et al., 2009c). In March 2013, the INTEGRAL IBIS telescope detected a hard transient at $9.3 \pm 1.4 \times 10^{-11}$ erg cm^{-2} s^{-1} (17-60 keV), at position 17:44:41.76, -29:48:18.0, uncertainty 4.2' (Krivonos et al., 2013). Krivonos et al. note that this position is consistent with XMMU J174445.5-295044, but suggest that follow-up observations are needed to verify whether it is the same source.

In this paper, we present Gemini NIFS spectroscopy of 2MASS J17444541-2950446, and conclude that its spectral type indicates a M2 III giant. We also describe a Swift/XRT observation permitting the confident identification of the 2013 INTEGRAL/IBIS transient (Krivonos et al., 2013) with XMMU J174445.5-295044. We combine these results to infer a peak $L_X > 4 \times 10^{34}$ erg s^{-1}. These results together allow us to confidently identify XMMU J174445.5-295044 as a symbiotic X-ray binary containing a neutron star or black hole accretor, rather than a white dwarf.

6.2   Data and Analysis

6.2.1   Swift/XRT

We observed XMMU J174445.5-295044 with *Swift/XRT* on March 30th, 2013 (two days after the INTEGRAL/IBIS detection of Krivonos et al. 2013) in photon-counting mode. The observation was interrupted after an on-source exposure of ~ 150 seconds due to a Gamma-ray burst alert. We detect a single source in the 23.6' diameter field, showing 7 counts. Using FTOOLS *xrtcentroid* we determine the position to be RA = 17:44:46.26s and DEC = -29:50:56.08″ with positional uncertainty of 9″, consistent within $<2\sigma$ with the position of XMMU J174445.5-295044. Given the lack of other X-ray sources nearby (see figure 4 of Heinke et al. 2009c), the Swift/XRT source is thus certainly the same as XMMU J174445.5-295044.

We reprocessed the Swift/XRT data (using HEASOFT 6.14), extracted a
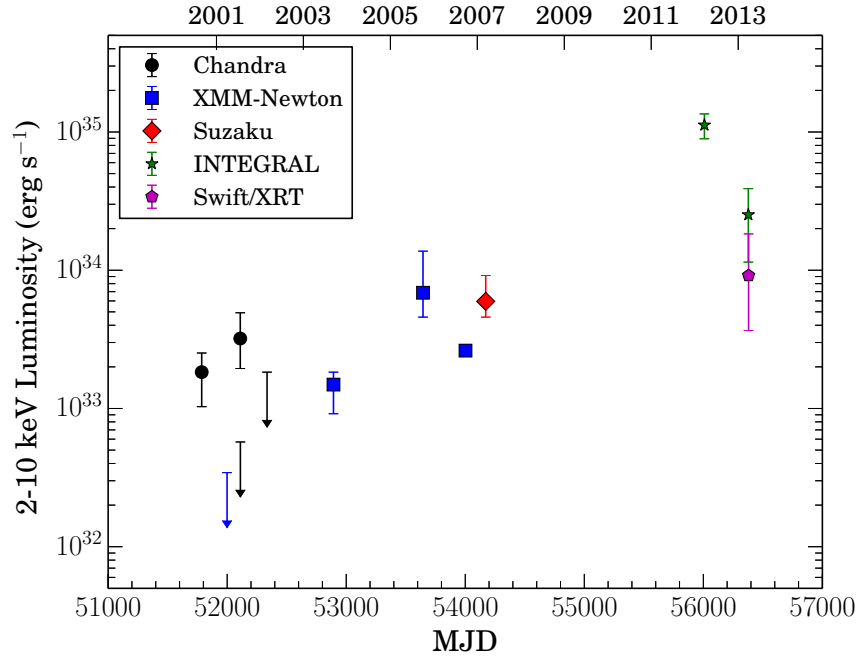
Figure 6.1: Long term X-ray light curve of XMMU J174445.5-295044, calculating X-ray luminosities in the 2-10 keV band using our calculated 3.1 kpc distance (§ 6.3.2). Errorbars do not include the distance uncertainty, so that intrinsic variations can be more clearly seen. *Chandra* (black circles & upper limits), *XMM-Newton* (blue squares & upper limits) and *Suzaku* (red diamonds) fluxes from Heinke et al. (2009c). *INTEGRAL* 2-10 keV fluxes (green stars) are extrapolated from the fluxes reported by Chenevez et al. (2012, JEM-X, 10-25 keV) and Krivonos et al. (2013, IBIS/ISGRI, 17-60 keV). Our *Swift/XRT* observation (magenta pentagon) is reported in § 6.2.1. The final *XMM-Newton* datapoint has statistical errorbars smaller than the marker size.

spectrum with XSELECT, and created an effective area file with *xrtmkarf*. We fit the Swift/XRT spectrum with an absorbed power-law using *cstat* statistics (Cash, 1979) in XSPEC 12.8.1, fixing the photon index to 1.18 (as found in the deepest and most-constrained observation of Heinke et al. 2009c). We measure $N_H = 4.5^{+7.2}_{-3.3} \times 10^{22}$ cm^{-2} and an unabsorbed 2-10 keV flux of $8.5^{+10.3}_{-5.0} \times 10^{-12}$ erg s^{-1} cm^{-2}, the second-highest 2-10 keV flux recorded from XMMU J174445.5-295044.

If the INTEGRAL/IBIS measurement is extrapolated (using the spectrum above) to the 2-10 keV band, the Swift/XRT flux measurement is 1/3 of the IN-TEGRAL measurement. Such a high flux from XMMU J174445.5-295044 only two days after the INTEGRAL/IBIS detection, combined with the lack of other detections within the 4.2′ INTEGRAL/IBIS error circle, indicates that XMMU J174445.5-295044 was the origin of the INTEGRAL/IBIS detection. The 2012 INTEGRAL/JEM-X detection (Chenevez et al., 2012), with a smaller error circle of 1.3′, can also be confidently assigned to XMMU J174445.5-295044.

We created long term X-ray lightcurves of XMMU J174445.5-295044, calculating X-ray luminosities in the 2-10 keV band using our calculated 3.1 kpc distance (see below). In Figure 6.1, we show the published detections of XMMU J174445.5-295044 (including our Swift measurement, and associating the two INTEGRAL detections, extrapolating their flux down to 2-10 keV).

6.2.2 Infrared data

Data and reduction

We observed XMMU J174445.5-295044 with Near-infrared Integral Field Spectrograph (NIFS, McGregor et al. 2002) mounted on the Fredrick C. Gillett telescope at Gemini-North observatory. The observation was done in queue mode on July 9th, 2012 under program ID GN-2012A-Q-114 (PI: C. O. Heinke). NIFS provides spectroscopy with spectral resolving power R∼ 5000 over a 3.0″×3.0″

field of view in the Z through K-band (9500 to 24000 Å). We performed the observation in K-band with standard methods for near-infrared, with a series of observations pointing on-source and blank sky. Blank sky observations were done in order to subtract sky emission from on-source observations. In order to remove telluric features in the spectrum of our target, we observed the A0V star HIP 88566 at similar airmass. For wavelength calibration, an exposure of Argon/Xenon arc lamps was taken. Also for spatial distortion removal and calibration, exposures with a Ronchi mask were taken.

We reduced and reprocessed the data using Gemini IRAF package V1.12 beta 2 included in IRAF[1] (V2.16) distributed in Ureka[2] 1.0 beta 5. NIFS package contains recipes for three stages of data reduction (baseline calibration, telluric data and science data) in *"nifsexamples"*[3]. In baseline calibration we made flat field and bad pixel map, performed wavelength calibration and determined the spatial curvature and spectral distortion in the Ronchi flat.

The spectra of A0V stars in the K band only show one significant feature, at Brγ (21661 Å). We removed this stellar feature from our reference spectrum to obtain a pure telluric spectrum. After extracting the one-dimensional spectrum of the telluric star, we divided the spectrum with a blackbody spectrum and included a Voigt profile fit to the Brγ feature (following Barbosa et al. 2008) to mimic the A0V spectrum of our calibration source. This spectrum was created using *mk1dspec* in *artdata* package. We assumed a temperature of $\sim$9800 K for the blackbody continuum of the A0V telluric star (Adelman, 2004) and determined the Voigt profile parameters by fitting with the task *splot*. We then eliminated telluric features in the science spectrum using the achieved pure telluric spectrum with the task *nftelluric*. The final output of the reduction

---

[1] IRAF is distributed by the National Optical Astronomy Observatory, which is operated by the Association of Universities for Research in Astronomy (AURA) under cooperative agreement with the National Science Foundation.

[2] Ureka is provided by Association of Universities for Research in Astronomy (AURA).

[3] http://www.gemini.edu/sciops/instruments/nifs/?q=node/10356

stage is calibrated telluric-corrected data in the form of a three-dimensional data cube with two spatial dimensions, each 62 pixels wide, and one spectral (wavelength) dimension of 2040 pixels. We extracted a one-dimensional spectrum by merging spatial dimensions inside a circular region with radius of 7 pixels centred on the source using DS9.

Spectral analysis

We measured the radial velocity of the source, using the *rvidlines* task in IRAF RV package to achieve a red/blue shift-corrected spectrum. In order to do this we first needed to identify a small number of prominent lines in the spectrum of this source. These include Al I (21170 Å), Si I (21360 Å), Ti (21789 Å, 21903 Å), Na I (22090 Å) and Ca I (22614 Å). *rvidlines* provided us with a velocity correction of -12$\pm$3 km s^{-1}, which was applied to the full spectrum. This corrected spectrum can be seen in Figure 6.2.

We used various available spectral libraries for late-type stars (Kleinmann and Hall, 1986; Wallace and Hinkle, 1997; Ramirez et al., 1997) to identify spectral features present in the spectrum. To obtain accurate identification and vacuum wavelength values we compared these identifications with data available in National Institute of Standards and Technology Atomic Spectra Database (NIST-ASD, Kramida et al. 2013). Figure 6.2 shows the rest-frame spectrum of XMMU J174445.5-295044 with all identified features. These features are tabulated in Table 6.1.

For two-dimensional stellar classification (spectral and luminosity) of the source we followed the method discussed by Ramirez et al. (1997); Ivanov et al. (2004); Comerón et al. (2004). This method consists of comparing the strength of a feature which is temperature-dependent with a feature which is temperature- and surface gravity-dependent. Following the method outlined in Comerón et al. (2004), we selected wavelength regions encompassing significant temperature-dependent features (Na I, Ca I), and one region representing

Table 6.1: Identified spectral lines in the spectrum. Reported wavelengths are in rest frame. References: 1- Kleinmann and Hall (1986), 2- Ramirez et al. (1997), 3- NIST-ASD. "?" indicates uncertain identifications.

Species	Wavelength(Å)	Reference
Fe I/Cs II (?)	20295	3
Ti I	20361	3
Fe II/B II (?)	20563	3
Si I	20923	1,3
Mg I	21067	1,3
Al I	21170	1,3
Si I	21360	1
Fe II/Ar II (?)	21506	3
Ti I	21789	1,3
Si I	21885	1
Ti I	21903	1,3
Ti I	22010	3
Sc I	22058	2,3
Si I	22069	2,3
Na I	22090	1,3
Ti I	22217	3
Fe I	22263	1,3
Fe I	22387	1,3
Ti I	22450	3
Ca I	22614	1,3
Fe I	22626	2,3
Ti I	22627	2,3
Ca I	22657	1,3
Fe I	22745	3
Mg I	22814	1,3
^{12}CO (2,0)	22935	1
^{12}CO (3,1)	23227	1
^{13}CO (2,0)	23448	1
^{12}CO (4,2)	23524	1
^{13}CO (3,1)	23739	1
^{12}CO (5,3)	23832	1

a temperature- and surface gravity-dependent feature (^{12}CO). For each feature, we use two nearby, featureless continuum regions to approximate the expected continuum level within the feature by linear interpolation. We used nearly the same feature and continuum definitions as Comerón et al. (2004) (Table 6.2). We made a small modification to the range of the blue continuum region for the Ca I feature given by Comerón et al. (2004), shortening it by 4 Å to avoid including the relatively strong nearby Ti I (22450 Å) line. This modification has an effect of < 0.2 % on the equivalent width measurement. These features and continua are represented in Figure 6.3. Finally we calculated an equivalent width for each feature, and compared these values to the values reported in Comerón et al. (2004).

To estimate errors, we divided the continuum regions into halves, and computed the equivalent widths using either half alone. We took the largest variation from our reported values as an estimate of the error in each measurement.

6.3 Results and Discussion

6.3.1 Two-dimensional spectral classification

Comerón et al. (2004) demonstrate that the ^{12}CO feature for supergiants always shows an equivalent width (EW) of > 25 Å (see their figures 8-13). We obtained EW[^{12}CO]$\approx 19.4 \pm 0.1$ Å, which is typical for giants or dwarfs (Comerón et al., 2004). Thus we can rule-out the possibility of a supergiant.

Ramirez et al. (1997) and Ivanov et al. (2004) show that log[EW(CO)/(EW(Ca I)+EW(Na I))] can be used to separate giants from dwarfs. Ramirez et al. (1997) show that this quantity should be between -0.22 and 0.06 for dwarfs, vs. between 0.37 and 0.61 for giants. We found this quantity to be 0.67 ± 0.06 for our source, in agreement with the estimated range for giants. Presence of fairly strong ^{13}CO bands in our spectrum is another indicator for a giant, as these features are invisible in a dwarf.

To estimate the temperature of this source, we used the first-order relationship between effective temperature (T_{eff}) and EW[^{12}CO] (in angstroms) for giants proposed by Ramirez et al. (1997):

$$T_{eff} = (5019 \pm 79) - (68 \pm 4) \times EW[^{12}CO] \qquad (6.1)$$

Considering the uncertainty in EW[^{12}CO], we found $T_{eff} = 3700 \pm 160$ K. According to van Belle et al. (1999), $T_{eff} = 3700$ K indicates M2 giant; using Richichi et al. (1999) suggests M1.5 while the relation in Ramirez et al. (1997) gives an M1.7 giant. Thus, adopting either the van Belle or Richichi calibration, the resulting spectral type is M2 III, with a reasonable range from M0 to M3. If we used the less detailed calibration from Ramirez et al 1997, we obtain a similar result of M1.7 (M0 to M3). Thus, we adopt M2 III as our spectral type, with a possible range from M0 to M3 III.

There is no evidence for a feature at Brγ in our spectrum, either before or after our telluric subtraction. Nespoli et al. (2010) see Brγ emission from two symbiotic X-ray binaries. However, the similar P-Cygni shape of the Brγ feature in both stars, and also in the supergiant X-ray binary IGR J16493-4348 studied by them with the same method, lend support to their hypothesis that this feature is a residual artifact of their telluric removal procedure (which is more complex than ours, involving using a G star as a second telluric reference).

6.3.2 Extinction, distance, and nature of the accretor

We use our identification of the spectral type, with the 2MASS photometry (Skrutskie et al., 2006) reported by Heinke et al. (2009c), to estimate the extinction, and thus the distance, to XMMU J174445.5-295044, in a similar way as Kaplan et al. (2007), but explicitly accounting for the difference between the K_S and K bands. Although the 2MASS colors were measured at a different time from the NIFS spectroscopy reported here, we do not expect large varia-

Figure 6.2: K-band spectrum of XMMU 174445.5-295044. Identified line profiles are listed in Table 6.1. Features identified using spectral libraries (Kleinmann and Hall, 1986; Ramirez et al., 1997) are marked with solid lines while features identified using NIST/ASD are marked with dashed lines. Ambiguous and uncertain identifications are labeled with "?".

Table 6.2: Definition of spectral features, chosen continuum intervals and measured equivalent width. We used definitions in Comerón et al. (2004) with a small modification to Ca I blue continuum (§ 6.2.2).

Feature	Band Center(Å)	$\delta\lambda$	Blue continuum Center(Å)	$\delta\lambda$	Red continuum Center(Å)	$\delta\lambda$	Equivalent width (Å)
Na I	22075	70	21940	60	22150	40	2.23±0.14
Ca I	22635	110	22507	53	22710	20	1.93±0.40
^{12}CO	22955	130	22500	160	22875	70	19.36±0.13
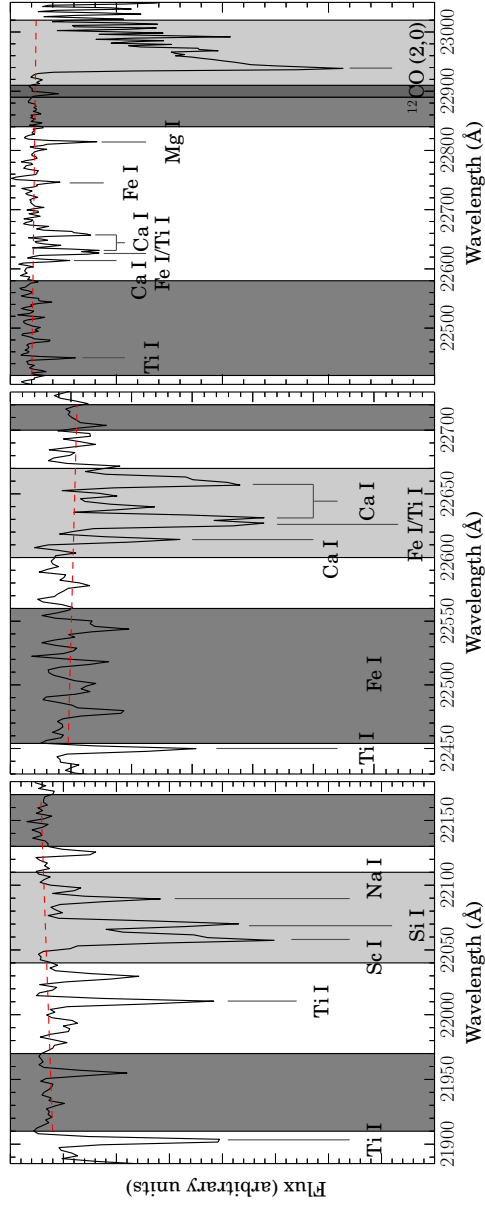
Figure 6.3: Chosen features and continua intervals used to obtain the spectral classification of the companion in this system. Left to right: Na I, Ca I, ^{12}CO(2,0). Light shaded regions show chosen regions for features and dark shaded regions represent chosen continua regions. These regions are tabulated in Table 6.2. The dashed lines represent interpolated continuum level in each case.

tions in the temperature or observed extinction of the giant, as the stars most affected by this are of later (>M5) spectral types (Habing, 1996).

M2 III stars have an absolute magnitude of $M_J = -3.92$ and intrinsic J-K_S colors of 1.12 (Covey et al., 2007). Heinke et al. (2009c) report a 2MASS magnitude of $m_J = 14.89$ in J for our object, and an observed J-K_S=4.72.

We use $A_J/A_V = 0.282$ (Cardelli et al., 1989), and $A_J/A_{K_s} = 2.5 \pm 0.2$ (Indebetouw et al., 2005). Thus we infer $A_V = \frac{(J-K_S)_{obs}-(J-K_S)}{(A_J/A_V)-(A_Ks/A_V)} = 21.3^{+1.9}_{-0.1}$, and $A_J = 6.0^{+0.5}_{-0.3}$. The extinction measurement converts (using N_H (cm^{-2}) = $(2.21 \pm 0.09) \times 10^{21} A_V$, Güver and Özel 2009), to $N_H = (4.7 \pm 0.5) \times 10^{22}$ cm^{-2}, which is below the X-ray measured values (measurements of $8.6 \pm 0.4 \times 10^{22}$ cm^{-2}, and $16^{+5}_{-4} \times 10^{22}$ cm^{-2}, from different observations) in Heinke et al. (2009c). This is consistent with expectations for a wind-accreting system, where much of the N_H is expected to be local to the compact object, and with the evidence for variation in N_H between different observations shown by Heinke et al. (2009c).

Using this A_J estimate, the expected M_J for a M2 III star, and the observed J magnitude, we can thus estimate d=3.1 kpc as the most likely distance to our object. The largest uncertainty in our distance estimate is our estimate of the absolute magnitude of the companion star. Allowing for a conservative 1-magnitude uncertainty on the absolute magnitude (estimated from Breddels et al. 2010; this is probably more precise than 1σ), we find d= $3.1^{+1.8}_{-1.1}$ kpc. This distance is consistent with our (small) radial velocity estimate, which would be typical of a disk star observed with a longitude very close to that of the galactic center ($l = 359.1°$), and with our measurement of the relative strengths of the CO and Na lines, the ratio of which is more consistent with disk giants than with giants in the bulge (Comerón et al., 2004).

From this distance estimate, we can infer the X-ray luminosities of XMMU J174445.5-295044, as plotted in Figure 6.1 (errors there do not include the distance uncertainties). The majority of the X-ray detections are between 10^{33} and 10^{34} erg s^{-1}, but the INTEGRAL/JEM-X detection in March 2012

(Chenevez et al., 2012) gives a (2-10 keV) X-ray luminosity of $(1.1\pm0.2) \times 10^{35}$ erg s^{-1} for $d = 3.1$ kpc; even at the lower limit on the distance (d = 2.0 kpc), the luminosity exceeds 4×10^{34} erg s^{-1} (Similarly, the March 2013 INTEGRAL/IBIS detection gives a (2-10 keV) $L_X = 2.5 \times 10^{34}$ erg s^{-1} for 3.1 kpc, or 1.1×10^{34} erg s^{-1} for the 2.0 kpc lower distance limit, which further confirms the high X-ray luminosity of XMMU J174445.5-295044). Combining this high peak X-ray luminosity (four times the maximum seen for any accreting white dwarf, Stacey et al. 2011) with the hard X-ray spectrum inferred from the later Integral/IBIS detection above 17 keV (Krivonos et al., 2013), we can confidently rule out a white dwarf nature for the accretor. Thus, we securely identify XMMU J174445.5-295044 as a symbiotic X-ray binary, with a neutron star (or, less likely, black hole) accreting from the wind of an M2 giant star.

XMMU J174445.5-295044 stands out from other symbiotic X-ray binaries only in not showing detectable X-ray pulsations (Heinke et al., 2009c). The complete absence of NIR spectroscopic evidence of accretion in our NIFS spectrum is typical of other symbiotic X-ray binaries with relatively low accretion rates. The lack of detected pulsations also means that the accretor could be a black hole, though black hole symbiotic X-ray binaries should be less common.

The increasing number of symbiotic binaries without detected emission lines in high-quality spectra being detected recently (van den Berg et al., 2006, 2012; Hynes et al., 2014) strongly suggests that there should be many more symbiotic stars (with white dwarf accretors) which also do not show optical/NIR spectroscopic evidence of accretion (van den Berg et al., 2006). Symbiotic systems may make up an important portion of the faint Galactic X-ray source population.

Chapter 7

Conclusions

7.1 Summary

Production of LMXBs in core-collapsed clusters   In Chapter 2, we calculated the stellar encounter rate for 124 Galactic globular clusters entirely based on observed data. Our model-independent method allowed us to treat all clusters (core-collapsed or otherwise) in the same manner and thus study the effects of core-collapse on populations of LMXBs in GCs. Additionally, we used Monte Carlo simulations to incorporate observational uncertainties (e.g., uncertainties in the observed surface brightness), and to estimate final uncertainties for stellar encounter rate values per cluster.

Previous calculations of stellar encounter rates generally assumed King-model profiles for the density of the cluster. While this is a reasonable assumption for many "normal" clusters, King profiles fail to describe the density profiles of core-collapsed GCs, and typically underestimate the cluster density in inner regions. This leads to underestimation of the value of the stellar encounter rate. With our calculation of a model-independent stellar encounter rate, we have been able to show that core-collapsed GCs tend to have lower populations of LMXBs compared to normal GCs with similar encounter rate values. These results provide suggestive evidence indicating that core-collapsed

GCs might be more efficient in binary destruction.

Evidence for low-level accretion during the rise (and decay) of transient LMXBs When decaying from an outburst ($L_X \sim 10^{35}$ erg/s), transient neutron star LMXBs show a thermal component in their X-ray spectrum. It has been suggested that this component might be either caused by low-level accretion, or due to neutron star crustal cooling.

In Chapter 3, we present the first observational evidence for presence of a thermal component in the spectrum of a neutron star LMXB during the rise to outburst (at $\sim 10^{35}$ erg/s). We show that as the system gets brighter and approaches the hard state, a non-thermal component dominates over the thermal component. The presence of a thermal component during the rise of outburst can only be explained by low-level accretion, thus indicating that the thermal component observed during the decay at similar luminosities is caused by low-level accretion as well.

Absence of low-level accretion in quiescent NS-LMXBs Neutron star LMXBs in quiescence ($L_X \sim 10^{32}$ erg/s) typically show a thermal spectrum, with a smaller power-law component in some cases. The origin of the thermal component has been generally attributed to heat from the interior, stored during accretion outbursts, emerging from the surface of the neutron star. However, there have also been suggestions that there might be contributions from low-level accretion to this thermal component (e.g. Zampieri et al., 1995). A clear signature of low-level accretion in quiescence would be fluctuations in the neutron star temperature on timescales of a few years. In Chapter 4, we look for signs of variability (over a decade) in the thermal spectra of 12 candidate neutron star qLMXBs. Ten of the sources within our sample show no evidence of variation in temperature, while two (NGC 6440 CX 1 and Terzan 5 CX 12) show marginal evidence for slow drops in temperature. These results are additional evidence suggesting the absence of low-level accretion in quiescent

neutron star LMXBs with no power law emission, thus indicating that the thermal emission is due to the deposited heat in the core of neutron star.

Photo-ionization and reflection in the faint UCXB 47 Tuc X9   47 Tuc X9 is a relatively bright ($L_X \sim$ a few $\times 10^{33}$ erg/s) quiescent LMXB (compared to quiescent LMXBs in globular clusters) in the core of 47 Tuc. While previously it was identified as a cataclysmic variable, recent radio studies suggested a black hole nature for the accretor in the system. Detection of strong carbon and oxygen emission lines in UV and X-ray spectra, respectively, hinted at high abundances of these elements in the system. This indicated that the companion might be a C/O white dwarf and that the system an ultra-compact X-ray binary. We obtain more X-ray data with *Chandra* and *NuSTAR* and perform spectral simulation and analysis. This analysis shows that describing the oxygen emission lines detected in the system requires photo-ionization in the system, presumably from an oxygen (and possibly carbon)-rich diffuse gas region embedding the inner part of the system. This provides additional evidence for the UCXB nature of the system. The NuSTAR spectrum of X9 clearly shows a reflection bump in the 10–30 keV interval, making X9 the faintest UCXB (to date) to show evidence of reflection.

7.2   Future work

Self-consistent spectral modeling for 47 Tuc X9   While in Chapter 5 we were able to prove the UCXB nature of 47 Tuc X9 and provide evidence for photo-ionized emission and reflection in the system, there are some caveats to our analysis, which we plan to address in the future. First, our photo-ionization model currently consists of pure oxygen. While most elements in a system with C/O white dwarf donor do not contribute to the X-ray spectrum, the effects of carbon could be detectable and thus should be incorporated. Sec-

163

ond, each of the reflection models we used have their own incompletenesses: traditional reflection models incorporated in XSpec (e.g., pexriv), do not consider hydrogen-deficient gas. On the other hand, currently available reflection models for UCXBs (e.g., $\text{Xillver}_C O$) do not fully incorporate the underlying continuum spectrum in a self-consistent way.

In a future study, we will attempt to prepare a self-consistent spectral model, incorporating effects of carbon (and possibly other elements) in photo-ionization, and a self-consistent reflection model with appropriate abundances for elements in the system.

Globular cluster properties and formation of X-ray binaries   Our results in Chapter 2 pave the path to integrating other cluster complexities and studying their effect on the formation of X-ray binaries. Model-independent calculated values of the stellar encounter rate with robust estimation of uncertainties could be reliably used to parametrize the correlation between cluster properties and X-ray binary populations.

As a next step, we will use our estimation of stellar encounter rate (the main parameter responsible for formation of binaries through encounters) and other available data, like the masses of GCs (a significant parameter representing the population of binaries formed primordially in the cluster), metallicity (thought to affect formation through encounters), and to parametrize the correlation between populations of LMXBs and GC properties, thus searching for empirical evidence for the role of these parameters in the formation of LMXBs in GCs.

Bibliography

A. A. Abdo, M. Ackermann, M. Ajello, W. B. Atwood, M. Axelsson, L. Baldini, J. Ballet, G. Barbiellini, M. G. Baring, D. Bastieri, B. M. Baughman, K. Bechtol, R. Bellazzini, B. Berenji, G. F. Bignami, R. D. Blandford, E. D. Bloom, E. Bonamente, A. W. Borgland, J. Bregeon, A. Brez, M. Brigida, P. Bruel, T. H. Burnett, G. A. Caliandro, R. A. Cameron, F. Camilo, P. A. Caraveo, P. Carlson, J. M. Casandjian, C. Cecchi, Ö. Çelik, E. Charles, A. Chekhtman, C. C. Cheung, J. Chiang, S. Ciprini, R. Claus, I. Cognard, J. Cohen-Tanugi, L. R. Cominsky, J. Conrad, R. Corbet, S. Cutini, C. D. Dermer, G. Desvignes, A. de Angelis, A. de Luca, F. de Palma, S. W. Digel, M. Dormody, E. do Couto e Silva, P. S. Drell, R. Dubois, D. Dumora, Y. Edmonds, C. Farnier, C. Favuzzi, S. J. Fegan, W. B. Focke, M. Frailis, P. C. C. Freire, Y. Fukazawa, S. Funk, P. Fusco, F. Gargano, D. Gasparrini, N. Gehrels, S. Germani, B. Giebels, N. Giglietto, F. Giordano, T. Glanzman, G. Godfrey, I. A. Grenier, M. H. Grondin, J. E. Grove, L. Guillemot, S. Guiriec, Y. Hanabata, A. K. Harding, M. Hayashida, E. Hays, G. Hobbs, R. E. Hughes, G. Jóhannesson, A. S. Johnson, R. P. Johnson, T. J. Johnson, W. N. Johnson, S. Johnston, T. Kamae, H. Katagiri, J. Kataoka, N. Kawai, M. Kerr, J. Knödlseder, M. L. Kocian, M. Kramer, M. Kuss, J. Lande, L. Latronico, M. Lemoine-Goumard, F. Longo, F. Loparco, B. Lott, M. N. Lovellette, P. Lubrano, G. M. Madejski, A. Makeev, R. N. Manchester, M. Marelli, M. N. Mazziotta, W. McConville, J. E. McEnery, M. A. McLaughlin, C. Meurer, P. F. Michelson, W. Mitthumsiri, T. Mizuno, A. A.

Moiseev, C. Monte, M. E. Monzani, A. Morselli, I. V. Moskalenko, S. Murgia, P. L. Nolan, J. P. Norris, E. Nuss, T. Ohsugi, N. Omodei, E. Orlando, J. F. Ormes, D. Paneque, J. H. Panetta, D. Parent, V. Pelassa, M. Pepe, M. Pesce-Rollins, F. Piron, T. A. Porter, S. Rainò, R. Rando, S. M. Ransom, P. S. Ray, M. Razzano, N. Rea, A. Reimer, O. Reimer, T. Reposeur, S. Ritz, L. S. Rochester, A. Y. Rodriguez, R. W. Romani, M. Roth, F. Ryde, H. F. W. Sadrozinski, D. Sanchez, A. Sander, P. M. Saz Parkinson, J. D. Scargle, T. L. Schalk, C. Sgrò, E. J. Siskind, D. A. Smith, P. D. Smith, G. Spandre, P. Spinelli, B. W. Stappers, J. L. Starck, E. Striani, M. S. Strickman, D. J. Suson, H. Tajima, H. Takahashi, T. Tanaka, J. B. Thayer, J. G. Thayer, G. Theureau, D. J. Thompson, S. E. Thorsett, L. Tibaldo, D. F. Torres, G. Tosti, A. Tramacere, Y. Uchiyama, T. L. Usher, A. Van Etten, V. Vasileiou, C. Venter, N. Vilchez, V. Vitale, A. P. Waite, E. Wallace, P. Wang, K. Watters, N. Webb, P. Weltevrede, B. L. Winer, K. S. Wood, T. Ylinen, and M. Ziegler. A Population of Gamma-Ray Millisecond Pulsars Seen with the Fermi Large Area Telescope. *Science*, 325:848, August 2009a. doi: 10.1126/science.1176113.

A. A. Abdo, M. Ackermann, M. Ajello, W. B. Atwood, M. Axelsson, L. Baldini, J. Ballet, G. Barbiellini, D. Bastieri, B. M. Baughman, K. Bechtol, R. Bellazzini, B. Berenji, R. D. Blandford, E. D. Bloom, E. Bonamente, A. W. Borgland, J. Bregeon, A. Brez, M. Brigida, P. Bruel, T. H. Burnett, G. A. Caliandro, R. A. Cameron, P. A. Caraveo, J. M. Casandjian, C. Cecchi, Ö. Çelik, E. Charles, S. Chaty, A. Chekhtman, C. C. Cheung, J. Chiang, S. Ciprini, R. Claus, J. Cohen-Tanugi, J. Conrad, S. Cutini, C. D. Dermer, F. de Palma, S. W. Digel, M. Dormody, E. do Couto e Silva, P. S. Drell, R. Dubois, D. Dumora, C. Farnier, C. Favuzzi, S. J. Fegan, W. B. Focke, M. Frailis, Y. Fukazawa, P. Fusco, F. Gargano, D. Gasparrini, N. Gehrels, S. Germani, B. Giebels, N. Giglietto, F. Giordano, T. Glanzman, G. Godfrey, I. A. Grenier, J. E. Grove, L. Guillemot, S. Guiriec, Y. Hanabata, A. K.

166

Harding, M. Hayashida, E. Hays, D. Horan, R. E. Hughes, G. Jóhannesson, A. S. Johnson, R. P. Johnson, T. J. Johnson, W. N. Johnson, T. Kamae, H. Katagiri, N. Kawai, M. Kerr, J. Knödlseder, F. Kuehn, M. Kuss, J. Lande, L. Latronico, M. Lemoine-Goumard, F. Longo, F. Loparco, B. Lott, M. N. Lovellette, P. Lubrano, A. Makeev, M. N. Mazziotta, W. McConville, J. E. McEnery, C. Meurer, P. F. Michelson, W. Mitthumsiri, T. Mizuno, A. A. Moiseev, C. Monte, M. E. Monzani, A. Morselli, I. V. Moskalenko, S. Murgia, P. L. Nolan, J. P. Norris, E. Nuss, T. Ohsugi, N. Omodei, E. Orlando, J. F. Ormes, D. Paneque, J. H. Panetta, D. Parent, V. Pelassa, M. Pepe, M. Pierbattista, F. Piron, T. A. Porter, S. Rainò, R. Rando, M. Razzano, N. Rea, A. Reimer, O. Reimer, T. Reposeur, S. Ritz, L. S. Rochester, A. Y. Rodriguez, R. W. Romani, M. Roth, F. Ryde, H. F.-W. Sadrozinski, D. Sanchez, A. Sander, P. M. Saz Parkinson, C. Sgrò, D. A. Smith, P. D. Smith, G. Spandre, P. Spinelli, J.-L. Starck, M. S. Strickman, D. J. Suson, H. Tajima, H. Takahashi, T. Tanaka, J. B. Thayer, J. G. Thayer, D. J. Thompson, L. Tibaldo, D. F. Torres, G. Tosti, A. Tramacere, Y. Uchiyama, T. L. Usher, V. Vasileiou, N. Vilchez, V. Vitale, P. Wang, N. Webb, B. L. Winer, K. S. Wood, T. Ylinen, and M. Ziegler. Detection of High-Energy Gamma-Ray Emission from the Globular Cluster 47 Tucanae with Fermi. *Science*, 325: 845, August 2009b. doi: 10.1126/science.1177023.

A. A. Abdo, M. Ackermann, W. B. Atwood, M. Axelsson, L. Baldini, J. Ballet, G. Barbiellini, D. Bastieri, M. Battelino, B. M. Baughman, K. Bechtol, R. Bellazzini, B. Berenji, E. D. Bloom, E. Bonamente, A. W. Borgland, J. Bregeon, A. Brez, M. Brigida, P. Bruel, T. H. Burnett, G. A. Caliandro, R. A. Cameron, P. A. Caraveo, J. M. Casandjian, C. Cecchi, E. Charles, A. Chekhtman, C. C. Cheung, J. Chiang, S. Ciprini, R. Claus, I. Cognard, J. Cohen-Tanugi, L. R. Cominsky, J. Conrad, S. Cutini, C. D. Dermer, A. de Angelis, F. de Palma, S. W. Digel, M. Dormody, E. d. C. e. Silva, P. S. Drell, R. Dubois, D. Dumora, C. Farnier, C. Favuzzi, W. B. Focke,

M. Frailis, Y. Fukazawa, S. Funk, P. Fusco, F. Gargano, D. Gasparrini, N. Gehrels, S. Germani, B. Giebels, N. Giglietto, F. Giordano, T. Glanzman, G. Godfrey, I. A. Grenier, M.-H. Grondin, J. E. Grove, L. Guillemot, S. Guiriec, Y. Hanabata, A. K. Harding, M. Hayashida, E. Hays, R. E. Hughes, G. Jóhannesson, A. S. Johnson, R. P. Johnson, T. J. Johnson, W. N. Johnson, T. Kamae, H. Katagiri, J. Kataoka, N. Kawai, M. Kerr, J. Knödlseder, M. L. Kocian, N. Komin, F. Kuehn, M. Kuss, J. Lande, L. Latronico, S.-H. Lee, M. Lemoine-Goumard, F. Longo, F. Loparco, B. Lott, M. N. Lovellette, P. Lubrano, G. M. Madejski, A. Makeev, M. Marelli, M. N. Mazziotta, W. McConville, J. E. McEnery, C. Meurer, P. F. Michelson, W. Mitthumsiri, T. Mizuno, A. A. Moiseev, C. Monte, M. E. Monzani, A. Morselli, I. V. Moskalenko, S. Murgia, P. L. Nolan, E. Nuss, T. Ohsugi, N. Omodei, E. Orlando, J. F. Ormes, B. Pancrazi, D. Paneque, J. H. Panetta, D. Parent, M. Pepe, M. Pesce-Rollins, F. Piron, T. A. Porter, S. Rainò, R. Rando, M. Razzano, A. Reimer, O. Reimer, T. Reposeur, S. Ritz, L. S. Rochester, A. Y. Rodriguez, R. W. Romani, F. Ryde, H. F.-W. Sadrozinski, D. Sanchez, A. Sander, P. M. S. Parkinson, C. Sgrò, E. J. Siskind, D. A. Smith, P. D. Smith, G. Spandre, P. Spinelli, J.-L. Starck, M. S. Strickman, D. J. Suson, H. Tajima, H. Takahashi, T. Tanaka, J. B. Thayer, J. G. Thayer, G. Theureau, D. J. Thompson, L. Tibaldo, D. F. Torres, G. Tosti, A. Tramacere, Y. Uchiyama, T. L. Usher, A. Van Etten, N. Vilchez, V. Vitale, A. P. Waite, K. Watters, N. Webb, K. S. Wood, T. Ylinen, and M. Ziegler. Pulsed Gamma Rays from the Millisecond Pulsar J0030+0451 with the Fermi Large Area Telescope. *ApJ*, 699:1171–1177, July 2009c. doi: 10.1088/0004-637X/699/2/1171.

A. A. Abdo, M. Ackermann, M. Ajello, L. Baldini, J. Ballet, G. Barbiellini, D. Bastieri, R. Bellazzini, R. D. Blandford, E. D. Bloom, E. Bonamente, A. W. Borgland, A. Bouvier, T. J. Brandt, J. Bregeon, M. Brigida, P. Bruel, R. Buehler, S. Buson, G. A. Caliandro, R. A. Cameron, P. A. Caraveo,

S. Carrigan, J. M. Casandjian, E. Charles, S. Chaty, A. Chekhtman, C. C. Cheung, J. Chiang, S. Ciprini, R. Claus, J. Cohen-Tanugi, J. Conrad, M. E. Decesar, C. D. Dermer, F. de Palma, S. W. Digel, E. D. C. E. Silva, P. S. Drell, R. Dubois, D. Dumora, C. Favuzzi, P. Fortin, M. Frailis, Y. Fukazawa, P. Fusco, F. Gargano, D. Gasparrini, N. Gehrels, S. Germani, N. Giglietto, F. Giordano, T. Glanzman, G. Godfrey, I. Grenier, M.-H. Grondin, J. E. Grove, L. Guillemot, S. Guiriec, D. Hadasch, A. K. Harding, E. Hays, P. Jean, G. Jóhannesson, T. J. Johnson, W. N. Johnson, T. Kamae, H. Katagiri, J. Kataoka, M. Kerr, J. Knödlseder, M. Kuss, J. Lande, L. Latronico, S.-H. Lee, M. Lemoine-Goumard, M. Llena Garde, F. Longo, F. Loparco, M. N. Lovellette, P. Lubrano, A. Makeev, M. N. Mazziotta, P. F. Michelson, W. Mitthumsiri, T. Mizuno, C. Monte, M. E. Monzani, A. Morselli, I. V. Moskalenko, S. Murgia, M. Naumann-Godo, P. L. Nolan, J. P. Norris, E. Nuss, T. Ohsugi, N. Omodei, E. Orlando, J. F. Ormes, B. Pancrazi, D. Parent, M. Pepe, M. Pesce-Rollins, F. Piron, T. A. Porter, S. Rainò, R. Rando, A. Reimer, O. Reimer, T. Reposeur, J. Ripken, R. W. Romani, M. Roth, H. F.-W. Sadrozinski, P. M. Saz Parkinson, C. Sgrò, E. J. Siskind, D. A. Smith, P. Spinelli, M. S. Strickman, D. J. Suson, H. Takahashi, T. Takahashi, T. Tanaka, J. B. Thayer, J. G. Thayer, L. Tibaldo, D. F. Torres, G. Tosti, A. Tramacere, Y. Uchiyama, T. L. Usher, V. Vasileiou, C. Venter, N. Vilchez, V. Vitale, A. P. Waite, P. Wang, N. Webb, B. L. Winer, Z. Yang, T. Ylinen, M. Ziegler, and Fermi LAT Collaboration. A population of gamma-ray emitting globular clusters seen with the Fermi Large Area Telescope. *A&A*, 524:A75, December 2010. doi: 10.1051/0004-6361/201014458.

S. J. Adelman. The physical properties of normal A stars. In J. Zverko, J. Ziznovsky, S. J. Adelman, and W. W. Weiss, editors, *The A-Star Puzzle*, volume 224 of *IAU Symposium*, pages 1–11, December 2004. doi: 10.1017/ S1743921304004314.

D. Altamirano, P. Casella, A. Patruno, R. Wijnands, and M. van der Klis. Intermittent Millisecond X-Ray Pulsations from the Neutron Star X-Ray Transient SAX J1748.9-2021 in the Globular Cluster NGC 6440. *ApJL*, 674: L45–L48, February 2008. doi: 10.1086/528983.

D. Altamirano, A. Patruno, C. O. Heinke, C. Markwardt, T. E. Strohmayer, M. Linares, R. Wijnands, M. van der Klis, and J. H. Swank. Discovery of a 205.89 Hz Accreting Millisecond X-ray Pulsar in the Globular Cluster NGC 6440. *ApJL*, 712:L58–L62, March 2010. doi: 10.1088/2041-8205/712/1/L58.

D. Altamirano, A. Ingram, M. van der Klis, R. Wijnands, M. Linares, and J. Homan. Low-frequency Quasi-periodic Oscillation from the 11 Hz Accreting Pulsar in Terzan 5: Not Frame Dragging. *ApJL*, 759:L20, November 2012a. doi: 10.1088/2041-8205/759/1/L20.

D. Altamirano, L. Keek, A. Cumming, G. R. Sivakoff, C. O. Heinke, R. Wijnands, N. Degenaar, J. Homan, and D. Pooley. A superburst candidate in EXO 1745-248 as a challenge to thermonuclear ignition models. *MNRAS*, 426:927–934, October 2012b. doi: 10.1111/j.1365-2966.2012.21769.x.

D. Altamirano, R. Wijnands, C. O. Heinke, G. R. Sivakoff, and D. Pooley. The new X-ray transient Swift J174805.3-244637 in Terzan 5 is a neutron star LMXB. *The Astronomer's Telegram*, 4264:1, July 2012c.

E. Anders and N. Grevesse. Abundances of the elements - Meteoritic and solar. *GCA*, 53:197–214, January 1989. doi: 10.1016/0016-7037(89)90286-X.

A. M. Archibald, S. Bogdanov, A. Patruno, J. W. T. Hessels, A. T. Deller, C. Bassa, G. H. Janssen, V. M. Kaspi, A. G. Lyne, B. W. Stappers, S. P. Tendulkar, C. R. D'Angelo, and R. Wijnands. Accretion-powered Pulsations in an Apparently Quiescent Neutron Star Binary. *ApJ*, 807:62, July 2015. doi: 10.1088/0004-637X/807/1/62.

M. Armas Padilla, N. Degenaar, A. Patruno, D. M. Russell, M. Linares, T. J. Maccarone, J. Homan, and R. Wijnands. X-ray softening in the new X-ray transient XTE J1719-291 during its 2008 outburst decay. *MNRAS*, 417: 659–665, October 2011. doi: 10.1111/j.1365-2966.2011.19308.x.

M. Armas Padilla, N. Degenaar, D. M. Russell, and R. Wijnands. Multiwavelength spectral evolution during the 2011 outburst of the very faint X-ray transient Swift J1357.2-0933. *MNRAS*, 428:3083–3088, February 2013a. doi: 10.1093/mnras/sts255.

M. Armas Padilla, N. Degenaar, and R. Wijnands. The X-ray spectral properties of very-faint persistent neutron star X-ray binaries. *MNRAS*, 434: 1586–1592, September 2013b. doi: 10.1093/mnras/stt1114.

M. Armas Padilla, R. Wijnands, and N. Degenaar. XMM-Newton and Swift spectroscopy of the newly discovered very-faint X-ray transient IGR J17494-3030. *MNRAS, submitted*, July 2013c.

K. A. Arnaud. XSPEC: The First Ten Years. In *ASP Conf. Ser. 101: Astronomical Data Analysis Software and Systems V*, page 17, 1996.

M. Auriere, L. Koch-Miramond, and S. Ortolani. The X-ray source in the core of 47 Tucanae. *A&A*, 214:113–122, April 1989.

M. Bagchi, D. R. Lorimer, and J. Chennamangalam. Luminosities of recycled radio pulsars in globular clusters. *MNRAS*, 418:477–489, November 2011. doi: 10.1111/j.1365-2966.2011.19498.x.

A. Bahramian, C. O. Heinke, G. R. Sivakoff, and J. C. Gladstone. Stellar Encounter Rate in Galactic Globular Clusters. *ApJ*, 766:136, April 2013. doi: 10.1088/0004-637X/766/2/136.

A. Bahramian, C. O. Heinke, G. R. Sivakoff, D. Altamirano, R. Wijnands, J. Homan, M. Linares, D. Pooley, N. Degenaar, and J. C. Gladstone. Dis-

covery of the Third Transient X-Ray Binary in the Galactic Globular Cluster Terzan 5. *ApJ*, 780:127, January 2014. doi: 10.1088/0004-637X/780/2/127.

A. Bahramian, C. O. Heinke, N. Degenaar, L. Chomiuk, R. Wijnands, J. Strader, W. C. G. Ho, and D. Pooley. Limits on thermal variations in a dozen quiescent neutron stars over a decade. *MNRAS*, 452:3475–3488, October 2015. doi: 10.1093/mnras/stv1585.

M. Balucinska-Church and D. McCammon. Photoelectric absorption cross sections with variable abundances. *ApJ*, 400:699, December 1992.

M. Bałucińska-Church, M. J. Church, and A. P. Smale. The orbital period of the dipping, bursting, globular cluster X-ray source XB 1746-371 from Rossi X-ray Timing Explorer observations. *MNRAS*, 347:334–338, January 2004. doi: 10.1111/j.1365-2966.2004.07218.x.

C. L. Barbosa, R. D. Blum, P. S. Conti, A. Damineli, and E. Figuerêdo. High Spatial Resolution Spectroscopy of W51 IRS 2E and IRS 2W: Two Very Massive Young Stars in Early Formation Stages. *ApJL*, 678:L55–L58, May 2008. doi: 10.1086/588500.

S. D. Barthelmy, L. M. Barbier, J. R. Cummings, E. E. Fenimore, N. Gehrels, D. Hullinger, H. A. Krimm, C. B. Markwardt, D. M. Palmer, A. Parsons, G. Sato, M. Suzuki, T. Takahashi, M. Tashiro, and J. Tueller. The Burst Alert Telescope (BAT) on the SWIFT Midex Mission. *SSR*, 120:143–164, October 2005. doi: 10.1007/s11214-005-5096-3.

G. Beccari, G. De Marchi, N. Panagia, and L. Pasquini. Hα photometry of low-mass stars in 47 Tucanae: chromospheric activity and exotica. *MNRAS*, 437:2621–2631, January 2014. doi: 10.1093/mnras/stt2074.

R. H. Becker, B. W. Smith, J. H. Swank, E. A. Boldt, S. S. Holt, P. J. Serlemit-

sos, and S. H. Pravdo. Spectral characteristics of 3U 1915-05, a burst source candidate. *ApJL*, 216:L101–L104, September 1977. doi: 10.1086/182520.

K. Belczyński, J. Mikołajewska, U. Munari, R. J. Ivison, and M. Friedjung. A catalogue of symbiotic stars. *AAPS*, 146:407–435, November 2000. doi: 10.1051/aas:2000280.

F. Bernardini and E. M. Cackett. Characterizing the quiescent X-ray variability of the black hole low-mass X-ray binary V404 Cyg. *MNRAS*, 439:2771–2780, April 2014. doi: 10.1093/mnras/stu140.

J. K. Blackburn. FTOOLS: A FITS Data Processing and Analysis Software Package. In R. A. Shaw, H. E. Payne, and J. J. E. Hayes, editors, *Astronomical Data Analysis Software and Systems IV*, volume 77 of *Astronomical Society of the Pacific Conference Series*, page 367, 1995.

S. Bogdanov and J. P. Halpern. Identification of the High-energy Gamma-Ray Source 3FGL J1544.6-1125 as a Transitional Millisecond Pulsar Binary in an Accreting State. *ApJL*, 803:L27, April 2015. doi: 10.1088/2041-8205/803/2/L27.

S. Bogdanov, J. E. Grindlay, and M. van den Berg. An X-Ray Variable Millisecond Pulsar in the Globular Cluster 47 Tucanae: Closing the Link to Low-Mass X-Ray Binaries. *ApJ*, 630:1029–1036, September 2005. doi: 10.1086/432249.

S. Bogdanov, C. O. Heinke, F. Özel, and T. Güver. Neutron Star Mass-Radius Constraints of the Quiescent Low-mass X-ray Binaries X7 and X5 in the Globular Cluster 47 Tuc. *ArXiv e-prints*, March 2016. 1603.01630.

P. Bordas, E. Kuulkers, J. Alfonso-Garzón, V. Beckmann, T. Bird, S. B. J. Chenevez, T. Courvoisier, M. Del Santo, A. Domingo, K. Ebisawa, C. Ferrigno, P. Jonker, P. Kretschmar, C. Markwardt, T. Oosterbroek, A. Paizis,

K. Pottschmidt, C. Sánchez-Fernández, and R. Wijnands. A hard X-ray transient in the direction of Terzan 5 detected by INTEGRAL. *The Astronomer's Telegram*, 2919:1, October 2010.

E. Bozzo, C. Ferrigno, J. Stevens, T. M. Belloni, J. Rodriguez, P. R. den Hartog, A. Papitto, I. Kreykenbohm, F. Fontani, and L. Gibaud. IGR J17361-4441: a possible new accreting X-ray binary in NGC 6388. *A&A*, 535:L1, November 2011. doi: 10.1051/0004-6361/201118022.

E. Bozzo, P. Romano, C. Ferrigno, S. Campana, M. Falanga, G. Israel, R. Walter, and L. Stella. XMM-Newton and Swift observations of XTE J1743-363. *A&A*, 556:A30, August 2013. doi: 10.1051/0004-6361/201321248.

E. Bozzo, E. Kuulkers, and C. Ferrigno. Swift/XRT observations of the X-ray transient in NGC6440. *The Astronomer's Telegram*, 7106:1, February 2015.

M. A. Breddels, M. C. Smith, A. Helmi, O. Bienaymé, J. Binney, J. Bland-Hawthorn, C. Boeche, B. C. M. Burnett, R. Campbell, K. C. Freeman, B. Gibson, G. Gilmore, E. K. Grebel, U. Munari, J. F. Navarro, Q. A. Parker, G. M. Seabroke, A. Siebert, A. Siviero, M. Steinmetz, F. G. Watson, M. Williams, R. F. G. Wyse, and T. Zwitter. Distance determination for RAVE stars using stellar models. *A&A*, 511:A90, February 2010. doi: 10.1051/0004-6361/200912471.

E. F. Brown, L. Bildsten, and R. E. Rutledge. Crustal Heating and Quiescent Emission from Transiently Accreting Neutron Stars. *ApJL*, 504:L95, September 1998.

E. F. Brown, L. Bildsten, and P. Chang. Variability in the Thermal Emission from Accreting Neutron Star Transients. *ApJ*, 574:920–929, August 2002. doi: 10.1086/341066.

D. N. Burrows, J. E. Hill, J. A. Nousek, J. A. Kennea, A. Wells, J. P. Osborne,

A. F. Abbey, A. Beardmore, K. Mukerjee, A. D. T. Short, G. Chincarini, S. Campana, O. Citterio, A. Moretti, C. Pagani, G. Tagliaferri, P. Giommi, M. Capalbi, F. Tamburelli, L. Angelini, G. Cusumano, H. W. Bräuninger, W. Burkert, and G. D. Hartner. The Swift X-Ray Telescope. *SSR*, 120: 165–195, October 2005. doi: 10.1007/s11214-005-5097-2.

E. M. Cackett, R. Wijnands, C. O. Heinke, P. D. Edmonds, W. H. G. Lewin, D. Pooley, J. E. Grindlay, P. G. Jonker, and J. M. Miller. X-Ray Variability during the Quiescent State of the Neutron Star X-Ray Transient in the Globular Cluster NGC 6440. *ApJ*, 620:922–928, February 2005. doi: 10.1086/427178.

E. M. Cackett, R. Wijnands, C. O. Heinke, D. Pooley, W. H. G. Lewin, J. E. Grindlay, P. D. Edmonds, P. G. Jonker, and J. M. Miller. A Chandra X-ray observation of the globular cluster Terzan 1. *MNRAS*, 369:407–415, June 2006a. doi: 10.1111/j.1365-2966.2006.10315.x.

E. M. Cackett, R. Wijnands, M. Linares, J. M. Miller, J. Homan, and W. H. G. Lewin. Cooling of the quasi-persistent neutron star X-ray transients KS 1731-260 and MXB 1659-29. *MNRAS*, 372:479–488, October 2006b. doi: 10.1111/j.1365-2966.2006.10895.x.

E. M. Cackett, R. Wijnands, J. M. Miller, E. F. Brown, and N. Degenaar. Cooling of the Crust in the Neutron Star Low-Mass X-Ray Binary MXB 1659-29. *ApJL*, 687:L87–L90, November 2008. doi: 10.1086/593703.

E. M. Cackett, E. F. Brown, J. M. Miller, and R. Wijnands. Quiescent X-ray Emission From Cen X-4: A Variable Thermal Component. *ApJ*, 720: 1325–1332, September 2010. doi: 10.1088/0004-637X/720/2/1325.

E. M. Cackett, J. K. Fridriksson, J. Homan, J. M. Miller, and R. Wijnands. Quiescent X-ray variability from the neutron star transient Aql X-1. *MNRAS*, 414:3006–3013, July 2011. doi: 10.1111/j.1365-2966.2011.18601.x.

P. B. Cameron, R. E. Rutledge, F. Camilo, L. Bildsten, S. M. Ransom, and S. R. Kulkarni. Variability of 19 Millisecond Pulsars in 47 Tucanae with Chandra HRC-S. *ApJ*, 660:587–594, May 2007. doi: 10.1086/512229.

F. Camilo and F. A. Rasio. Pulsars in Globular Clusters. In F. A. Rasio & I. H. Stairs, editor, *Binary Radio Pulsars*, volume 328 of *ASP Conf. Ser.*, page 147, July 2005.

S. Campana and L. Stella. The Evolution of the High-Energy Tail in the Quiescent Spectrum of the Soft X-Ray Transient Aquila X-1. *ApJ*, 597: 474–478, November 2003. doi: 10.1086/378349.

S. Campana, S. Mereghetti, L. Stella, and M. Colpi. X-ray variability in the quiescent state of Centaurus X-4. *A&A*, 324:941–942, August 1997.

S. Campana, M. Colpi, S. Mereghetti, L. Stella, and M. Tavani. The neutron stars of Soft X-ray Transients. *A&A Rev.*, 8:279–316, 1998.

S. Campana, G. L. Israel, L. Stella, F. Gastaldello, and S. Mereghetti. The Variable Quiescence of Centaurus X-4. *ApJ*, 601:474–478, January 2004.

S. Campana, L. Stella, and J. A. Kennea. Swift Observations of SAX J1808.4-3658: Monitoring the Return to Quiescence. *ApJL*, 684:L99–L102, September 2008. doi: 10.1086/592002.

J. A. Cardelli, G. C. Clayton, and J. S. Mathis. The relationship between infrared, optical, and ultraviolet extinction. *ApJ*, 345:245–256, October 1989.

B. W. Carney. The Constancy of [alpha/Fe] in Globular Clusters of Differing [Fe/H] and Age. *PASP*, 108:900, October 1996.

W. Cash. Parameter estimation in astronomy through application of the likelihood ratio. *ApJ*, 228:939–947, March 1979. doi: 10.1086/156922.

A. Catuneanu, C. O. Heinke, G. R. Sivakoff, W. C. G. Ho, and M. Servillat. Mass/radius Constraints on the Quiescent Neutron Star in M13 Using Hydrogen and Helium Atmospheres. *ApJ*, 764:145, February 2013. doi: 10.1088/0004-637X/764/2/145.

Y. Cavecchi, A. Patruno, B. Haskell, A. L. Watts, Y. Levin, M. Linares, D. Altamirano, R. Wijnands, and M. van der Klis. Implications of Burst Oscillations from the Slowly Rotating Accreting Pulsar IGR J17480-2446 in the Globular Cluster Terzan 5. *ApJL*, 740:L8, October 2011. doi: 10.1088/2041-8205/740/1/L8.

D. Chakrabarty, J. A. Tomsick, B. W. Grefenstette, D. Psaltis, M. Bachetti, D. Barret, S. E. Boggs, F. E. Christensen, W. W. Craig, F. Fürst, C. J. Hailey, F. A. Harrison, V. M. Kaspi, J. M. Miller, M. A. Nowak, V. Rana, D. Stern, D. R. Wik, J. Wilms, and W. W. Zhang. A Hard X-Ray Power-law Spectral Cutoff in Centaurus X-4. *ApJ*, 797:92, December 2014. doi: 10.1088/0004-637X/797/2/92.

M. Chakraborty, S. Bhattacharyya, and A. Mukherjee. Terzan 5 transient IGR J17480-2446: variation of burst and spectral properties with spectral states. *MNRAS*, 418:490–499, November 2011. doi: 10.1111/j.1365-2966.2011.19499.x.

P. Chang and L. Bildsten. Evolution of Young Neutron Star Envelopes. *ApJ*, 605:830–839, April 2004. doi: 10.1086/382271.

P. Charles, W. Clarkson, R. Cornelisse, and C. Shih. Observational properties of accretion discs: Precessing and warped? *New A Rev.*, 51:768–774, May 2008. doi: 10.1016/j.newar.2008.03.025.

S. Chatterjee, S. Umbreit, J. M. Fregeau, and F. A. Rasio. Understanding the dynamical state of globular clusters: core-collapsed versus non-core-collapsed. *MNRAS*, 429:2881–2893, March 2013. doi: 10.1093/mnras/sts464.

J. Chenevez, E. Kuulkers, J. Alfonso-Garzon, V. Beckmann, T. Bird, S. Brandt, M. Del Santo, A. Domingo, K. Ebisawa, P. Jonker, P. Kretschmar, C. Mark-wardt, T. Oosterbroek, A. Paizis, K. Pottschmidt, C. Sanchez-Fernandez, and R. Wijnands. INTEGRAL Galactic Bulge monitoring detects activity from XMMU J174445.5-295044 with JEM-X. *The Astronomer's Telegram*, 4000, March 2012.

L. Chomiuk, J. Strader, T. J. Maccarone, J. C. A. Miller-Jones, C. Heinke, E. Noyola, A. C. Seth, and S. Ransom. A Radio-selected Black Hole X-Ray Binary Candidate in the Milky Way Globular Cluster M62. *ApJ*, 777:69, November 2013. doi: 10.1088/0004-637X/777/1/69.

G. W. Clark. X-ray binaries in globular clusters. *ApJL*, 199:L143–L145, August 1975.

M. Colpi, U. Geppert, D. Page, and A. Possenti. Charting the Temperature of the Hot Neutron Star in a Soft X-Ray Transient. *ApJL*, 548:L175–L178, February 2001.

F. Comerón, J. Torra, C. Chiappini, F. Figueras, V. D. Ivanov, and S. J. Ribas. A search for late-type supergiants in the inner regions of the Milky Way. *A&A*, 425:489–508, October 2004. doi: 10.1051/0004-6361:20040312.

S. Corbel, J. A. Tomsick, and P. Kaaret. On the Origin of Black Hole X-Ray Emission in Quiescence: Chandra Observations of XTE J1550-564 and H1743-322. *ApJ*, 636:971–978, January 2006. doi: 10.1086/498230.

S. Corbel, E. Koerding, and P. Kaaret. Revisiting the radio/X-ray flux correlation in the black hole V404 Cyg: from outburst to quiescence. *MNRAS*, 389:1697–1702, October 2008. doi: 10.1111/j.1365-2966.2008.13542.x.

R. Cornelisse, J. J. M. in't Zand, F. Verbunt, E. Kuulkers, J. Heise, P. R. den Hartog, M. Cocchi, L. Natalucci, A. Bazzano, and P. Ubertini. Six years of

BeppoSAX Wide Field Cameras observations of nine galactic type I X-ray bursters. *A&A*, 405:1033–1042, July 2003. doi: 10.1051/0004-6361:20030629.

K. R. Covey, Ž. Ivezić, D. Schlegel, D. Finkbeiner, N. Padmanabhan, R. H. Lupton, M. A. Agüeros, J. J. Bochanski, S. L. Hawley, A. A. West, A. Seth, A. Kimball, S. M. Gogarten, M. Claire, D. Haggard, N. Kaib, D. P. Schneider, and B. Sesar. Stellar SEDs from 0.3 to 2.5 μm: Tracing the Stellar Locus and Searching for Color Outliers in the SDSS and 2MASS. *AJ*, 134:2398–2417, December 2007. doi: 10.1086/522052.

A. Cumming. Models of Type I X-Ray Bursts from 4U 1820-30. *ApJ*, 595: 1077–1085, October 2003. doi: 10.1086/377446.

C. R. D'Angelo and H. C. Spruit. Episodic accretion on to strongly magnetic stars. *MNRAS*, 406:1208–1219, August 2010. doi: 10.1111/j.1365-2966.2010. 16749.x.

C. R. D'Angelo and H. C. Spruit. Accretion discs trapped near corotation. *MNRAS*, 420:416–429, February 2012. doi: 10.1111/j.1365-2966.2011.20046. x.

C. R. D'Angelo, J. K. Fridriksson, C. Messenger, and A. Patruno. The radiative efficiency of a radiatively inefficient accretion flow. *MNRAS*, 449:2803–2817, May 2015. doi: 10.1093/mnras/stv465.

F. D'Antona, P. Ventura, V. Caloi, A. D'Ercole, E. Vesperini, R. Carini, and M. Di Criscienzo. Terzan 5: An Alternative Interpretation for the Split Horizontal Branch. *ApJL*, 715:L63–L67, June 2010. doi: 10.1088/2041-8205/ 715/2/L63.

A. Davidsen, R. Malina, and S. Bowyer. The optical counterpart of GX 1 + 4 - A symbiotic star. *ApJ*, 211:866–871, February 1977. doi: 10.1086/154996.

D. de Martino, T. Belloni, M. Falanga, A. Papitto, S. Motta, A. Pellizzoni, Y. Evangelista, G. Piano, N. Masetti, J.-M. Bonnet-Bidaud, M. Mouchet, K. Mukai, and A. Possenti. X-ray follow-ups of XSS J12270-4859: a low-mass X-ray binary with gamma-ray Fermi-LAT association. *A&A*, 550:A89, February 2013. doi: 10.1051/0004-6361/201220393.

N. Degenaar and R. Wijnands. The soft quiescent spectrum of the transiently accreting 11-Hz X-ray pulsar in the globular cluster Terzan 5. *MNRAS*, 412: L68–L72, March 2011. doi: 10.1111/j.1745-3933.2011.01007.x.

N. Degenaar and R. Wijnands. Strong X-ray variability in the quiescent state of the neutron star low-mass X-ray binary EXO 1745-248. *MNRAS*, 422: 581–589, May 2012. doi: 10.1111/j.1365-2966.2012.20636.x.

N. Degenaar, E. F. Brown, and R. Wijnands. Evidence for crust cooling in the transiently accreting 11-Hz X-ray pulsar in the globular cluster Terzan 5. *MNRAS*, 418:L152–L156, November 2011a. doi: 10.1111/j.1745-3933.2011. 01164.x.

N. Degenaar, M. T. Wolff, P. S. Ray, K. S. Wood, J. Homan, W. H. G. Lewin, P. G. Jonker, E. M. Cackett, J. M. Miller, E. F. Brown, and R. Wijnands. Further X-ray observations of EXO 0748-676 in quiescence: evidence for a cooling neutron star crust. *MNRAS*, 412:1409–1418, April 2011b. doi: 10.1111/j.1365-2966.2010.17562.x.

N. Degenaar, R. Wijnands, E. F. Brown, D. Altamirano, E. M. Cackett, J. Fridriksson, J. Homan, C. O. Heinke, J. M. Miller, D. Pooley, and G. R. Sivakoff. Continued Neutron Star Crust Cooling of the 11 Hz X-Ray Pulsar in Terzan 5: A Challenge to Heating and Cooling Models? *ApJ*, 775:48, September 2013a. doi: 10.1088/0004-637X/775/1/48.

N. Degenaar, R. Wijnands, and J. M. Miller. A Direct Measurement of the Heat

Release in the Outer Crust of the Transiently Accreting Neutron Star XTE J1709-267. *ApJL*, 767:L31, April 2013b. doi: 10.1088/2041-8205/767/2/L31.

N. Degenaar, R. Wijnands, A. Bahramian, G. R. Sivakoff, C. O. Heinke, E. F. Brown, J. K. Fridriksson, J. Homan, E. M. Cackett, A. Cumming, J. M. Miller, D. Altamirano, and D. Pooley. Neutron star crust cooling in the Terzan 5 X-ray transient Swift J174805.3-244637. *MNRAS*, 451:2071–2081, August 2015. doi: 10.1093/mnras/stv1054.

B. Deufel, C. P. Dullemond, and H. C. Spruit. X-ray spectra from protons illuminating a neutron star. *A&A*, 377:955–963, October 2001.

E. W. Deutsch, B. Margon, and S. F. Anderson. Ultracompact X-Ray Binaries in Globular Clusters: Variability of the Optical Counterpart of X1832-330 in NGC 6652. *ApJL*, 530:L21–L24, February 2000.

A. Dieball, C. Knigge, D. R. Zurek, M. M. Shara, K. S. Long, P. A. Charles, D. C. Hannikainen, and L. van Zyl. An Ultracompact X-Ray Binary in the Globular Cluster M15 (NGC 7078). *ApJL*, 634:L105–L108, November 2005. doi: 10.1086/498712.

S. Djorgovski. Physical Parameters of Galactic Globular Clusters. In *ASP Conf. Ser. 50: Structure and Dynamics of Globular Clusters*, page 373, 1993.

S. Djorgovski and I. R. King. A preliminary survey of collapsed cores in globular clusters. *ApJL*, 305:L61–L65, June 1986. doi: 10.1086/184685.

C. Done, M. Gierliński, and A. Kubota. Modelling the behaviour of accretion flows in X-ray binaries. Everything you always wanted to know about accretion but were afraid to ask. *AAPR*, 15:1–66, December 2007. doi: 10.1007/s00159-007-0006-1.

A. Dotter, A. Sarajedini, and S.-C. Yang. Globular Clusters in the Outer

Galactic Halo: AM-1 and Palomar 14. *AJ*, 136:1407–1414, October 2008. doi: 10.1088/0004-6256/136/4/1407.

P. D. Edmonds, R. L. Gilliland, C. O. Heinke, and J. E. Grindlay. An Extensive Census of Hubble Space Telescope Counterparts to Chandra X-Ray Sources in the Globular Cluster 47 Tucanae. I. Astrometry and Photometry. *ApJ*, 596:1177–1196, October 2003a.

P. D. Edmonds, R. L. Gilliland, C. O. Heinke, and J. E. Grindlay. An Extensive Census of Hubble Space Telescope Counterparts to Chandra X-Ray Sources in the Globular Cluster 47 Tucanae. II. Time Series and Analysis. *ApJ*, 596: 1197–1219, October 2003b.

M. C. Engel, C. O. Heinke, G. R. Sivakoff, K. G. Elshamouty, and P. D. Edmonds. A 2.15 hr Orbital Period for the Low-mass X-Ray Binary XB 1832-330 in the Globular Cluster NGC 6652. *ApJ*, 747:119, March 2012. doi: 10.1088/0004-637X/747/2/119.

A. A. Esin, J. E. McClintock, and R. Narayan. Advection-dominated Accretion and the Spectral States of Black Hole X-Ray Binaries: Application to Nova MUSCAE 1991. *ApJ*, 489:865, November 1997. doi: 10.1086/304829.

A. C. Fabian, J. E. Pringle, and M. J. Rees. Tidal capture formation of binary systems and X-ray sources in globular clusters. *MNRAS*, 172:15P, August 1975.

R. P. Fender, E. Gallo, and P. G. Jonker. Jet-dominated states: an alternative to advection across black hole event horizons in 'quiescent' X-ray binaries. *MNRAS*, 343:L99–L103, August 2003. doi: 10.1046/j.1365-8711.2003.06950.x.

R. P. Fender, T. M. Belloni, and E. Gallo. Towards a unified model for black

hole X-ray binary jets. *MNRAS*, 355:1105–1118, December 2004. doi: 10. 1111/j.1365-2966.2004.08384.x.

R. P. Fender, D. M. Russell, C. Knigge, R. Soria, R. I. Hynes, and M. Goad. An anticorrelation between X-ray luminosity and Hα equivalent width in X-ray binaries. *MNRAS*, 393:1608–1616, March 2009. doi: 10.1111/j.1365-2966. 2008.14299.x.

F. R. Ferraro, E. Dalessandro, A. Mucciarelli, G. Beccari, R. M. Rich, L. Origlia, B. Lanzoni, R. T. Rood, E. Valenti, M. Bellazzini, S. M. Ransom, and G. Cocozza. The cluster Terzan 5 as a remnant of a primordial building block of the Galactic bulge. *Natur*, 462:483–486, November 2009. doi: 10.1038/nature08581.

D. Foight, T. Guver, F. Ozel, and P. Slane. Probing X-ray Absorption and Optical Extinction in the Interstellar Medium Using Chandra Observations of Supernova Remnants. *ArXiv e-prints*, April 2015. 1504.07274.

J. M. Fregeau. X-Ray Binaries and the Current Dynamical States of Galactic Globular Clusters. *ApJL*, 673:L25–L28, January 2008. doi: 10.1086/527375.

P. C. Freire, F. Camilo, M. Kramer, D. R. Lorimer, A. G. Lyne, R. N. Manchester, and N. D'Amico. Further results from the timing of the millisecond pulsars in 47 Tucanae. *MNRAS*, 340:1359–1374, April 2003.

P. C. C. Freire, A. A. Abdo, M. Ajello, A. Allafort, J. Ballet, G. Barbiellini, D. Bastieri, K. Bechtol, R. Bellazzini, R. D. Blandford, E. D. Bloom, E. Bonamente, A. W. Borgland, M. Brigida, P. Bruel, R. Buehler, S. Buson, G. Caliandro, R. Cameron, F. Camilo, P. A. Caraveo, C. Cecchi, Ö. Çelik, E. Charles, A. Chekhtman, C. C. Cheung, J. Chiang, S. Ciprini, R. Claus, I. Cognard, J. Cohen-Tanugi, L. R. Cominsky, F. de Palma, C. D. Dermer, E. do Couto e Silva, M. Dormody, P. S. Drell, R. Dubois, D. Dumora, C. M. Espinoza, C. Favuzzi, S. J. Fegan, E. C. Ferrara, W. B. Focke, P. Fortin,

Y. Fukazawa, P. Fusco, F. Gargano, D. Gasparrini, N. Gehrels, S. Germani, N. Giglietto, F. Giordano, M. Giroletti, T. Glanzman, G. Godfrey, I. A. Grenier, M.-H. Grondin, J. E. Grove, L. Guillemot, S. Guiriec, D. Hadasch, A. K. Harding, G. Jóhannesson, A. S. Johnson, T. J. Johnson, S. Johnston, H. Katagiri, J. Kataoka, M. Keith, M. Kerr, J. Knödlseder, M. Kramer, M. Kuss, J. Lande, L. Latronico, S.-H. Lee, M. Lemoine-Goumard, F. Longo, F. Loparco, M. N. Lovellette, P. Lubrano, A. G. Lyne, R. N. Manchester, M. Marelli, M. N. Mazziotta, J. E. McEnery, P. F. Michelson, T. Mizuno, A. A. Moiseev, C. Monte, M. E. Monzani, A. Morselli, I. V. Moskalenko, S. Murgia, T. Nakamori, P. L. Nolan, J. P. Norris, E. Nuss, T. Ohsugi, A. Okumura, N. Omodei, E. Orlando, M. Ozaki, D. Paneque, D. Parent, M. Pesce-Rollins, M. Pierbattista, F. Piron, T. A. Porter, S. Rainò, S. M. Ransom, P. S. Ray, A. Reimer, O. Reimer, T. Reposeur, S. Ritz, R. W. Romani, M. Roth, H. F.-W. Sadrozinski, P. M. S. Saz Parkinson, C., R. Shannon, E. J. S. Siskind, D. A., P. D. Smith, P. Spinelli, B. W. Stappers, D. J. Suson, H. Takahashi, T. Tanaka, T. M. Tauris, J. B. Thayer, G. Theureau, D. J. Thompson, S. E. Thorsett, L. Tibaldo, D. F. Torres, G. Tosti, E. Troja, J. Vandenbroucke, A. Van Etten, V. Vasileiou, C. Venter, G. Vianello, N. Vilchez, V. Vitale, A. P. Waite, P. Wang, K. S. Wood, Z. Yang, M. Ziegler, and S. Zimmer. Fermi Detection of a Luminous γ-Ray Pulsar in a Globular Cluster. *Science*, 334:1107, November 2011. doi: 10.1126/science.1207141.

J. K. Fridriksson, J. Homan, R. Wijnands, M. Méndez, D. Altamirano, E. M. Cackett, E. F. Brown, T. M. Belloni, N. Degenaar, and W. H. G. Lewin. Rapid Cooling of the Neutron Star in the Quiescent Super-Eddington Transient XTE J1701-462. *ApJ*, 714:270–286, May 2010. doi: 10.1088/0004-637X/714/1/270.

J. K. Fridriksson, J. Homan, R. Wijnands, E. M. Cackett, D. Altamirano,

N. Degenaar, E. F. Brown, M. Méndez, and T. M. Belloni. The Variable Quiescent X-Ray Emission of the Transient Neutron Star XTE J1701-462. *ApJ*, 736:162, August 2011. doi: 10.1088/0004-637X/736/2/162.

A. S. Fruchter and W. M. Goss. Deep Radio Imaging of Globular Clusters and the Cluster Pulsar Population. *ApJ*, 536:865–874, June 2000.

A. Fruscione, J. C. McDowell, G. E. Allen, N. S. Brickhouse, D. J. Burke, J. E. Davis, N. Durham, M. Elvis, E. C. Galle, D. E. Harris, D. P. Huenemoerder, J. C. Houck, B. Ishibashi, M. Karovska, F. Nicastro, M. S. Noble, M. A. Nowak, F. A. Primini, A. Siemiginowska, R. K. Smith, and M. Wise. CIAO: Chandra's data analysis system. In *Society of Photo-Optical Instrumentation Engineers (SPIE) Conference Series*, volume 6270, page 62701V, June 2006. doi: 10.1117/12.671760.

M. Y. Fujimoto, T. Hanawa, and S. Miyaji. Shell flashes on accreting neutron stars and X-ray bursts. *ApJ*, 247:267–278, July 1981. doi: 10.1086/159034.

E. Gallo, R. P. Fender, and G. G. Pooley. A universal radio-X-ray correlation in low/hard state black hole binaries. *MNRAS*, 344:60–72, September 2003. doi: 10.1046/j.1365-8711.2003.06791.x.

D. K. Galloway, M. P. Muno, J. M. Hartman, D. Psaltis, and D. Chakrabarty. Thermonuclear (Type I) X-Ray Bursts Observed by the Rossi X-Ray Timing Explorer. *ApJ Supp*, 179:360–422, December 2008. doi: 10.1086/592044.

J. García and T. R. Kallman. X-ray Reflected Spectra from Accretion Disk Models. I. Constant Density Atmospheres. *ApJ*, 718:695–706, August 2010. doi: 10.1088/0004-637X/718/2/695.

J. García, T. R. Kallman, and R. F. Mushotzky. X-ray Reflected Spectra from Accretion Disk Models. II. Diagnostic Tools for X-ray Observations. *ApJ*, 731:131, April 2011. doi: 10.1088/0004-637X/731/2/131.

J. García, T. Dauser, C. S. Reynolds, T. R. Kallman, J. E. McClintock, J. Wilms, and W. Eikmann. X-Ray Reflected Spectra from Accretion Disk Models. III. A Complete Grid of Ionized Reflection Calculations. *ApJ*, 768: 146, May 2013. doi: 10.1088/0004-637X/768/2/146.

E. Gardner and C. Done. Jets and the accretion flow in low-luminosity black holes. *MNRAS*, 434:3454–3462, October 2013. doi: 10.1093/mnras/stt1257.

K. Gebhardt, D. Richstone, E. A. Ajhar, T. R. Lauer, Y.-I. Byun, J. Kormendy, A. Dressler, S. M. Faber, C. Grillmair, and S. Tremaine. The Centers of Early-Type Galaxies With HST. III. Non-Parametric Recovery of Stellar Luminosity Distribution. *AJ*, 112:105, July 1996. doi: 10.1086/117992.

N. Gehrels. Confidence limits for small numbers of events in astrophysical data. *ApJ*, 303:336–346, April 1986.

N. Gehrels, G. Chincarini, P. Giommi, K. O. Mason, J. A. Nousek, A. A. Wells, N. E. White, S. D. Barthelmy, D. N. Burrows, L. R. Cominsky, K. C. Hurley, F. E. Marshall, P. Mészáros, P. W. A. Roming, L. Angelini, L. M. Barbier, T. Belloni, S. Campana, P. A. Caraveo, M. M. Chester, O. Citterio, T. L. Cline, M. S. Cropper, J. R. Cummings, A. J. Dean, E. D. Feigelson, E. E. Fenimore, D. A. Frail, A. S. Fruchter, G. P. Garmire, K. Gendreau, G. Ghisellini, J. Greiner, J. E. Hill, S. D. Hunsberger, H. A. Krimm, S. R. Kulkarni, P. Kumar, F. Lebrun, N. M. Lloyd-Ronning, C. B. Markwardt, B. J. Mattson, R. F. Mushotzky, J. P. Norris, J. Osborne, B. Paczynski, D. M. Palmer, H.-S. Park, A. M. Parsons, J. Paul, M. J. Rees, C. S. Reynolds, J. E. Rhoads, T. P. Sasseen, B. E. Schaefer, A. T. Short, A. P. Smale, I. A. Smith, L. Stella, G. Tagliaferri, T. Takahashi, M. Tashiro, L. K. Townsley, J. Tueller, M. J. L. Turner, M. Vietri, W. Voges, M. J. Ward, R. Willingale, F. M. Zerbi, and W. W. Zhang. The Swift Gamma-Ray Burst Mission. *ApJ*, 611:1005–1020, August 2004. doi: 10.1086/422091.

M. Gierliński and C. Done. The X-ray spectrum of the atoll source 4U 1608-52. *MNRAS*, 337:1373–1380, December 2002. doi: 10.1046/j.1365-8711.2002.06009.x.

M. Gierliński, A. A. Zdziarski, J. Poutanen, P. S. Coppi, K. Ebisawa, and W. N. Johnson. Radiation mechanisms and geometry of Cygnus X-1 in the soft state. *MNRAS*, 309:496–512, October 1999. doi: 10.1046/j.1365-8711.1999.02875.x.

M. Gilfanov, M. Revnivtsev, R. Sunyaev, and E. Churazov. The millisecond X-ray pulsar/burster SAX J1808.4-3658: the outburst light curve and the power law spectrum. *A&A*, 338:L83–L86, October 1998.

M. Gilfanov, M. Revnivtsev, and S. Molkov. Boundary layer, accretion disk and X-ray variability in the luminous LMXBs. *A&A*, 410:217–230, October 2003. doi: 10.1051/0004-6361:20031141.

J. Gladstone, C. Done, and M. Gierliński. Analysing the atolls: X-ray spectral transitions of accreting neutron stars. *MNRAS*, 378:13–22, June 2007. doi: 10.1111/j.1365-2966.2007.11675.x.

O. Y. Gnedin, H. Zhao, J. E. Pringle, S. M. Fall, M. Livio, and G. Meylan. The Unique History of the Globular Cluster ω Centauri. *ApJL*, 568:L23–L26, March 2002. doi: 10.1086/340319.

J. E. Grindlay, P. Hertz, J. E. Steiner, S. S. Murray, and A. P. Lightman. Determination of the mass of globular cluster X-ray sources. *ApJL*, 282: L13–L16, July 1984.

J. E. Grindlay, C. Heinke, P. D. Edmonds, and S. S. Murray. High-Resolution X-ray Imaging of a Globular Cluster Core: Compact Binaries in 47Tuc. *Science*, 292:2290–2295, June 2001.

M. Guainazzi, A. N. Parmar, and T. Oosterbroek. An anomalous low-state from the globular cluster X-ray source X 1732-304 (Terzan 1). *A&A*, 349: 819–824, September 1999.

S. Guillot and R. E. Rutledge. Rejecting Proposed Dense Matter Equations of State with Quiescent Low-mass X-Ray Binaries. *ApJL*, 796:L3, November 2014. doi: 10.1088/2041-8205/796/1/L3.

S. Guillot, R. E. Rutledge, and E. F. Brown. Neutron Star Radius Measurement with the Quiescent Low-mass X-ray Binary U24 in NGC 6397. *ApJ*, 732:88, May 2011. doi: 10.1088/0004-637X/732/2/88.

S. Guillot, M. Servillat, N. A. Webb, and R. E. Rutledge. Measurement of the Radius of Neutron Stars with High Signal-to-noise Quiescent Low-mass X-Ray Binaries in Globular Clusters. *ApJ*, 772:7, July 2013. doi: 10.1088/ 0004-637X/772/1/7.

T. Güver and F. Özel. The relation between optical extinction and hydrogen column density in the Galaxy. *MNRAS*, 400:2050–2053, December 2009. doi: 10.1111/j.1365-2966.2009.15598.x.

H. J. Habing. Circumstellar envelopes and Asymptotic Giant Branch stars. *AAPR*, 7:97–207, 1996. doi: 10.1007/PL00013287.

D. Haggard, A. M. Cool, J. Anderson, P. D. Edmonds, P. J. Callanan, C. O. Heinke, J. E. Grindlay, and C. D. Bailyn. Hubble Space Telescope Advanced Camera for Surveys Imaging of ω Centauri: Optical Counterpart for the Quiescent Low-Mass X-Ray Binary. *ApJ*, 613:512–516, September 2004. doi: 10.1086/421549.

W. E. Harris. A Catalog of Parameters for Globular Clusters in the Milky Way. *AJ*, 112:1487, October 1996.

F. A. Harrison, W. W. Craig, F. E. Christensen, C. J. Hailey, W. W. Zhang, S. E. Boggs, D. Stern, W. R. Cook, K. Forster, P. Giommi, B. W. Grefenstette, Y. Kim, T. Kitaguchi, J. E. Koglin, K. K. Madsen, P. H. Mao, H. Miyasaka, K. Mori, M. Perri, M. J. Pivovaroff, S. Puccetti, V. R. Rana, N. J. Westergaard, J. Willis, A. Zoglauer, H. An, M. Bachetti, N. M. Barrière, E. C. Bellm, V. Bhalerao, N. F. Brejnholt, F. Fuerst, C. C. Liebe, C. B. Markwardt, M. Nynka, J. K. Vogel, D. J. Walton, D. R. Wik, D. M. Alexander, L. R. Cominsky, A. E. Hornschemeier, A. Hornstrup, V. M. Kaspi, G. M. Madejski, G. Matt, S. Molendi, D. M. Smith, J. A. Tomsick, M. Ajello, D. R. Ballantyne, M. Baloković, D. Barret, F. E. Bauer, R. D. Blandford, W. N. Brandt, L. W. Brenneman, J. Chiang, D. Chakrabarty, J. Chenevez, A. Comastri, F. Dufour, M. Elvis, A. C. Fabian, D. Farrah, C. L. Fryer, E. V. Gotthelf, J. E. Grindlay, D. J. Helfand, R. Krivonos, D. L. Meier, J. M. Miller, L. Natalucci, P. Ogle, E. O. Ofek, A. Ptak, S. P. Reynolds, J. R. Rigby, G. Tagliaferri, S. E. Thorsett, E. Treister, and C. M. Urry. The Nuclear Spectroscopic Telescope Array (NuSTAR) High-energy X-Ray Mission. *ApJ*, 770:103, June 2013. doi: 10.1088/0004-637X/770/2/103.

G. Hasinger and M. van der Klis. Two patterns of correlated X-ray timing and spectral behaviour in low-mass X-ray binaries. *A&A*, 225:79–96, November 1989.

C. O. Heinke, P. D. Edmonds, J. E. Grindlay, D. A. Lloyd, H. N. Cohn, and P. M. Lugger. A Chandra X-Ray Study of the Dense Globular Cluster Terzan 5. *ApJ*, 590:809–821, June 2003a.

C. O. Heinke, J. E. Grindlay, P. D. Edmonds, D. A. Lloyd, S. S. Murray, H. N. Cohn, and P. M. Lugger. A Chandra X-ray Study of the Globular Cluster M80. *ApJ*, 598:516–526, November 2003b.

C. O. Heinke, J. E. Grindlay, D. A. Lloyd, and P. D. Edmonds. X-Ray Studies

of Two Neutron Stars in 47 Tucanae: Toward Constraints on the Equation of State. *ApJ*, 588:452–463, May 2003c.

C. O. Heinke, J. E. Grindlay, P. M. Lugger, H. N. Cohn, P. D. Edmonds, D. A. Lloyd, and A. M. Cool. Analysis of the Quiescent Low-Mass X-ray Binary Population in Galactic Globular Clusters. *ApJ*, 598:501–515, November 2003d.

C. O. Heinke, J. E. Grindlay, and P. D. Edmonds. Three Additional Quiescent Low-Mass X-Ray Binary Candidates in 47 Tucanae. *ApJ*, 622:556–564, March 2005a. doi: 10.1086/427795.

C. O. Heinke, J. E. Grindlay, P. D. Edmonds, H. N. Cohn, P. M. Lugger, F. Camilo, S. Bogdanov, and P. C. Freire. A Deep Chandra Survey of the Globular Cluster 47 Tucanae: Catalog of Point Sources. *ApJ*, 625:796–824, June 2005b. doi: 10.1086/429899.

C. O. Heinke, G. B. Rybicki, R. Narayan, and J. E. Grindlay. A Hydrogen Atmosphere Spectral Model Applied to the Neutron Star X7 in the Globular Cluster 47 Tucanae. *ApJ*, 644:1090–1103, June 2006a. doi: 10.1086/503701.

C. O. Heinke, R. Wijnands, H. N. Cohn, P. M. Lugger, J. E. Grindlay, D. Pooley, and W. H. G. Lewin. Faint X-Ray Sources in the Globular Cluster Terzan 5. *ApJ*, 651:1098–1111, November 2006b. doi: 10.1086/507884.

C. O. Heinke, H. N. Cohn, and P. M. Lugger. The Discovery of a Very Faint X-Ray Transient in the Globular Cluster M15. *ApJ*, 692:584–593, February 2009a. doi: 10.1088/0004-637X/692/1/584.

C. O. Heinke, P. G. Jonker, R. Wijnands, C. J. Deloye, and R. E. Taam. Further Constraints on Thermal Quiescent X-Ray Emission from SAX J1808.4-3658. *ApJ*, 691:1035–1041, February 2009b. doi: 10.1088/0004-637X/691/2/1035.

190

C. O. Heinke, J. A. Tomsick, F. Yusef-Zadeh, and J. E. Grindlay. Two Rapidly Variable Galactic X-ray Transients Observed with Chandra, XMM-Newton, and Suzaku. *ApJ*, 701:1627–1635, August 2009c. doi: 10.1088/0004-637X/701/2/1627.

C. O. Heinke, D. Altamirano, H. N. Cohn, P. M. Lugger, S. A. Budac, M. Servillat, M. Linares, T. E. Strohmayer, C. B. Markwardt, R. Wijnands, J. H. Swank, C. Knigge, C. Bailyn, and J. E. Grindlay. Discovery of a Second Transient Low-Mass X-ray Binary in the Globular Cluster NGC 6440. *ApJ*, 714:894–903, May 2010. doi: 10.1088/0004-637X/714/1/894.

C. O. Heinke, R. Wijnands, D. Altamirano, D. Pooley, and G. R. Sivakoff. Brightening and hardening of new X-ray transient in globular cluster Terzan 5. *The Astronomer's Telegram*, 4249:1, July 2012.

C. O. Heinke, N. Ivanova, M. C. Engel, K. Pavlovskii, G. R. Sivakoff, T. F. Cartwright, and J. C. Gladstone. Galactic Ultracompact X-Ray Binaries: Disk Stability and Evolution. *ApJ*, 768:184, May 2013. doi: 10.1088/0004-637X/768/2/184.

C. O. Heinke, H. N. Cohn, P. M. Lugger, N. A. Webb, W. C. G. Ho, J. Anderson, S. Campana, S. Bogdanov, D. Haggard, A. M. Cool, and J. E. Grindlay. Improved mass and radius constraints for quiescent neutron stars in ω Cen and NGC 6397. *MNRAS*, 444:443–456, October 2014. doi: 10.1093/mnras/stu1449.

B. Hendricks, P. B. Stetson, D. A. VandenBerg, and M. Dall'Ora. A New Reddening Law for M4. *AJ*, 144:25, July 2012. doi: 10.1088/0004-6256/144/1/25.

P. Hertz and J. E. Grindlay. An X-ray survey of globular clusters and their X-ray luminosity function. *ApJ*, 275:105–119, December 1983.

J. W. T. Hessels, S. M. Ransom, I. H. Stairs, P. C. C. Freire, V. M. Kaspi, and F. Camilo. A Radio Pulsar Spinning at 716 Hz. *Science, in press; astro-ph/0601337*, January 2006.

J. W. T. Hessels, S. M. Ransom, I. H. Stairs, V. M. Kaspi, and P. C. C. Freire. A 1.4 GHz Arecibo Survey for Pulsars in Globular Clusters. *ApJ*, 670:363–378, November 2007. doi: 10.1086/521780.

J. G. Hills. The formation of binaries containing black holes by the exchange of companions and the X-ray sources in globular clusters. *MNRAS*, 175:1P–4P, April 1976.

W. C. G. Ho and C. O. Heinke. A neutron star with a carbon atmosphere in the Cassiopeia A supernova remnant. *Natur*, 462:71–73, November 2009. doi: 10.1038/nature08525.

J. Homan and D. Pooley. Chandra Identification of the 2012 Transient in Terzan 5. *The Astronomer's Telegram*, 4302:1, August 2012.

J. Homan, J. K. Fridriksson, R. Wijnands, E. M. Cackett, N. Degenaar, M. Linares, D. Lin, and R. A. Remillard. A Strongly Heated Neutron Star in the Transient Z Source MAXI J0556-332. *ApJ*, 795:131, November 2014. doi: 10.1088/0004-637X/795/2/131.

J. Homan, D. Pooley, and C. Heinke. Chandra identification of the current X-ray transient in NGC 6440. *The Astronomer's Telegram*, 7183:1, March 2015.

L. Homer, P. A. Charles, T. Naylor, J. van Paradijs, M. Auriere, and L. Koch-Miramond. Periodic UV modulation of X1850-087: a double degenerate binary in the globular cluster NGC 6712? *MNRAS*, 282:L37–L46, October 1996.

C. Y. Hui, K. S. Cheng, and R. E. Taam. Dynamical Formation of Millisecond Pulsars in Globular Clusters. *ApJ*, 714:1149–1154, May 2010. doi: 10.1088/ 0004-637X/714/2/1149.

C. Y. Hui, K. S. Cheng, Y. Wang, P. H. T. Tam, A. K. H. Kong, D. O. Chernyshov, and V. A. Dogiel. The Fundamental Plane of Gamma-ray Globular Clusters. *ApJ*, 726:100, January 2011. doi: 10.1088/0004-637X/726/2/ 100.

J. R. Hurley and M. M. Shara. A direct N-body model of core-collapse and core oscillations. *MNRAS*, 425:2872–2879, October 2012. doi: 10.1111/j. 1365-2966.2012.21668.x.

R. I. Hynes, M. A. P. Torres, C. O. Heinke, T. J. Maccarone, V. J. Mikles, C. T. Britt, C. Knigge, S. Greiss, P. G. Jonker, D. Steeghs, G. Nelemans, R. M. Bandyopadhyay, and C. B. Johnson. CXOGBS J173620.2-293338: A Candidate Symbiotic X-Ray Binary Associated with a Bulge Carbon Star. *ApJ*, 780:11, January 2014. doi: 10.1088/0004-637X/780/1/11.

A. F. Illarionov and R. A. Sunyaev. Why the Number of Galactic X-ray Stars Is so Small? *A&A*, 39:185, February 1975.

S. A. Ilovaisky, M. Auriere, L. Koch-Miramond, C. Chevalier, J.-P. Cordoni, and R. A. Crowe. The 17.1-h optical and X-ray orbital period of AC 211/X 2127 + 119 in M15. *A&A*, 270:139–150, March 1993.

R. Indebetouw, J. S. Mathis, B. L. Babler, M. R. Meade, C. Watson, B. A. Whitney, M. J. Wolff, M. G. Wolfire, M. Cohen, T. M. Bania, R. A. Benjamin, D. P. Clemens, J. M. Dickey, J. M. Jackson, H. A. Kobulnicky, A. P. Marston, E. P. Mercer, J. R. Stauffer, S. R. Stolovy, and E. Churchwell. The Wavelength Dependence of Interstellar Extinction from 1.25 to 8.0 μm Using GLIMPSE Data. *ApJ*, 619:931–938, February 2005. doi: 10.1086/426679.

J. J. M. in't Zand, F. Verbunt, T. E. Strohmayer, A. Bazzano, M. Cocchi, J. Heise, M. H. van Kerkwijk, J. M. Muller, L. Natalucci, M. J. S. Smith, and P. Ubertini. A new X-ray outburst in the globular cluster NGC 6440: SAX J1748.9-2021. *A&A*, 345:100–108, May 1999.

J. J. M. in't Zand, M. H. van Kerkwijk, D. Pooley, F. Verbunt, R. Wijnands, and W. H. G. Lewin. Identification of the Optical and Quiescent Counterparts to the Bright X-Ray Transient in NGC 6440. *ApJL*, 563:L41–L44, December 2001.

J. J. M. in't Zand, F. Hulleman, C. B. Markwardt, M. Méndez, E. Kuulkers, R. Cornelisse, J. Heise, T. E. Strohmayer, and F. Verbunt. Bursts, eclipses, dips and a refined position for the luminous low-mass X-ray binary in the globular cluster Terzan 6. *A&A*, 406:233–243, July 2003. doi: 10.1051/0004-6361:20030681.

J. J. M. in't Zand, A. Cumming, M. V. van der Sluys, F. Verbunt, and O. R. Pols. On the possibility of a helium white dwarf donor in the presumed ultracompact binary 2S 0918-549. *A&A*, 441:675–684, October 2005. doi: 10.1051/0004-6361:20053002.

J. J. M. in't Zand, P. G. Jonker, and C. B. Markwardt. Six new candidate ultracompact X-ray binaries. *A&A*, 465:953–963, April 2007. doi: 10.1051/0004-6361:20066678.

N. Isobe, T. Mihara, M. Kohama, M. Suzuki, M. Matsuoka, S. Ueno, H. Tomida, N. Kawai, J. Kataoka, A. Yoshida, K. Yamaoka, H. Tsunemi, E. Miyata, H. Negoro, M. Nakajima, and M. Morii. High sensitivity all sky X-ray monitor and survey with MAXI. In S. Ritz, P. Michelson, and C. A. Meegan, editors, *The First GLAST Symposium*, volume 921 of *American Institute of Physics Conference Series*, pages 440–441, July 2007. doi: 10.1063/1.2757391.

V. D. Ivanov, M. J. Rieke, C. W. Engelbracht, A. Alonso-Herrero, G. H. Rieke, and K. L. Luhman. A Medium-Resolution Near-Infrared Spectral Library of Late-Type Stars. I. *ApJ Supp*, 151:387–397, April 2004. doi: 10.1086/381752.

N. Ivanova, C. O. Heinke, F. A. Rasio, K. Belczynski, and J. M. Fregeau. Formation and evolution of compact binaries in globular clusters - II. Binaries with neutron stars. *MNRAS*, 386:553–576, May 2008. doi: 10.1111/j.1365-2966.2008.13064.x.

Ž. Ivezić, A.J. Connolly, J.T. Vanderplas, and A. Gray. *Statistics, Data Mining and Machine Learning in Astronomy.* Princeton University Press, 2014.

H. M. Johnston, S. R. Kulkarni, and E. S. Phinney. X-Ray binaries and recycled pulsars. In *'X-Ray binaries and the formation of binary and millisecond radio pulsars', Dordrecht: Kluwer, 1992, ed. Van Den Heuvel, E. P. J.; Rappaport, S. A.*, pages 349–364, 1992.

P. G. Jonker, M. Méndez, G. Nelemans, R. Wijnands, and M. van der Klis. Chandra observations of the neutron star soft X-ray transient RX J170930.2 - 263927 returning to quiescence. *MNRAS*, 341:823–831, May 2003. doi: 10.1046/j.1365-8711.2003.06450.x.

P. G. Jonker, D. K. Galloway, J. E. McClintock, M. Buxton, M. Garcia, and S. Murray. Optical and X-ray observations of the neutron star soft X-ray transient XTE J1709-267. *MNRAS*, 354:666–674, November 2004a.

P. G. Jonker, R. Wijnands, and M. van der Klis. The faint neutron star soft X-ray transient SAX J1810.8-2609 in quiescence. *MNRAS*, 349:94–98, March 2004b.

A. Jordán, P. Côté, L. Ferrarese, J. P. Blakeslee, S. Mei, D. Merritt, M. Milosavljević, E. W. Peng, J. L. Tonry, and M. J. West. The ACS Virgo Cluster Survey. III. Chandra and Hubble Space Telescope Observations of

Low-Mass X-Ray Binaries and Globular Clusters in M87. *ApJ*, 613:279–301, September 2004. doi: 10.1086/422545.

A. Jordán, G. R. Sivakoff, D. E. McLaughlin, J. P. Blakeslee, D. A. Evans, R. P. Kraft, M. J. Hardcastle, E. W. Peng, P. Côté, J. H. Croston, A. M. Juett, D. Minniti, S. Raychaudhury, C. L. Sarazin, D. M. Worrall, W. E. Harris, K. A. Woodley, M. Birkinshaw, N. J. Brassington, W. R. Forman, C. Jones, and S. S. Murray. Low-Mass X-Ray Binaries and Globular Clusters in Centaurus A. *ApJL*, 671:L117–L120, December 2007. doi: 10.1086/525524.

T. Kallman and M. Bautista. Photoionization and High-Density Gas. *ApJ Supp*, 133:221–253, March 2001. doi: 10.1086/319184.

D. L. Kaplan, A. M. Levine, D. Chakrabarty, E. H. Morgan, D. K. Erb, B. M. Gaensler, D.-S. Moon, and P. B. Cameron. Lost and Found: A New Position and Infrared Counterpart for the X-Ray Binary Scutum X-1. *ApJ*, 661: 437–446, May 2007. doi: 10.1086/513712.

J. I. Katz. Two kinds of stellar collapse. *Natur*, 253:698, February 1975.

S. J. Kenyon. *The symbiotic stars.* 1986.

B. Kimmig, A. Seth, I. I. Ivans, J. Strader, N. Caldwell, T. Anderton, and D. Gregersen. Measuring Consistent Masses for 25 Milky Way Globular Clusters. *AJ*, 149:53, February 2015. doi: 10.1088/0004-6256/149/2/53.

I. King. The structure of star clusters. I. an empirical density law. *AJ*, 67:471, October 1962. doi: 10.1086/108756.

I. R. King. The structure of star clusters. III. Some simple dynamical models. *AJ*, 71:64, February 1966.

S. G. Kleinmann and D. N. B. Hall. Spectra of late-type standard stars in the region 2.0-2.5 microns. *ApJ Supp*, 62:501–517, November 1986. doi: 10.1086/191149.

C. Knigge, D. R. Zurek, M. M. Shara, K. S. Long, and R. L. Gilliland. A Far-Ultraviolet Survey of 47 Tucanae. II. The Long-Period Cataclysmic Variable AKO 9. *ApJ*, 599:1320–1332, December 2003.

C. Knigge, A. Dieball, J. Maíz Apellániz, K. S. Long, D. R. Zurek, and M. M. Shara. Stellar Exotica in 47 Tucanae. *ApJ*, 683:1006–1030, August 2008. doi: 10.1086/589987.

F. Koliopanos, M. Gilfanov, and L. Bildsten. X-ray diagnostics of chemical composition of the accretion disc and donor star in ultra-compact X-ray binaries. *MNRAS*, 432:1264–1273, June 2013. doi: 10.1093/mnras/stt542.

A. K. H. Kong, C. Y. Hui, and K. S. Cheng. Fermi Discovery of Gamma-ray Emission from the Globular Cluster Terzan 5. *ApJL*, 712:L36–L39, March 2010. doi: 10.1088/2041-8205/712/1/L36.

A. Kramida, Yu. Ralchenko, J. Reader, and and NIST ASD Team. NIST Atomic Spectra Database (ver. 5.1), [Online]. Available: `http://physics.nist.gov/asd` [2014, January 26]. National Institute of Standards and Technology, Gaithersburg, MD., 2013.

H. A. Krimm, S. T. Holland, R. H. D. Corbet, A. B. Pearlman, P. Romano, J. A. Kennea, J. S. Bloom, S. D. Barthelmy, W. H. Baumgartner, J. R. Cummings, N. Gehrels, A. Y. Lien, C. B. Markwardt, D. M. Palmer, T. Sakamoto, M. Stamatikos, and T. N. Ukwatta. The Swift/BAT Hard X-Ray Transient Monitor. *ApJ Supp*, 209:14, November 2013. doi: 10.1088/0067-0049/209/1/14.

R. Krivonos, A. Lutovinov, S. Molkov, M. Revnivtsev, S. Tsygankov, and R. Sunyaev. INTEGRAL/IBIS detects a new hard X-ray transient IGR J17446-2948 in the Galactic Center region. *The Astronomer's Telegram*, 4924:1, March 2013.

197

A. K. Kulkarni and M. M. Romanova. Accretion to magnetized stars through the Rayleigh-Taylor instability: global 3D simulations. *MNRAS*, 386:673–687, May 2008. doi: 10.1111/j.1365-2966.2008.13094.x.

S. R. Kulkarni, P. Hut, and S. McMillan. Stellar black holes in globular clusters. *Natur*, 364:421–423, July 1993. doi: 10.1038/364421a0.

E. Kuulkers, S. E. Shaw, A. Paizis, J. Chenevez, S. Brandt, T. J.-L. Courvoisier, A. Domingo, K. Ebisawa, P. Kretschmar, C. B. Markwardt, N. Mowlavi, T. Oosterbroek, A. Orr, D. Rísquez, C. Sanchez-Fernandez, and R. Wijnands. The INTEGRAL Galactic bulge monitoring program: the first 1.5 years. *A&A*, 466:595–618, May 2007. doi: 10.1051/0004-6361:20066651.

B. Lanzoni, F. R. Ferraro, E. Dalessandro, A. Mucciarelli, G. Beccari, P. Miocchi, M. Bellazzini, R. M. Rich, L. Origlia, E. Valenti, R. T. Rood, and S. M. Ransom. New Density Profile and Structural Parameters of the Complex Stellar System Terzan 5. *ApJ*, 717:653–657, July 2010. doi: 10.1088/0004-637X/717/2/653.

J.-P. Lasota. The disc instability model of dwarf novae and low-mass X-ray binary transients. *New A Rev.*, 45:449–508, June 2001. doi: 10.1016/S1387-6473(01)00112-9.

J. M. Lattimer and A. W. Steiner. Neutron Star Masses and Radii from Quiescent Low-mass X-Ray Binaries. *ApJ*, 784:123, April 2014. doi: 10.1088/0004-637X/784/2/123.

W. H. G. Lewin, J. van Paradijs, and R. E. Taam. X-Ray Bursts. *SSR*, 62:223–389, September 1993. doi: 10.1007/BF00196124.

D. Lin, R. A. Remillard, and J. Homan. Evaluating Spectral Models and the X-Ray States of Neutron Star X-Ray Transients. *ApJ*, 667:1073–1086, October 2007. doi: 10.1086/521181.

M. Linares, D. Chakrabarty, and M. van der Klis. On the Cooling Tails of Thermonuclear X-ray Bursts: The IGR J17480-2446 Link. *ApJL*, 733:L17, June 2011. doi: 10.1088/2041-8205/733/2/L17.

M. Linares, D. Altamirano, D. Chakrabarty, A. Cumming, and L. Keek. Millihertz Quasi-periodic Oscillations and Thermonuclear Bursts from Terzan 5: A Showcase of Burning Regimes. *ApJ*, 748:82, April 2012. doi: 10.1088/0004-637X/748/2/82.

M. Linares, A. Bahramian, C. Heinke, R. Wijnands, A. Patruno, D. Altamirano, J. Homan, S. Bogdanov, and D. Pooley. The neutron star transient and millisecond pulsar in M28: from sub-luminous accretion to rotation-powered quiescence. *MNRAS*, 438:251–261, February 2014. doi: 10.1093/mnras/stt2167.

N. R. Lomb. Least-squares frequency analysis of unequally spaced data. *APSS*, 39:447–462, February 1976. doi: 10.1007/BF00648343.

G. J. M. Luna, J. L. Sokoloski, K. Mukai, and T. Nelson. Symbiotic stars in X-rays. *A&A*, 559:A6, November 2013. doi: 10.1051/0004-6361/201220792.

R. S. Lynch and S. M. Ransom. A New Pulsar in Green Bank Telescope Searches of 10 Globular Clusters. *ApJL*, 730:L11, March 2011. doi: 10.1088/2041-8205/730/1/L11.

T. J. Maccarone. Using radio emission to detect isolated and quiescent accreting black holes. *MNRAS*, 360:L30–L34, June 2005. doi: 10.1111/j.1745-3933.2005.00039.x.

T. J. Maccarone and M. B. Peacock. On the reliability of proxies for globular cluster collision rates. *MNRAS*, 415:1875–1882, August 2011. doi: 10.1111/j.1365-2966.2011.18831.x.

T. J. Maccarone, A. Kundu, S. E. Zepf, and K. L. Rhode. A black hole in a globular cluster. *Natur*, 445:183–185, January 2007. doi: 10.1038/nature05434.

O. K. Madej, J. García, P. G. Jonker, M. L. Parker, R. Ross, A. C. Fabian, and J. Chenevez. X-ray reflection in oxygen-rich accretion discs of ultracompact X-ray binaries. *MNRAS*, 442:1157–1165, August 2014. doi: 10.1093/mnras/stu884.

P. Magdziarz and A. A. Zdziarski. Angle-dependent Compton reflection of X-rays and gamma-rays. *MNRAS*, 273:837–848, April 1995. doi: 10.1093/mnras/273.3.837.

D. Maitra and C. D. Bailyn. Evolution of Spectral States of Aquila X-1 during the 2000 Outburst. *ApJ*, 608:444–453, June 2004. doi: 10.1086/382746.

K. Makishima, T. Ohashi, H. Inoue, K. Koyama, M. Matsuoka, T. Murakami, M. Oda, Y. Ogawara, N. Shibazaki, Y. Tanaka, I. Kondo, S. Hayakawa, H. Kunieda, F. Makino, K. Masai, F. Nagase, Y. Tawara, S. Miyamoto, H. Tsunemi, and K. da Yamashita. Discovery of two new X-ray burst sources in the globular clusters Terzan 1 and Terzan 5. *ApJL*, 247:L23–L25, July 1981. doi: 10.1086/183581.

C. B. Markwardt and J. H. Swank. 4U 1715-390 and NGC 6440 in Outburst. *The Astronomer's Telegram*, 495:1–+, May 2005.

N. Masetti, D. Dal Fiume, G. Cusumano, L. Amati, C. Bartolini, S. Del Sordo, F. Frontera, A. Guarnieri, M. Orlandini, E. Palazzi, A. N. Parmar, A. Piccioni, and A. Santangelo. X-ray and optical monitoring of the peculiar source 4U 1700+24/V934 Her. *A&A*, 382:104–117, January 2002. doi: 10.1051/0004-6361:20011543.

N. Masetti, M. Orlandini, E. Palazzi, L. Amati, and F. Frontera. M-type giants

as optical counterparts of X-ray sources 4U 1700+24 and 4U 1954+319. *A&A*, 453:295–299, July 2006. doi: 10.1051/0004-6361:20065025.

N. Masetti, R. Landi, M. L. Pretorius, V. Sguera, A. J. Bird, M. Perri, P. A. Charles, J. A. Kennea, A. Malizia, and P. Ubertini. IGR J16194-2810: a new symbiotic X-ray binary. *A&A*, 470:331–337, July 2007. doi: 10.1051/0004-6361:20077509.

N. Masetti, U. Munari, A. A. Henden, K. L. Page, J. P. Osborne, and S. Starrfield. Is CGCS 5926 a symbiotic X-ray binary? *A&A*, 534:A89, October 2011. doi: 10.1051/0004-6361/201117260.

D. Massari, A. Mucciarelli, E. Dalessandro, F. R. Ferraro, L. Origlia, B. Lanzoni, G. Beccari, R. M. Rich, E. Valenti, and S. M. Ransom. High-resolution Reddening Map in the Direction of the Stellar System Terzan 5. *ApJL*, 755: L32, August 2012. doi: 10.1088/2041-8205/755/2/L32.

M. Matsuoka, K. Kawasaki, S. Ueno, H. Tomida, M. Kohama, M. Suzuki, Y. Adachi, M. Ishikawa, T. Mihara, M. Sugizaki, N. Isobe, Y. Nakagawa, H. Tsunemi, E. Miyata, N. Kawai, J. Kataoka, M. Morii, A. Yoshida, H. Negoro, M. Nakajima, Y. Ueda, H. Chujo, K. Yamaoka, O. Yamazaki, S. Nakahira, T. You, R. Ishiwata, S. Miyoshi, S. Eguchi, K. Hiroi, H. Katayama, and K. Ebisawa. The MAXI Mission on the ISS: Science and Instruments for Monitoring All-Sky X-Ray Images. *PASJ*, 61:999–1010, October 2009. doi: 10.1093/pasj/61.5.999.

J. E. Maxwell, P. M. Lugger, H. N. Cohn, C. O. Heinke, J. E. Grindlay, S. A. Budac, G. A. Drukier, and C. D. Bailyn. X-Ray Binaries in the Ultrahigh Encounter Rate Globular Cluster NGC 6388. *ApJ*, 756:147, September 2012. doi: 10.1088/0004-637X/756/2/147.

M. Mayer and J. E. Pringle. Time-dependent models of two-phase accretion

discs around black holes. *MNRAS*, 376:435–456, March 2007. doi: 10.1111/ j.1365-2966.2007.11448.x.

D. McConnell, A. A. Deshpande, T. Connors, and J. G. Ables. The radio luminosity distribution of pulsars in 47 Tucanae. *MNRAS*, 348:1409–1414, March 2004.

P. McGregor, J. Hart, P. Conroy, L. Pfitzner, G. Bloxham, D. Jones, M. Downing, M. Dawson, P. Young, M. Jarnyk, and J. van Harmelen. Gemini Near-infrared Integral Field Spectrograph (NIFS). *SPIE*, 4841:178, 2002.

D. E. McLaughlin and R. P. van der Marel. Resolved Massive Star Clusters in the Milky Way and Its Satellites: Brightness Profiles and a Catalog of Fundamental Parameters. *ApJ Supp*, 161:304–360, December 2005. doi: 10.1086/497429.

J. P. McMullin, B. Waters, D. Schiebel, W. Young, and K. Golap. CASA Architecture and Applications. In R. A. Shaw, F. Hill, and D. J. Bell, editors, *Astronomical Data Analysis Software and Systems XVI*, volume 376 of *Astronomical Society of the Pacific Conference Series*, page 127, October 2007.

R. Mewe, E. H. B. M. Gronenschild, and G. H. J. van den Oord. Calculated X-radiation from optically thin plasmas. V. *AAPS*, 62:197–254, November 1985.

R. Mewe, J. R. Lemen, and G. H. J. van den Oord. Calculated X-radiation from optically thin plasmas. VI - Improved calculations for continuum emission and approximation formulae for nonrelativistic average Gaunt factors. *AAPS*, 65:511–536, September 1986.

G. Meylan and D. C. Heggie. Internal dynamics of globular clusters. *AAPR*, 8:1–143, 1997. doi: 10.1007/s001590050008.

T. Mihara, M. Nakajima, M. Sugizaki, M. Serino, M. Matsuoka, M. Kohama, K. Kawasaki, H. Tomida, S. Ueno, N. Kawai, J. Kataoka, M. Morii, A. Yoshida, K. Yamaoka, S. Nakahira, H. Negoro, N. Isobe, M. Yamauchi, and I. Sakurai. Gas Slit Camera (GSC) onboard MAXI on ISS. *PASJ*, 63: 623, November 2011.

J. M. Miller, E. M. Cackett, and R. C. Reis. On Neutral Absorption and Spectral Evolution in X-Ray Binaries. *ApJL*, 707:L77–L81, December 2009. doi: 10.1088/0004-637X/707/1/L77.

J. M. Miller, D. Maitra, E. M. Cackett, S. Bhattacharyya, and T. E. Strohmayer. A Fast X-ray Disk Wind in the Transient Pulsar IGR J17480-2446 in Terzan 5. *ApJL*, 731:L7, April 2011. doi: 10.1088/2041-8205/731/1/L7.

J. M. Miller, M. L. Parker, F. Fuerst, M. Bachetti, D. Barret, B. W. Grefenstette, S. Tendulkar, F. A. Harrison, S. E. Boggs, D. Chakrabarty, F. E. Christensen, W. W. Craig, A. C. Fabian, C. J. Hailey, L. Natalucci, F. Paerels, V. Rana, D. K. Stern, J. A. Tomsick, and W. W. Zhang. Constraints on the Neutron Star and Inner Accretion Flow in Serpens X-1 Using NuSTAR. *ApJL*, 779:L2, December 2013. doi: 10.1088/2041-8205/779/1/L2.

J. C. A. Miller-Jones, J. Strader, C. O. Heinke, T. J. Maccarone, M. van den Berg, C. Knigge, L. Chomiuk, E. Noyola, T. D. Russell, A. C. Seth, and G. R. Sivakoff. Deep radio imaging of 47 Tuc identifies the peculiar X-ray source X9 as a new black hole candidate. *MNRAS*, 453:3918–3931, November 2015. doi: 10.1093/mnras/stv1869.

M. Morscher, S. Umbreit, W. M. Farr, and F. A. Rasio. Retention of Stellar-mass Black Holes in Globular Clusters. *ApJL*, 763:L15, January 2013. doi: 10.1088/2041-8205/763/1/L15.

M. Morscher, B. Pattabiraman, C. Rodriguez, F. A. Rasio, and S. Umbreit. The Dynamical Evolution of Stellar Black Holes in Globular Clusters. *ApJ*, 800:9, February 2015. doi: 10.1088/0004-637X/800/1/9.

S. Motta, A. D'Aı, A. Papitto, A. Riggio, T. di Salvo, L. Burderi, T. Belloni, L. Stella, and R. Iaria. X-ray bursts and burst oscillations from the slowly spinning X-ray pulsar IGR J17480-2446 (Terzan 5). *MNRAS*, 414:1508–1516, June 2011. doi: 10.1111/j.1365-2966.2011.18483.x.

B. W. Murphy, H. N. Cohn, and P. M. Lugger. Fokker-Planck Models for M15 Without a Central Black Hole: The Role of the Mass Function. *ApJ*, 732: 67, May 2011. doi: 10.1088/0004-637X/732/2/67.

U. Murset, B. Wolff, and S. Jordan. X-ray properties of symbiotic stars. II. Systems with colliding winds. *A&A*, 319:201–210, March 1997.

D. M. Nataf, A. Gould, P. Fouqué, O. A. Gonzalez, J. A. Johnson, J. Skowron, A. Udalski, M. K. Szymański, M. Kubiak, G. Pietrzyński, I. Soszyński, K. Ulaczyk, Ł. Wyrzykowski, and R. Poleski. Reddening and Extinction toward the Galactic Bulge from OGLE-III: The Inner Milky Way's R_V ~ 2.5 Extinction Curve. *ApJ*, 769:88, June 2013. doi: 10.1088/0004-637X/769/2/88.

I. Negueruela, P. Reig, M. H. Finger, and P. Roche. Detection of X-ray pulsations from the Be/X-ray transient A 0535+26 during a disc loss phase of the primary. *A&A*, 356:1003–1009, April 2000.

G. Nelemans and P. G. Jonker. Ultra-compact (X-ray) binaries. *New A Rev.*, 54:87–92, March 2010. doi: 10.1016/j.newar.2010.09.021.

G. Nelemans, P. G. Jonker, and D. Steeghs. Optical spectroscopy of (candidate) ultracompact X-ray binaries: constraints on the composition of the donor stars. *MNRAS*, 370:255–262, July 2006. doi: 10.1111/j.1365-2966. 2006.10496.x.

G. Nelemans, L. R. Yungelson, M. V. van der Sluys, and C. A. Tout. The chemical composition of donors in AM CVn stars and ultracompact X-ray binaries: observational tests of their formation. *MNRAS*, 401:1347–1359, January 2010. doi: 10.1111/j.1365-2966.2009.15731.x.

L. A. Nelson, S. A. Rappaport, and P. C. Joss. The evolution of ultrashort period binary systems. *ApJ*, 304:231–240, May 1986. doi: 10.1086/164156.

E. Nespoli, J. Fabregat, and R. E. Mennickent. K-band spectroscopy of IGR J16358-4726 and IGR J16393-4643: two new symbiotic X-ray binaries. *A&A*, 516:A94, June 2010. doi: 10.1051/0004-6361/200913410.

M. S. Noble, L. Ji, A. Young, and J. C. Lee. Parallelizing the XSTAR Photoionization Code. In D. A. Bohlender, D. Durand, and P. Dowler, editors, *Astronomical Data Analysis Software and Systems XVIII*, volume 411 of *Astronomical Society of the Pacific Conference Series*, page 301, September 2009.

M. A. Nowak, S. Heinz, and M. C. Begelman. Hiding in Plain Sight: Chandra Observations of the Quiescent Neutron Star 4U 2129+47 in Eclipse. *ApJ*, 573:778–788, July 2002.

E. Noyola and K. Gebhardt. Surface Brightness Profiles of Galactic Globular Clusters from Hubble Space Telescope Images. *AJ*, 132:447–466, August 2006. doi: 10.1086/505390.

A. A. Nucita, S. Carpano, and M. Guainazzi. XMM observation of 1RXS J180431.1-273932: a new M-type X-ray binary with a 494 s-pulse period neutron star? *A&A*, 474:L1–L4, October 2007. doi: 10.1051/0004-6361: 20078005.

F. Özel, D. Psaltis, T. Güver, G. Baym, C. Heinke, and S. Guillot. The Dense

Matter Equation of State from Neutron Star Radius and Mass Measurements. *ApJ*, 820:28, March 2016. doi: 10.3847/0004-637X/820/1/28.

D. Page, J. M. Lattimer, M. Prakash, and A. W. Steiner. Minimal Cooling of Neutron Stars: A New Paradigm. *ApJ Supp*, 155:623–650, December 2004. doi: 10.1086/424844.

Z. Pan, G. Hobbs, D. Li, A. Ridolfi, P. Wang, and P. Freire. Discovery of two new pulsars in 47 Tucanae (NGC 104). *MNRAS*, 459:L26–L30, June 2016. doi: 10.1093/mnrasl/slw037.

A. Papitto, A. D'Aì, S. Motta, A. Riggio, L. Burderi, T. di Salvo, T. Belloni, and R. Iaria. The spin and orbit of the newly discovered pulsar IGR J17480-2446. *A&A*, 526:L3, February 2011. doi: 10.1051/0004-6361/201015974.

A. Papitto, T. Di Salvo, L. Burderi, T. M. Belloni, L. Stella, E. Bozzo, A. D'Aì, C. Ferrigno, R. Iaria, S. Motta, A. Riggio, and A. Tramacere. The pulse profile and spin evolution of the accreting pulsar in Terzan 5, IGR J17480-2446, during its 2010 outburst. *MNRAS*, 423:1178–1193, June 2012. doi: 10.1111/j.1365-2966.2012.20945.x.

A. Papitto, C. Ferrigno, E. Bozzo, N. Rea, L. Pavan, L. Burderi, M. Burgay, S. Campana, T. di Salvo, M. Falanga, M. D. Filipović, P. C. C. Freire, J. W. T. Hessels, A. Possenti, S. M. Ransom, A. Riggio, P. Romano, J. M. Sarkissian, I. H. Stairs, L. Stella, D. F. Torres, M. H. Wieringa, and G. F. Wong. Swings between rotation and accretion power in a binary millisecond pulsar. *Natur*, 501:517–520, September 2013. doi: 10.1038/nature12470.

A. Papitto, D. de Martino, T. M. Belloni, M. Burgay, A. Pellizzoni, A. Possenti, and D. F. Torres. X-ray coherent pulsations during a sub-luminous accretion disc state of the transitional millisecond pulsar XSS J12270-4859. *MNRAS*, 449:L26–L30, April 2015. doi: 10.1093/mnrasl/slv013.

F. Paresce, G. de Marchi, and F. R. Ferraro. Possible cataclysmic variable in the core of the globular cluster 47 Tucanae. *Natur*, 360:46–48, November 1992.

A. Patruno, D. Altamirano, A. Watts, M. Armas Padilla, Y. Cavecchi, N. Degenaar, M. Kalamkar, R. Kaur, P. Soleri, Y. J. Yang, M. van der Klis, R. Wijnands, P. Casella, M. Linares, N. Rea, C. O. Heinke, and D. Pooley. Detection of pulsations and identification of SAX J1748.9-2021 as the X-ray transient in NGC 6440. *The Astronomer's Telegram*, 2407, January 2010.

A. Patruno, P. Bult, A. Gopakumar, J. M. Hartman, R. Wijnands, M. van der Klis, and D. Chakrabarty. Accelerated Orbital Expansion and Secular Spin-down of the Accreting Millisecond Pulsar SAX J1808.4-3658. *ApJL*, 746:L27, February 2012. doi: 10.1088/2041-8205/746/2/L27.

J. Patterson, J. Kemp, D. A. Harvey, R. E. Fried, R. Rea, B. Monard, L. M. Cook, D. R. Skillman, T. Vanmunster, G. Bolt, E. Armstrong, J. McCormick, T. Krajci, L. Jensen, J. Gunn, N. Butterworth, J. Foote, M. Bos, G. Masi, and P. Warhurst. Superhumps in Cataclysmic Binaries. XXV. q$_{crit}$, ϵ(q), and Mass-Radius. *PASP*, 117:1204–1222, November 2005. doi: 10.1086/447771.

M. B. Peacock, T. J. Maccarone, C. Z. Waters, A. Kundu, S. E. Zepf, C. Knigge, and D. R. Zurek. Wide Field CAMera survey of M31 globular clusters: low-mass X-ray binaries. *MNRAS*, 392:L55–L59, January 2009. doi: 10.1111/j.1745-3933.2008.00588.x.

F. Peng, E. F. Brown, and J. W. Truran. Sedimentation and Type I X-Ray Bursts at Low Accretion Rates. *ApJ*, 654:1022–1035, January 2007. doi: 10.1086/509628.

R. M. Plotkin, E. Gallo, and P. G. Jonker. The X-Ray Spectral Evolution of Galactic Black Hole X-Ray Binaries toward Quiescence. *ApJ*, 773:59, August 2013. doi: 10.1088/0004-637X/773/1/59.

D. Pooley and P. Hut. Dynamical Formation of Close Binaries in Globular Clusters: Cataclysmic Variables. *ApJL*, 646:L143–L146, August 2006. doi: 10.1086/507027.

D. Pooley, W. H. G. Lewin, F. Verbunt, L. Homer, B. Margon, B. M. Gaensler, V. M. Kaspi, J. M. Miller, D. W. Fox, and M. van der Klis. Chandra Observation of the Globular Cluster NGC 6440 and the Nature of Cluster X-Ray Luminosity Functions. *ApJ*, 573:184–190, July 2002. doi: 10.1086/340498.

D. Pooley, W. H. G. Lewin, S. F. Anderson, H. Baumgardt, A. V. Filippenko, B. M. Gaensler, L. Homer, P. Hut, V. M. Kaspi, J. Makino, B. Margon, S. McMillan, S. Portegies Zwart, M. van der Klis, and F. Verbunt. Dynamical Formation of Close Binary Systems in Globular Clusters. *ApJL*, 591:L131–L134, July 2003. doi: 10.1086/377074.

D. Pooley, J. Homan, C. Heinke, M. Linares, D. Altamirano, and W. Lewin. Chandra Identification of the Transient in Terzan 5: Not the 2000 Transient. *The Astronomer's Telegram*, 2974:1, October 2010.

D. Pooley, J. Homan, D. Altamirano, N. Degenaar, C. O. Heinke, W. Lewin, G. R. Sivakoff, and R. Wijnands. Chandra Identification of the 2011 Transient in Terzan 5: Same as the 2000 Transient. *The Astronomer's Telegram*, 3743:1, November 2011a.

D. Pooley, J. Homan, C. O. Heinke, G. R. Sivakoff, D. Altamirano, J. E. Maxwell, H. Cohn, and P. Lugger. Chandra localisation of IGR J17361-4441 in the globular cluster NGC 6388. *The Astronomer's Telegram*, 3627:1, September 2011b.

R. Popham and R. Sunyaev. Accretion Disk Boundary Layers around Neutron Stars: X-Ray Production in Low-Mass X-Ray Binaries. *ApJ*, 547:355–383, January 2001. doi: 10.1086/318336.

P. Predehl, E. Costantini, G. Hasinger, and Y. Tanaka. XMM-Newton observation of the galactic centre - evidence against the X-ray reflection nebulae model? *Astronomische Nachrichten*, 324:73–76, 2003.

R. Protassov, D. A. van Dyk, A. Connors, V. L. Kashyap, and A. Siemiginowska. Statistics, Handle with Care: Detecting Multiple Model Components with the Likelihood Ratio Test. *ApJ*, 571:545–559, May 2002.

G. Pszota, H. Zhang, F. Yuan, and W. Cui. Origin of X-ray emission from transient black hole candidates in quiescence. *MNRAS*, 389:423–428, September 2008. doi: 10.1111/j.1365-2966.2008.13587.x.

M. Rajagopal and R. W. Romani. Model Atmospheres for Low-Field Neutron Stars. *ApJ*, 461:327, April 1996.

S. V. Ramirez, D. L. Depoy, J. A. Frogel, K. Sellgren, and R. D. Blum. Luminosity and Temperature from Near-Infrared Spectra of Late-Type Giant Stars. *AJ*, 113:1411–1420, April 1997. doi: 10.1086/118356.

S. M. Ransom. Twenty Years of Searching for (and Finding) Globular Cluster Pulsars. In C. Bassa, Z. Wang, A. Cumming, & V. M. Kaspi, editor, *40 Years of Pulsars: Millisecond Pulsars, Magnetars and More*, volume 983 of *AIP Conf. Ser.*, pages 415–423, February 2008. doi: 10.1063/1.2900267.

S. M. Ransom, J. W. T. Hessels, I. H. Stairs, P. C. C. Freire, F. Camilo, V. M. Kaspi, and D. L. Kaplan. Twenty-One Millisecond Pulsars in Terzan 5 Using the Green Bank Telescope. *Science*, 307:892–896, February 2005. doi: 10.1126/science.1108632.

P. Reig, V. Doroshenko, and A. Zezas. The quiescent state of the accreting X-ray pulsar SAX J2103.5+4545. *MNRAS*, 445:1314–1320, December 2014. doi: 10.1093/mnras/stu1840.

R. A. Remillard and J. E. McClintock. X-Ray Properties of Black-Hole Binaries. *ARAA*, 44:49–92, September 2006. doi: 10.1146/annurev.astro.44.051905.092532.

A. Richichi, L. Fabbroni, S. Ragland, and M. Scholz. A homogeneous temperature calibration for K and M giants with an extension to the coolest stars. *A&A*, 344:511–520, April 1999.

A. Riggio, L. Burderi, T. Di Salvo, A. Papitto, E. Egron, T. Belloni, A. D'Aì, R. Iaria, M. Floris, S. Motta, V. Testa, M. T. Menna, and N. R. Robba. Subarcsecond Location of IGR J17480-2446 with Rossi XTE. *ApJL*, 754: L11, July 2012. doi: 10.1088/2041-8205/754/1/L11.

R. W. Romani. Model atmospheres for cooling neutron stars. *ApJ*, 313:718–726, February 1987.

P. Romano, S. Campana, G. Chincarini, J. Cummings, G. Cusumano, S. T. Holland, V. Mangano, T. Mineo, K. L. Page, V. Pal'Shin, E. Rol, T. Sakamoto, B. Zhang, R. Aptekar, S. Barbier, S. Barthelmy, A. P. Beardmore, P. Boyd, D. N. Burrows, M. Capalbi, E. E. Fenimore, D. Frederiks, N. Gehrels, P. Giommi, M. R. Goad, O. Godet, S. Golenetskii, D. Guetta, J. A. Kennea, V. La Parola, D. Malesani, F. Marshall, A. Moretti, J. A. Nousek, P. T. O'Brien, J. P. Osborne, M. Perri, and G. Tagliaferri. Panchromatic study of GRB 060124: from precursor to afterglow. *A&A*, 456:917–927, September 2006. doi: 10.1051/0004-6361:20065071.

M. M. Romanova, G. V. Ustyugova, A. V. Koldoba, and R. V. E. Lovelace. Magnetohydrodynamic Simulations of Disk-Magnetized Star Interactions in the Quiescent Regime: Funnel Flows and Angular Momentum Transport. *ApJ*, 578:420–438, October 2002. doi: 10.1086/342464.

R. E. Rutledge, L. Bildsten, E. F. Brown, G. G. Pavlov, and V. E. Zavlin. The

Thermal X-Ray Spectra of Centaurus X-4, Aquila X-1 , and 4U 1608-522 in Quiescence. *ApJ*, 514:945–951, April 1999.

R. E. Rutledge, L. Bildsten, E. F. Brown, G. G. Pavlov, and V. E. Zavlin. The Quiescent X-Ray Spectrum of the Neutron Star in Centaurus X-4 Observed with Chandra/ACIS-S. *ApJ*, 551:921–928, April 2001.

R. E. Rutledge, L. Bildsten, E. F. Brown, G. G. Pavlov, and V. E. Zavlin. A Possible Transient Neutron Star in Quiescence in the Globular Cluster NGC 5139. *ApJ*, 578:405–412, October 2002a.

R. E. Rutledge, L. Bildsten, E. F. Brown, G. G. Pavlov, and V. E. Zavlin. Variable Thermal Emission from Aquila X-1 in Quiescence. *ApJ*, 577:346–358, September 2002b.

R. E. Rutledge, L. Bildsten, E. F. Brown, G. G. Pavlov, V. E. Zavlin, and G. Ushomirsky. Crustal Emission and the Quiescent Spectrum of the Neutron Star in KS 1731-260. *ApJ*, 580:413–422, November 2002c.

M. Salaris and A. Weiss. Metal-rich globular clusters in the galactic disk: new age determinations and the relation to halo clusters. *A&A*, 335:943–953, July 1998.

M. Salaris, E. V. Held, S. Ortolani, M. Gullieuszik, and Y. Momany. Deep near-infrared photometry of the globular cluster 47 Tucanae. Reconciling theory and observations. *A&A*, 476:243–253, December 2007. doi: 10.1051/0004-6361:20078445.

R. J. Sault, P. J. Teuben, and M. C. H. Wright. A Retrospective View of MIRIAD. In R. A. Shaw, H. E. Payne, and J. J. E. Hayes, editors, *Astronomical Data Analysis Software and Systems IV*, volume 77 of *Astronomical Society of the Pacific Conference Series*, page 433, 1995.

J. D. Scargle. Studies in astronomical time series analysis. II - Statistical aspects of spectral analysis of unevenly spaced data. *ApJ*, 263:835–853, December 1982.

D. J. Schlegel, D. P. Finkbeiner, and M. Davis. Maps of Dust Infrared Emission for Use in Estimation of Reddening and Cosmic Microwave Background Radiation Foregrounds. *ApJ*, 500:525, June 1998. doi: 10.1086/305772.

M. Serino, T. Mihara, M. Matsuoka, S. Nakahira, M. Sugizaki, Y. Ueda, N. Kawai, and S. Ueno. Superburst with Outburst from EXO 1745-248 in Terzan 5 with MAXI. *PASJ*, 64:91, October 2012.

M. Servillat, C. O. Heinke, W. C. G. Ho, J. E. Grindlay, J. Hong, M. van den Berg, and S. Bogdanov. Neutron star atmosphere composition: the quiescent, low-mass X-ray binary in the globular cluster M28. *MNRAS*, 423:1556–1561, June 2012. doi: 10.1111/j.1365-2966.2012.20976.x.

S. Sigurdsson and L. Hernquist. Primordial black holes in globular clusters. *Natur*, 364:423–425, July 1993. doi: 10.1038/364423a0.

A. C. Sippel and J. R. Hurley. Multiple stellar-mass black holes in globular clusters: theoretical confirmation. *MNRAS*, 430:L30–L34, March 2013. doi: 10.1093/mnrasl/sls044.

G. R. Sivakoff, A. Jordán, C. L. Sarazin, J. P. Blakeslee, P. Côté, L. Ferrarese, A. M. Juett, S. Mei, and E. W. Peng. The Low-Mass X-Ray Binary and Globular Cluster Connection in Virgo Cluster Early-Type Galaxies: Optical Properties. *ApJ*, 660:1246–1263, May 2007. doi: 10.1086/513094.

M. F. Skrutskie, R. M. Cutri, R. Stiening, M. D. Weinberg, S. Schneider, J. M. Carpenter, C. Beichman, R. Capps, T. Chester, J. Elias, J. Huchra, J. Liebert, C. Lonsdale, D. G. Monet, S. Price, P. Seitzer, T. Jarrett, J. D. Kirkpatrick, J. E. Gizis, E. Howard, T. Evans, J. Fowler, L. Fullmer, R. Hurt,

R. Light, E. L. Kopan, K. A. Marsh, H. L. McCallon, R. Tam, S. Van Dyk, and S. Wheelock. The Two Micron All Sky Survey (2MASS). *AJ*, 131: 1163–1183, February 2006. doi: 10.1086/498708.

M. Smits, T. J. Maccarone, A. Kundu, and S. E. Zepf. The globular cluster mass/low mass X-ray binary correlation: implications for kick velocity distributions from supernovae. *A&A*, 458:477–484, November 2006. doi: 10.1051/0004-6361:20065298.

A. Sollima, M. Bellazzini, and J.-W. Lee. A Comparison between the Stellar and Dynamical Masses of Six Globular Clusters. *ApJ*, 755:156, August 2012. doi: 10.1088/0004-637X/755/2/156.

W. S. Stacey, C. O. Heinke, R. F. Elsner, P. D. Edmonds, M. C. Weisskopf, and J. E. Grindlay. Transient Extremely Soft X-ray Emission from the Unusually Bright Cataclysmic Variable in the Globular Cluster M3: A New CV X-ray Luminosity Record? *ApJ*, 732:46–+, May 2011. doi: 10.1088/0004-637X/732/1/46.

W. S. Stacey, C. O. Heinke, H. N. Cohn, P. M. Lugger, and A. Bahramian. An Examination of the X-Ray Sources in the Globular Cluster NGC 6652. *ApJ*, 751:62, May 2012. doi: 10.1088/0004-637X/751/1/62.

A. W. Steiner, J. M. Lattimer, and E. F. Brown. The Equation of State from Observed Masses and Radii of Neutron Stars. *ApJ*, 722:33–54, October 2010. doi: 10.1088/0004-637X/722/1/33.

A. W. Steiner, J. M. Lattimer, and E. F. Brown. The Neutron Star Mass-Radius Relation and the Equation of State of Dense Matter. *ApJL*, 765:L5, March 2013. doi: 10.1088/2041-8205/765/1/L5.

L. Stella, W. Priedhorsky, and N. E. White. The discovery of a 685 second

orbital period from the X-ray source 4U 1820 - 30 in the globular cluster NGC 6624. *ApJL*, 312:L17–L21, January 1987.

J. Strader, L. Chomiuk, T. J. Maccarone, J. C. A. Miller-Jones, and A. C. Seth. Two stellar-mass black holes in the globular cluster M22. *Natur*, 490: 71–73, October 2012. doi: 10.1038/nature11490.

T. E. Strohmayer and C. B. Markwardt. EXO 1745-248 is an 11 Hz Eclipsing Pulsar. *The Astronomer's Telegram*, 2929:1, October 2010.

T. E. Strohmayer, C. B. Markwardt, D. Pereira, and E. A. Smith. A Refined Orbital Solution and the Transient Pulsar in Terzan 5 is Not Eclipsing. *The Astronomer's Telegram*, 2946:1–+, October 2010.

W. Sutantyo. The formation of globular cluster X-ray sources through neutron star-giant collisions. *A&A*, 44:227–230, November 1975.

P. H. T. Tam, A. K. H. Kong, C. Y. Hui, K. S. Cheng, C. Li, and T.-N. Lu. Gamma-ray Emission from the Globular Clusters Liller 1, M80, NGC 6139, NGC 6541, NGC 6624, and NGC 6752. *ApJ*, 729:90, March 2011. doi: 10.1088/0004-637X/729/2/90.

S. P. Tendulkar, C. Yang, H. An, V. M. Kaspi, A. M. Archibald, C. Bassa, E. Bellm, S. Bogdanov, F. A. Harrison, J. W. T. Hessels, G. H. Janssen, A. G. Lyne, A. Patruno, B. Stappers, D. Stern, J. A. Tomsick, S. E. Boggs, D. Chakrabarty, F. E. Christensen, W. W. Craig, C. A. Hailey, and W. Zhang. NuSTAR Observations of the State Transition of Millisecond Pulsar Binary PSR J1023+0038. *ApJ*, 791:77, August 2014. doi: 10.1088/0004-637X/791/2/77.

V. Testa, T. di Salvo, F. D'Antona, M. T. Menna, P. Ventura, L. Burderi, A. Riggio, R. Iaria, A. D'Aì, A. Papitto, and N. Robba. The

near-IR counterpart of ¡ASTROBJ¿IGR J17480-2446¡/ASTROBJ¿ in ¡AS-TROBJ¿Terzan 5¡/ASTROBJ¿. *A&A*, 547:A28, November 2012. doi: 10.1051/0004-6361/201219904.

A. J. Tetarenko, A. Bahramian, G. R. Sivakoff, E. Tremou, M. Linares, V. Tudor, J. C. A. Miller-Jones, C. O. Heinke, L. Chomiuk, J. Strader, D. Altamirano, N. Degenaar, T. Maccarone, A. Patruno, A. Sanna, and R. Wijnands. Disc-Jet Coupling in the Terzan 5 Neutron Star X-ray Binary EXO 1745-248. *MNRAS*, April 2016a. doi: 10.1093/mnras/stw1013.

B. E. Tetarenko, A. Bahramian, R. M. Arnason, J. C. A. Miller-Jones, S. Repetto, C. O. Heinke, T. J. Maccarone, L. Chomiuk, G. R. Sivakoff, J. Strader, F. Kirsten, and W. Vlemmings. The first low-mass black hole X-ray binary identified in quiescence outside of a globular cluster. *ArXiv e-prints*, May 2016b. 1605.00270.

L. Titarchuk. Generalized Comptonization models and application to the recent high-energy observations. *ApJ*, 434:570–586, October 1994.

S. C. Trager, I. R. King, and S. Djorgovski. Catalogue of Galactic globular-cluster surface-brightness profiles. *AJ*, 109:218–241, January 1995.

G. Ushomirsky and R. E. Rutledge. Time-variable emission from transiently accreting neutron stars in quiescence due to deep crustal heating. *MNRAS*, 325:1157–1166, August 2001. doi: 10.1046/j.1365-8711.2001.04515.x.

E. Valenti, F. R. Ferraro, and L. Origlia. Near-Infrared Properties of 24 Globular Clusters in the Galactic Bulge. *AJ*, 133:1287–1301, April 2007. doi: 10.1086/511271.

G. T. van Belle, B. F. Lane, R. R. Thompson, A. F. Boden, M. M. Colavita, P. J. Dumont, D. W. Mobley, D. Palmer, M. Shao, G. X. Vasisht, J. K. Wallace, M. J. Creech-Eakman, C. D. Koresko, S. R. Kulkarni, X. P. Pan,

and J. Gubler. Radii and Effective Temperatures for G, K, and M Giants and Supergiants. *AJ*, 117:521–533, January 1999. doi: 10.1086/300677.

M. van den Berg, J. Grindlay, S. Laycock, J. Hong, P. Zhao, X. Koenig, E. M. Schlegel, H. Cohn, P. Lugger, R. M. Rich, A. K. Dupree, G. H. Smith, and J. Strader. ChaMPlane Discovery of Candidate Symbiotic Binaries in Baade's and Stanek's Windows. *ApJL*, 647:L135–L138, August 2006. doi: 10.1086/506613.

M. van den Berg, K. Penner, J. Hong, J. E. Grindlay, P. Zhao, S. Laycock, and M. Servillat. The ChaMPlane Bright X-Ray Sources – Galactic Longitudes l = 2° -358° . *ApJ*, 748:31, March 2012. doi: 10.1088/0004-637X/748/1/31.

J. van Paradijs, W. Penninx, and W. H. G. Lewin. On the relation between X-ray burst properties and the persistent X-ray luminosity. *MNRAS*, 233: 437–450, July 1988.

J.T. Vanderplas, A.J. Connolly, Ž. Ivezić, and A. Gray. Introduction to astroml: Machine learning for astrophysics. In *Conference on Intelligent Data Understanding (CIDU)*, pages 47 –54, oct. 2012. doi: 10.1109/CIDU.2012.6382200.

F. Verbunt. Binary Evolution and Neutron Stars in Globular Clusters. In G. Piotto, G. Meylan, S. G. Djorgovski, and M. Riello, editors, *New Horizons in Globular Cluster Astronomy*, volume 296 of *Astronomical Society of the Pacific Conference Series*, page 245, 2003.

F. Verbunt and G. Hasinger. Nine X-ray sources in the globular cluster 47 Tucanae. *A&A*, 336:895–901, August 1998.

F. Verbunt and P. Hut. The Globular Cluster Population of X-Ray Binaries. In *IAU Symp. 125: The Origin and Evolution of Neutron Stars*, page 187, 1987.

F. Verbunt and W. H. G. Lewin. *Globular cluster X-ray sources*, pages 341–379. In: Compact Stellar X-ray Sources, eds. W.H.G. Lewin and M. van der Klis (Cambridge: Cambridge Univ. Press), April 2006.

F. Verbunt and G. Meylan. Mass segregation and formation of X-ray sources in globular clusters. *A&A*, 203:297–305, September 1988.

F. Verbunt, W. Bunk, G. Hasinger, and H. M. Johnston. The ROSAT XRT Sky Survey of X-ray sources in globular clusters. *A&A*, 300:732, August 1995.

D. A. Verner, G. J. Ferland, K. T. Korista, and D. G. Yakovlev. Atomic Data for Astrophysics. II. New Analytic FITS for Photoionization Cross Sections of Atoms and Ions. *ApJ*, 465:487, July 1996. doi: 10.1086/177435.

L. Wallace and K. Hinkle. Medium-Resolution Spectra of Normal Stars in the K Band. *ApJ Supp*, 111:445, August 1997. doi: 10.1086/313020.

A. R. Walsh, E. M. Cackett, and F. Bernardini. Investigating variability of quiescent neutron stars in the globular clusters NGC 6440 and Terzan 5. *MNRAS*, 449:1238–1250, May 2015. doi: 10.1093/mnras/stv315.

F. M. Walter, K. O. Mason, J. T. Clarke, J. Halpern, J. E. Grindlay, S. Bowyer, and J. P. Henry. Discovery of a 50 minute binary period and a likely 22 magnitude optical counterpart for the X-ray burster 4U 1915-05. *ApJL*, 253: L67–L71, February 1982. doi: 10.1086/183738.

R. S. Warwick, A. J. Norton, M. J. L. Turner, M. G. Watson, and R. Willingale. A survey of the galactic plane with EXOSAT. *MNRAS*, 232:551–564, June 1988.

N. A. Webb and D. Barret. Constraining the Equation of State of Supranuclear Dense Matter from XMM-Newton Observations of Neutron Stars in Globular Clusters. *ApJ*, 671:727–733, December 2007. doi: 10.1086/522877.

M. C. Weisskopf, B. Brinkman, C. Canizares, G. Garmire, S. Murray, and L. P. Van Speybroeck. An Overview of the Performance and Scientific Results from the Chandra X-Ray Observatory. *PASP*, 114:1–24, January 2002. doi: 10.1086/338108.

N. E. White and L. Angelini. The Discovery of a Second Luminous Low-Mass X-Ray Binary in the Globular Cluster M15. *ApJL*, 561:L101–L105, November 2001.

R. Wijnands, M. Guainazzi, M. van der Klis, and M. Méndez. XMM-Newton Observations of the Neutron Star X-Ray Transient KS 1731-260 in Quiescence. *ApJL*, 573:L45–L49, July 2002a.

R. Wijnands, J. Homan, and R. Remillard. A new X-ray outburst of XB 1745-25 in the globular cluster Terzan 5. *The Astronomer's Telegram*, 101:1, July 2002b.

R. Wijnands, J. M. Miller, and Q. D. Wang. Chandra Observations of the Bursting X-Ray Transient SAX J1747.0-2853 during Low-Level Accretion Activity. *ApJ*, 579:422–429, November 2002c. doi: 10.1086/342788.

R. Wijnands, M. Nowak, J. M. Miller, J. Homan, S. Wachter, and W. H. G. Lewin. A Chandra Observation of the Neutron Star X-Ray Transient and Eclipsing Binary MXB 1659-29 in Quiescence. *ApJ*, 594:952–960, September 2003.

R. Wijnands, C. O. Heinke, D. Pooley, P. D. Edmonds, W. H. G. Lewin, J. E. Grindlay, P. G. Jonker, and J. M. Miller. The Hard Quiescent Spectrum of the Neutron Star X-Ray Transient EXO 1745-248 in the Globular Cluster Terzan 5. *ApJ*, 618:883–890, January 2005. doi: 10.1086/426127.

R. Wijnands, D. Altamirano, C. O. Heinke, G. R. Sivakoff, and D. Pooley.

A new X-ray transient in the globular cluster Terzan 5. *The Astronomer's Telegram*, 4242:1, July 2012.

R. Wijnands, N. Degenaar, and D. Page. Testing the deep-crustal heating model using quiescent neutron-star very-faint X-ray transients and the possibility of partially accreted crusts in accreting neutron stars. *MNRAS*, 432:2366–2377, July 2013. doi: 10.1093/mnras/stt599.

R. Wijnands, N. Degenaar, M. Armas Padilla, D. Altamirano, Y. Cavecchi, M. Linares, A. Bahramian, and C. O. Heinke. Low-level accretion in neutron star X-ray binaries. *MNRAS*, 454:1371–1386, December 2015. doi: 10.1093/mnras/stv1974.

J. Wilms, A. Allen, and R. McCray. On the Absorption of X-Rays in the Interstellar Medium. *ApJ*, 542:914–924, October 2000. doi: 10.1086/317016.

W. E. Wilson, R. H. Ferris, P. Axtens, A. Brown, E. Davis, G. Hampson, M. Leach, P. Roberts, S. Saunders, B. S. Koribalski, J. L. Caswell, E. Lenc, J. Stevens, M. A. Voronkov, M. H. Wieringa, K. Brooks, P. G. Edwards, R. D. Ekers, B. Emonts, L. Hindson, S. Johnston, S. T. Maddison, E. K. Mahony, S. S. Malu, M. Massardi, M. Y. Mao, D. McConnell, R. P. Norris, D. Schnitzeler, R. Subrahmanyan, J. S. Urquhart, M. A. Thompson, and R. M. Wark. The Australia Telescope Compact Array Broad-band Backend: description and first results. *MNRAS*, 416:832–856, September 2011. doi: 10.1111/j.1365-2966.2011.19054.x.

K. A. Woodley, R. Goldsbury, J. S. Kalirai, H. B. Richer, P.-E. Tremblay, J. Anderson, P. Bergeron, A. Dotter, L. Esteves, G. G. Fahlman, B. M. S. Hansen, J. Heyl, J. Hurley, R. M. Rich, M. M. Shara, and P. B. Stetson. The Spectral Energy Distributions of White Dwarfs in 47 Tucanae: The Distance to the Cluster. *AJ*, 143:50, February 2012. doi: 10.1088/0004-6256/143/2/50.

H. Worpel, D. K. Galloway, and D. J. Price. Evidence for Accretion Rate Change during Type I X-Ray Bursts. *ApJ*, 772:94, August 2013. doi: 10.1088/0004-637X/772/2/94.

D. G. Yakovlev and C. J. Pethick. Neutron Star Cooling. *ARAA*, 42:169–210, September 2004.

F. Yuan and W. Cui. Radio-X-Ray Correlation and the "Quiescent State" of Black Hole Sources. *ApJ*, 629:408–413, August 2005. doi: 10.1086/431453.

L. Zampieri, R. Turolla, S. Zane, and A. Treves. X-ray spectra from neutron stars accreting at low rates. *ApJ*, 439:849–853, February 1995.

S. Zane, R. Turolla, and A. Treves. Magnetized Atmospheres around Neutron Stars Accreting at Low Rates. *ApJ*, 537:387–395, July 2000. doi: 10.1086/309027.

V. E. Zavlin, G. G. Pavlov, and Y. A. Shibanov. Model neutron star atmospheres with low magnetic fields. I. Atmospheres in radiative equilibrium. *A&A*, 315:141–152, November 1996.

A. Zocchi, G. Bertin, and A. L. Varri. A dynamical study of Galactic globular clusters under different relaxation conditions. *A&A*, 539:A65, March 2012. doi: 10.1051/0004-6361/201117977.

D. R. Zurek, C. Knigge, T. J. Maccarone, A. Dieball, and K. S. Long. An Ultracompact X-Ray Binary in the Globular Cluster NGC 1851. *ApJ*, 699:1113–1118, July 2009. doi: 10.1088/0004-637X/699/2/1113.

Appendix

Complete form of tables 2.2 & 2.5

Tables 2.2 and 2.5 as presented in Chapter 2 are only a portion of the complete tables. Here I present both tables in their entirety.

Name	E(B-V)	(m-M)	D(kpc)	σ_c(km/s)	σ Ref.	SBP Ref.	CC	$\delta\mu$	Γ	Lower bound	Upper bound
Terzan 5	2.61±0.10	21.27±0.2	5.98	8.06±2.58	g	l	n	0.20	6800.00	3780.00	7840.00
NGC 7078	0.1±0.02	15.39±0.1	10.3	13.5±0.9	h	n	c	0.14	4510.0	3520.0	5870.0
NGC 6715	0.15±0.02	17.58±0.1	26.4	10.5±0.3	h	n	n	0.03	2520.0	2250.0	2750.0
Terzan 6	2.35±0.35	21.44±0.1	6.78	5.27±1.69	g	t	c	0.1	2470.0	753.0	7540.0
NGC 6441	0.47±0.07	16.78±0.1	11.6	18.0±0.2	h	n	n	0.1	2300.0	1660.0	3270.0
NGC 6266	0.47±0.07	15.63±0.1	6.83	14.3±0.4	h	n	c	0.16	1670.0	1100.0	2380.0
NGC 1851	0.02±0.01	15.47±0.1	12.0	10.4±0.5	h	n	n	0.06	1530.0	1340.0	1730.0
NGC 6440	1.07±0.16	17.95±0.1	8.45	13.71±4.3	g	t	n	0.11	1400.0	923.0	2030.0
NGC 6624	0.28±0.04	15.36±0.1	7.91	5.4±0.5	h	n	c	0.06	1150.0	972.0	1260.0
NGC 6681	0.07±0.01	14.99±0.1	9.01	5.2±0.5	h	n	c	0.12	1040.0	848.0	1310.0
NGC 104	0.04±0.01	13.37±0.1	4.46	11.0±0.3	h	n	n	0.08	1000.0	866.0	1150.0
NGC 5824	0.13±0.02	17.94±0.1	32.1	11.6±0.5	h	n	n	0.1	984.0	829.0	1160.0
Palomar 2	1.24±0.19	21.01±0.1	27.1	4.7±1.5	g	t	n	0.36	929.0	374.0	1770.0
NGC 2808	0.22±0.03	15.59±0.1	9.59	13.4±1.2	h	n	n	0.03	923.0	840.0	990.0
NGC 6388	0.37±0.06	16.13±0.1	9.92	18.9±0.8	h	n	n	0.1	899.0	686.0	1140.0
NGC 6293	0.36±0.05	16.0±0.1	9.48	7.7±1.3	h	n	c	0.2	847.0	608.0	1220.0
NGC 362	0.05±0.01	14.83±0.1	8.61	6.4±0.3	h	t	c	0.1	735.0	618.0	872.0

NGC 6652	0.09±0.01	15.28±0.1	10.0	5.9±1.89	g	n	n	0.11	700.0	511.0	992.0
NGC 6284	0.28±0.04	16.79±0.1	15.2	6.3±0.9	h	n	c	0.08	666.0	561.0	788.0
NGC 6626	0.4±0.06	14.95±0.1	5.52	8.6±1.3	h	n	n	0.05	648.0	557.0	732.0
NGC 6093	0.18±0.03	15.56±0.1	10.0	12.4±0.6	h	n	n	0.05	532.0	463.0	591.0
NGC 7089	0.06±0.01	15.5±0.1	11.5	8.2±0.6	h	n	n	0.07	518.0	447.0	596.0
NGC 5286	0.24±0.04	16.08±0.1	11.6	8.1±1.0	h	n	n	0.07	458.0	397.0	516.0
NGC 6752	0.04±0.01	13.13±0.1	3.99	4.9±0.4	h	n	c	0.21	401.0	275.0	583.0
NGC 6541	0.14±0.02	14.82±0.1	7.54	8.2±2.1	h	n	c	0.07	386.0	323.0	481.0
NGC 6453	0.64±0.1	17.3±0.1	11.5	3.05±0.98	g	t	c	0.15	371.0	282.0	499.0
NGC 6522	0.48±0.07	15.92±0.1	7.7	6.7±0.7	h	t	c	0.14	363.0	264.0	476.0
NGC 6517	1.08±0.16	18.48±0.1	10.6	13.08±4.1	g	t	n	0.1	338.0	240.0	490.0
NGC 7099	0.03±0.01	14.64±0.1	8.12	5.5±0.4	h	n	c	0.18	324.0	243.0	448.0
NGC 6864	0.16±0.02	17.09±0.1	20.8	10.3±1.5	h	t	n	0.14	307.0	225.0	402.0
NGC 6139	0.75±0.11	17.35±0.1	10.1	9.33±2.99	g	t	n	0.14	307.0	218.0	401.0
NGC 6528	0.54±0.08	16.17±0.1	7.93	3.81±1.22	g	n	n	0.14	278.0	229.0	392.0
NGC 6341	0.02±0.01	14.65±0.1	8.27	6.0±0.4	h	n	n	0.06	270.0	241.0	300.0
NGC 6273	0.38±0.06	15.9±0.1	8.8	9.71±3.11	g	t	n	0.12	200.0	161.0	267.0
NGC 5272	0.01±0.01	15.07±0.1	10.1	5.5±0.3	h	n	n	0.06	194.0	176.0	227.0

NGC 5694	0.09±0.01	18.0±0.1	35.0	5.8±0.8	h	n	n	0.11	191.0	157.0	243.0
NGC 6256	1.09±0.16	18.44±0.1	10.2	6.6±2.6	h	t	c	0.2	169.0	109.0	288.0
NGC 5904	0.03±0.01	14.46±0.1	7.47	5.5±0.4	h	n	n	0.12	164.0	134.0	203.0
NGC 6638	0.41±0.06	16.14±0.1	9.41	4.95±1.58	g	t	n	0.11	137.0	110.0	176.0
NGC 5946	0.54±0.08	16.79±0.1	10.5	4.0±2.9	h	t	c	0.14	134.0	89.4	168.0
NGC 6333	0.38±0.06	15.67±0.1	7.91	6.86±2.19	g	n	n	0.22	131.0	89.2	190.0
NGC 6402	0.6±0.09	16.69±0.1	9.25	6.41±2.05	g	t	n	0.14	124.0	93.8	156.0
NGC 6304	0.54±0.08	15.52±0.1	5.88	6.09±1.95	g	t	n	0.15	123.0	101.0	177.0
NGC 6325	0.91±0.14	17.29±0.1	7.83	5.9±1.3	h	t	c	0.16	118.0	72.4	163.0
NGC 6380	1.17±0.18	18.81±0.1	10.8	4.63±1.48	g	t	c	0.17	116.0	71.3	184.0
NGC 1904	0.01±0.01	15.59±0.1	12.9	5.3±0.4	h	n	c	0.08	116.0	102.0	135.0
NGC 6544	0.76±0.11	14.71±0.1	2.96	15.24±4.8	g	t	c	0.21	111.0	74.5	179.0
NGC 6558	0.44±0.07	15.7±0.1	7.37	3.1±0.9	h	t	c	0.12	105.0	85.7	131.0
NGC 6355	0.77±0.12	17.21±0.1	9.22	5.52±1.77	g	t	c	0.16	99.2	73.5	140.0
NGC 6642	0.4±0.06	15.79±0.1	8.13	4.7±1.5	g	t	c	0.14	97.8	73.3	129.0
NGC 5139	0.12±0.02	13.94±0.1	5.17	16.8±0.3	h	t	n	0.14	90.4	70.0	117.0
NGC 6637	0.18±0.03	15.28±0.1	8.8	5.9±1.89	g	n	n	0.1	89.9	71.8	126.0
NGC 6356	0.28±0.04	16.76±0.1	15.0	7.74±2.48	g	t	n	0.07	88.1	74.4	108.0

NGC 6397	0.18±0.03	12.37±0.1	2.3	4.5±0.2	h	n	c	0.13	84.1	65.8	102.0
NGC 6656	0.34±0.05	13.6±0.1	3.23	7.8±0.3	h	t	n	0.17	77.5	51.6	109.0
NGC 6316	0.54±0.08	16.77±0.1	10.4	9.71±3.11	g	t	n	0.14	77.0	62.2	102.0
NGC 6553	0.63±0.09	15.83±0.1	5.96	8.19±2.62	g	t	n	0.16	69.0	50.2	95.8
NGC 6205	0.02±0.01	14.33±0.1	7.14	7.1±0.4	h	n	n	0.12	68.9	54.3	87.0
NGC 5927	0.45±0.07	15.82±0.1	7.67	5.59±1.79	g	t	n	0.09	68.2	57.9	80.9
NGC 5986	0.28±0.04	15.96±0.1	10.4	6.6±2.11	g	t	n	0.08	61.9	51.5	77.8
Palomar 10	1.66±0.25	19.01±0.1	5.93	3.75±1.2	g	t	n	0.08	59.0	23.5	102.0
NGC 6760	0.77±0.12	16.72±0.1	7.36	6.6±2.11	g	t	n	0.21	56.9	37.5	83.5
NGC 6569	0.53±0.08	16.83±0.1	10.9	7.17±2.3	g	t	n	0.24	53.6	32.8	83.8
NGC 6229	0.01±0.01	17.45±0.1	30.4	5.59±1.79	g	t	n	0.15	47.6	38.2	78.6
NGC 6342	0.46±0.07	16.08±0.1	8.53	5.2±2.1	h	t	c	0.17	44.8	32.3	59.2
NGC 6401	0.72±0.11	17.35±0.1	10.5	6.16±1.97	g	t	n	0.12	44.0	33.3	55.0
NGC 6539	1.02±0.15	17.62±0.1	7.79	5.9±1.89	g	t	n	0.24	42.1	26.8	70.7
NGC 6717	0.22±0.03	14.94±0.1	7.11	3.24±1.04	g	t	n	0.22	39.8	26.1	61.6
NGC 6287	0.6±0.09	16.72±0.1	9.38	5.01±1.6	g	n	n	0.11	36.3	28.6	44.0
NGC 5024	0.02±0.01	16.32±0.1	17.8	4.4±0.9	h	t	n	0.15	35.4	25.8	47.8
NGC 6254	0.28±0.04	14.08±0.1	4.39	6.6±0.8	h	n	n	0.06	31.4	27.3	35.7

NGC 6712	0.45±0.07	15.6±0.1	6.93	4.3±0.4	h	n	n	0.07	30.8	24.2	36.4
NGC 6934	0.1±0.02	16.28±0.1	15.6	5.1±1.1	h	t	n	0.17	29.9	21.7	41.9
NGC 6779	0.26±0.04	15.68±0.1	9.44	4.0±0.6	h	t	n	0.21	27.7	18.5	39.9
NGC 6121	0.35±0.05	12.82±0.1	2.22	4.0±0.2	h	t	n	0.18	26.9	17.3	38.5
Terzan 2	1.87±0.28	20.17±0.1	7.49	2.35±0.75	g	t	c	0.16	22.1	7.71	50.7
Palomar 11	0.35±0.05	16.72±0.1	13.4	2.35±0.75	g	t	n	0.22	20.8	13.7	32.0
NGC 5634	0.05±0.01	17.16±0.1	25.1	4.19±1.34	g	t	n	0.22	20.2	12.7	34.4
NGC 4147	0.02±0.01	16.49±0.1	19.3	2.6±0.7	h	t	n	0.24	16.6	10.2	29.1
Palomar 6	1.46±0.22	18.34±0.1	5.79	5.14±1.65	g	t	n	0.1	15.5	7.75	28.7
NGC 1261	0.01±0.01	16.09±0.1	16.2	4.89±1.56	g	t	n	0.19	15.4	11.1	26.0
NGC 6218	0.19±0.03	14.01±0.1	4.83	4.5±0.4	h	t	n	0.18	13.0	8.97	18.4
NGC 6584	0.1±0.02	15.96±0.1	13.4	4.38±1.4	g	t	n	0.15	11.8	8.44	17.2
NGC 6723	0.05±0.01	14.84±0.1	8.65	5.08±1.63	g	c	c	0.21	11.4	7.01	19.4
NGC 7006	0.05±0.01	18.23±0.1	41.2	3.36±1.08	g	t	n	0.17	9.4	6.15	14.3
IC 1276	1.08±0.16	17.01±0.1	5.4	2.98±0.95	g	t	n	0.26	7.97	4.26	16.0
NGC 3201	0.24±0.04	14.2±0.1	4.91	5.0±0.2	h	t	n	0.21	7.17	4.9	10.7
NGC 6171	0.33±0.05	15.05±0.1	6.39	4.1±0.3	h	t	n	0.14	6.77	5.05	9.11
NGC 6352	0.22±0.03	14.43±0.1	5.62	3.43±1.1	g	n	n	0.1	6.74	5.44	8.45

226

NGC 4590	0.05±0.01	15.21±0.1	10.2	2.5±0.4	h	t	n	0.18	5.82	4.12	8.51
NGC 6235	0.31±0.05	16.26±0.1	11.4	2.92±0.93	g	t	n	0.19	5.75	4.16	8.47
NGC 6366	0.71±0.11	14.94±0.1	3.53	1.3±0.5	h	t	n	0.22	5.14	3.38	7.89
NGC 6981	0.05±0.01	16.31±0.1	17.0	2.92±0.93	g	t	n	0.22	4.69	2.93	7.21
NGC 6362	0.09±0.01	14.68±0.1	7.59	2.8±0.4	h	t	n	0.14	4.56	3.53	6.07
NGC 2298	0.14±0.02	15.6±0.1	10.7	3.24±1.04	g	n	n	0.14	4.31	3.1	5.79
TON 2	1.24±0.19	18.41±0.1	8.19	2.73±0.87	g	t	n	0.16	4.29	2.56	8.01
Palomar 8	0.32±0.05	16.53±0.1	12.8	1.59±0.51	g	t	n	0.22	4.22	3.01	6.88
NGC 6809	0.08±0.01	13.89±0.1	5.35	4.0±0.3	h	t	n	0.2	3.23	2.23	4.61
NGC 6144	0.36±0.05	15.86±0.1	8.89	2.35±0.75	g	t	n	0.16	3.14	2.29	4.21
NGC 2419	0.08±0.01	19.83±0.1	82.4	4.0±0.6	h	t	n	0.12	2.8	2.27	3.55
Terzan 9	1.76±0.26	19.71±0.1	7.09	1.33±0.43	g	t	c	0.13	1.71	0.751	3.38
Terzan 7	0.07±0.01	17.01±0.1	22.8	1.08±0.35	g	t	n	0.24	1.59	0.956	2.68
NGC 6426	0.36±0.05	17.68±0.1	20.5	2.35±0.75	g	t	n	0.24	1.58	1.06	2.67
NGC 6101	0.05±0.01	16.1±0.1	15.4	2.73±0.87	g	t	n	0.18	0.974	0.687	1.54
Palomar 1	0.15±0.02	15.7±0.1	11.1	0.57±0.18	g	t	n	0.2	0.895	0.654	1.49
NGC 5897	0.09±0.01	15.76±0.1	12.4	2.73±0.87	g	n	n	0.06	0.851	0.662	1.21
IC4499	0.23±0.03	17.08±0.1	18.7	2.5±0.5	h	t	n	0.22	0.797	0.525	1.21

NGC 288	0.03±0.01	14.84±0.1	8.9	2.9±0.3	h	t	n	0.16	0.766	0.561	1.05
HP 1	1.12±0.17	18.05±0.1	8.23	4.32±1.38	g	t	c	0.25	0.662	0.359	1.07
NGC 6496	0.15±0.02	15.74±0.1	11.3	4.13±1.32	g	t	n	0.31	0.657	0.368	1.27
Palomar 12	0.02±0.01	16.46±0.1	19.0	0.83±0.26	g	t	n	0.4	0.397	0.181	0.817
NGC 6535	0.34±0.05	15.22±0.1	6.81	2.4±0.5	h	n	n	0.38	0.388	0.196	0.777
Terzan 1	1.99±0.3	20.31±0.1	6.73	0.95±0.3	g	t	c	0.14	0.292	0.122	0.566
NGC 5466	0.02±0.01	16.02±0.1	15.5	1.7±0.2	h	t	n	0.12	0.239	0.192	0.306
NGC 4372	0.39±0.06	15.03±0.1	5.81	3.75±1.2	g	t	n	0.43	0.233	0.109	0.598
NGC 7492	0.04±0.01	17.1±0.1	24.8	1.2±1.0	h	t	n	0.25	0.192	0.115	0.435
NGC 5053	0.01±0.01	16.23±0.1	17.3	1.4±0.2	h	t	n	0.24	0.105	0.0688	0.166
Palomar 3	0.04±0.01	19.95±0.1	92.3	0.83±0.26	g	t	n	0.12	0.0409	0.0311	0.0601
Palomar 4	0.01±0.01	20.21±0.1	108.	1.02±0.33	g	t	n	0.13	0.0189	0.0152	0.0298
ARP2	0.1±0.02	17.59±0.1	28.5	0.76±0.24	g	t	n	0.2	0.00518	0.0033	0.00803
AM1	0.02±0.01	20.45±0.1	119.	0.76±0.24	g	t	n	0.3	0.00419	0.00249	0.00883
Palomar 5	0.03±0.01	16.92±0.1	23.2	1.1±0.2	h	t	n	0.19	0.00212	0.00149	0.00298
Palomar 14	0.04±0.01	19.54±0.1	76.4	0.4±0.1	h	t	n	0.14	0.00186	0.0014	0.00273
Palomar 13	0.05±0.01	17.23±0.1	26.0	0.9±0.3	h	t	n	0.45	0.00109	0.00047	0.00277

Table 7.1: The complete version of Table 2.2. All Galactic globular clusters we calculated integrated stellar encounter rate for, with the basic input data for them, their Γ values (normalized to give NGC 104's Γ=1000), and 1-σ bounds. $\delta\mu$ is the assumed error on surface brightness profile. σ Ref. represents the reference of velocity dispersion (g: G02, h: HC) and SBP Ref shows the reference for surface brightness profile (l: L10, n: NG06, t: T95). "c" in the CC column denotes a core-collapsed cluster while "n" indicates none-core collapse (from HC). Note that for Terzan5, extinction calculation is based on Massari et al 2012. To calculate A_v based on this value, we used R_v = 2.83; although for the rest we assumed R_v = 3.1.

Name	$4\pi\sigma_c^{-1}\int\rho^2(r)r^2dr$	$-\delta$	$+\delta$	$\rho_c^2 r_c^3\sigma_c^{-1}$	$-\delta$	$+\delta$	$\rho_c^{1.5}r_c^2$	$-\delta$	$+\delta$
Terzan 5	6.80E+3	3.02E+3	1.04E+3	1.86E+3	9.34E+2	1.99E+3	1.40E+3	2.85E+2	3.23E+2
Terzan 5	6.80E+03	3.02E+03	1.04E+03	1.86E+03	9.34E+02	1.99E+03	1400.0	285.0	323.0
NGC 7078	4.51E+003	9.86E+02	1.36E+03	5.01E+03	2.77E+02	3.00E+02	6460.0	176.0	166.0
NGC 6715	2.52E+003	2.74E+02	2.26E+02	2.55E+03	1.33E+02	1.05E+02	2030.0	43.5	51.1
Terzan 6	2.47E+003	1.72E+03	5.07E+03	1.78E+03	8.51E+02	2.34E+03	1300.0	241.0	279.0
NGC 6441	2.30E+003	6.35E+02	9.74E+02	2.56E+03	1.84E+02	1.80E+02	3150.0	103.0	108.0
NGC 6266	1.67E+003	5.69E+02	7.09E+02	2.02E+03	1.86E+02	1.71E+02	2470.0	81.5	77.8
NGC 1851	1.53E+003	1.86E+02	1.98E+02	1.54E+03	7.66E+01	6.98E+01	1910.0	54.1	54.8
NGC 6440	1.40E+003	4.77E+02	6.28E+02	1.54E+03	5.43E+02	1.02E+03	1750.0	147.0	155.0
NGC 6624	1.15E+003	1.78E+02	1.13E+02	1.20E+03	1.13E+02	1.51E+02	1080.0	26.1	24.5
NGC 6681	1.04E+003	1.92E+02	2.67E+02	9.81E+02	6.04E+01	6.59E+01	964.0	27.5	26.3
NGC 104	1.00E+003	1.34E+02	1.54E+02	1.00E+03	4.81E+01	4.64E+01	1000.0	28.5	30.8
NGC 5824	9.84E+002	1.55E+02	1.71E+02	9.16E+02	4.15E+01	4.89E+01	1220.0	31.8	29.8
Palomar 2	9.29E+002	5.55E+02	8.36E+02	1.18E+03	4.43E+02	8.02E+02	457.0	48.9	42.7
NGC 2808	9.23E+002	8.27E+01	6.72E+01	1.15E+03	9.79E+01	1.11E+02	1210.0	24.9	26.7
NGC 6388	8.99E+002	2.13E+02	2.38E+02	9.53E+02	7.52E+01	7.41E+01	1770.0	48.9	44.1
NGC 6293	8.47E+002	2.39E+02	3.77E+02	9.18E+02	1.51E+02	2.24E+02	1220.0	32.6	30.0

NGC 362	7.35E+002	1.17E+02	1.37E+02	8.09E+02	3.61E+01	3.31E+01	569.0	14.9	15.6
NGC 6652	7.00E+002	1.89E+02	2.92E+02	7.03E+02	1.29E+02	3.60E+02	805.0	22.5	21.3
NGC 6284	6.66E+002	1.05E+02	1.22E+02	7.50E+02	9.82E+01	1.22E+02	797.0	19.5	17.6
NGC 6626	6.48E+002	9.11E+01	8.38E+01	6.43E+02	1.03E+02	1.28E+02	688.0	19.2	17.9
NGC 6093	5.32E+002	6.88E+01	5.91E+01	6.23E+02	3.22E+01	3.71E+01	937.0	20.8	21.2
NGC 7089	5.18E+002	7.14E+01	7.76E+01	5.22E+02	3.02E+01	3.12E+01	441.0	11.8	12.6
NGC 5286	4.58E+002	6.07E+01	5.84E+01	5.16E+02	5.85E+01	6.87E+01	569.0	14.0	11.4
NGC 6752	4.01E+002	1.26E+02	1.82E+02	3.84E+02	2.25E+01	2.42E+01	374.0	9.86	11.3
NGC 6541	3.86E+002	6.31E+01	9.52E+01	3.30E+02	5.82E+01	8.92E+01	567.0	13.0	15.1
NGC 6453	3.71E+002	8.87E+01	1.28E+02	2.70E+02	8.07E+01	1.41E+02	183.0	8.75	8.57
NGC 6522	3.63E+002	9.85E+01	1.13E+02	3.73E+02	4.66E+01	6.28E+01	467.0	15.2	14.9
NGC 6517	3.38E+002	9.75E+01	1.52E+02	3.59E+02	1.25E+02	2.47E+02	661.0	55.0	61.3
NGC 7099	3.24E+002	8.12E+01	1.24E+02	2.46E+02	1.42E+01	1.34E+01	366.0	10.5	10.0
NGC 6139	3.07E+002	8.21E+01	9.54E+01	3.52E+02	1.11E+02	2.26E+02	407.0	23.7	23.1
NGC 6864	3.07E+002	8.93E+01	9.35E+01	3.01E+02	3.52E+01	3.96E+01	370.0	9.87	7.83
NGC 6528	2.78E+002	4.95E+01	1.14E+02	2.78E+02	8.24E+01	1.21E+02	233.0	8.2	9.65
NGC 6341	2.70E+002	2.90E+01	3.01E+01	3.18E+02	1.52E+01	1.98E+01	265.0	6.95	6.69
NGC 6273	2.00E+002	3.86E+01	6.66E+01	2.35E+02	5.67E+01	1.02E+02	246.0	7.32	6.68

NGC 5272	1.94E+002	1.80E+01	3.31E+01	2.14E+02	1.03E+01	9.97E+00	167.0	3.99	5.75
NGC 5694	1.91E+002	3.44E+01	5.22E+01	2.21E+02	2.22E+01	2.78E+01	205.0	5.87	5.29
NGC 6256	1.69E+002	6.04E+01	1.19E+02	1.28E+02	4.99E+01	1.11E+02	242.0	20.0	22.5
NGC 5904	1.64E+002	3.04E+01	3.86E+01	1.51E+02	8.60E+00	8.74E+00	120.0	3.41	3.05
NGC 6638	1.37E+002	2.71E+01	3.86E+01	1.18E+02	3.01E+01	5.40E+01	103.0	3.39	2.77
NGC 5946	1.34E+002	4.46E+01	3.36E+01	1.36E+02	6.12E+01	2.60E+02	122.0	4.42	5.08
NGC 6333	1.31E+002	4.18E+01	5.91E+01	1.54E+02	3.83E+01	7.56E+01	153.0	3.85	4.05
NGC 6402	1.24E+002	3.02E+01	3.18E+01	1.44E+02	3.84E+01	8.05E+01	106.0	4.64	4.21
NGC 6304	1.23E+002	2.20E+01	5.38E+01	1.33E+02	3.91E+01	7.05E+01	150.0	5.72	5.87
NGC 6325	1.18E+002	4.56E+01	4.47E+01	1.07E+02	3.16E+01	4.64E+01	189.0	14.9	13.5
NGC 1904	1.16E+002	4.47E+01	6.76E+01	1.18E+02	6.40E+00	6.64E+00	126.0	2.84	4.2
NGC 6380	1.16E+002	1.42E+01	1.91E+01	1.39E+02	5.07E+01	1.07E+02	96.2	8.95	10.6
NGC 6544	1.11E+002	3.65E+01	6.78E+01	1.18E+02	3.61E+01	6.63E+01	462.0	27.8	25.7
NGC 6558	1.05E+002	1.93E+01	2.62E+01	9.61E+01	2.39E+01	4.00E+01	109.0	3.59	3.35
NGC 6355	9.92E+001	2.57E+01	4.11E+01	8.74E+01	2.53E+01	5.36E+01	130.0	7.86	7.27
NGC 6642	9.78E+001	2.45E+01	3.13E+01	1.01E+02	2.71E+01	4.32E+01	112.0	2.98	3.05
NGC 5139	9.04E+001	2.04E+01	2.63E+01	9.78E+01	4.43E+00	4.59E+00	144.0	3.78	3.68
NGC 6637	8.99E+001	1.81E+01	3.60E+01	8.95E+01	1.99E+01	3.86E+01	92.4	2.23	2.27

NGC 6356	8.81E+001	1.37E+01	2.02E+01	9.95E+01	2.37E+01	4.27E+01	110.0	2.54	2.63
NGC 6397	8.41E+001	1.83E+01	1.83E+01	8.40E+01	4.29E+00	4.40E+00	146.0	3.69	3.26
NGC 6656	7.75E+001	2.59E+01	3.19E+01	8.26E+01	6.07E+00	5.69E+00	92.4	2.45	2.16
NGC 6316	7.70E+001	1.48E+01	2.54E+01	7.86E+01	2.25E+01	4.14E+01	131.0	5.04	4.64
NGC 6553	6.90E+001	1.88E+01	2.68E+01	8.22E+01	2.37E+01	4.40E+01	103.0	4.53	5.01
NGC 6205	6.89E+001	1.46E+01	1.81E+01	8.59E+01	4.45E+00	3.86E+00	89.9	2.55	2.67
NGC 5927	6.82E+001	1.03E+01	1.27E+01	3.96E+02	1.13E+02	1.94E+02	251.0	8.75	7.77
NGC 5986	6.19E+001	1.04E+01	1.59E+01	5.23E+01	1.27E+01	2.36E+01	56.1	1.46	1.27
Palomar 10	5.90E+001	3.55E+01	4.28E+01	1.37E+02	5.78E+01	1.26E+02	75.8	10.9	11.2
NGC 6760	5.69E+001	1.94E+01	2.66E+01	6.39E+01	2.19E+01	3.04E+01	77.0	4.23	4.38
NGC 6569	5.36E+001	2.08E+01	3.02E+01	6.28E+01	1.74E+01	3.07E+01	72.8	2.71	2.91
NGC 6229	4.76E+001	9.36E+00	3.10E+01	4.80E+01	8.80E+00	1.59E+01	49.9	1.21	1.6
NGC 6342	4.48E+001	1.25E+01	1.44E+01	5.02E+01	1.46E+01	3.25E+01	83.7	2.74	3.14
NGC 6401	4.40E+001	1.07E+01	1.10E+01	5.02E+01	1.49E+01	2.67E+01	60.2	3.04	3.79
NGC 6539	4.21E+001	1.53E+01	2.86E+01	4.04E+02	1.37E+02	2.61E+02	271.0	21.1	24.2
NGC 6717	3.98E+001	1.37E+01	2.18E+01	4.01E+01	9.80E+00	1.38E+01	46.1	1.27	1.02
NGC 6287	3.63E+001	7.70E+00	7.70E+00	4.48E+01	1.30E+01	2.06E+01	52.3	2.29	2.33
NGC 5024	3.54E+001	9.60E+00	1.24E+01	3.46E+01	4.61E+00	7.06E+00	28.5	0.807	0.736

NGC 6254	3.14E+001	4.08E+00	3.16E+01	3.76E+00	4.28E+00	42.8	1.04	0.988
NGC 6712	3.08E+001	6.64E+00	3.86E+01	4.97E+00	5.73E+00	33.4	1.22	0.879
NGC 6934	2.99E+001	8.22E+00	2.83E+01	4.07E+00	5.89E+00	31.8	0.789	0.943
NGC 6779	2.77E+001	9.16E+00	2.92E+01	3.94E+00	4.25E+00	25.9	0.586	0.569
NGC 6121	2.69E+001	9.56E+00	3.66E+01	3.18E+00	2.95E+00	34.5	0.982	0.884
Terzan 2	2.21E+001	1.44E+01	1.30E+01	5.71E+00	1.25E+01	19.6	2.72	3.86
Palomar 11	2.08E+001	7.11E+00	2.93E+01	7.21E+00	1.34E+01	12.4	0.274	0.333
NGC 5634	2.02E+001	7.50E+00	2.12E+01	4.42E+00	7.09E+00	24.5	0.7	0.693
NGC 4147	1.66E+001	6.36E+00	1.61E+01	3.06E+00	5.04E+00	14.9	0.443	0.366
Palomar 6	1.55E+001	7.75E+00	3.97E+01	1.53E+01	3.59E+01	40.2	4.72	5.16
NGC 1261	1.54E+001	4.30E+00	1.62E+01	3.08E+00	5.26E+00	17.9	0.433	0.655
NGC 6218	1.30E+001	4.03E+00	1.56E+01	1.40E+00	1.24E+00	18.1	0.415	0.36
NGC 6584	1.18E+001	3.36E+00	2.03E+01	4.10E+00	8.02E+00	22.0	0.627	0.524
NGC 6723	1.14E+001	4.39E+00	1.21E+01	2.25E+00	4.62E+00	13.9	0.4	0.361
NGC 7006	9.40E+000	3.25E+00	6.49E+00	1.40E+00	2.27E+00	6.46	0.184	0.172
IC 1276	7.97E+000	3.71E+00	8.62E+00	3.07E+00	5.78E+00	7.78	0.666	0.763
NGC 3201	7.17E+000	2.27E+00	6.05E+00	3.42E-01	4.07E-01	8.45	0.226	0.187
NGC 6171	6.77E+000	1.72E+00	7.27E+00	6.65E-01	7.10E-01	9.65	0.288	0.22

234

NGC 6352	6.74E+000	1.30E+00	1.71E+00	1.04E+01	2.31E+00	4.25E+00	12.5	0.309	0.277
NGC 4590	5.82E+000	1.70E+00	2.69E+00	5.22E+00	6.78E-01	6.62E-01	4.58	0.127	0.125
NGC 6235	5.75E+000	1.59E+00	2.72E+00	6.92E+00	1.63E+00	3.74E+00	7.11	0.187	0.173
NGC 6366	5.14E+000	1.76E+00	2.75E+00	9.32E+00	2.90E+00	6.60E+00	4.06	0.22	0.211
NGC 6981	4.69E+000	1.76E+00	2.52E+00	4.26E+00	8.75E-01	1.67E+00	4.12	0.121	0.115
NGC 6362	4.56E+000	1.03E+00	1.51E+00	3.78E+00	3.51E-01	4.11E-01	3.57	0.0957	0.0855
NGC 2298	4.31E+000	1.21E+00	1.48E+00	3.93E+00	8.74E-01	1.49E+00	5.37	0.131	0.126
Ton 2	4.29E+000	1.73E+00	3.72E+00	6.85E+00	2.60E+00	4.49E+00	6.45	0.667	0.747
Palomar 8	4.22E+000	1.21E+00	2.66E+00	5.05E+00	1.28E+00	2.27E+00	3.03	0.0894	0.061
NGC 6809	3.23E+000	1.00E+00	1.38E+00	2.83E+00	1.71E-01	1.71E-01	3.65	0.1	0.106
NGC 6144	3.14E+000	8.50E-01	1.07E+00	4.53E+00	1.18E+00	1.93E+00	3.61	0.119	0.0816
NGC 2419	2.80E+000	5.32E-01	7.54E-01	3.56E+00	3.76E-01	4.44E-01	3.37	0.0856	0.0954
Terzan 9	1.71E+000	9.59E-01	1.67E+00	1.67E+00	6.80E-01	1.91E+00	2.79	0.374	0.503
Terzan 7	1.59E+000	6.34E-01	1.09E+00	1.05E+00	2.30E-01	3.85E-01	0.625	0.0183	0.0157
NGC 6426	1.58E+000	5.18E-01	1.09E+00	2.63E+00	6.92E-01	9.68E-01	2.68	0.0838	0.0644
NGC 6101	9.74E-001	2.87E-01	5.67E-01	1.10E+00	2.23E-01	4.12E-01	1.21	0.034	0.0329
Palomar 1	8.95E-001	2.41E-01	6.00E-01	1.38E-02	3.00E-03	5.99E-03	0.0477	0.00111	0.00112
NGC 5897	8.51E-001	1.89E-01	3.57E-01	1.09E+00	2.42E-01	4.45E-01	1.16	0.0303	0.0301

IC 4499	7.97E-001	2.72E-01	4.12E-01	8.77E-01	1.42E-01	2.01E-01	0.941	0.0192	0.0215
NGC 288	7.66E-001	2.05E-01	2.84E-01	9.86E-01	7.59E-02	8.04E-02	1.23	0.0358	0.0349
HP 1	6.62E-001	3.03E-01	4.07E-01	5.32E-01	1.83E-01	3.76E-01	2.75	0.238	0.239
NGC 6496	6.57E-001	2.89E-01	6.16E-01	1.30E+00	2.74E-01	5.15E-01	2.02	0.0442	0.0492
Palomar 12	3.97E-001	2.16E-01	4.20E-01	3.68E-01	6.98E-02	1.67E-01	0.542	0.0139	0.0162
NGC 6535	3.88E-001	1.92E-01	3.89E-01	3.70E-01	7.05E-02	1.02E-01	1.42	0.0397	0.0331
Terzan 1	2.92E-001	1.70E-01	2.74E-01	3.45E-01	1.55E-01	3.33E-01	0.626	0.104	0.116
NGC 5466	2.39E-001	4.75E-02	6.66E-02	1.61E-01	1.28E-02	1.38E-02	0.181	0.0049	0.00576
NGC 4372	2.33E-001	1.24E-01	3.65E-01	1.64E+00	4.25E-01	7.20E-01	2.28	0.0639	0.0613
NGC 7492	1.92E-001	7.65E-02	2.43E-01	1.80E+00	7.37E-01	7.05E+00	0.861	0.0241	0.025
NGC 5053	1.05E-001	3.62E-02	6.10E-02	1.78E-01	1.86E-02	1.67E-02	0.15	0.00352	0.00565
Palomar 3	4.09E-002	9.84E-03	1.92E-02	3.12E-02	6.70E-03	1.18E-02	0.027	0.000741	0.000848
Palomar 4	1.89E-002	3.66E-03	1.09E-02	3.35E-02	6.28E-03	9.72E-03	0.0337	0.000886	0.00144
Arp 2	5.18E-003	1.88E-03	2.85E-03	7.37E-03	1.62E-03	2.69E-03	0.00884	0.000325	0.000324
Am 1	4.19E-003	1.70E-03	4.64E-03	7.10E-03	1.40E-03	2.73E-03	0.00977	0.000359	0.000319
Palomar 5	2.12E-003	6.27E-04	8.61E-04	4.26E-03	5.86E-04	6.46E-04	0.0069	0.000365	0.000395
Palomar 14	1.86E-003	4.59E-04	8.72E-04	3.19E-03	5.81E-04	9.44E-04	0.0025	0.000218	0.000216
Palomar 13	1.09E-003	6.20E-04	1.68E-03	2.00E-03	4.44E-04	8.02E-04	0.00483	0.000209	0.000185

Name								
NGC 6540	12.1	12.6	263.0	1.22E+02	6.58E+01	2.27E+02	–	–
UKS 1	37.0	27.2	100.0	3.90E+01	2.37E+01	1.00E+02	–	–
Terzan 12	7.22	6.36	35.8	1.00E+02	4.08E+01	9.29E+01	–	–
NGC 6749	5.11	4.29	38.5	4.07E+01	2.09E+01	5.15E+01	–	–
NGC 4833	0.559	0.61	25.0	1.08E+01	5.64E+00	2.30E+01	–	–
NGC 6838	0.0445	0.0471	2.05	1.46E-01	1.38E-01	1.47E+00	–	–
Terzan 3	0.0412	0.0565	0.89	6.52E-01	3.67E-01	1.18E+00	–	–
Terzan 8	0.00172	0.00222	0.0793	3.11E-02	2.03E-02	8.41E-02	–	–
Palomar 15	0.000793	0.000682	0.0222	1.11E-02	5.73E-03	2.36E-02	–	–
Terzan 10	1160.0	803.0	4430.0	–	–	–	–	–
Liller 1	164.0	87.2	391.0	–	–	–	–	–
Djorg 2	3.57	3.38	46.4	–	–	–	–	–
Djorg 1	1.25	1.37	9.04	–	–	–	–	–
1636-283	0.0482	0.0698	1.72	–	–	–	–	–
Rup 106	0.00767	0.0081	0.359	–	–	–	–	–
BH 176	0.0056	0.00549	0.146	–	–	–	–	–
E 3	0.0018	0.00204	0.0759	–	–	–	–	–
Eridanus	0.000926	0.00102	0.0339	–	–	–	–	–

| Am 4 | — | — | — | — | 0.0026 | 0.000137 | 0.000155 |

Table 7.2: The complete version of Table 2.5. Γ calculations and 1-σ error estimations based on different equations, all normalized assuming $\Gamma_{NGC104} = 1000$.